UNIVERSITY OF CALIFORNIA, SAN DIEGO

Structural and Functional Design Strategies of Biological Keratinous Materials

A dissertation submitted in partial satisfaction of the requirements
for the degree Doctor of Philosophy

in

Materials Sciences and Engineering

by

Bin Wang

Committee in charge:

Marc A. Meyers, Chair
David J. Benson
Vlado Lubarda
Xanthippi Markenscoff
Joanna McKittrick

2016

The Dissertation of Bin Wang is approved, and it is acceptable in quality and form for publication on microfilm and electronically:

_____

_____

_____

_____

_____

Chair

University of California, San Diego

2016

DEDICATION

This work is dedicated to my family – you have always been so supportive to my endeavors.

TABLE OF CONTENTS

LIST OF FIGURES

LIST OF TABLES

ACKNOWLEDGEMENTS

My advisor, Professor Marc André Meyers, tops the list of people to whom I am deeply grateful throughout my time in the U.S. He accepted me into his group as a Ph.D. student, and advised me with his extraordinary wisdom and passion. It is his continuous support, guidance and advice that gradually mold me into a disciplined and independent researcher; I respect him as an investigator, explorer and human being. Thank you so much for all the invaluable advise to me throughout the past four years. The enthusiasm and passion that you have brought will always be greatly influential to me. I would like to quote one Chinese aphorism here to express my sincere admiration and gratitude to you: *一日为师 终身为父 He who is a mentor for a day is the father for a lifetime.*

My gratefulness also goes to all the members of my Committee: Professor Vlado Lubarda, Professor Joanna McKittrick, Professor Xanthippi Markenscoff, and Professor David J. Benson. It is a privilege to have all of you participate in my projects, offering me constructive suggestions, valuable inspirations and strong support in my dissertation. I am grateful to Professor Sungho Jin who sat into my Senate Exam providing inspiring suggestions and helped me on fundings.

I wish to take the opportunity here to thank Professor Gustaf Arrhenius from the Scripps Institute of Oceanography, who helped me so much in x-ray diffraction with great patience and warmest encouragement, Professor Jennifer Taylor from the Scripps Institute of Oceanography, who provided helpful suggestions to my feather project and allowed me

to use her lab equipment freely, Professor David Parry from Massey University, who spent a lot of his valuable time discussing crystalline structure of keratin with me, and Professor Bingfeng Wang, who worked with me and supported me in many aspects in study and life. I acknowledge Dr. Wen Yang for help in the beginning of my projects and my life here.

I must thank my lovely friends for their enormous support and help, both personally and professionally: Vincent Sherman, Tarah Sullivan, Steve Naleway, Eric Hahn, Andrei Pissarenko, Andrew Marquez, Maria Isabel López Fierro, Tane Remington, Jae-Young Jung, Shiteng Zhao, Daniel Yu, Mike Frank, Frances Su, Yue Wu, Shuang Cui, Yang Shi, Tiantian Zhang. It has been a great time being with all of you, and I am so lucky and delighted to be your friend. If I were given the chance to choose where to do my graduate study again, undoubtedly I would choose here again, for the reason that you are here.

Finally, I am greatly indebted to my family, my parents, younger sister, elder sister and brother-in-law, and parents-in-law, for your unconditional understanding and endless supporting my study, without which I would not be able to complete my Ph.D. Last, but definitely not the least, my sincerest gratitude belongs to my husband, Yinghao Chu, the most wonderful man and best friend in my life. You led me into a new world of wonderfulness and amazingness and we embrace together whatever life gives us. I thank you with all my heart and soul for your unfailing love to me, the most treasure that I cherish in my life. I love you today more than yesterday, but less than I will tomorrow.

Chapter 3, in part, is published as a review article in *Progress in Materials Science* (2014/2015 Impact factor 27.417), and co-authored with W Yang, J McKittrick and M Meyers of UCSD. The dissertation author is the first author of this work.

Chapter 4, in part, is accepted as a research article in *Acta Biomaterialia* (2014/2015 Impact factor 6.025), and co-authored with W. Yang, V Sherman and M Meyers of UCSD. The dissertation author is the first author of this work.

Chapter 5, in full, is in preparation as two manuscripts for publication with co-author M Meyers of UCSD. The dissertation author is the first author of these manuscripts.

VITA

2016 Ph.D. Materials Science and Engineering, University of California, San Diego
2012 M.S. Material Processing Engineering, Zhengzhou University, China
2006-2012 B.S. Materials Science and Engineering, Zhengzhou University, China

Publications

- B Wang, M Meyers. Seagull feather shaft: correlation between structure and mechanical responses, submitted to *Acta Biomater* (IF: 6.205)
- B Wang, M Meyers. Light like a feather: a fibrous natural composite with a shape factor changing from round to square. submitted to *Science* (IF:33.61)
- B Wang, W Yang, V Sherman, M Meyers. Pangolin armor: overlapping, structure, and mechanical properties of the keratinous scales. *Acta Biomater* (IF: 6.205), 2016, accepted.
- B Wang, W Yang, J McKittrick, M Meyers. Keratin: structure, mechanical properties, occurrence in biological organisms and efforts at bioinspiration. *Prog Mater Sci* (IF:27.417), 76(2016), 229-318
- YH Chu, MA Meyers, B Wang, et al. A sustainable substitute for ivory: the Jarina seed from the Amazon. *Scientific Reports* (IF:5.578), 2015, 14387
- BF Wang, F Xie, B Wang, X Luo. Microstructure and properties of the Ti/Al_2O_3/NiCr composites fabricated by explosive compaction/cladding. *Mater Sci Eng C Mater Biol Appl* (IF:3.088), 50(2015),423-331
- BF Wang, ZL Liu, B Wang, ST Zhao, et al. Microstructural evolution in adiabatic shear band in the ultrafine-grained austenitic stainless steel processed by multi-axial compression. *Mater Sci Eng A* (IF:2.567), 611(2014), 100-107
- B Wang, SK Guan, J Wang, LG Wang, SJ Zhu. Effects of Nd on microstructures and properties of extruded Mg–2Zn–0.46Y–xNd alloys for stent application. *Mater Sci Eng B* (IF:2.169), 176(2011), 1673-1678
- B Wang, JH Gao, LG Wang, SJ Zhu, SK Guan. Biocorrosion of coated Mg–Zn–Ca alloy under constant compressive stress close to that of human tibia. *Mater Lett* (IF:2.489), 70(2011),174-176
- JH Gao, SK Guan, ZW Ren, YF Sun, SJ Zhu, B Wang. Homogeneous corrosion of high pressure torsion treated Mg-Zn-Ca alloy in simulated body fluid. *Mater Lett* (IF:2.489), 65(2011), 691-693
- SK Guan, J Wang, LG Wang, SJ Zhu, B Wang, et al. Mg-Zn-Y-Nd alloy for novel biodegradable vascular stents and preparation method thereof. Chinese Patent, 2011, CN102220529A
- SK Guan, JH Hu, et al, B Wang, B Chen. Mg alloys development and surface modification for biomedical application. *Mg INTECH*, Austria, 2011, P109–152

ABSTRACT OF THE DISSERTATION

Structural and Functional Design Strategies of Biological Keratinous Materials

by

Bin Wang

Doctor of Philosophy in Materials Sciences and Engineering

University of California, San Diego, 2016

Professor Marc André Meyers, Chair

Keratinous materials are omnipresent, encompassing terrestrial, aerial and aquatic territories; they form diverse epidermal appendages and serve various interesting functions, triggering the curiosity of humans and inspiring the inventions of novel structures. Among these, pangolin scales and the feather shaft are systematically and analytically studied, answering the questions how the scales function as an armor and the shaft fulfills flight, which contribute to advancing the current knowledge of natural keratinous materials and providing valuable insights in developing new bioinspired designs.

The pangolin is the only known mammal that has keratinous scales covering the

main body. Arboreal and ground pangolin scales show an overlapping pattern in a hexagonal arrangement to provide multi-layered coverage. Scales show three regions in the solid interior that features flattened cells forming crossed lamellae, rarely seen in most keratinous materials. Two dimensional x-ray diffraction reveals the presence of α-helices and possible β-sheet, and the microfibrils are crossed in a range of directions. Scales show an interlocking interface between lamellae, which results from the suture-like cell membrane complex. Scales are transverse isotropic and show a strain-rate dependence, which favor the function in resisting external forces from multi-directions.

The feather shaft, a naturally refined lightweight and stiff flight material, is distinguished in having a changing shape factor: circular at the calamus but square towards the distal rachis; this produces a tailored flexural stiffness along the shaft length fulfilling the local stress requirements. The cortex has a complex fibrous hierarchical structure, both making the shaft longitudinally strong, dorsal-ventrally stiff and torsionally rigid, yet capable of desirable deflection and twisting. Filling the cortex with foamy medulla introduces a synergistic strengthening and toughening mechanisms. Flexure of the shaft reveals decreasing flexural properties towards the distal end; nevertheless, the density-normalized flexural stiffness almost remains the same, and the specific flexural strength increases by 48% at the distal shaft. Knowledge from the structure design of the feather shaft have potentials in developing aircraft materials and biomedical scaffolds.

1 Introduction

1.1 Materials Science and Engineering

It is a truism that materials science underlies all technological advances, and historically, materials are probably more closely related to our culture than people have realized. For example, early civilizations have been designated by the level of their materials' development, e.g. Stone Age, Bronze Age, Iron Age. Materials science and engineering is an interdisciplinary field concerned with inventing new materials and improving known ones by developing a deep and thorough understanding of the microstructure-property-processing relationships, which has been a fascinating research area ever since its inception in the 1950s [1].

There is always a need for refining materials, which is the driving force that advances our society. Over billions of years of evolution, nature has produced a plenty of extremely efficient biological materials, and has become a continuing source of inspirations for engineers: the observation that lotus leaves are always clean despite growing in muddy water led to the production of a self-cleaning paint, Lotusan [2]; dry adhesive tape has been made using the adhesive mechanism of gecko feet [3], [4]; Velcro is a biomimetic invention that has copied burrs to and uses small flexible hooks to reversibly attach to fluffy surfaces. Indeed, people have looked to nature for inspiration for more than 3000 years (since the Chinese first tried to make an artificial silk) [3]. The

accuracy, efficacy and ingenuity of biological systems have always been admired by scientists, who endeavor to learn from these evolutionary refinements and apply the natural designs to develop new materials and technologies. Biomimetics, the science of imitating nature, is thus an emerging multidisciplinary study embracing the practical use of mechanisms and functions of biological science to satisfy engineering needs, leading to the fabrication of novel materials with prominent mechanical properties.

1.2 Biomimetics and Biological Materials Science

The rising field of Biomimetics can be divided into two categories [5]: first, investigating the structures of biological materials at all possible hierarchical scales to deduce the fundamentals of their unique structural designs and then mimick these by current available techniques; second, mastering the molecular synthesis and processing mechanisms and applying these hitherto unknown methodologies to produce new materials superior to those engineered counterparts. Therefore, the study of biological materials, Biological Materials Science, indispensably paves the way for the next exciting step of inventing new materials by providing insights with heretofore unexploited mechanisms of natural designs for synthesizing modern materials [5]–[8]. It involves investigating both structures and physical functions of natural materials with the goal of designing and engineering new functional materials, incorporating Biology as one of the main constituents of Biological Materials Science, shown in Fig1.1 (adapted from [1], [9]).

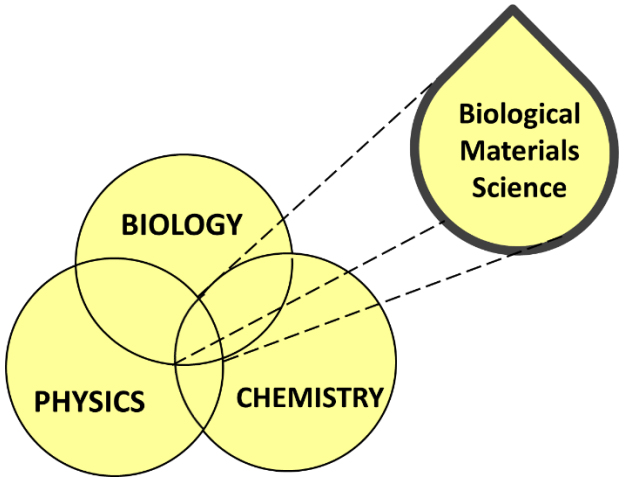

Figure 1.1 Biological materials science at the intersection of physics, chemistry and biology.

Being a young and fascinating research area, Biological Materials Science has rapidly emerged to be at the forefront of materials research [10]. The classic work by Thompson [11] in 1917, On growth and form, was considered as the foundation: investigating the shape and form of various biological systems and relating them to their engineering functions. This initiated the flow of research on biological materials from a mechanistic perspective with the goal to derive mechanisms and principles to develop modern materials. Other works of significance in this field include books such as Cellular solids [12], Bones: structure and mechanics [13], Mechanical design in organisms [14], Structural biological materials [7]. There are a number of review papers, on biological materials [1], [10], [15], on biomineralization [16], [17], on hierarchical structure of natural materials [18] presenting the rapid development and prominence of Biological Materials Science. And there are several international conferences dedicated to this theme, Mechanics and Biomaterials & Tissues (2005, 2006, 2009, 2011) organized by the Journal

of Mechanical Behavior of Biomedical Materials and by yearly Biological Materials Science Symposia held at the TMSAIME meeting (2006-2011) [10]. This field is gaining increasing global recognition, and the potential of the field of biological materials continues attracting the interest of an increasing number of researchers.

1.3 Natural designs: structure and mechanical properties

Nature has achieved materials with properties and mechanisms that go far beyond the current know-how of materials industries [19]. The major strategic function of structural biological materials is mechanical support, providing stiffness, strength and toughness, allowing stretch and flexure or acting as a spring. The particular tactics of how each component or system carries out support depend on its mechanical properties [14]. From the theory and practice of materials science, mechanical engineering and biology, mechanical properties of components and systems are structure sensitive, and can be explained in terms of their structure. Then, the most intriguing feature of biological systems is perhaps exploring the direct link between the mechanical functions and the highly organized microstructures, which is the theme of present work.

Functions, properties and structures can be discussed in terms of models and principles of design. The idea that biological materials and structures have functions implies that they are “designed”, adapted for particular functions. In any species, the organisms with structures more appropriate for particular functions will be selected. This, along with the genetic variations occurred in the population, means that the structure will

change through the generations. This indicates that the structure is appropriate for some functions in the past, and gradually refined to better serve that function. Thus, the structure can be considered to be designed and the designing is performed by natural selection. Natural selection takes account not only of how the structure performs functions, but also how this interacts with all the other processes that the organism must carry out [14].

Biological materials not only enjoy optimized propertiers-as strength, toughness or compliance-they exhibit several optimized properties simultaneously, the concept of multifunctionality [6], [19]. For example, the insect antennae are mechanically robust, self-repairing; they can detect chemical and thermal information and convey this for processing, and can undergo controlled and rapid changes in shape orientation [19].

Biological materials have unique structures and characteristics that distinguish them from their synthetic counterparts. The complex components necessary to fully understand biological systems are shown in Fig.1.2 [20]:

Self-assembly – the structures are assembled from the bottom-up, rather than from the top-down as many synthetic processes.

Self-healing – biological materials have the capability to reverse the effects of damage by healing, whereas synthetic materials undergo irreversible damage.

Evolution, environmental constraints – the available principle used elements are oxygen, nitrogen, hydrogen, calcium, phosphorous and carbon, whereas the common synthetic metals (iron, aluminum, copper) are absent, or present in minute quantities (the

processing requires high temperature not often available in natural organisms). But this constraint is not omnipresent, since certain bacterium can live at high temperature of 113^{o}C [21], and more complex organisms can live around the mid-ocean hydrothermal vents [22].

Hydration – the properties are highly dependent on the water content in the structure.

Synthesis conditions – the majority of biological materials are fabricated in an aqueous environment at ambient temperature and pressure (~300K, 1 atm).

Functionality – many components serve more than one purpose, and thus are called 'multifunctional'.

Hierarchical structure – they have different scale levels of structural organizations ranging from nano-, micro- to macro, which confer distinct properties.

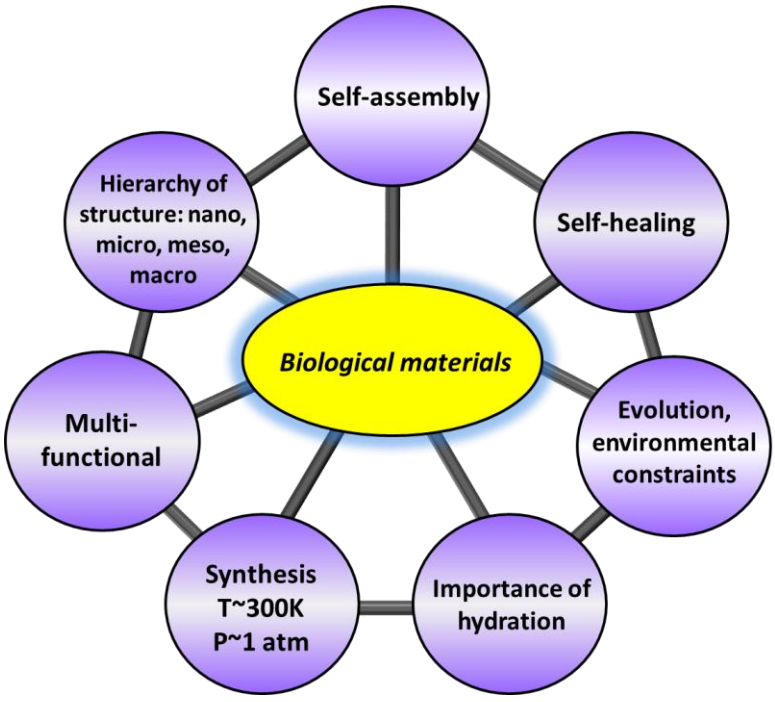

Figure 1.2 Schematic representation of characteristic constraints (inspired by [9]) [20].

1.4 Hierarchical structure and polymer composites

Most biological materials are composites based on biopolymers and some minerals, refined by nature through millions of years. The bone is a noteworthy example of natural biological composite consisting of tropocollagen molecules intercalated with nanoscale minerals (hydroxyapatite). Wood is a fibrous composite: cellulose fibers in a lignin matrix; the cellulose fibers have high tensile strength but are very flexible, while the lignin matrix joins the fibers and furnishes the stiffness [23].

The remarkable efficiency of natural materials (their performance per unit mass), using a limited chemical palette (proteins, polysaccharides and calcium salts) arranged in elaborate interwoven structures, has advantages over the engineered materials [24]. Fig1.2 shows a plot of the Young's modulus as a function of density for natural materials compared with synthetic materials. It is clear that (a) the density of natural (biological) systems is low (rarely exceeds 3), whereas synthetic structural materials often have densities in the 4-10 range; (b) there is a broad range in both Young moduli (from 0.001 to 100 GPa) and strengths (0.1 to 1000 MPa). Since minimizing the density of materials is often the goal in engineering, it behooves the materials scientists to examine biological materials to gain new insights into the design for new materials [10].

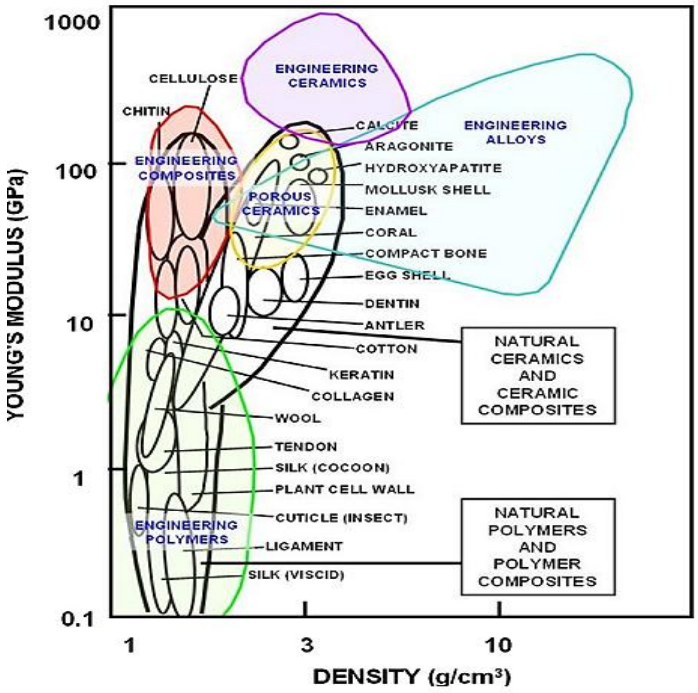

Figure 1.3 Young's modulus as a function of density for biological materials, overlaid with synthetic materials [10], [12], [25].

Despite the relatively weak constituents, their combination yields materials with outstanding properties and functionalities that have attracted increasing attention from material scientists. Woods have strength per unit weight comparable with that of the strongest steels; silks can be stronger and stiffer than high tensile steels; shell, bone, and antler have toughness an order of magnitude greater than engineering ceramics [26]. In their specific mechanical properties, biological materials can match most technical materials [27].

The secret for achieving this is usually the complex hierarchically organized structure. Take the bone as a typical example, shown in Fig. 1.4: collagen molecules (length~300nm, diameter~1.5 nm) and hydroxyapatite platelets (diameter~100nm,

thickness 2~4nm) combine to form orientated mineralized collagen fibrils (diameter~100nm), then make up fiber bundles on micrometer scale, which in turn are arranged in lamella within osteons and trabeculae (also micrometer scale), which then compose the overall organ on the centimeter scale. Such architecture enables the bone to exhibit exceptional strength and toughness (cortical bone, E 6-20GPa, Strength 30-150 MPa [13]. Also, the abalone shell owes its extraordinary mechanical properties to the hierarchical architecture, starting at the nanolevel, with an organic layer having a thickness of 20-30 nm, proceeding with single crystals of the aragonite polymorph of $CaCO_3$, consisting of "bricks" with dimensions of 0.5-10 um (microstructure), and finishing with layers approximately 0.3 mm (mesostructure) [20], [28].

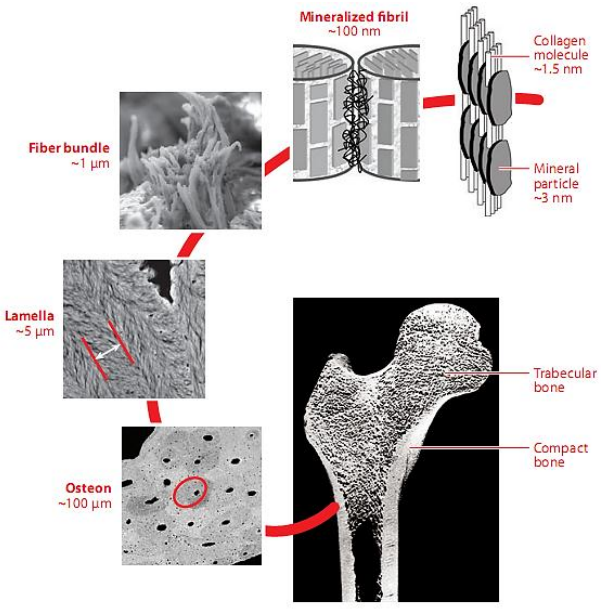

Figure 1.4 Sketch of the hierarchical structure of a human femur [28].

The natural biological composites can be categorized into several groups, shown in Table 1 [5]. Examples of the biogenic small inorganic particles include the iron clusters

that form at the center of ferritin molecular cages in organisms [29] and the ultrafine magnetic particles that are found in bacteria [30]. For ceramic/ceramic composites, there are cases in which minerals appears to be present alone in the structure. For example, in the teeth of sea-urchin, cross section at the cutting edge of a tooth exposes a composite of a matrix of amorphous $CaCO_3$ with crystalline calcitic $CaCO_3$ fibers embedded in it [5]. The ceramic/organic composites can easily be found in biological systems, including bones in vertebrates, teeth in fishes and mammals, shells in mollusks, and the typical example, nacre, and have been widely studied [31]–[33]. There are numerous stiff biological composites of fibrous organic components embedded in a soft organic matrix, that are analogs of fiber- or particle- reinforced polymeric composites [34]. Tendon (which connects muscle and bone), silk (found in cocoons of silk moths), cuticle (the exoskeleton of insects), etc. are several of these polymeric composites in biological systems [5], [35].

Table 1.1 A chart showing categorization of virous biological composites, their micro- and nano-design and physical properties [5].

Material/composite	Example	Micro- or nano-level	Properties
Small particles	Bacterial	N	Magnetic
	algal	N	Electronic, optical
Ceramic/ceramic	Sea-urchin	B	Mechanical (wear resistant)
Ceramic/polymer	Mollusk	N, H	Mechanical (tough, strong), ferroelastic
	Bone	N, H	Ferroelastic
	dentin	N, H	Ferroelastic
Polymer/polymer		N, H	Mechanical, ferroelastic, optical
Laminated	Cuticle	N, H	Mechanical, optical
Fiber/matrix	Tendon	N, H	Mechanical, ferroelastic
Fiber/fiber	Silk	N	Mechanical (tensile props.)
Liquid crystalline/matrix	Mocus	N	Rheological

N: nano, M: micro, B: both M and N, H: hierarchical.

The natural polymer composites exhibit exceptional mechanical properties considering the mainly weak polymeric constituents. The silk and spider web possess an

elastic modulus (in the order of 10GPa) and a maximum strength (over 1 GPa) that is parallel to that of steel [36], [37]; wool fibers typically have a tenacity of 140-180 MPa and an initial modulus of 2.7-3.9 GPa, at 65% relative humidity and 20 ℃ [38]; the arthropod exoskeleton, a laminated biological composite composed of chitin fibers embedded in a protein matrix, can successfully support the body and resist mechanical loads [20]. Undoubtedly, those biological materials with superior properties and unexploited designs are of great interest for the fabrication of novel bio-inspired engineered materials.

1.5 Keratinous materials and research focus

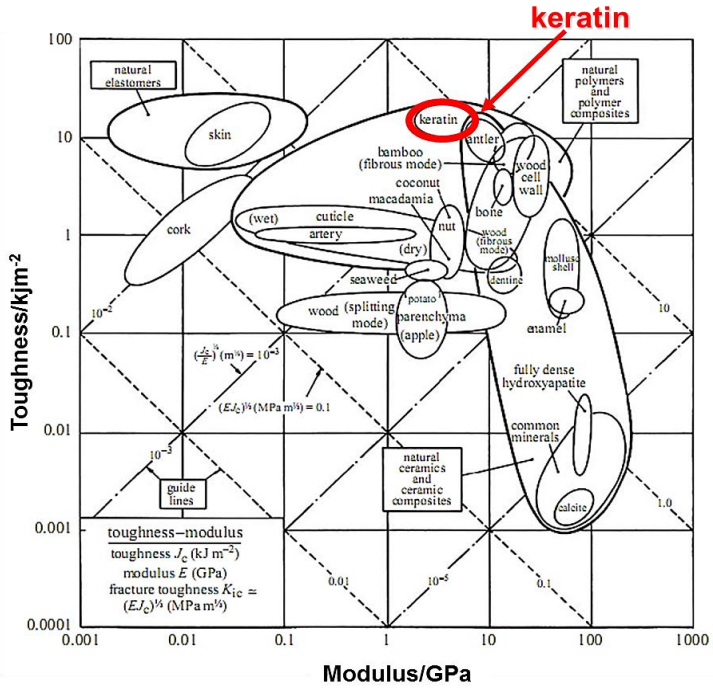

Figure 1.5 A material property chart for natural materials, plotting toughness against Young's modulus [25].

Keratin represents the most abundant structural protein in the epithelial cells [39]. It is, after collagen, the most important biopolymer in animals [40]. Keratinous materials

are formed by keratinized cells arranged in a variety of organizations and exhibit complex hierarchical structure ranging from nano scale to centimeter scale. They are among the toughest biological materials, according to the Ashby map in Fig. 1.5 [25], serving as a wide variety of interesting functions, e.g. scales to armor body, horns to combat aggressors, hagfish slime as defense against predators, nails and claws to increase prehension, hair and fur to protect against the environment. All these fascinating features have triggered great interest of many researchers in recent years, since the study bridging the structure and mechanical functions of natural keratinous materials will virtually expand the current knowledge of materials science and thus, inspire the engineering of novel functional materials.

Among keratinous materials, the pangolin scales were found in our research group that they serve as excellent flexible dermal armor: they are very hard to penetrate, are flexible to form a ball shape and can provide cutting action. However, until very recent, there are only two reports [41], [42] on pangolin scales on the structure and mechanical properties. Therefore, a thorough investigation of the mechanical functions of pangolin scales correlating to the structure would contribute to current knowledge of biological materials research.

On the other hand, how birds fly has fascinated humans since very early days; even Leonardo da Vinci had written a paper [43] examining flight behavior of birds and proposing the mechanisms. Among the unique characteristics enabling birds to fly, the

feathers are the most essential component contributing to flight [44]. The feathers have always been a hot topic to researchers due to their extraordinary properties both stiff and lightweight, which are also the core concerns of modern aircraft materials. Although literature on feathers abound, studies have been focusing on the general mechanical properties of rachis cortex, e.g. flexural strength, tensile strength [45], and our understanding on this naturally designed flight structure, the feather shaft, is superficial and quite limited.

This study intends to focus on the structural design strategies of terrestrial and avian keratinous materials, the pangolin scales as flexible dermal armor and the feather shaft as flight material, which would provide new knowledge that contribute to the current library of natural keratinous materials and valuable insights in developing keratin-inspired structures.

2 Research outline

In the wonderful natural world full of highly functionalized materials, keratinous materials stand out with their unique favorable properties and ingenious designs. This makes them a great resource for biomimetic studies, a fascinating research area attracting increasing attention and awaiting more in-depth explorations.

Keratinous materials serve a variety of mechanical functions according to the host organisms. The pangolin scales are exceptional flexible dermal armor, but has not been investigated from this perspective; the feather shaft represents one naturally optimized flight material, whereas the knowledge correlating the structural design and the mechanical functions is quite fragmented and limited.

This work includes a thorough investigation of the structural design strategies of one mammalian keratin as armor, the pangolin scales, and one avian keratin as lightweight and stiff flight material, the feather shaft.

The novel findings, analytical studies and outlooks/thoughts for future work presented here would help expand the current knowledge database of biological materials, and are of great value to the development of new bioinspired structures/designs that could range armor material, aircraft structure, biomedical and navy applications.

3 Review of keratins and keratinous materials

Keratins refer to a group of insoluble and filament-forming proteins produced in epithelial cells of vertebrates; they belong to the superfamily of intermediate filament proteins [46], and form the bulk of the horny layer of the epidermis and the epidermal appendages such as hair, nails, horns, feathers. These keratinous materials, having a high content of cysteine that distinguishes them from other proteins, are typically durable, tough and unreactive to the natural environment; they are assumed to provide mechanical support and diverse protective functions in the adaptation of vertebrates to the external environment [47], [48].

3.1 Classification of keratin

Keratins and keratinous materials are often discussed in terms of α- and β-keratins[49]. Based on X-ray diffraction, keratins can be classified into α-pattern, β-pattern, feather-pattern and amorphous pattern [48], [50]–[53]. The feather pattern has been considered as β-pattern since both show the same characteristic reflections, which has been well-accepted [54]. The amorphous pattern represents the component of the amorphous matrix (detailed in Section 2.2.1) in α-keratinous tissues [55]. Because the ordered structures (α- or β-patterns) dominate the X-ray diffraction, keratinous materials are conveniently distinguished by these ordered components. Additionally, the two regular secondary structures, α-helices and β-sheets, are the two major internal supportive structures in proteins [56]; thus, they are usually used to classify keratins.

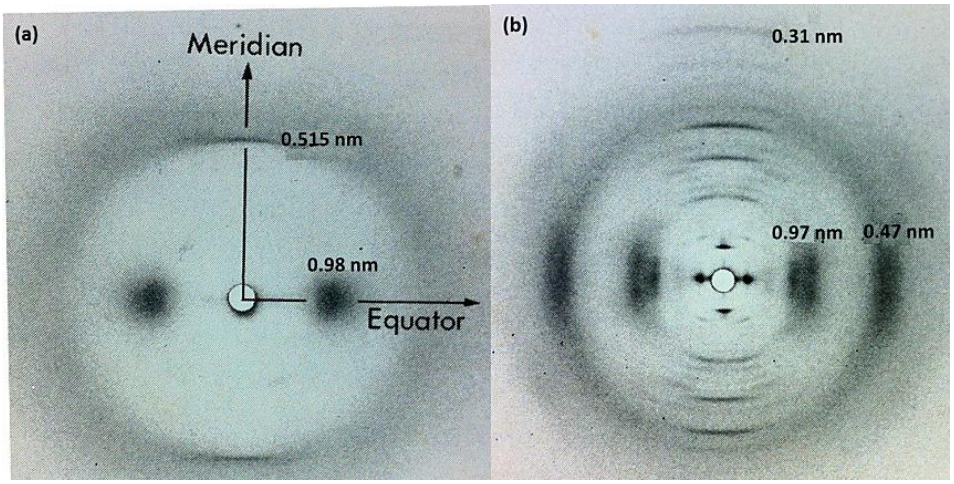

Figure 3.1 X-ray diffraction patterns of (a) α-keratin and (b) β-keratin [48].

Fig. 2.1 shows the wide-angle X-ray diffraction patterns of these two types of keratins: the α-keratin gives a pattern with an equatorial reflection of spacing 0.98 nm (this corresponds to the distance between α-helical axes) and a meridional reflection of spacing 0.515 nm (relates to the α-helix pitch projection). The β-keratin has a prominent axial repeat of 0.31 nm reflection (the distance between residues along the chain in a β-sheet), the ~0.47 nm equatorial arc (the distance between chains in a β-sheet) and the broad equatorial reflection at 0.97 nm (corresponds to intersheet distance) [48], [52], [57], [58]. α-keratin is mostly found in mammals, and it is the primary constituent of wool, hair, nails, hooves, horns and the stratum corneum (outermost layer of skin). The β-form is the major component of hard avian and reptilian tissues, such as feathers, claws and beaks of birds, and scales and claws of reptiles [10], listed in Table 2.1. Wool, as a representative α-keratin material, has been extensively studied, as well as feathers as a typical β-keratin material. Wool and feathers will be discussed as representatives of α-keratin and β-keratin,

respectively, in Section 2.2.1.

Table 3.1 Distribution of α- and β-keratin

α-keratin	**wool,** hair**,** quills, fingernails, horns, hooves; stratum corneum ;
β-keratin	**feathers**, avian beaks and claws, reptilian claws and scales;
α- and β-keratin	reptilian epidermis, pangolin scales;

In addition, there are other classifications being used in the literature. In terms of modes of biosynthesis [59] and the amount of sulfur cross links [60], keratins can be classified as soft keratins (e.g. stratum corneum) usually weakly consolidated and with a lower amount of sulfur and lipids, and hard keratins found in hair, nails, claws, beaks, quills, which have a more coherent structure and a higher amount of sulfur [48]. Keratins are also discussed in terms of mammalian keratin, reptilian keratin and avian keratin. .

3.2 Biochemistry, molecular structure and mechanical properties of α- and β-keratins

3.2.1 Biochemistry of α- and β-keratins

3.2.1.1 Biochemical and molecular analysis

The systematic protein biochemical analyses of human cells and tissues revealed the diversity of human keratin polypeptides [61]–[63]; these proteins were separated into type I (acidic) and type II (basic to neutral) keratins. A new consensus nomenclature for mammalian keratin genes and proteins to accommodate functional genes and pseudogenes classifies the 54 functional keratin genes as epithelial and hair keratins (28 type I keratin genes with 17 epithelial and 11 hair keratins, and 26 type II keratin genes with 20 epithelial

and 6 hair keratins) [47].

α-keratin can only constitute its filamentous state through the coiled coil assembly and heteropolymeric pair (deterodimer) formation of type I and type II (1:1) protein molecules [46], [64]. This is the monomeric unit of the keratin intermediate filament (IF); it consists of two chains (shown in Fig. 2.2a, [39], [65]). Each one contains a central alpha-helical rod (about 46 nm in length) with non-helical C- and N-terminal regions[66], [67] which are involved in bonding with other IF molecules and matrix.

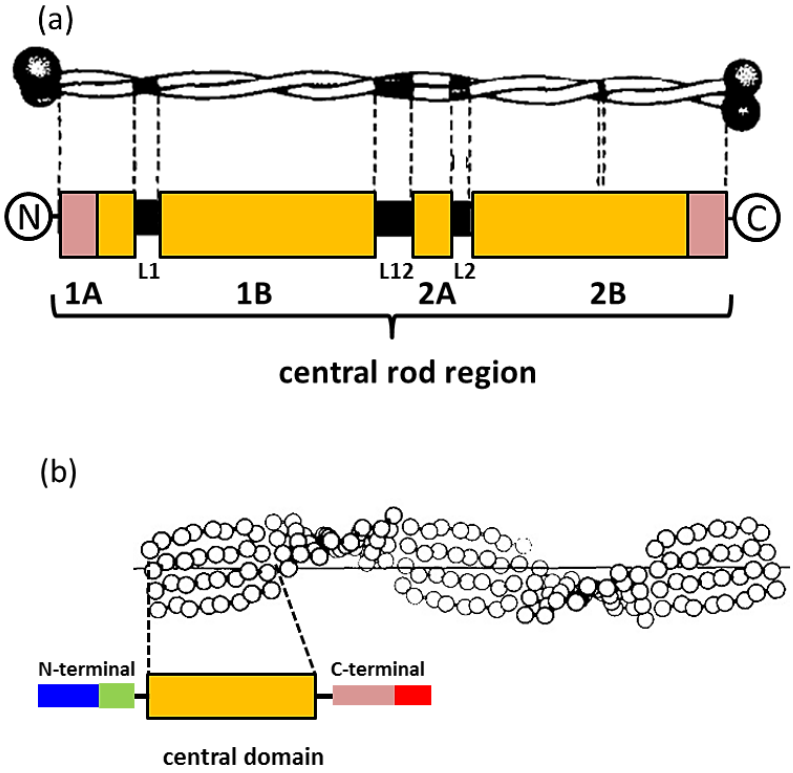

Figure 3.2 Molecular units of (a) α intermediate filament and (b) β-keratin filament. (a) The heterodimer includes non-helical N- and C-terminal domains and a central region (~46 nm in length), which has the α-helical coiled coil segments (1A, 1B, 2A, 2B), short links (L1, L12 and L2) and a 'stutter' (adapted from [39], [65]). (b) The upper illustrates the distorted sheet and the lower schematic represents a molecule with central domain and N- and C-terminal domains. The central domain (~34 residues in length) consists of β-forming residues (adapted from [48], [54]).

For β-keratin, the unit molecule of the filaments also consists of three domains: the central domain with residues forming β-sheet and the N- and C-terminal domains (seen in Fig. 2.2b) with different lengths and compositions depending on specific keratinous tissues [48], [54], [68]. The central domain has been the focus in the literature for the molecular structure of β-keratin filament. It is the central part of one polypeptide chain folding several times that forms a pleated sheet structure, the region within two dotted lines shown in Fig. 2.2b. The other two parts of the chain form the N- and C-terminal domains [54].

For α- and β-keratins, the unit molecules, heterodimer and one distorted pleated sheet, respectively, contain a central domain and two terminal domains. The length of the central region is about 45 nm [69] and the diameter about 2 nm [70]. For the β-keratin, the length of central region is about 2.3 nm and the diameter about 2 nm [48]. The keratin assembly for α-keratin involves the organization of dimers into IFs, the terminal domains link with other molecules and matrix proteins, and the terminal domains and matrix proteins wind around IFs to form keratin [54], [71]. While for β-keratin, the pleated sheets arrange into filaments, C- and N- terminal domains compose the matrix and wind central domain, forming the keratin [54].

3.2.1.2 Solubility and amino acid compositions

Keratins are naturally insoluble due to intermolecular disulfide linkages [48], intramolecular disulfide linkages [72], and interchain peptide linkages [73], [74]. For α-

keratinous materials, reduction, oxidation and sulfitolysis methods have been used to generate satisfactory amounts of the derivatives [48], [75]–[78]; while for β-keratinous materials, which have not been as extensively investigated as α-keratin, alkaline thioglycollate and a combination of a disulfide bond-breaking reagent and a protein denaturant were described in literature [79], [80]. There are also reports discussing degraded keratins produced by partial hydrolysis (with acid, alkali or enzymes) of wool, hair and feathers. The keratin fragments from hydrolysis are used in the manufacture of cosmetics, artificial leather and filaments [81]. For amino acid analysis, the acid hydrolysis of proteins and automated ion-exchange chromatography are used routinely [82]. The residue percent of wool (representing α-keratin) and feathers (representing β-keratin) are summarized in Table 2.2 [48], [83], [84]. It is clear that both show high content of half cystine (cysteine plus half cystine), which provides the disulfide bonds and distinguishes keratin as high-sulfur protein from other biopolymers. Whole wool shows a higher residue percent of half cystine and glutamic acid than whole feather rachis. The higher contents of glycine, proline and serine in feather rachis may be correlated with the lack of helical secondary structure. Both exhibit very low content of histidine and methionine. It was also reported that the derivatives from reduced wool could be precipitated into high-sulfur and low-sulfur components [48]; while for feather rachis, only minor differences were found between the compositions of the various fractions and no evidence for high- or low-sulfur components was obtained [84].

Table 3.2 Amino acid composition (residues per 100 residues) of representative α- and β-keratin materials.

Whole wool (representing α-keratin)	Whole feather rachis (representing β-keratin)
Alanine……5.5	Alanine……8.7
Arginine……6.6	Arginine……3.8
Aspartic acid[a]……6.5	Aspartic acid[a]……5.6
Half cystine[b]……11.4	Half cystine[b]……7.8
Glutamic acid[c]……11.3	Glutamic acid[c]……6.9
Glycine……8.8	Glycine……13.7
Histidine……0.8	Histidine……0.2
Isoleucine……3.4	Isoleucine……3.2
Leucine……7.8	Leucine……8.3
Lysine……3.0	Lysine……0.6
Methionine……0.5	Methionine……0.1
Phenylalanine……2.5	Phenylalanine……3.1
Proline……6.0	Proline……9.8
Serine……9.6	Serine……14.1
Threonine……6.1	Threonine……4.1
Tyrosine……4.1	Tyrosine……1.4
Valine……5.9	Valine……7.8
[48], [83]	Tryptophan……0.7 [80]

[a] Including asparagine;

[b] Content of cysteine plus half cystine in original keratin;

[c] Including glutamine;

3.2.1.3 Biosynthesis of keratins

Keratins are synthesized and regulated by messenger ribonucleic acid (mRNA) inside keratinocytes. A general scheme for the cytodifferentiation of keratinocytes is shown in Fig. 2.3 [48]. After the cell undergoes a critical mitosis, one or both daughter cells are switched to keratin production. Then, synthesis of stable keratin mRNA begins, followed by the synthesis of the keratin proteins. As the keratinocyte approaches maturity, the production of RNA and other cellular proteins stops and the nucleus starts degradation.

The cell begins keratin stabilization and finally dies, filled with keratin.

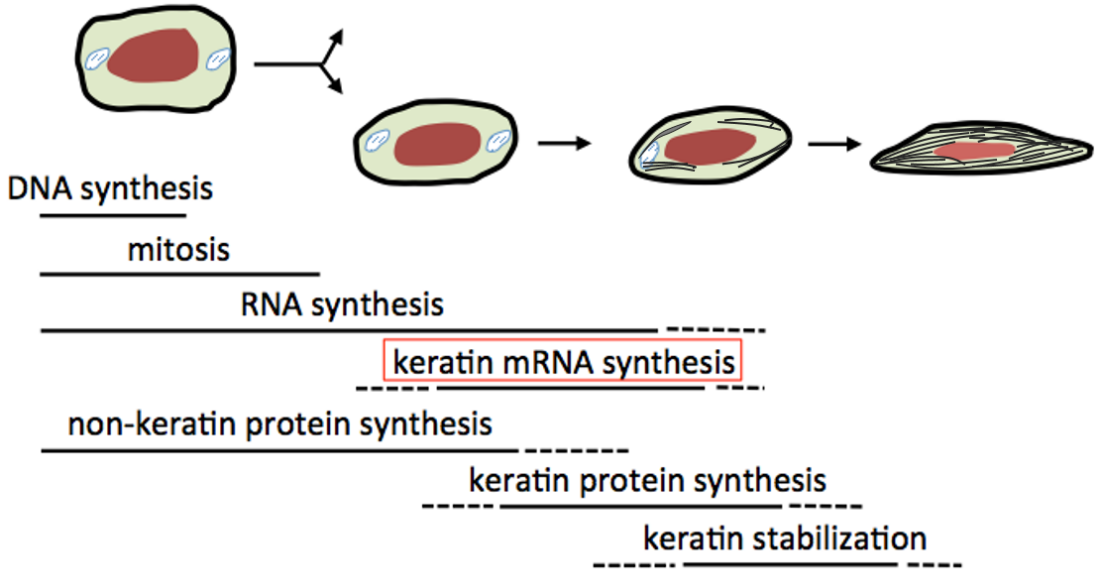

Figure 3.3 Schematic illustration of the biosynthesis of keratin. Cells undergo DNA synthesis and mitosis and later RNA synthesis; then synthesis of keratin mRNA and of keratin proteins proceeds. Finally, as cells mature, keratin stabilization begins and cells die filled with keratin [48].

It has been suggested [85] that keratin synthesis (red rectangle in Fig. 2.3) occurs at the surface of the fibrils (bundles of filaments) inside the cell. The newly synthesized proteins from the m-RNA-polysome complex aggregate with the preexisting filaments while still attached to the polyribosome. The polyribosomes are held in close proximity to the fibril until the chain is completed and released. During this period other chains grow on the polyribosome, thus providing further sites of aggregation with the fibril and so the process continues. In addition, there is also post-synthetic chemical modification of keratins, which is keratin stabilization by the formation of disulfide linkages [48].

The syntheses of α- and β-keratins appear to follow different courses, which are

related to the different structural organizations. Wool and hair (α-keratin) contain two distinct types of structural proteins (low-sulfur proteins for IFs and high-sulfur proteins for matrix) and there is a difference in the time course of synthesizing these two components. However, feathers (β-keratin) involve only one type of protein, and there are no distinct phases in the synthesis of the proteins. The proteins appear to increase in a coordinated fashion, and the detailed mechanism is poorly known [48], [86]–[89].

3.2.1.4 Formation of keratinous materials

Keratinous materials are formed by intracellularly synthesized keratins [90] through epidermal cells which build up at the outermost layer of skin. The formation of keratinous materials involving keratin development and ultrastructural changes, transforming living and functional cells into cornified structurally stable dead cells [91], [92]. Stratum corneum in mammalian epidermis (representing α-keratin), feathers (representing β-keratin) are discussed.

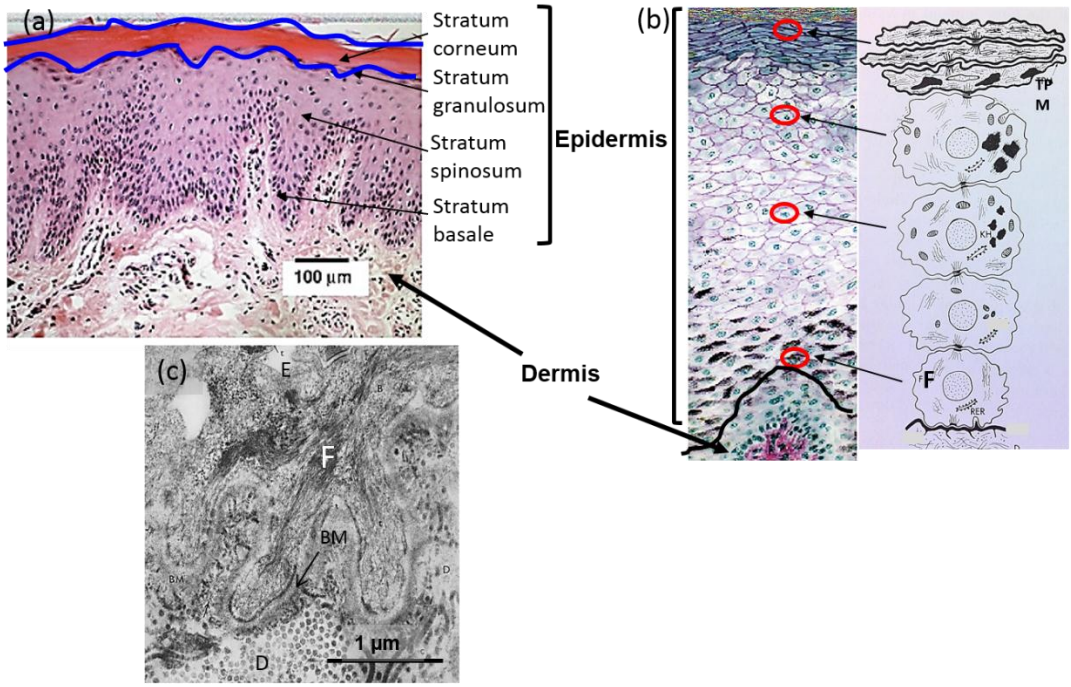

Figure 3.4 (a) Diagram of cross section of stained bovine skin that shows the epidermal layers [90]. (b) Micrograph of a bovine hoof [90] and a schematic diagram of the epidermal cells showing the structural changes during keratinization. Bundles of filaments (F) have developed in the cytoplasm of basal cells. In stratum granulosum, aggregated keratohyline granules are visible. In the last stage, the plasma membranes thicken (TPM) and the major cytoplasmic components disappear except for the fibrils [93]; (c) transmission electron micrograph of the border between the basal layer of the epidermal cells (E) and the dermis (D) that shows the basement membrane (BM) and the filaments as bundles (F) in the cytoplasm of basal cells [94].

The mammalian epidermis consists of four distinguishable layers of cells (shown in Fig. 2.4a and b): stratum basale, stratum spinosum, stratum granulosum and stratum corneum. Cells in the first three layers are differentiating keratinocytes while the outermost stratum corneum is composed of dead keratin-filled corneocytes [90]. The stratum basale is about one cell thick and separates the basal layer from the dermis, following the contours of the finger-like process of the epidermal cells. Fig. 8b shows the epidermal cells illustrating the keratin development and structural changes [90]. In the stratum basale, cells

begin to proliferate and the cytoplasm of cells contains fine filaments (F in Fig. 8c), which measure about 5 nm in diameter and are of indeterminate length. These filaments frequently occur in bundles or fibrils [48]. Cells move outward and differentiate. In the stratum spinosum, keratin synthesis proceeds at a high rate. The cells are star-shape and there is a dramatic increase in the cytoplasmic content of fibrils [94], which were reported to be 7~8 nm in diameter [95]. The stratum granulosum layer indicates the border between differentiation and cornification processes, in which cells have undergone a change in shape so that their dimensions parallel to the skin surface are much greater than those in the direction of growth. The salient feature is the appearance and accumulation in the cytoplasm of keratohyline granules (a protein structure involved in keratinization). It was reported that at high magnification, filaments (filaments of the final keratin in the stratum corneum) are observed to pass through keratohyalin granules [94], [95]. As the cells proceed outward to the stratum corneum, an abrupt transition takes place involving complete filling of the cytoplasm with keratin and the removal of the nucleus, the keratohyalin granules and all of the cytoplasmic organelles [48]. The cells are flattened and dense with filament-amorphous matrix structure (the matrix was reported to be derived from keratohylin [96], finalizing the keratinization process [48], [93].

For the formation of feathers, it has been reported [97] that the events occurring along the time line include: (i) the initiation of a pin feather (the developing feather rising from epidermis, Fig. 2.5a), (ii) elongation of the pin feather, (iii) production, differentiation,

and maturation of cells comprising calamus, rachis, barbs and barbules (feather components shown in Fig. 2.5), and (iv) regression of dermal core (proliferating part at the basal of feather) during final calamus maturation. Figs. 2.5 a-c illustrates the developing process from a pinfeather to a down feather [98], [99]. In the germinal layer (Germinal Collar in Fig. 2.5b) of the follicle, mitotic activity produces densely-packed, polygonal immature feather keratinocytes that contribute to a pin feather visible above skin. The pin feather of an embryonic chick shows longitudinal barb ridges (Fig. 2.5b) that consist of several kinds of cells that later develop into separated barbs with opposite branching barbules (forming the vanes). The continuing production of keratinocytes pushes previously formed differentiating and mature tissues to move outward. The sheath (formed by outermost epidermal cells encasing the growing feather), feather and dermal tissues are generated proximally. Along with the feather growing, the sheath and feather tissues differentiate, mature, die, and dehydrate as they move distally. Once a feather reaches length appropriate for a specific body location and/or species, proximal cell proliferation diminishes drastically, and the epidermal tissues no longer move distally but remain stationary and mature in situ. During these periods, different kinds of cells undergo the keratinization process in different time courses [48], [99]. Fig. 2.5d and e show the regeneration of feather (developing feather during molt): at the base of the calamus (germinal collar) a new germ is formed for the second generation of feather; the barb ridges develop into barbs and merge to form rachis, and gradually a pennaceous feather grow

from the follicle with calamus, rachis and barbs.

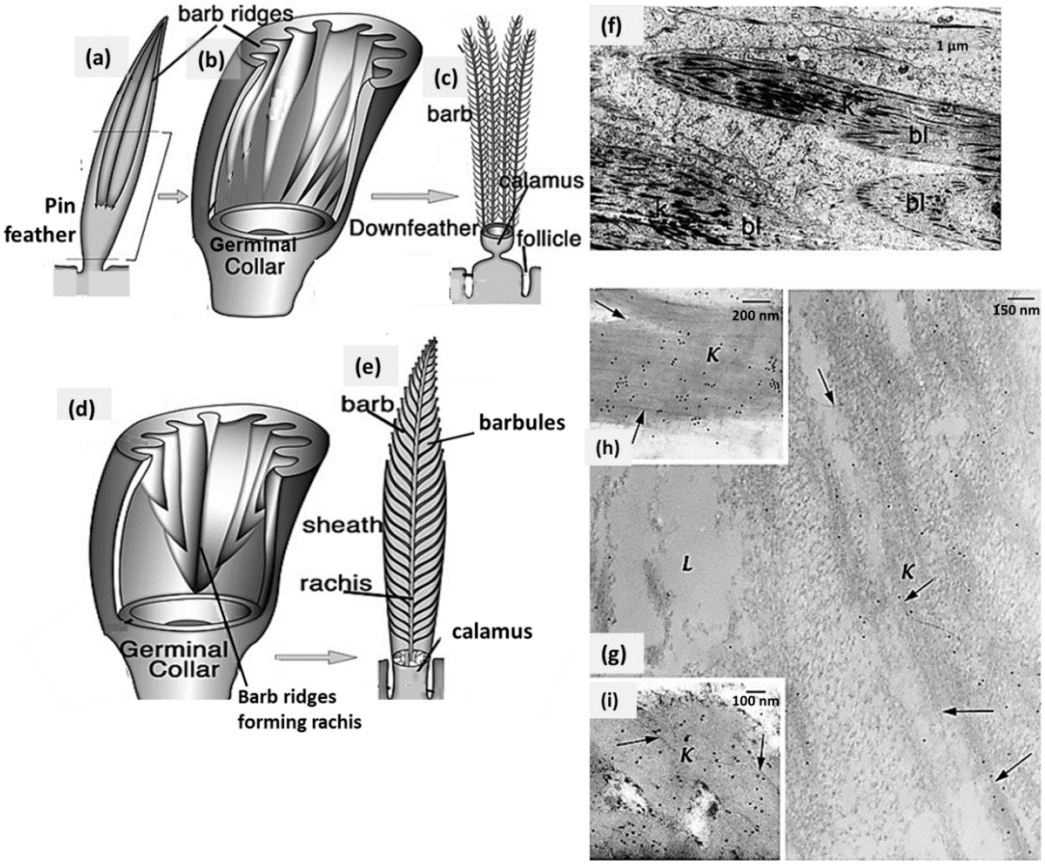

Figure 3.5 Schematic of the development from an immature feather (pin feather) to an adult feather and electron micrographs showing the keratin development. (a) A pin filament from an embryonic chick with longitudinal barb ridges. (b) Separated barb ridges originating from the germinal collar. (c) Barbs with barbules formed from barb ridges attached to the calamus. (d) A new germ is formed at the germinal collar (the base of calamus) for the second generation of the feather. The barb ridges develop into barbs and merge to form the rachis; (e) A feather showing the calamus, rachis and vanes (formed by barbs and barbules). (f) Elongated barbule cells (bl) in the chick after 13 days incubation. Keratin bundles (k) are assembled into long filaments [98]; (g) Keratin bundles (K) among the cytoplasm and lipid material (L) of a cell of chick wing feathers. Arrows indicate 10 nm thick filaments; (h) Detail of large keratin bundles (arrows point to 10 nm dense filaments); (i) Mature cell showing filaments (arrows) among the electron-pale and amorphous matrix [99].

It has been reported that keratin fibrils about 3 nm in diameter appear in the

cytoplasm and extend the length of the barb ridge cell from 13-day chick embryo [100]. Fig. 2.5f shows long and parallel keratin bundles (kl) in elongated barbule cells (bl) in the chick at about 13 days incubation [98]. As the embryo ages, the size of the filament bundles increases. Finally, the fibrils cease growing, coalesce and dehydrate while other cytoplasmic organelles are resorbed from the cell [48]. The cytoplasmic keratin bundles (K), lipid material (L) from a differentiating cell in chick wing feather cortex are shown in Fig. 2.5g, and the detailed view of the keratin bundles and filament-matrix structure in a mature cell in Figs. 9 j, k [99].

It is interesting to note that during the formation of feathers which are exclusively made of (β-) keratins [101], [102], studies [103], [104] indicated the presence of α-keratins in developing feather [105],[106]: a small amount of α-keratins of intermediate filament type forms the early keratin clumps in barb and barbule cells. These initial nuclei are rapidly coated/degraded and replaced by large amounts of feather keratins, which turn the keratin bundles into corneous materials where no signs of α-intermediate filaments are seen [102].

3.2.2 Molecular structure of α- and β-keratins

3.2.2.1 Filament-matrix structure at nanoscale

Both α- and β-keratinous materials show a fine filament-matrix structure at the nanoscale. The ‘filament’, for α-keratins, denotes the ‘intermediate filament (IF)’ which

represents the structural feature seen by transmission electron microscopy and shows an intermediate size (7-10 nm in diameter) between two other major classes of filamentous structures: microfilaments (actin, 7 nm) and microtubules (24 nm) [70]. For β-keratins, the 'filament' is called 'beta-keratin filament' and has a diameter of 3-4 nm [54], [55]. Fig. 2.6 presents transmission electron micrographs of the filament-matrix structure for typical α-keratinous (IFs in hair) and β-keratinous materials (beta-keratin filaments in feather rachis). Table 2.3 compares the major structural characteristics of α- and β-keratins. The filaments are ordered components composed by tightly bonded polypeptide chains and are considered as crystalline portions [57]. The α-keratin IF and the beta-keratin filament show different sizes and generate distinct x-ray diffraction patterns (seen in Fig. 2.1 and Table 2.3). In addition, the α-keratin has specialized constituent proteins: several kinds of low-sulfur proteins compose the IFs [107] while the matrix consists of high-sulfur and high-glycine-tyrosine proteins [48]. For β-keratin, there are no different types of proteins [48]; the filament and matrix are incorporated into one single protein [54]. Finally, the molecular mass of α-keratin ranges from 40-68 kDa, which is much larger than that of β-keratin, 10-22 kDa [89].

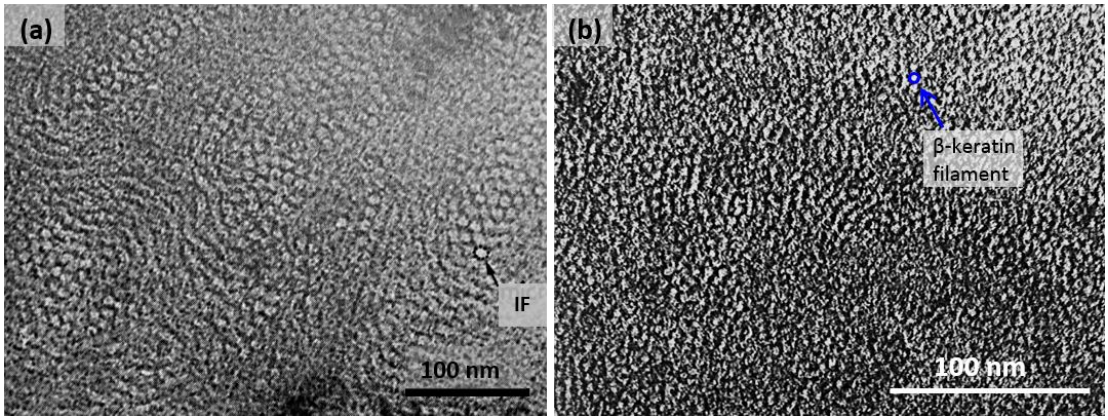

Figure 3.6 Transmission electron micrographs of typical keratinous materials with clear filament-matrix structure: (a) cross section of a human hair (α-keratin), stained with osmium tetroxide, showing 7 nm diameter intermediate filaments embedded in a darker matrix; (b) cross section of a seagull feather rachis (β-keratin), stained with potassium permanganate, showing the 3.5 nm diameter β-keratin filaments differentiated by the densely stained matrix [48].

Table 3.3 Basic structures of α- and β-keratins

	α-keratin	β-keratin
Similarity: structural feature	filament-matrix structure: IFs and beta-keratin filaments embedded in an amorphous matrix; IFs and beta-keratin filaments give characteristic x-ray diffraction patterns	
Diameters of the filaments (nm)	IFs: ~7	Beta-keratin filaments: 3~4
X-ray diffraction patterns [48], [57]	equatorial reflection with spacing 0.98 nm and a meridional reflection with spacing 0.515 nm	axial repeat of 0.31 nm reflection and the equatorial reflection ~0.47 nm
Constituting proteins	the IFs consist of several kinds of low-sulfur proteins [107], while the matrix consists of high-sulfur and high-glycine-tyrosine proteins [48]	do not have two different types of proteins [48]; the filament and matrix are incorporated into one single protein [54]
Characteristic structure	based on α-helical structure;	based on β-pleated sheet structure;
Molecular mass [89]	40-68 kDa	10-22 kDa

3.2.2.2 Molecular structure and formation of the filaments

The differences of molecular structure and formation of the filaments are the most important features that distinguish α- and β-keratins [56], [65], [108], [109], shown in Figs. 2.7 and 2.8. The α-keratin proteins are organized as coiled coils. The α-helix conformation for the polypeptide chains was first postulated independently by Pauling and Crick [110], [111], shortly after Pauling, Corey, and Branson [112] identified the structure as consisting of two helically wound chains of polypeptides. Naturally occurring α-helices found in proteins are all right-handed. The helical structure is stabilized by the hydrogen bonds (red circled line in Fig. 2.7a, [113]) inside the helix chain, causing the chain to twist and exhibit a helical shape. Fig. 2.7b shows the IF formation process [56], [114]: two isolated right-handed α-helix chains form a left-handed coiled-coil, the dimer (45 nm long, the heterodimer discussed in Section 2.2.1), by disulfide cross links; then dimers aggregate end-to-end and stagger side-by-side via disulfide bonds [115] to form a protofilament (about 2 nm diameter); two protofilaments laterally associate into a protofibril; four protofibrils combine into a circular or helical IF with a diameter of 7 nm. It is clear that the IF is based on coiled-coil structure. Then, the IFs pack into a supercoiled conformation, and link with the matrix proteins. The sulfur-rich amorphous keratin matrix consists of protein chains that have a high amount of cysteine residues or high amounts of glycine, tyrosine and phenylalanine residues [116].

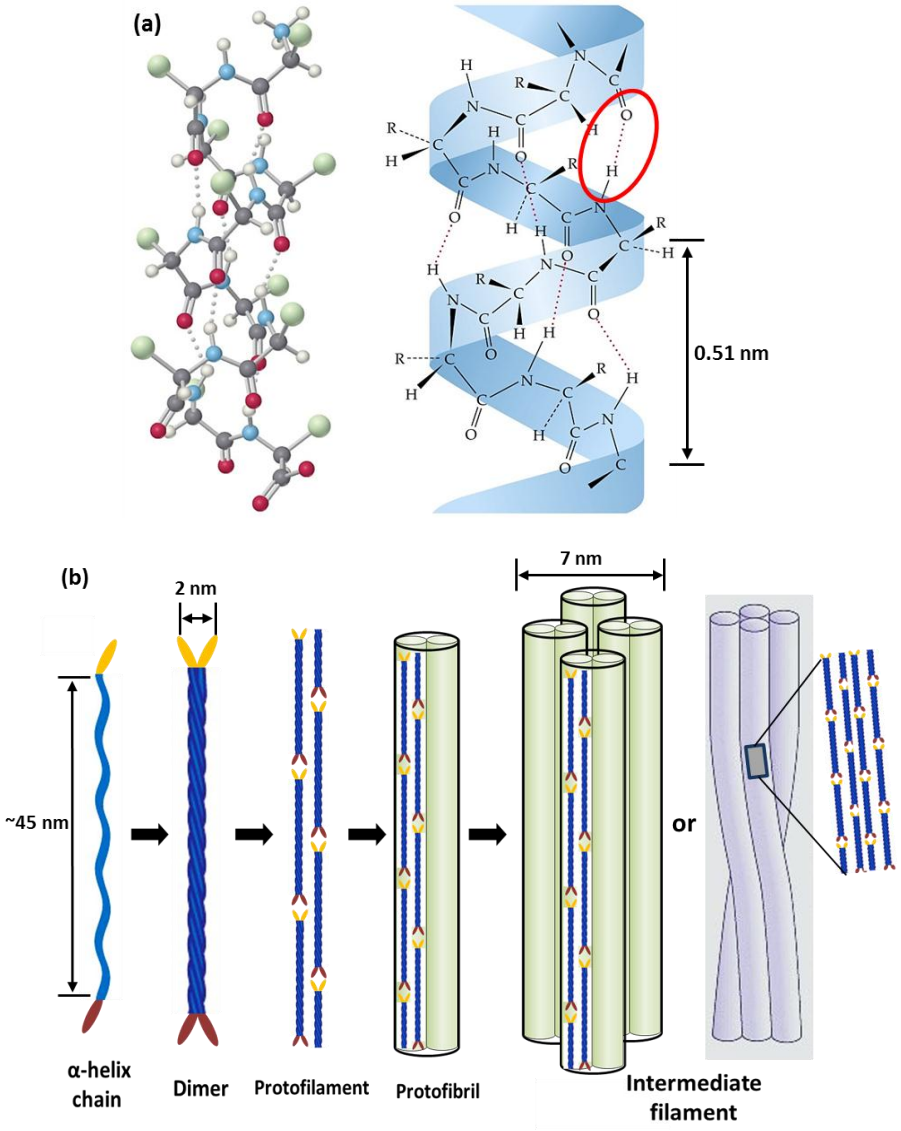

Figure 3.7 Intermediate filament structure of α-keratin: (a) ball-and-stick model of the polypeptide chain, and α-helix showing the hydrogen bonds (red ellipse) and the 0.51 nm pitch of the helix [113]; (b) schematic of the intermediate filament formation (reproduced based on [56], [114]): α-helix chains twist to form the dimers, which assemble to form the protofilament. Four protofilaments organize into the intermediate filament.

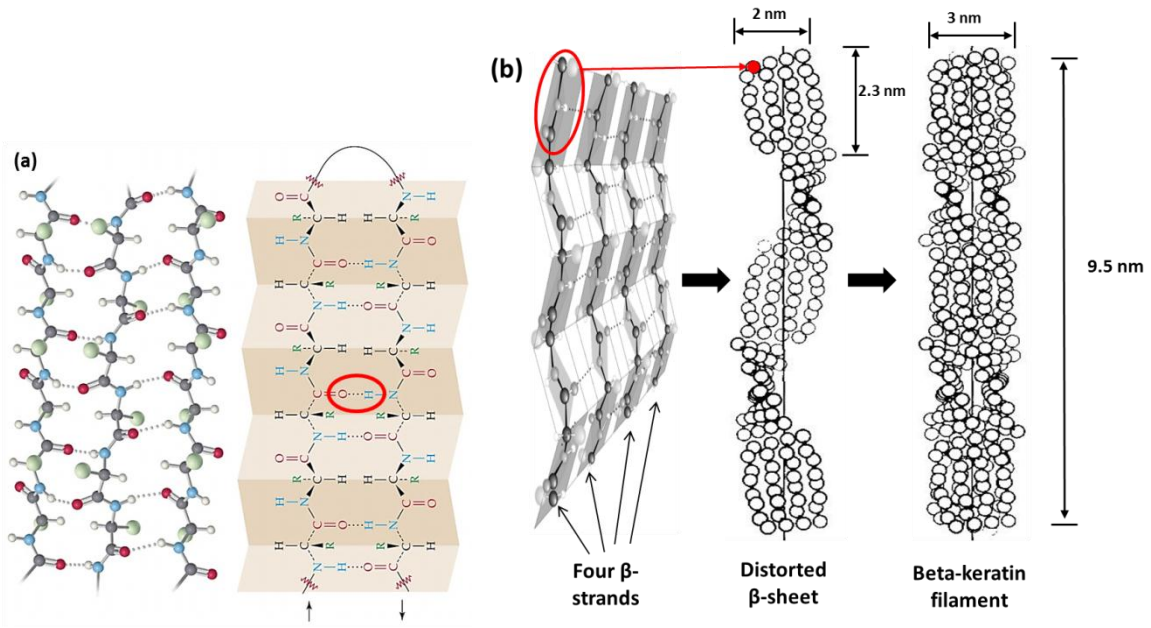

Figure 3.8 Structure of the beta-keratin filaments: (a) ball-and-stick model of the polypeptide chain, and illustration of the pleated beta-sheet [113]); (b) schematic drawing of the formation of beta-keratin filament (adapted from [48]): one polypeptide chain folds to form four β-strands which twist to form the distorted β-sheet. Two sheets assemble to form a beta-keratin filament.

The molecular structure and assembly mechanisms of IF proteins, which α-keratins belong to, can be found in the literature [46]. Although there has not been a high-resolution characterization of keratin IFs, recent studies have reported the crystal structure within the heterodimeric coiled-coil region [117]. Keratins are expected to share structural homology with vimentin, an IF protein, and the crystal structure of vimentin in the literature [118], [119] can provide useful information to the understanding of keratin structure. In addition to keratin, fibrin and myosin also form IFs.

For β-keratin, the pleated-sheet (Fig. 2.8a, [113]) consists of laterally packed β-strands which can be parallel or antiparallel (more stable), and the chains are held together

by intermolecular hydrogen bonds (red circled line in Fig. 2.8a). The pleated sheet structure is stabilized by two factors: the hydrogen bonds between beta strands contribute to forming a sheet and the planarity of the peptide bond forces a β-sheet to be pleated [56]. The formation of beta-keratin filament involves (Fig. 2.8b): the central region of one polypeptide chain folds to form four lateral beta-strands which then link through hydrogen bonding, resulting in a pleated sheet; then, the sheet distorts to lie in a left-handed helical ruled surface; each residue (marked by red circle in Fig. 2.8b) is represented by a sphere in the model (red dot in Fig. 2.8b); two pleated sheets are related by a horizontal diad, superpose and run in opposite directions, forming the filament with a diameter of 4 nm (a pitch length of 9.5 nm and four turns per unit). The terminal parts (not shown in Fig. 2.8b) of the peptide chains wind around the β-keratin filaments and form the matrix [54]. Therefore, keratins can be considered as a polymer/polymer composite of crystalline filaments embedded in an amorphous matrix.

3.3 Keratin research history

The earliest use of keratins should come from a Chinese herbalist, Li Shi-Zhen in the 16th century for medicinal application [120]. The word “keratin” firstly appears in literature around 1850 for materials that make up hard tissues such as horns [121].

During the early twentieth century, the research focus had been to extract keratin from animals and human hair: a patent [122] described a process for extracting keratins from horns using lime; it was reported that keratins can be converted into proteins soluble

in alkali or acid [79]. With the biological properties of keratin extracts known, their medical applications became hot topics, including keratin powders for cosmetics and coatings for drugs [123], [124]. During 1920s, the focus changed from keratin products to the structure and properties of keratin proteins, recognizing that different keratin forms are present in keratin extracts [121].

During World War II and after that, the driving forces of keratin research were textile production as well as its medical, cosmetic and engineering applications. In 1940, in Australia, the Council for Scientific and Industrial Research established the Division of Protein Chemistry to better understand the structure and chemistry of fibers to expand the potential applications of wool and keratins, and produced the first complete diagram of a hair fiber (Fig. 2.13, [125]). There were more than 700 applications of keratin-based inventions submitted to the Japanese patent office in the thirty years after that [121]. In the 1950s and earlier, the University of Leeds and the Wool Industries Research Association in the UK showed that wool and other fibers consist of an outer cuticle with flat overlapping cells and a central cortex with elongated cells [126].

Since the 1970s, advances in the extraction and characterization of keratins have led to the exponentially growing knowledge of keratin and keratinous materials [48], [127], [128]. On the one hand, this enabled the increased production of keratin-based powders, films, gels, and coatings [129]. Keratin based biomaterials in medical applications show a good potential [130], [131]. Wound healing, drug delivery, tissue engineering, cosmetics,

and medical devices continued to be popular subjects for keratin-based research in the past decades[121]. On the other hand, the enhanced understanding of keratins has fueled the research area of biological keratinous materials with the aim to create bioinspired materials. Some keratinized materials with interesting properties, such as skin [132], quills [133], [134], fingernails [135], horns [136], [137], whelk egg capsules [138], bird feathers [139], [140], have been studied, with the hopes to obtain mechanisms and principles to design new functional materials, such as light-weight composites, and energy-absorbent materials [141]. This is a new and fascinating area, awaiting more and in-depth explorations.

3.4 Structure and mechanical properties of keratinous materials

Keratinous materials show the typical filament-matrix structure and exhibit a wide range of mechanical properties. Fig. 2.9 summarizes the transmission electron micrographs of keratinous materials composed of α-keratin and β-keratin [48], [94], [100], [142], [143]. For all figures except for a, e and g, the filaments are perpendicular to the foil plane and therefore show circular profile. Stratum corneum, wool, quill, horn, and fingernail show clear IFs embedded in an amorphous matrix (electron dense, dark background). The diameters of the IFs (~7 nm) appear to be substantially constant, but there are wide variations in the IFs orientations. Feather and claw exhibit beta-keratin filaments (3~4 nm diameter) embedded in an electron dense matrix.

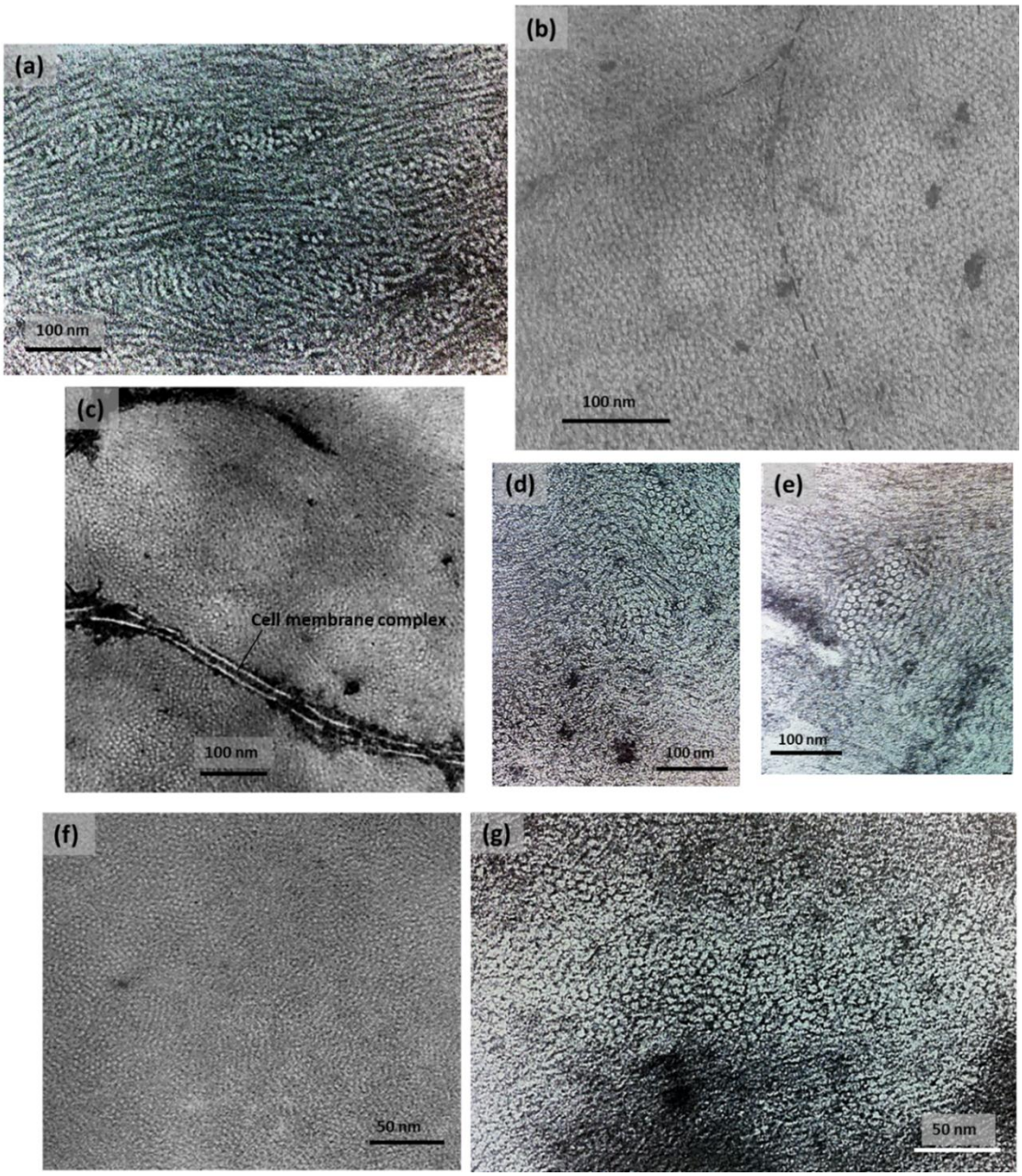

Figure 3.9 Transmission electron micrographs showing the filament-matrix structure of α-(a-e)and β- (f,g) keratinous materials:: (a) stratum corneum of human skin [94], (b) Merino wool fiber [143], (c) porcupine quill tip (with cell membrane complex indicated) [142], (d) bovine horn and (e) human nail [48], (f) seagull feather rachis [100] and (g) fowl claw [48]. The 7 nm diameter intermediate filaments and 3 nm diameter beta-keratin filaments embedded in matrix are observed.

Fig. 2.10 compares the tensile stress-strain curves of several typical keratinous

materials (whale baleen from [144], wool from [38]). All curves are characterized by a response that resembles that of metals: (a) a linear portion, corresponding to the elastic region, with a Young's modulus ranging from 1 to 5 GPa; (b) a plastic region with a much lower slope; (c) a slope change corresponding to strengthening (slope increase) or failure (slope decrease).

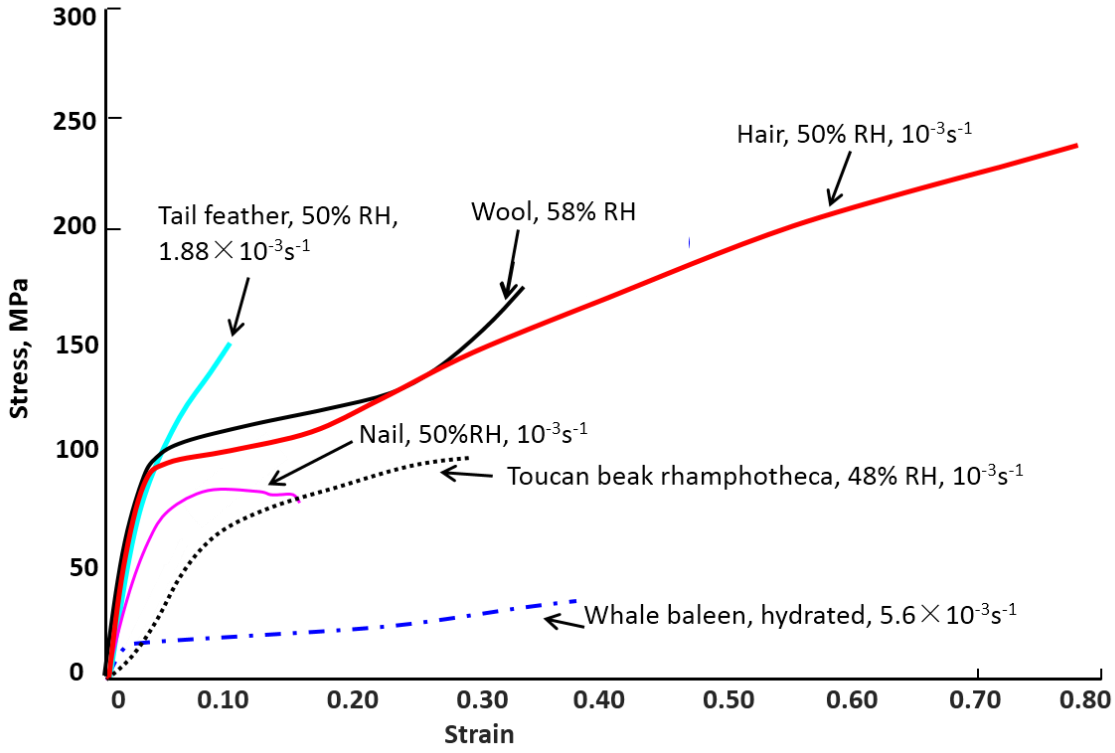

Figure 3.10 Tensile stress-strain curves of several typical keratinous materials (wool from [38], whale baleen from [144]).

Table 3.4 Mechanical properties of different keratinous materials.

Materials	Young's modulus (GPa)	Fracture strength (MPa)	Fracture strain	RH (relative humidity)	Ref.
Stratum corneum	1	18		10% RH	[145]
	0.005	2		100% RH	
Wool		260	0.30	0%RH	[38], [128]
	4.5			65%RH	
	2.5	180	0.57	100% RH	
Quill	2.7	146	0.25	65% RH	[146]
	1.0	60	0.49	100% RH	
Horn	3.9	77	0.035	50% RH	[147]
	0.7	25	0.61	Soaked in water	
Whale Baleen	1.2	30	0.35	Immersed in sea water	[144]
Hagfish slime threads	0.006	180	2.2	Tested in sea water	[148]
Feather	3.7	221.0	0.092	0% RH	[149]
	1.5	106.3	0.163	100% RH	
Beak	1.3	47.5	0.122	50% RH	[150]
Claw	2.7	90.3	0.057	0% RH	[149]
	2.1	68.7	0.067	50% RH	
	0.14	14.3	0.205	100% RH	
Snake epidermis*	3.43~4.73 (inner to outer)			43% RH	[151]
Pangolin scale	0.963	72.43	0.13	50% RH	[152]

* Effective elastic modulus from nanoindentation.

Hair and wool show an initial linear region, a yield region with an inflection and a post-yield region where the materials stiffen and break. Nails show similar curve with lower stiffness and strength. Whale baleen in hydrated condition also exhibits the three regions but substantially lowered strength and longer yield region. The feather shows an elastic modulus that is similar to wool, but fractures without an obvious yield region. The

toucan beak is less stiff and shows somewhat a yield region. These different responses are a consequence of the structural organizations of the filaments and matrix, the arrangements of keratinized cells and/or sample preparation. The small diameters of wool, hair and hagfish slime threads lead to greater ductility because crack formation and propagation are retarded and the α to β transformation provides an additional strain.

Table 2.4 lists the mechanical properties of different keratinous materials. It is clear that their mechanical behavior is highly dependent on hydration levels, and the mechanical properties encompass a large variation: the Young's modulus and strength range from 0.005 to 4.5 GPa and 18 to 221 MPa, respectively under similar relative humidity. This will be detailed in each keratinous tissue in the following sections.

3.4.1 Keratinous materials based on α-keratin

3.4.1.1 Stratum corneum

Stratum corneum is the outermost layer of mammalian skin (about 20-40 μm thick) and serves as a diffusion barrier, defense from external attack and even camouflage from predators [1]. It is composed of flattened cornified keratinocytes; these anucleated cells are embedded in a lipid-rich intercellular matrix. The keratin filaments extend throughout the entire cytoplasm in a web like pattern, and integrate at cell-cell junctions, maximizing the mechanical support [153]. From the top surface planar view (Fig. 2.11, [154]), overlapping layers (about 15 to 20 layers) of dead cells with approximately 25-45 μm in diameter are

observed [155]. The cells are continuously exfoliating and being replaced by those from the living layers beneath. These cells migrate through the epidermis towards the surface of skin, which takes approximately fourteen days [156]. In most of the cells, the cytoplasmic space is completely filled with filaments (IFs) about 7 nm in diameter embedded in a matrix of high sulfur proteins. The IFs are arranged in a variety of orientations (Fig. 2.9a).

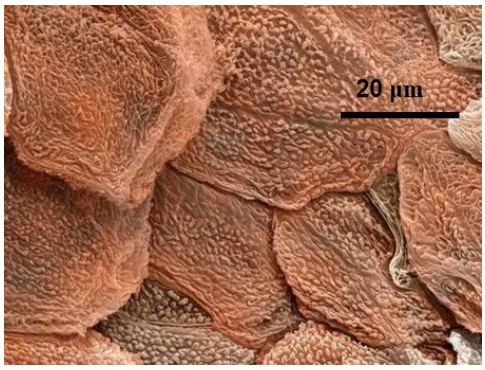

Figure 3.11 Colored scanning electron micrograph of top surface of stratum corneum of human skin, showing the overlapping, layered keratinocytes [154].

The mechanical properties are highly dependent on the relative humidity, temperature and loading orientation. Fig. 2.12 shows the tensile stress-strain curves of new born rat stratum corneum. With increasing moisture content and temperature, both modulus and strength decrease, but breaking strain increase [157]. This is related to a molecular relaxation process, and the strong plasticizing action of water facilitates the glass transition temperature of the fibrous protein component to migrate to lower temperatures with increasing moisture content. With more absorbed water, the interchain hydrogen bonds between amide and carbonyl groups are replaced by direct water-polymer linkages, and the segmental mobility of the macromolecular backbone increases, thus reducing the strength

[157]. The Young's moduli of porcine stratum corneum measured by nanoindentation were reported to be 10 (wet) and 100 MPa (dry) [158]. In-plane tensile moduli of human stratum corneum ranges from 5 to 1000 MPa with decreasing water content [145]. The in-plane tests show cohesive strengths of 2 to 18 MPa in testing environments of 100-0% relative humidity, and out-of-plane strengths of 0.1-0.8 MPa (100-45% relative humidity) [145].

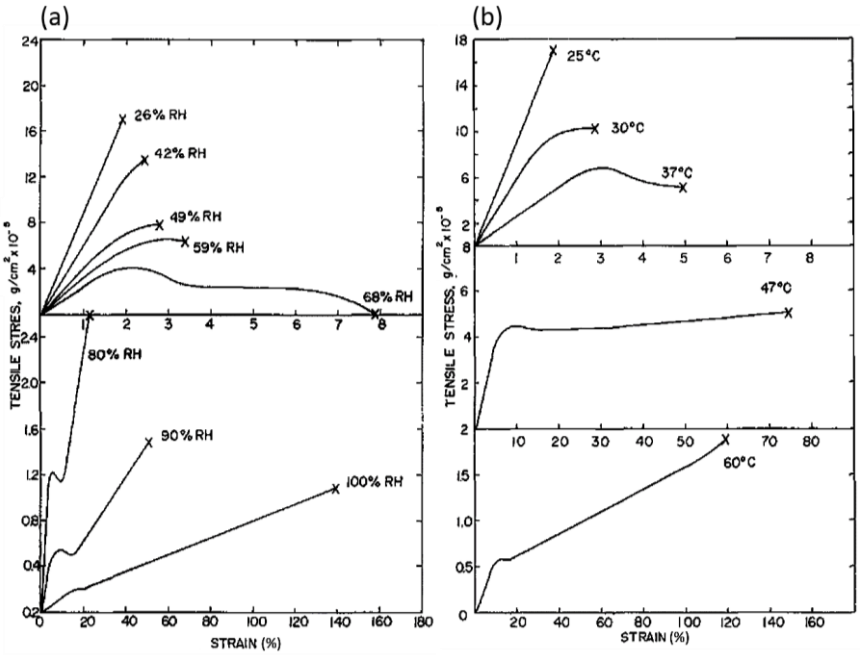

Figure 3.12 Tensile tests (stress-strain curves) of new born rat stratum corneum at strain rate of 0.5 cm/min [157]: (a) curves at 25^0C and different humidities; (b) curves at 10% water content at different temperatures.

In vitro adhesion tests reveal that the human stratum corneum shows a graded intercellular delamination behavior: delamination energies increase from ~3 Jm^{-2} near the surface to ~15 Jm^{-2} for the inner layers, while the delipidized specimens show initial delamination closer to the stratum corneum center and higher delamination energies than untreated ones [159]. Studies of the effects of solar UV radiation on the barrier function of

stratum corneum revealed that with increasing UV exposure to 800 Jcm^{-2}, equivalent to 60 continuous days radiation, the stiffness remains constant but the fracture stress decreases, and the fracture strain and delamination energy decrease significantly, indicating the damage to the intercellular cohesion [160].

3.4.1.2 Wool and hair

Wool is a noteworthy example of the hard keratinous material. It is by far the most important animal fiber used in textile application, and the structure and mechanical behavior have been extensively studied [48], [53], [65], [125], [128], [161], [162]. A clean wool fiber contains approximately 82% keratinous proteins with a high concentration of cysteine. About 17% is protein material of low cysteine content termed ‘non-keratinous material’ located primarily in the cell membrane complex, and about 1% of non-proteinaceous material consists of waxy lipids, plus a small amount of polysaccharide material [163].

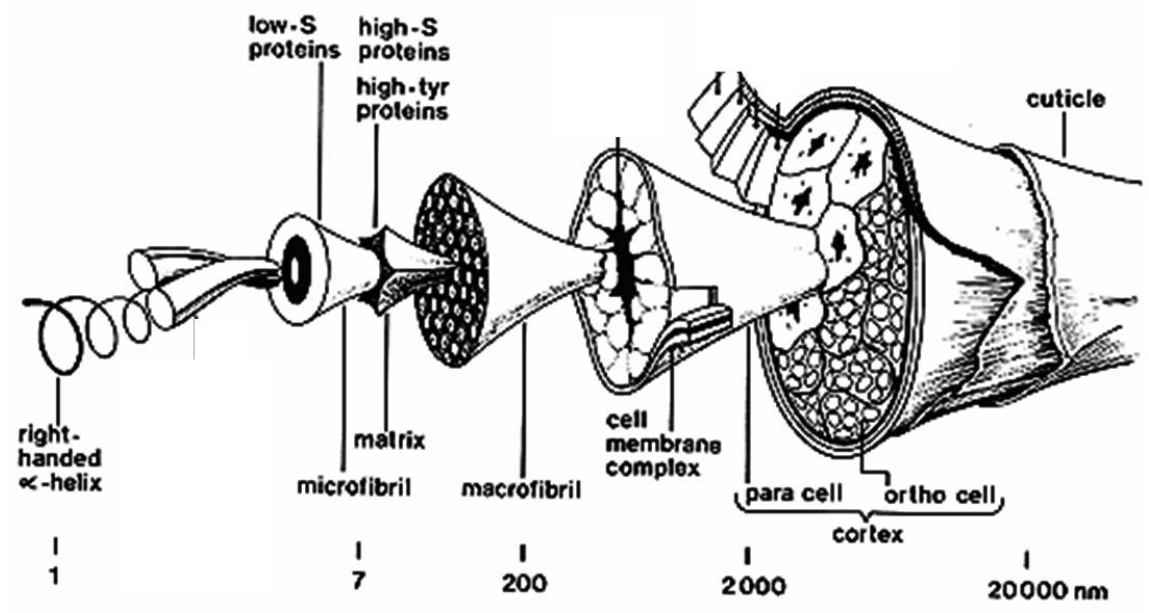

Figure 3.13 Schematic of the hierarchical structure of a fine merino wool fiber [125].

Wool fibers (with a diameter ~20 μm) consist of cells: flattened cuticle cells form a sheath around the cortical cells and continuous intercellular materials. Fig. 2.13 shows the hierarchical structure of a merino wool fiber [125]: the outermost layer, cuticle, consists of overlapping scales and it constitutes about 10% weight of the total fiber. The middle cortex, formed by spindle-shaped cells about 100 μm long, consists of orthocortex and paracortex, which have different assemblies of structural components and lead to the curly nature of the wool [164]. Lipid-rich cell membrane complex holds the cortical cells together in which macrofibrils formed by IFs (microfibrils in Fig. 2.13) and matrix proteins are observed. At the nanoscale, the α-helix chains associate into IFs, and then are embedded in a sulfur-rich matrix, which consists of proteins, nuclear remnants, cell membrane complex, intercellular cement.

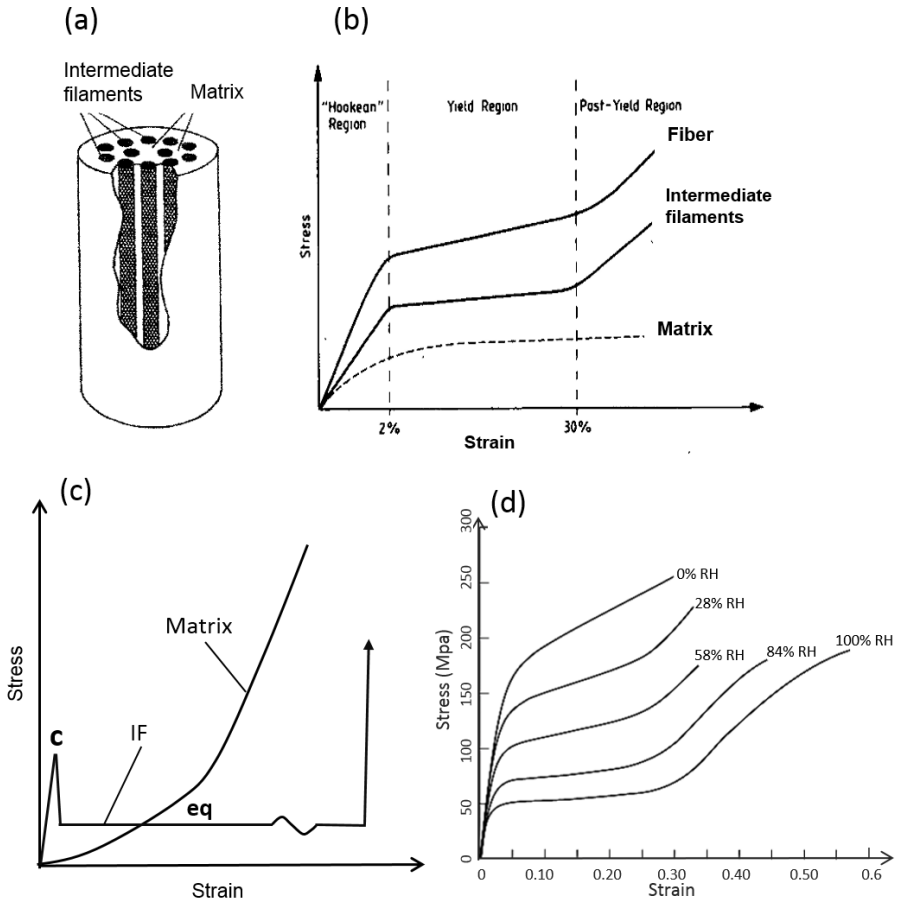

Figure 3.14 (a) Two-phase composite model for a wool fiber: cylinders of intermediate filaments (IFs) embedded in matrix [165]; (b) schematic stress–strain curve proposed for a wool fiber in water (not drawn to scale) [166]; (c) stress–strain curves of independent IF and matrix from a modified two-phase model (c, critical stress; eq, equilibrium stress) (reproduced from [167]); (d) stress-strain curves of wool fibers at different relative humidities (RH) [38].

The tensile properties of wool are largely understood in terms of the two-phase composite model (Fig. 2.14a): crystalline IFs are embedded in an amorphous, water-sensitive matrix [165]. Several variations of this model have been used [161], [166]–[171], and a review has critically evaluated the relevant models [172]. Present below are the essential elements of the two-phase model (rule of mixtures). It is assumed that both the

IFs and matrix undergo the same strain. This is actually a simplification, because sliding of the IF in the matrix takes place and the interfacial shear stresses between them are not constant.

At each strain ε:

$$\sigma = V_f \sigma_f + V_m \sigma_m \quad (1)$$

where V_f and V_m are volume fractions of IF and matrix, and σ_f and σ_m are stresses acting on IF and matrix. The IFs and matrix stresses have functional dependencies of the strain, $f_f(\varepsilon)$ and $f_m(\varepsilon)$. Thus, the general expression, applicable to any strain ε, is:

$$\sigma = V_f f_f(\varepsilon) + V_m f_m(\varepsilon) \quad (2)$$

Fig. 2.14b shows the stress-strain curves of IFs, matrix and the fiber from a modified two-phase model for α-keratin fibers [166]. Three distinct regions can be discerned: a near linear region (Hookean region) up to 2% strain which is associated with stretching of the α-helices with changes in bond angles without significant change in structure within the IFs [172]. Between 2% to 30% strain, the yield region, the unfolding of α-helices into the β-sheet configuration occurs and progresses in the IFs. In the post-yield region (after 30% strain), the fiber stiffens and breaks [173]. X-ray analysis has shown that the α to β transformation proceeds gradually through both the yield and post-yield regions [174].

Fig. 2.14c shows the predicted stress-train curves of separate IF and matrix based on another two-phase model [167]: the curve for IF increases initially to a critical stress

(point c) where unfolding of α-helices and formation of β-phase starts, then the stress drops to an equilibrium stress (eq) and remains constant as the transition of α to β proceeds until completion; further increase in stress stretches the β-form elastically. The matrix is assumed to be a cross-linked elastomer and shows smoothly increasing stress as strain increases, and the curve fits exactly a large large-strain rubber-elasticity stress-strain relationship Eq. (6) [175] for up to 35% strain:

$$\sigma = \left({}^{NkT}/_{3}\right) n^{\frac{1}{2}} [L^{-1}\left({}^{\lambda}/_{n^{\frac{1}{2}}}\right) - \lambda^{\frac{3}{2}} L^{-1}\left({}^{1}/_{\lambda^{\frac{1}{2}} n^{\frac{1}{2}}}\right)] \quad (3)$$

where σ is stress, N is the number of chains per unit volume, k is the Boltzmann's constant, T is the temperature, n is the number of random links between cross-links, λ is the stretch ratio ($\lambda = \varepsilon + 1$), and L is the Langevin function, defined, for a general variable x, as $L(x) = cothx - {}^{1}/_{x}$. The Treloar equation is based on entropic effects associated with chain extension. Recent studies on whelk egg capsules, which also show the α-helix→β-sheet transition that is reversible, have found that the process is driven more by internal energy than entropy changes [138], [176].

There is general agreement in the literature as to the structure-mechanical relationships in the Hookean and yield regions [168], but studies explaining the post-yield region are still somewhat questionable. Some explanations accounting for the increase of slope in this region are: the straining of the stretched matrix in parallel with IFs at the equilibrium stress [167], [170], [172]; the manner in which β-structured zones expand from

the center of α coil domains to the periphery [177]; the unfolding of the remaining α-helices produces the increase [166]; the further extension of the unfolding α-helices and extending the matrix protein jammed alongside the IFs.

The hydration has a great influence on the longitudinal tensile properties. The dehydration of wool fibers increases the tensile modulus approximately three-fold, but increases the torsional modulus by a factor of 15 [165]. The smaller change in tensile modulus indicates that the IFs, carrying the majority of the stress in this direction, are only slightly affected by decreased hydration. However, the large change in torsional modulus indicates that the matrix properties are strongly affected by hydration. In torsion, the matrix carries a large portion of the applied stress. It can be concluded that dehydration affects the properties of the matrix to a far greater degree than it does the IFs [128]. Fig. 2.14d [38] shows that the yield stress and breaking stress decrease with increased water content, which was attributed to the action of water in the α-keratin-water network: as a cross link between keratin chains, as a swelling agent reducing interchain interaction, and as a plasticizer of the keratin structure [178]. The tensile strength of wool decreases from 260 to 150 MPa as the relative humidity increases from 0% to 100%. Considering that the density of keratinous materials is around 1 g/cm^3, wool has specific strengths (tensile strength/density) ranging from 150 to 260 kNm/kg, comparable to that of stainless steel, about 250 kNm/kg (2000 MPa and 7.9 g/cm^3 as the tensile strength and density, respectively).

Hair is another important fiber that has been widely used and studied. The structure

of hair shows many features same as wool except for a larger diameter (~80 μm): the fiber consists of flattened cuticle cells overlapping around cortical cells and a central medulla (may be discontinuous or absent); the cortex forms bulk of the hair shaft and is composed of paracortex with hexagonally aligned IFs in matrix and orthocortex with IFs arranged in a whorl-like pattern, shown in Fig. 2.15 [179]. The proportions of paracortical and orthocortical cells determine the straightness of hair.

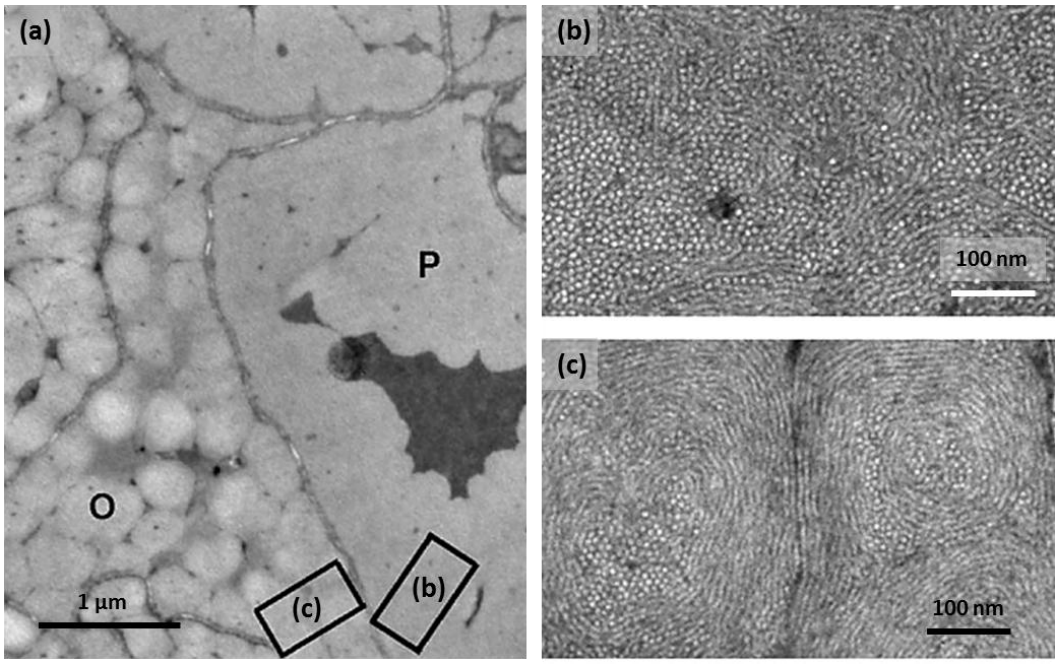

Figure 3.15 Transmission electron micrographs of a red deer hair: (a) cross section of the hair showing the paracortex (P) and orthocortex (O). High magnification images of rectangular regions (b and c) are shown in (b) and (c); (b) hexagonally arranged IFs embedded in matrix in paracortex; (c) IFs arranged in a whorl-like pattern in orthocortex [179].

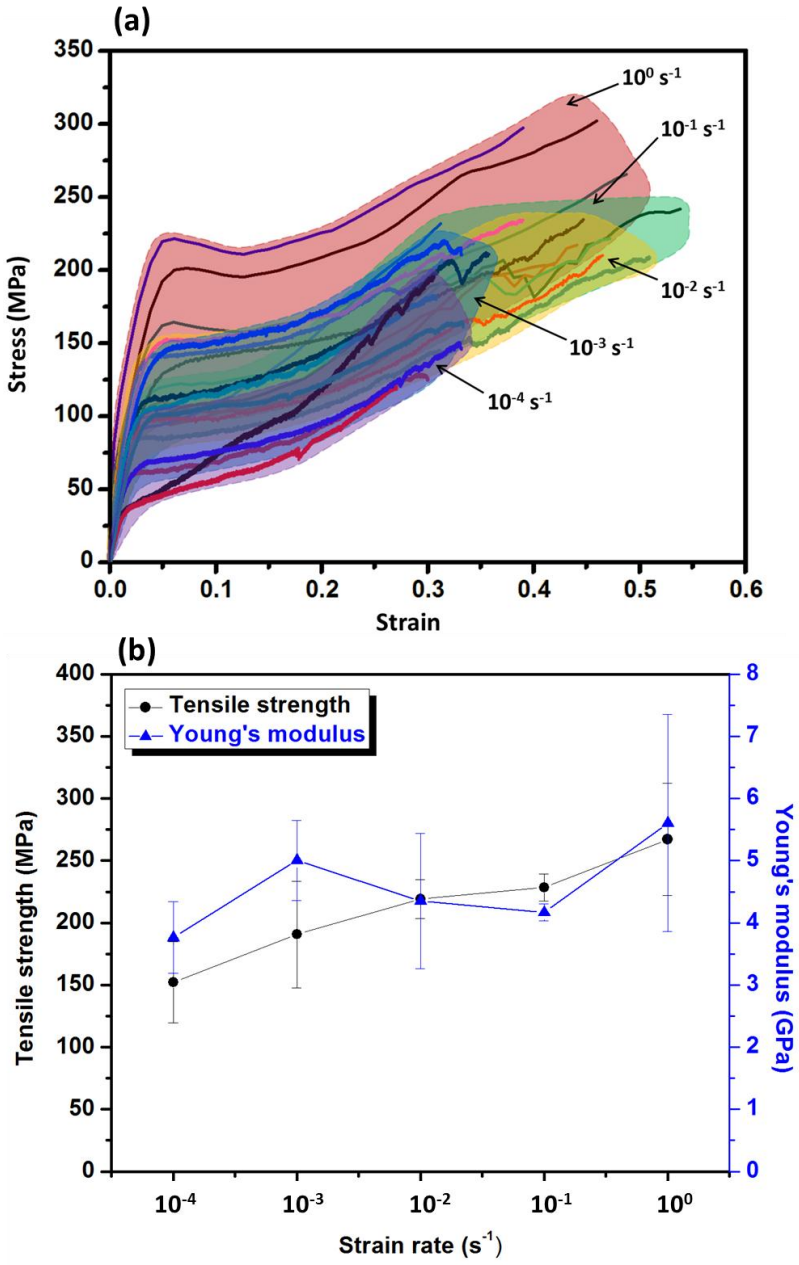

Figure 3.16 Tensile results of human hair at different strain rates [180]: (a) stress-strain curves grouped for each strain rate; (b) Young's modulus and tensile stress as a function of strain rate (error bars indicate standard deviation).

The mechanical properties of hair have been studied, but not as extensively as wool. Fig. 2.16 shows the tensile stress-strain curves and results of human hair at different strain rates [180]. All curves show the three regions typical of α-keratin: a linear Hookean region,

a yield region and a post-yield region. It is clear that as strain rate increases, the yield stress, tensile strength and Young's modulus increase from 100 MPa to 220 MPa, from 160 to 250 MPa, and from 4 to 5.5 GPa, respectively.

3.4.1.3 Hooves

Hooves are hard keratinous materials. The hoof wall copes with a diversity of high ground-reaction forces and transfers these to the bony skeleton, and any damages remain in the hoof until that part is worn off. Therefore, the hoof wall must be capable to withstand repeated high stresses, and studies show that the stratum medium (the central epidermal layer) of hoof wall is one of the most fracture-resistant biological materials known [181].

The hoof wall has been considered as a multi-level hierarchical composite, shown in Fig. 2.17a [182]. It is composed of flattened, keratinized cells that are organized into 200-300 μm diameter tubules (along the hoof length) with medullary or hollow cavities (~50 μm) and intertubular materials that lie at large angles relative to the long axis of tubules, forming a macroscale composite [181], [183]–[185]. In addition, hooves are formed from α-keratin that has been considered as fiber-reinforced composite at nanoscale. Fig. 2.17b shows a circularly polarized light micrograph of the cross section of a tubule (areas a, b and c) and associated tubule material at outer hoof wall region overlaid with cell boundaries [181]. Medullary cavities appear dark in the centers of tubules. Cells of the tubule cortex are organized into concentrically arranged lamellae, where each lamella is

composed of a single layer of cells.

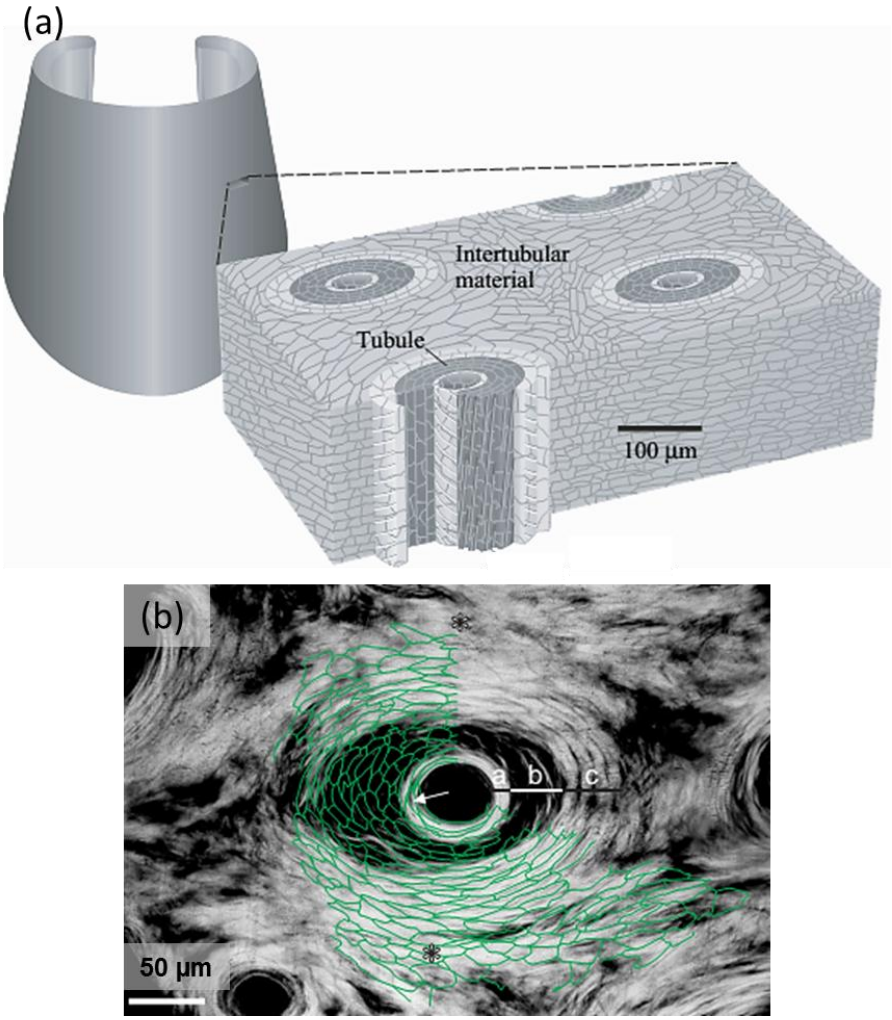

Figure 3.17 (a) Schematic drawing of the equine hoof wall showing cells organized into tubules and intertubular materials [182]. (b) Circularly polarized light micrograph of cross section of a tubule and intertubular material from equine hoof wall. Green curves overlaid are cell boundaries from the section under non-polarized light. The lightest areas show molecules close to the plane of section while darker areas show molecules oriented perpendicular to the plane of section. Tubule cortical lamellae types are indicated as a, b and c [181].

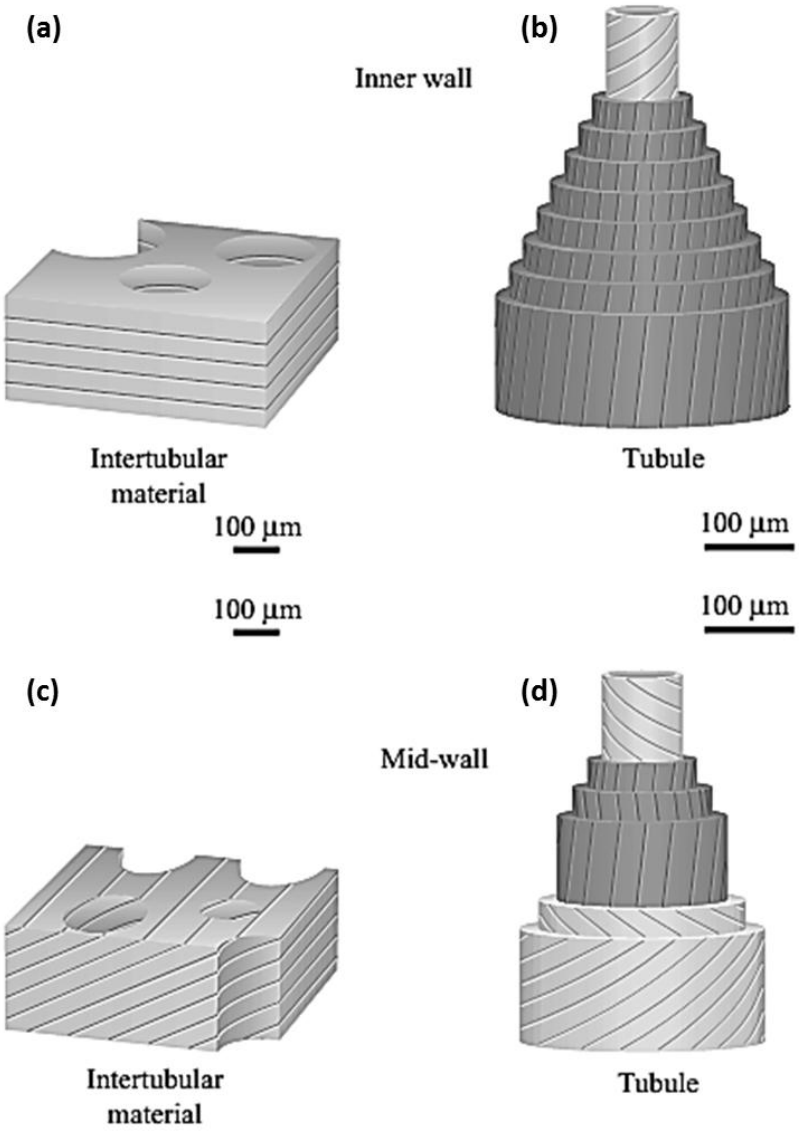

Figure 3.18 Schematic illustrations of the packing orientations of IFs in both intertubular material and tubule at different locations of equine hoof wall. At inner wall: IFs plane in (a) intertubular material and (b) tubule; At middle wall: IFs plane in (c) intertubular material and (d) tubule [182].

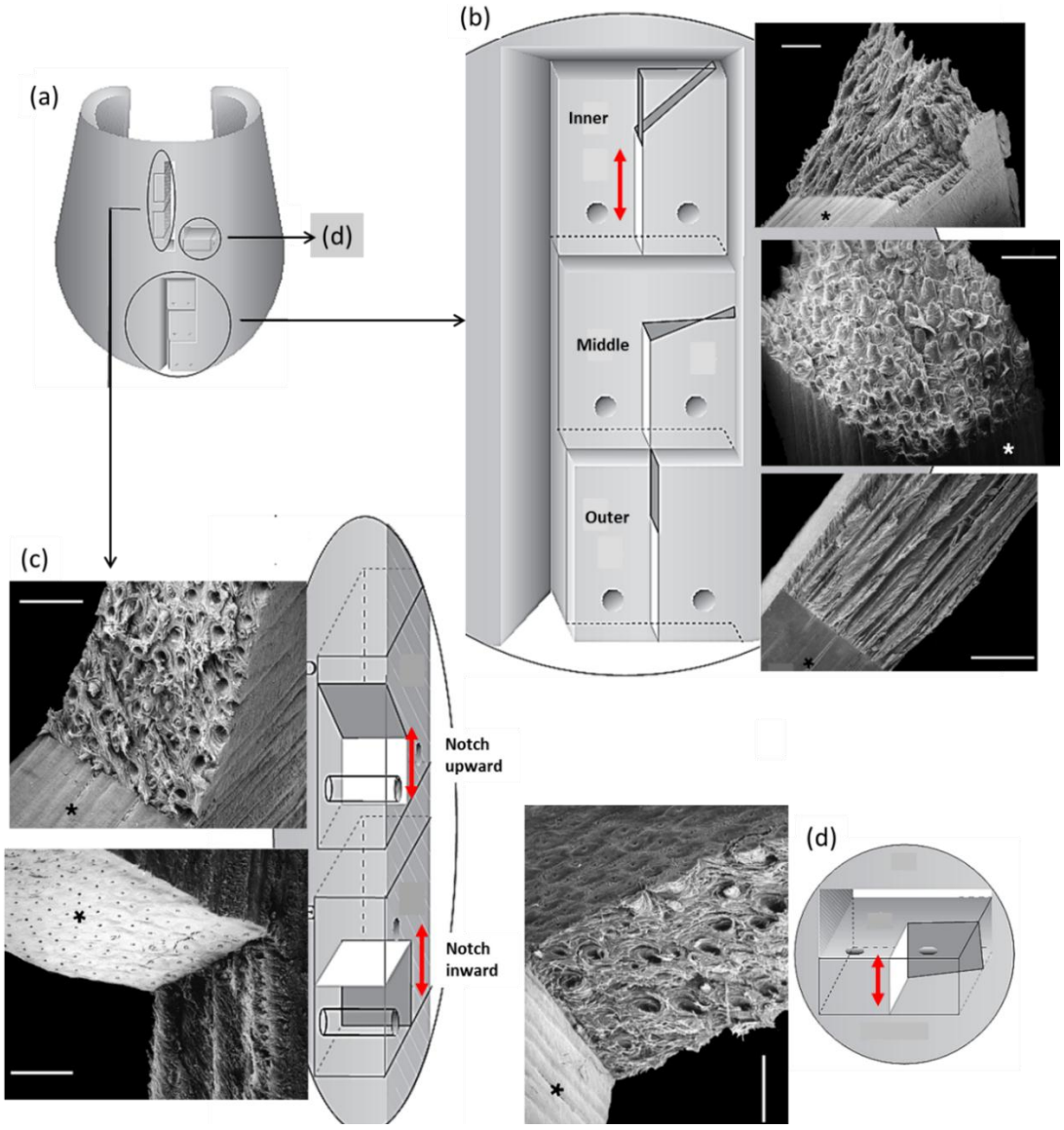

Figure 3.19 Crack diversion mechanisms (white areas indicate notch surfaces with asterisks, and dark gray areas fracture surfaces) and scanning electron micrographs of fracture surfaces of equine hoof (scale bars, 1 mm). Red arrows indicate the tubule direction. (a) Specimens in three groups: along the thickness direction, at middle region with notches parallel and perpendicular to tubules, and at middle region with notches trans-passing tubule axis. (b) At inner, middle and outer regions of the hoof wall with notches upward parallel to tubule axis and the crack paths, and the fracture surfaces. (c) Specimens with notches upward and inward and the crack paths, and the fracture surfaces. (d) Specimens with notch inward and the crack path, and the fracture surface [181].

The packing arrangement of IFs varies along the hoof wall thickness, revealed via

polarized light microscopy [181]. From Fig. 2.18 [182], at the inner wall, the intertubular material shows that most of the IFs are aligned nearly perpendicular to the tubule axis, while the tubules show inner type lamellae that have cross-helical IF orientation (helical angles 40~60 °) and lamellae (surrounding the inner type) that are wound in register in right-handed helical (helical angles 0~12 °) (Fig. 2.18b). At the middle wall, the intertubular material shows IFs arranged in planes in an acute angle (Fig. 2.18c), while the tubules show three types of lamellae: inner, middle and outer. The inner lamellae are similar to those in the inner wall, the middle lamellae cross between adjacent lamellae (0~33 °) and the outer lamellae show crossed helices from adjacent lamellae (helical angles 50~60 °). By taking advantage of varying tubule and intertubular material organizations and altering the orientations and volume fractions of IFs along the hoof wall thickness, the substructures are able to provide high fracture toughness and controll crack growth. The structural complexity enables the hoof wall to absorb much energy as the crack grows (by separating the two phases of the composite [186]), occurring at the level of the IFs and matrix of keratin, at cell boundaries within the hoof wall, and at the level of the tubular and intertubular components [185], [187].

The mechanical properties of hoof wall are modulated through hydration gradient and a complex structure design [181], [187]. There are two hydration gradients within the hoof: a horizontal one where the outer surfaces of the hoof have low hydration levels and the interior, adjacent to the dermis, maintains a high hydration level, and a vertical gradient,

hydration decreasing from the germinative region to the distal contact surface. Longitudinal tensile results on the central epidermal layer of horse hoof wall specimens at various hydration levels show that the Young's modulus increases significantly with decreasing hydration: 0.41 GPa at 100% RH to 14.6 GPa at 0% RH. The stress-strain curves indicate a general increase in modulus and a decrease in maximum strain with decreasing hydration. The hydration effect was attributed to water more strongly influencing the properties of the matrix phase than the IFs, similar to wool [187].

Fracture tests (pre-notch along the tubule direction) showed that the fracture toughness reaches a maximum at 75% RH (22.8 kJm^{-2}), which is an order of magnitude higher than that measured for fresh bone (1.0-3.0 kJm^{-2}, [188]). This indicates that the hoof wall keratin is remarkably fracture-resistant. In many materials a decrease in hydration can adversely affect the notch sensitivity and fracture properties, making them brittle. At very high hydration levels the load carrying capacity is severely decreased due to the lowering of the yield stress. It was reported that the hoof wall midway possesses water contents 17~24% by mass [189], which is the in the same range for the 75% RH [187], indicating that the hoof wall keratin appears to function *in vivo* at the hydration state closely matching the optimum condition for fracture toughness.

The observation of the fracture surface at different locations and orientations reveals the crack diversion mechanisms preventing cracks from reaching the living tissue of hoof [181]. The tubules reinforce the hoof wall against fracture inward to inner tissue,

and cracks along the tubule direction would be diverted by intertubular material to external surface. Fig. 2.19 shows schematic illustrations and scanning electron micrographs of the crack paths and fracture surfaces of specimens (compact tension) at inner, middle and outer regions in stratum medium and along different orientations. Along the hoof wall thickness direction with notches parallel to the tubule axis (white areas in Fig. 2.19b), crack paths in the inner region tend to bifurcate to two directions (along the tubule axis and along the intertubular IF plane). In the middle region (where the dominant component is intertubular material) advancing cracks clearly deviate towards the circumferential direction following the intertubular IF plane (fracture surface shows the cross section of the tubule material, Fig. 2.19b Middle with the schematic and scanning electron micrograph), while at the outer region cracks propagate along the tubule axis. Fig. 2.19c shows that in the middle region, cracks in specimens with upward notches (along the tubule axis) are redirected to external surface along the intertubular IF plane, and in specimens notched inwards (perpendicular to the tubule axis) the cracks deviate downwards, following the intertubular IF plane. In Fig. 2.19d, the crack path in specimens notched inwards (transverse to the tubule axis) is also redirected to along the intertubular IF plane. It was concluded that the mid-wall diversion mechanism of intertubular material inhibits inward and upward crack propagation, and that the inner- and outer-wall diversion mechanisms prevent inward crack propagation [181], [185].

Hooves undergo constant impact with the hard soil whereas horns impact during

combat. Although these velocities are not very high, less than 10 m/s, they nevertheless generate stress waves traveling through the material, which should be attenuated in order not to damage the underlying live tissues, primarily the bone. Thus, mechanisms to dampen the propagation of stress waves operate. The following are proposed to be the principal ones: (a) decay of wave produced by viscoelastic response of keratin; (b) scattering of wave by cylindrical tubules and internal interfaces.

3.4.1.4 Hagfish slime threads

Hagfishes are living fossils since there has been little evolutionary change in some of them over the last 300 million years [190]. Shown in Fig. 2.20a [191], they live on the bottom of deep waters and have an eel-shaped body without fish scales. They have a very special and complex jawless feeding apparatus, and the two pairs of keratinous teeth are anchored to dental plates, a bilaterally folding, paired series of cartilages, seen in Fig. 2.20b [192]. The most startling feature is that the hagfishes, when threatened or provoked, are able to excrete surprising quantities of slime which has keratin IFs bundles (slime threads) in a woven structure holding the slime (indicated by the arrow in Fig. 2.20c, [193]). The unique defense mechanism lies in that the slime contains mucins (proteins with the ability to form gels) bonded together with keratin threads, which can expand once contact with seawater to become almost three orders of magnitude more dilute than typical mucous secretion, and effectively chokes the predators with this gill-clogging slime [192], shown

in Fig. 2.20d,e. A hagfish (*Eptatretus cirrhatus*) immediately produces a large amount of slime into the mouth of a shark as the shark is trying to eat it; thus, not being able to remove the slime, the shark has to release the hagfish.

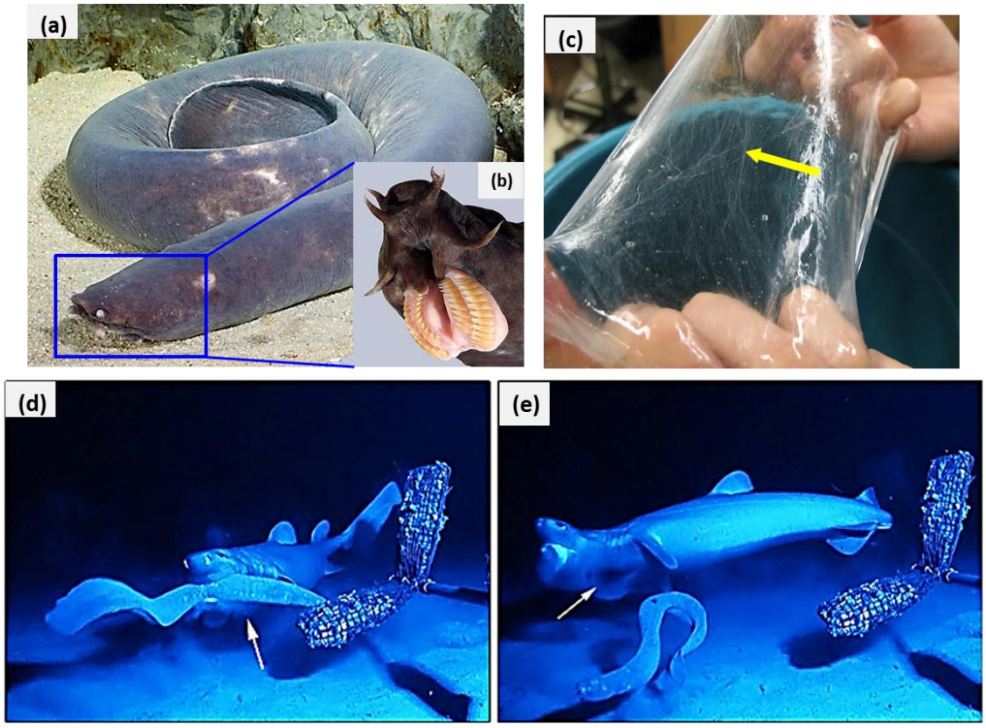

Figure 3.20 (a) A Broadgilled hagfish (Eptatretus cirrhatus) resting in a spiral shape [191]. (b) Head of the Broadgilled hagfish with keratinous teeth on dental plate [192]; (c) hagfish slime and the slime threads, showing a chaotic woven structure that holds the sheets of slime together (indicated by a yellow arrow) [193]; Hagfish slime function as a defense against gill-breathing predator: (d) A seal shark (Dalatias licha) is trying to bite and swallow the hagfish (Eptatretus cirrhatus), but the hagfish projects jets of slime (arrows) into the predator's mouth. The slime secretion took less than 0.4 sec. (e) Choked, the predator releases the hagfishes and gags in an attempt to remove slime from its mouth and gill chamber [192].

It is reported that the hagfish slime is formed as the slime glands eject a two-component exudate comprised of coiled threads (also called 'skeins', coiled bundles of keratin IFs) and mucin vesicles into seawater (indicated by arrow and arrowheads in Fig.

2.21a, respectively) [194]. The rapid deployment of hagfish slime upon secretion involves hydrodynamic forces and the presence of mucin vesicles assisting the unraveling of skeins into long threads (seen in Fig. 2.21b). The process has been studied and proposed as consisting of the following steps [194], [195]: (a) slime exudate is expulsed into convectively mixing seawater; (b) the swelling and elongation of mucin vesicles form mucin strands; (c) these mucin strands attach to the thread skeins and transmit the hydrodynamic forces to the thread skeins, thereby initiating unraveling; (d) entanglement of the threads and mucin strands results in the complete unraveling of thread skeins, forming the whole slime that is a highly complex network of mucin strands (0.0015%), slime threads (0.002%) and seawater (99.996%).

Figs. 2.21 c and d depict the threads (arrow) and mucin strands (arrowhead) in whole hagfish slime. All of these are in contrast to most IFs which function intracellularly. The IF-rich threads by the hagfish gland thread cells are released extracellularly to interact with mucins and seawater, modifying the viscoelastic properties of the mucous exudate [196].

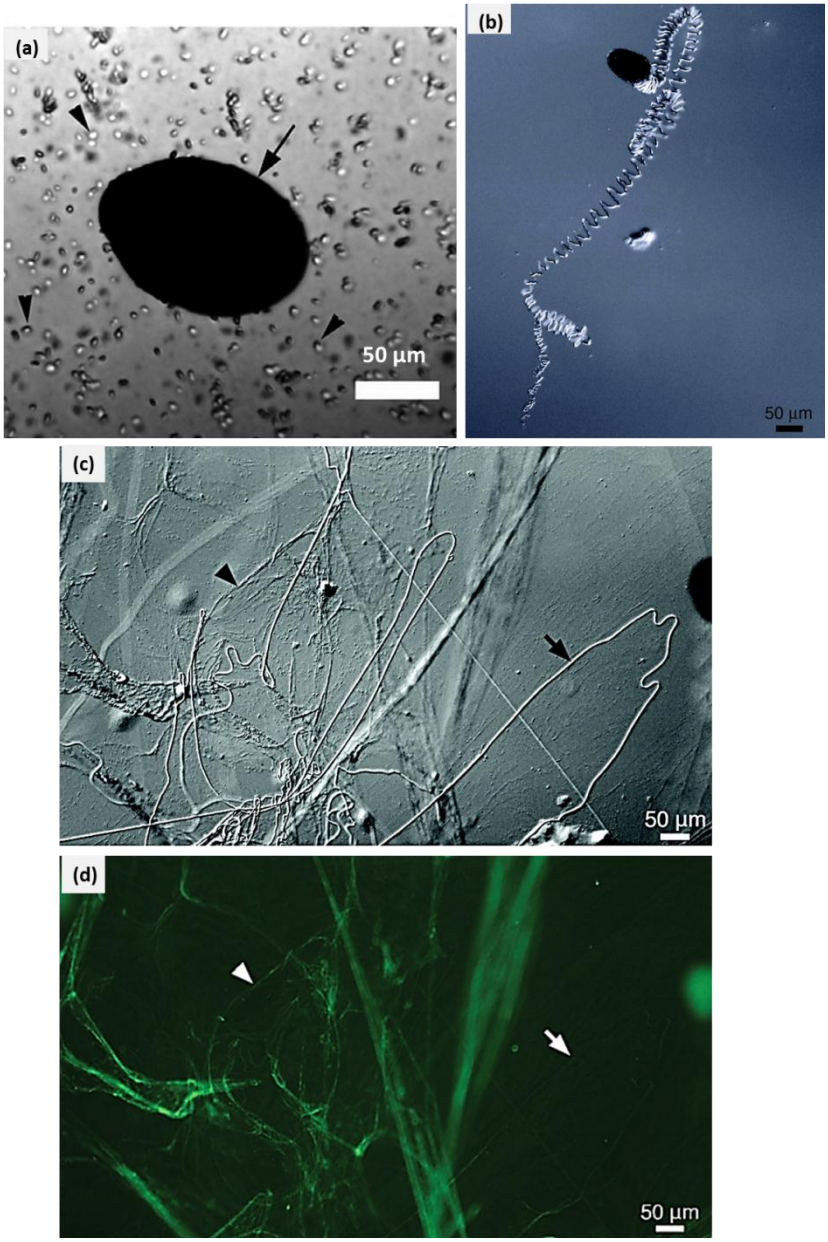

Figure 3.21 Structural characterization of the hagfish slime threads (bundles of keratin IFs): (a) a concentrated exudate (forming the slime) released by the slime glands; it contains both coiled slime threads (skeins) (arrow) and mucin vesicles (arrowheads) that rupture in seawater [194]; (b) differential interference contrast (DIC) image of partially unraveled thread skein in seawater illustrating their coiled structure [195]; (c) DIC image of the whole slime network depicting unraveled threads (arrow) and mucin strands (arrowhead) connecting threads; (d) fluorescence image of the same area in (c) highlighting the mucin network (arrowhead) [195].

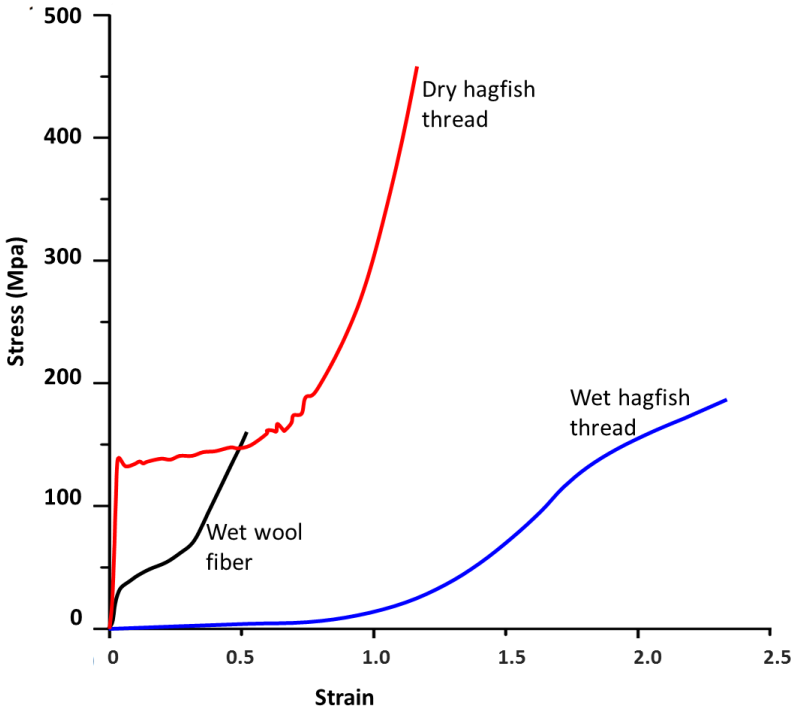

Figure 3.22 Tensile stress-strain curves of hagfish threads in seawater (blue), wet wool fibers (black) and a hagfish thread tested in air (red) (reproduced from [197]).

Hagfish slime threads have been considered as a matrix-free keratin IFs model since they consist of tightly packed and aligned IFs [148]. Mechanical tests on slime threads under different conditions (see stress-strain curves in Fig. 2.22) show that threads in seawater exhibit a low initial stiffness (6 MPa), high tensile strength (180 MPa) and a large extensibility, up to strain of 2.2 which is attributed to the soft elastomeric terminal domains of IFs [148]. In comparison, the dry threads show a high initial stiffness of 3.6 GPa, which is about 600 times the one for hydrated threads, and a high tensile stress of 530 MPa and maximum strain of 1.0. The dramatic mechanical difference between hydrated and dry threads indicates that matrix-free IFs are remarkably hydration sensitive [197]. Note that this is not contrary to the accepted view that in hydrated hard α-keratinous materials the

matrix proteins interact with water molecules more than IFs, since the threads consists of only IFs but no matrix. It should also be mentioned that the strength of dry slime threads reaches 560 MPa, the highest value reported for any keratin. This may be due to the absence of the amorphous matrix and to a scale effect, the cross sectional dimension being very small (~4.5 μm).

It is interesting that compared with the significant hydration sensitivity of hagfish slime threads, hard α-keratinous materials are much less dependent on hydration (initial tensile modulus drops by a factor of 2.7 after hydrated [197], [198]. This indicates that the matrix helps the IFs to resist swelling and maintain high stiffness and strength [195]. In addition, the mechanical properties of dry threads are comparable to those of hydrated hard α-keratinous materials, e.g. wool, suggesting that IFs in hydrated wool are maintained in a partly dry state [197]. This is supported by the fact that hard α-keratins do not swell nearly as much as slime threads when placed in water. It is also possible that the amorphous phase blocks the direct access of water to the IFs, and this hydration is decreased. The inhibition of swelling is also a possible factor.

Mechanical studies on mucins and whole slime reveal that the slime threads provide elasticity and dominate the slime's mechanical properties, while the mucins impart additional viscosity and assist in the rapid deployment of the slime into the mature state. Measurement of mucin mechanics demonstrates that the mucins are not capable of providing shear linkage between adjacent slime threads, indicating that the hagfish slime

cannot be considered as a fiber-reinforced composite. This is not necessary since the threads have enough length to span the entire slime network [194].

3.4.2 Keratinous materials based on β-keratin

3.4.2.1 Feathers

Feathers are typical hard keratinous materials, and are unique features that distinguish the birds from other animals. Flight feathers consist of a central shaft and two lateral vanes composed of barbs which are comprised of hooked barbules, and primarily aid the generation of thrust and lift; thus they must be must be lightweight, sufficiently strong/stiff and resistant to wear-induced damage, since they can be replaced only at certain times during molting [199]. The central shaft provides main mechanical support, and can be divided into calamus, the most proximal region anchors into the bird's skin, and rachis which is above the skin supporting the vanes. The inside of the hollow feather shaft is filled with air at the calamus and a foam core (medulla) at the rachis. The external shell (cortex) has dorsal, ventral and lateral walls (Fig. 2.23).

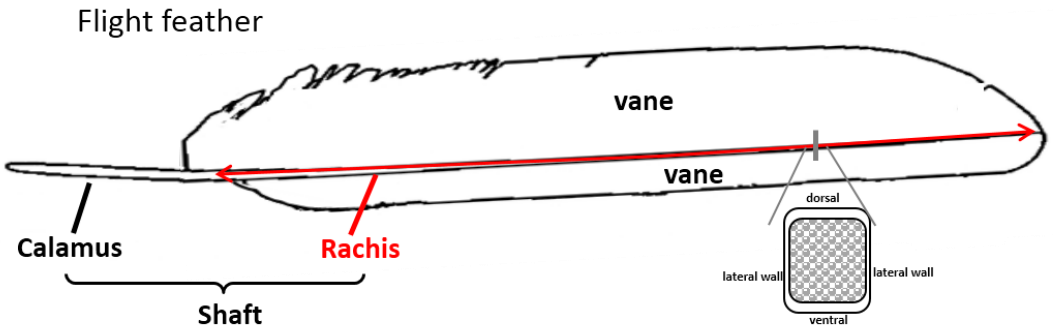

Figure 3.23 Components of a flight feather including calamus, rachis and asymmetrical

vanes (adapted from [200]).

The feather rachis has been mainly considered as a cylinder or rectangular shell filled with foam core, and the mechanical studies generally focus on macroproperties including flexural strength, stiffness, tensile strength [45] from pigeon, chicken [201], peacock [202], and toucan [140]. It is concluded that the variations of tensile Young's modulus of feather rachis among different species were low, reporting the mean value of dorsal cortex strips from eight species of birds about 2.5 GPa [45]. Water content has significant effect on the mechanical properties, shown in Fig. 2.24 [203]. The wet (100% relative humidity) exhibit substantially decreased compressive strength. At the same time, there is a synergy between the medulla and cortex; the rachis, which is a composite of medulla of cortex, shows superior compressive properties than those estimated by the sum of each through a rule-of-mixtures (Fig. 2.24 c,d).

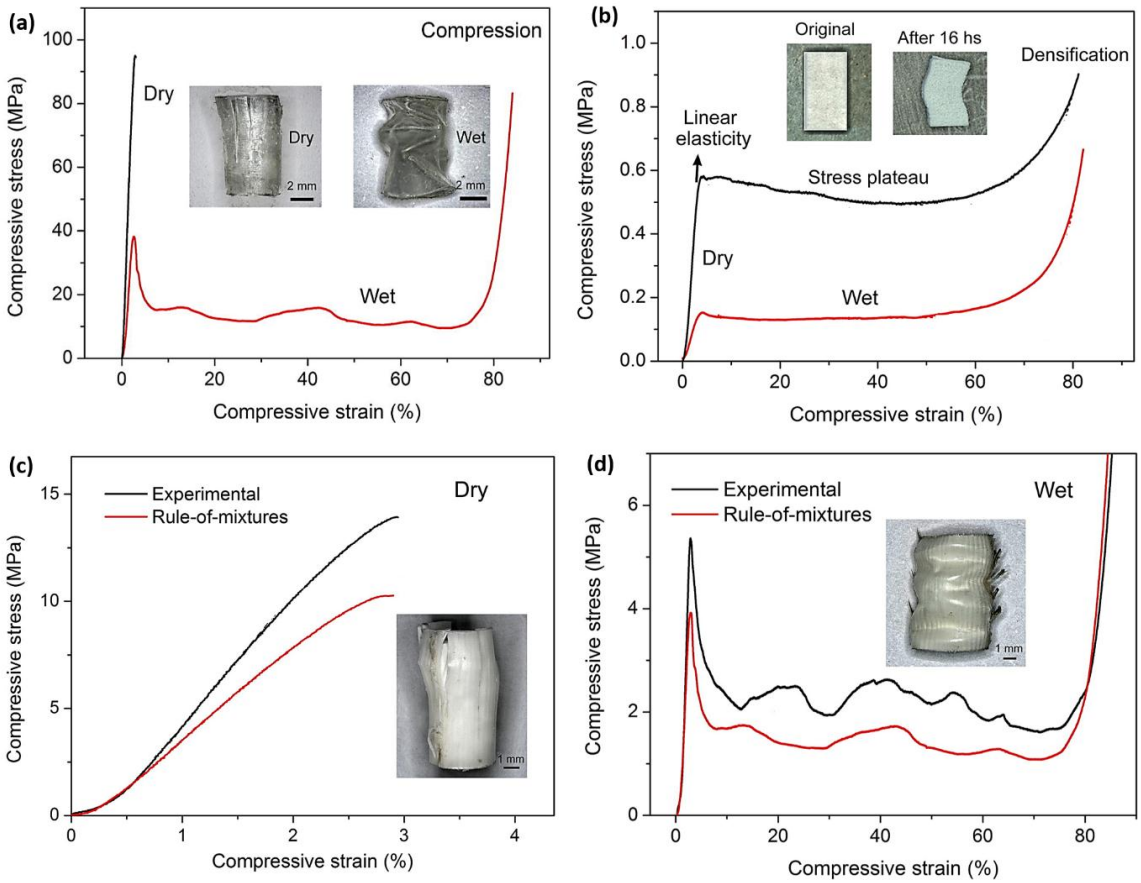

Figure 3.24 Compressive behavior of tail feather from peacock: (a) stress-strain curves of cortex at dry and wet conditions; (b) stress-strain curves of medullary foam at dry and wet conditions; stress-strain curves of experimental overall rachis and the calculated ones at (c) dry and (d) wet conditions [203].

Studies on characterizing the fine structure of feathers through x-ray diffraction[52], [54], [68], [204], [205] and transmission electron microscopy [100] allow us to know that the feathers are based on beta-keratin structure, which involves polypeptide chains organizing into β-keratin filaments surrounded by matrix protein chains [206]. Molecular studies of the keratinization reveal that the feathers are formed by matured and dead keratinocytes whose properties are determined during formation [98]. There have been very few studies detailing the fibrous structure; the fibrils comprising the feather rachis are

reported to be anisotropic, e.g. an increase of axially aligned keratin molecules towards the tip [207], the circumferential and axial fibers in rachis cortex and crossed-fibers in lateral walls observed by selectively degrading the matrix proteins [208], while direct characterization of the dorsal, lateral and ventral cortices along the shaft length remain needed. Nanoindentation is well-suited to examine the local mechanical properties of materials, and a few studies use this to test the modulus and hardness of barn owl and pigeon feathers with indents not spanning all cortex [200], of mute swan, bald eagle and partridge feathers with indents only at calcamus [209], and of peacock feather with indents not specifying the location [203].

3.4.2.2 Beak ramphotheca

The rhamphotheca (surface layer) of bird beaks is composed of hard keratinous material, and it enables the beaks to serve a variety of functions, such as foraging, feeding, fighting, social interaction and grooming [210], [211]. Avian beaks continuously grow and are composed of bone and keratin [212]. They are typical low-weight, sandwich-structured composites. The toucan beak is both long and thick, with a density about 0.1 g/m^3. The beak comprises one-third of total length of the bird, but makes up only one twentieth of its mass [150]. Fig. 2.25 shows the morphology and microstructure of a Toco toucan beak [150], [213], [214]. It consists of an exterior keratin shell, the rhamphotheca, and an interior, bony foam with a fibrous network. From Fig. 2.25c the internal foam exhibits a closed-cell

configuration, and most of the cells are sealed by membranes. The total outer shell thickness varies between 0.5 and 0.75 mm, consisting of multiple layers of keratin scales (Fig. 2.25d). The thickness and diameter of each scale are approximately 2-10 μm and 30-60 μm respectively.

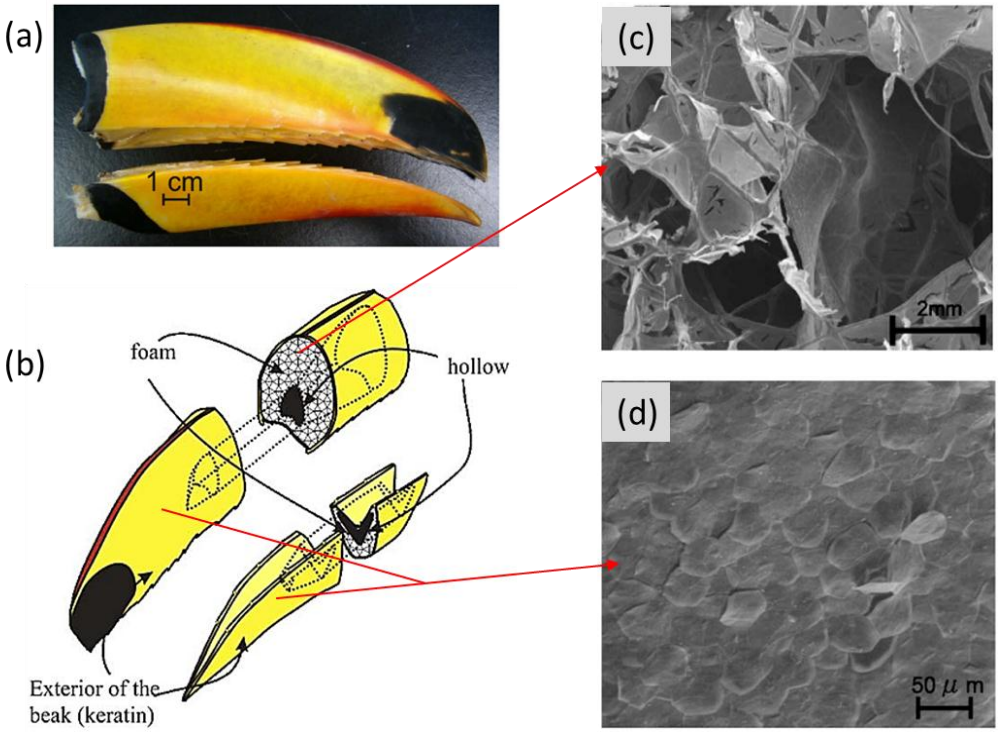

Figure 3.25 Structure of a Toco toucan beak: (a) Photograph of the beak showing maxilla and mandible [214]; (b) schematic showing internal and external structure; (c) scanning electron micrograph of the interior of beak, showing the foam with closed cells (several are crushed/ripped); (d) scanning electron micrograph of the rhamphotheca,(keratinous surface) showing the keratin scales [213].

Fig. 2.26 shows typical tensile stress-strain curves of the rhamphotheca of a Toco toucan beak along different orientations [213]. There is significant scatter in the results (Fig. 2.26b), but no systematic difference in Young's modulus and yield strength along the transverse and longitudinal directions (the mean Young's modulus is 1.4 GPa and the yield

strength is 30 MPa). Thus the rhamphotheca can be considered transversely isotropic. Fig. 2.26c shows the compressive stress-strain curves of the interior foam, which is bone and not keratin. The plateau region is associated with the collapse of the cell walls, and the densification of the cell walls occurs after the plateau [150], [213].

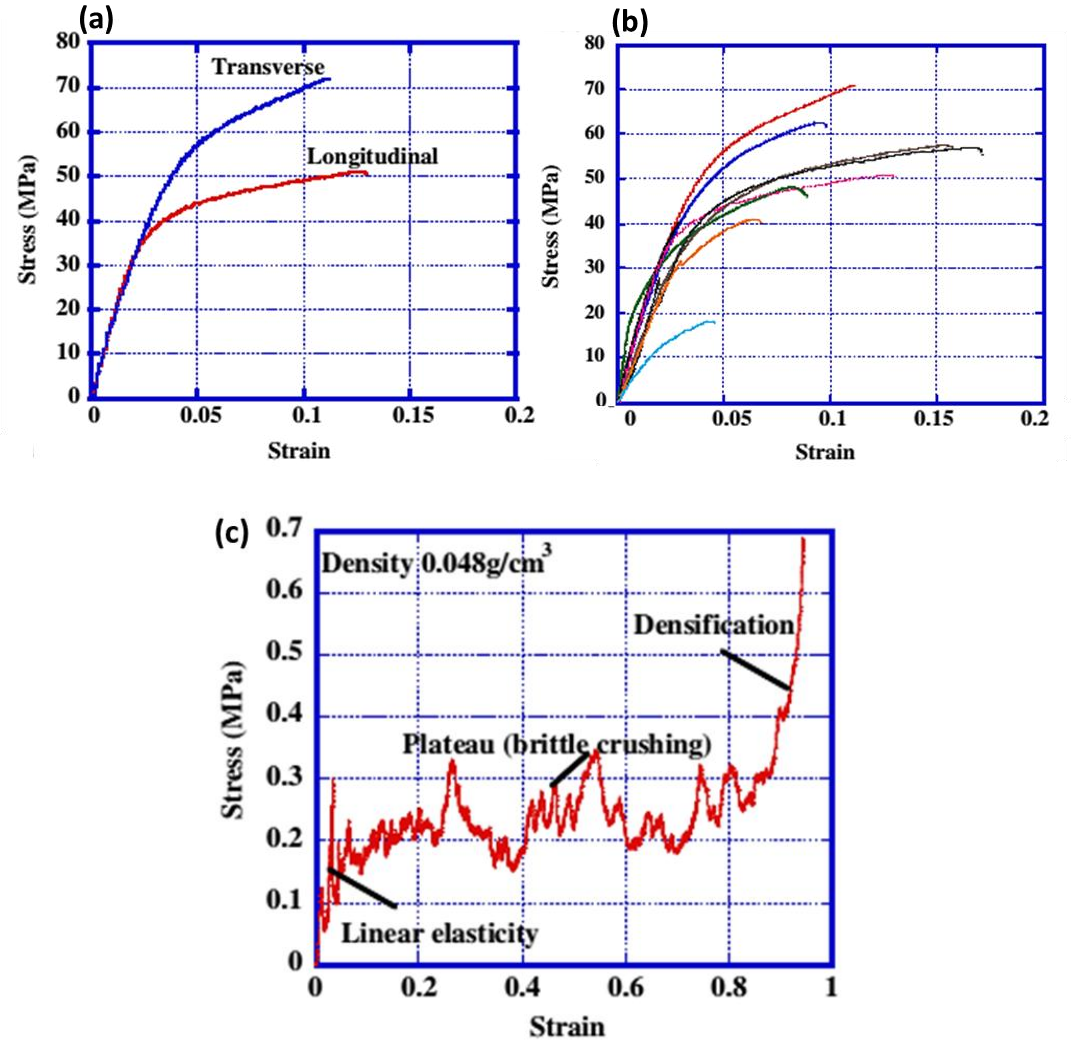

Figure 3.26 Mechanical properties of a Toco toucan beak: (a) representative tensile stress-strain curves of the rhamphotheca along transverse and longitudinal orientations [213]; (b) tensile stress-strain curves showing the scatter of results; (c) compressive stress-strain curve of the interior foam showing characteristic cellular response [150].

As a polymeric composite, the rhamphotheca of the toucan beak shows strain-rate

dependence and the tensile failure mode changes from keratin scale pull-out to brittle scale fracture as the strain rate increases. The pulled out scales are the result of viscoplastic shear of the interscale material at low strain rate which enables a large amount of molecules to move and change their configurations and the scales to slide. At high strain rate (1.5×10^{-3}/s), the keratin scales are fail in tension, which is characterized as brittle failure. When the yield stress approaches the UTS, brittle fracture of the scales occurs over viscoplastic deformation of the interscale material. The transition from pull out to brittle fracture is governed by the criterion,

$$\sigma_t \leq \sigma_g \text{ or } \sigma_t \geq \sigma_g , \quad (4)$$

where σ_t is the fracture stress and σ_g is the flow stress by interscale gliding. The strain rate dependence of σ_g can be expressed as

$$\sigma_g = \mathrm{k}\dot{\varepsilon}^m \quad (5)$$

where m is the strain rate sensitivity. The competition between viscoplastic shear of the interscale material and brittle fracture is similar to the response showed by the abalone shell in tension [215].

3.4.2.3 Claws

Claws are curved, pointed appendages found at the end of digits in most amniotes (terrestrial egg laying animals), and they differ from nails which are flat and do not possess a sharp point. Claws of birds and reptiles show a β-type structure, which are the subjects

in this section; whereas the claws of mammals are not because they show an α-type. The claw functions are catching and holding prey, digging, climbing and grooming. Fig. 2.27 shows the morphologies during a mouse claw development [216]. It begins on the webbed digits on the 14th day of gestation with a slight thickening of the epidermis near the tip of the digit (Fig. 2.27a,b). By 15 days a groove on the dorsal and lateral surfaces of the digit outlines the proximal border of the claw field. A proximal fold starts to form at the proximal groove at 16 days of gestation (Fig. 2.27c,d). The claw develops and reaches the end of the digit by birth at 21 days of gestation (Fig. 2.27e,f), and at this time it is similar to adult claw (Fig. 2.27g,h). The claw is curved both longitudinally and laterally and extends well beyond the end of the digit.

Claws consist of a superficial and a deep layers of hard keratin, these two layers being produced by the basal and terminal matrices respectively [217], [218]. The beta-keratin filaments are oriented parallel to the direction of growth in claws of various species and at intermediate angles in claws of some primates [219], e.g. marmosets and tamarins. A transmission electron micrograph (Fig. 2.9g) of fowl claw shows clearly beta-keratin filaments with about 3.5 nm in diameter embedded in a dark (densely stained) matrix [48].

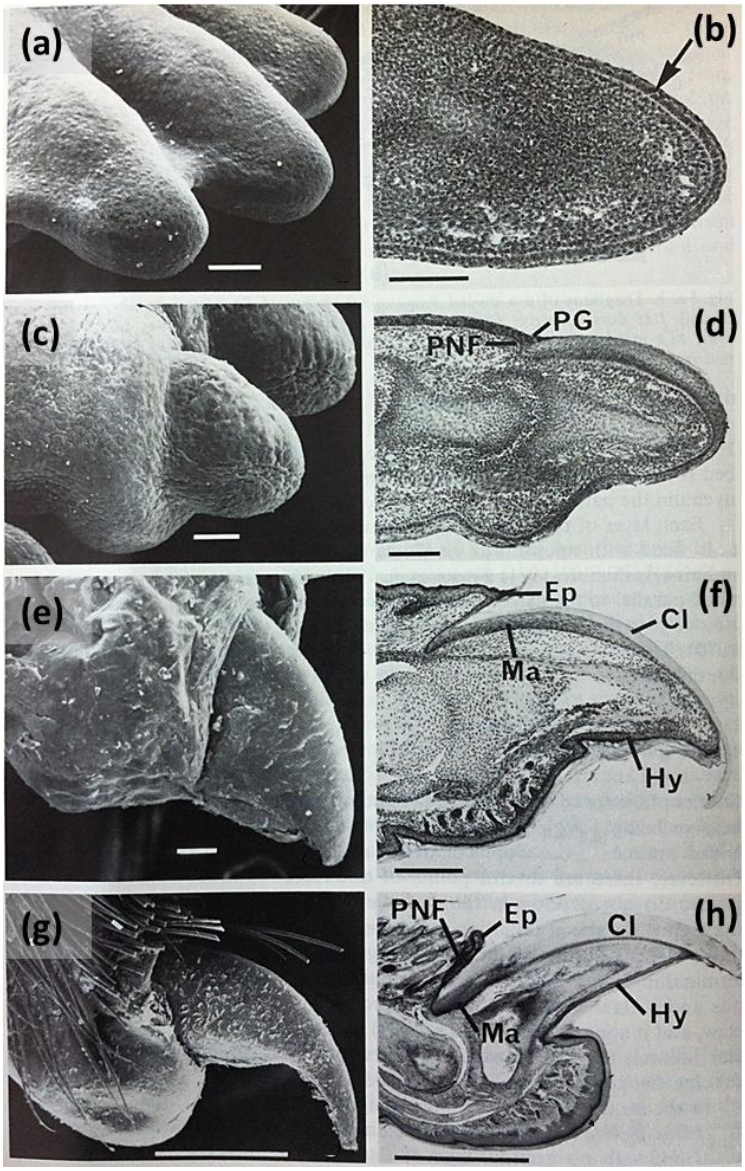

Figure 3.27 Surface views (a,c,e,g) and longitudinal sections (b,d,f,h) of digits of fetal (a-b 14 days of gestation, c-d 16 days gestation), newborn (e,f) and adult mice (g,h) showing evolution of the claw morphology. Arrow in (b) indicates the initial epidermal thickening of claw. Cl claw; Ep eponychium (the thickened layer between the claw and epidermis); Hy hyponychium (the thickened epithelium under claw); Ma matrix; PG proximal groove; PNF proximal nail fold. Scale bars: (a-f), 0.1 mm; (g-h), 1.0 mm [216].

Claws have to transmit and withstand substantial forces during locomotion, and must resist abrasive wear from contact with substrates [220], [221]. The mechanical properties of claws have not been studied widely or in detail. It is reported that for ostrich

claw keratin, the tensile Young's modulus along the length direction is 1.84 GPa and that perpendicular to claw length is 1.33 GPa [222]. This weak anisotropy is compared with horse hooves which have comparable modulus (2-3 GPa) and are 10-40% less stiff transversely than longitudinally [223], [224]. The porcupine quills are only about 10% as stiff transversely as longitudinally [128]. The mechanical anisotropy of keratins comes from the preferential orientation of fibers, which is correlated with the real loading conditions the animals and tissues experience. The explanation for the weak anisotropy of claws may be that the loadings that the claws endure through life are less predictable or do not have a preferred direction [222].

Hydration plays a role in the tensile mechanical properties of ostrich claw [149]. As the relative humidity (RH) increases from 0% to 100%, the Young's modulus and tensile strength decrease significantly, from 2.7 to 0.14 GPa, and from 90.3 to 14.3 MPa, respectively, while the strain to failure increases. This trend is similar to those of α-keratinous materials. As it was reported [222] that claw keratin tends toward isotropy in Young's modulus along and across the claw axis, it is suggested that the claw keratin is less ordered and more sensitive to hydration [149].

3.4.3 Keratinous materials based on α- and β-keratin

3.4.3.1 Reptilian epidermis

The epidermis of reptiles synthesizes both α- and β-keratins [101], [225]–[231].

The α-layer of squamates (lizards and snakes), turtle leg and neck epidermis, and crocodilian epidermis, yields an α-type x-ray diffraction pattern [205] and consists of 7~8 nm diameter filaments in an amorphous matrix [232]. The β-layer of squamate scales, turtle and tortoise shell epidermis and crocodilian epidermis yields a β-type X-ray diffraction, and consists of 3 nm filaments in an amorphous matrix [233].

The reptilian epidermis has certain characteristics in common whereas among the orders of reptiles, the anatomy of the epidermis differs remarkably [233], [234]. We discuss below the nature of keratins in reptiles.

Squamata. Lizard epidermis is composed of a complex sequence of cornified layers consisting of the Oberhäutchen (from German: little surface skin), beta, mesos, and alpha layers (shown in Fig. 2.28, [235]), which all rest upon a stratum of living cells. Fig. 2.29 shows a transmission electron micrograph of the beta-layer of desert iguana, and the structure with 3 nm filaments embedded in matrix [233]. The snake (Kenyan sand boa *Gongylophis colubrinus*) epidermis also shows similar structure including the Oberhäutchen layer, beta-layer (thick), mesos-layer (2-10 layers of flattened cells containing α-filaments), alpha-layers (several keratinized cell layers), lacunar tissue (1-4 cell layers) and the clear layer (lies directly above the stratum germativum), shown in Fig. 2.30 [151].

Crocodilia. The cornified epidermis of crocodilians (crocodilian scales) varies in composition. It has the characteristics of a beta layer (corneocytes about 0.3-0.6 μm thick

composed of β-keratin) and the hinge region appears like a mesos layer with characteristics of both α- and β-keratins [230], [233], [234], [236].

Testudines. The cornified epidermis of the carapace of the turtles and tortoises is composed of β-keratin which is firmly attached to the underlying living cells. The pliable epidermis of their head, neck and leg skin is composed of α-keratin over a layer of living cells [101], [233], [237], [238].

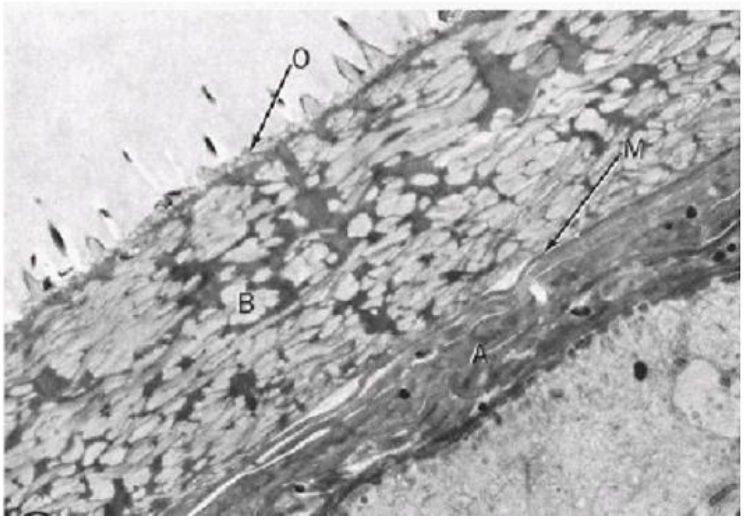

Figure 3.28 Cross section of epidermis of American chameleon showing both α- and β-keratin layers. O: oberhäutchen layer; B: beta layer; M: meso layer; A: alpha layer [235].

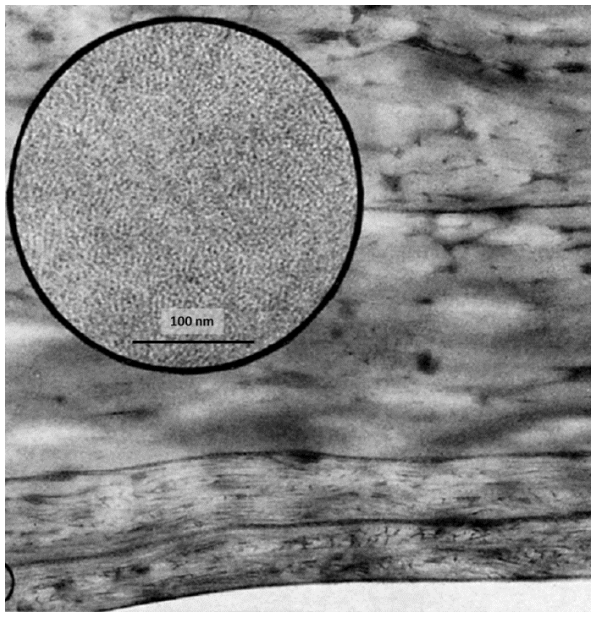

Figure 3.29 Transmission electron micrographs of the epidermis of the desert iguana, Dipsosaurus dorsalis. The β layer (upper) is compact without visible cell outlines. The insert shows the β pattern keratin consisting of 3 nm filaments embedded in amorphous matrix. The bottom of the figure is the mesos-layer where the cells become more reticulated. The mesos experiences a transition from the β to the α layer and the filaments yields an α-keratin pattern [233].

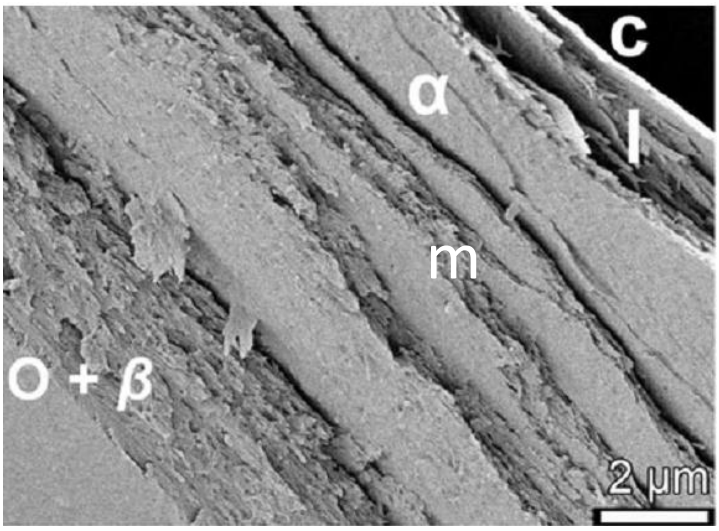

Figure 3.30 Cryo-scanning electron micrograph of the epidermis of the ventral scale from the Kenyan sand boa Gongylophis colubrinus. The epidermis consists of (from outside to inside): Oberhäutchen+β-layer (O+β), mesos-layer (m), α-layer (α), lacunar tissue (l), and clear layer (c) [151].

The mechanical properties of epidermis from reptilians have been investigated. Tensile tests on skin strips (the outer from the inner layer of the dermis, 0.30 mm) from a gecko (*Ailuronyx seychellensis)* show a breaking stress of 0.9 MPa, an elastic modulus of 4.6 MPa and failure strain at 0.3 [239]. Mechanical studies on the epidermis shed in four snake species demonstrate that all species show a gradient in properties: the integument consists of hard, robust outer scale layers (Oberhäutchen and beta-layer) with a higher effective modulus and higher hardness, and soft, flexible inner scale layers (alpha- and clear layers) [151], [240]. Fig. 2.31 shows the nanoindentation results for the outer scale layers and inner scale layers of ventral scales from Kenyan sand boa *Gongylophis colubrinus* [151] as a function of indentation depth. It is clear that the outer scale layers exhibit much higher values all through the load-displacement than the inner scale layers (Fig. 2.31a), and thus the effective modulus obtained for outer scale layers (4.1 GPa) is higher than that of the inner scale layers (3.2 GPa). There is also a difference between the hardness values of the outer (0.28 GPa) and inner (0.14 GPa) scale layers. Compared with other keratinous materials and considering the mechanical variations of α- and β-keratins, it was suggested that the β-layers' main function is to protect the epidermis against abrasion [241], and that the high abrasion resistance of snake epidermis is due to the material property gradient of the integument from a hard and inflexible outside to a soft and elastic inside [151]. For a system involving large loads under pressure against abrasion, such a design leads to more uniform stress distribution and the minimization of the probability of

local stress concentration [12], [242]. This is similar to other biological materials, such as tooth, in which the hard enamel envelops the soft pulp, with gradient of material properties to endure high amounts of stress under pressure, a key feature against abrasion wear [242], [243]. Fish scales use the same design concept, a highly mineralized surface and a tougher foundation.

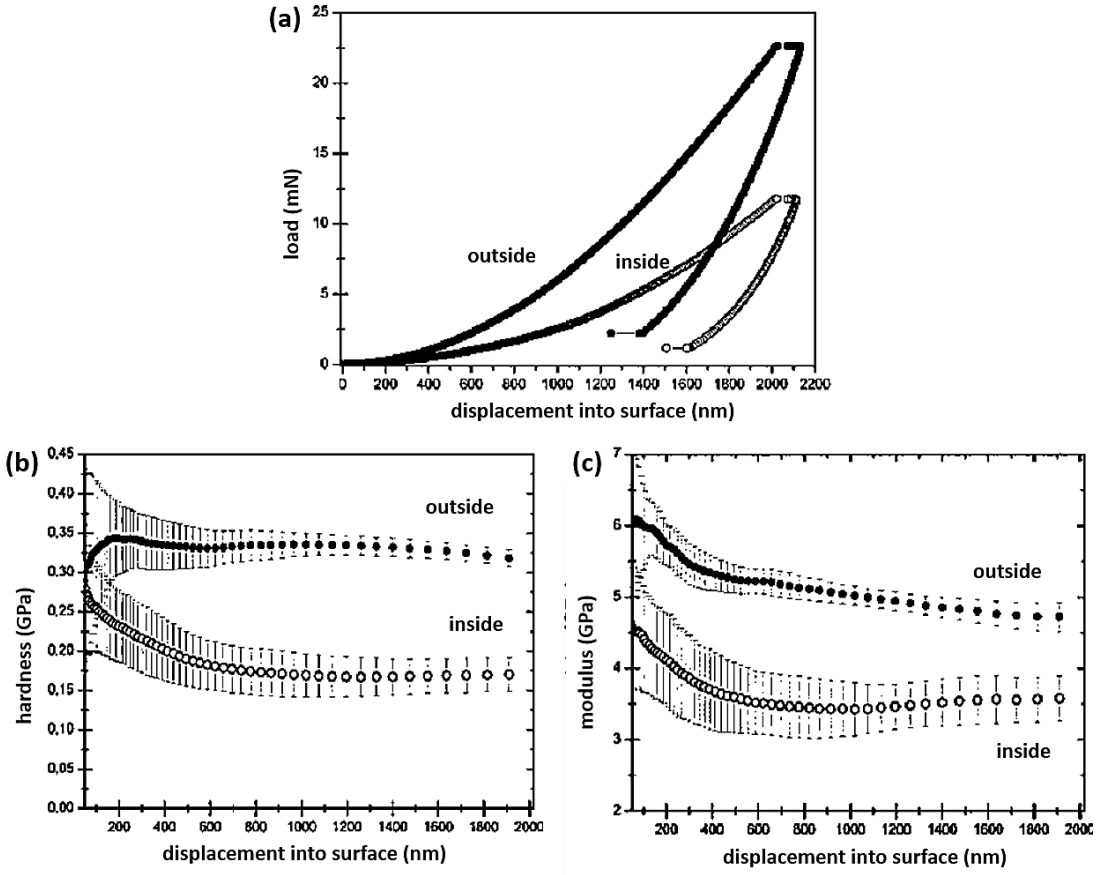

Figure 3.31 Variation in nanoindentation from the outer (outside) and inner (inside) scale layers in Kenyan sand boa Gongylophis colubrinus. (a) Load-penetration curves; (b) Hardness variation with penetration in outer and inner layers; (c) Effective elastic modulus as a function of penetration for outer and inner layers. The error bars denote the standard deviations [151].

3.4.3.2 Pangolin scales

The pangolin is the only known mammal with a distinct adaptation: overlapping keratinous scales covering the body as flexible dermal armor [244]. Fig. 2.32a shows the protective function: the pangolin, when threatened by predators (in this case, a lion), curls up into a ball with only the hard and sharp-edged scales projecting outwards, providing protection and defense. The name, pangolin, comes from the Malay word, pengguling, meaning "something that rolls up" (Oxford dictionary). In 1820 an armor coat made of pangolin scales was presented to the King George III (Fig. 2.32b). The pangolins are nocturnal animals and feed on ants and termites, thus obtaining the alternative name, scaly anteaters. They are found naturally in tropical regions throughout Africa and Asia. There are eight species of pangolins, which are often divided into ground pangolins that dig and remain in underground burrows, and arboreal pangolins living in hollow trees. Typical ground pangolin (Chinese pangolin) and forest pangolin (African Tree pangolin) and their scales are shown in Fig. 2.32c,d. The African tree pangolins have relatively long tails (about 54% of total length) to help in climbing and hanging on trees, and the scales show a much higher ratio of length over width than those of the Chinese pangolin (the scale length is parallel to the scale growth direction indicated by red arrows).The scales and skin make up about 25 wt% of the pangolin's body mass [245], and the scales cover everywhere of the animal except the ventral head, ventral trunk, the inner surface of the limbs, and the

foot pads [246]. Pangolin scales originate from the thick skin and continue to grow throughout the life like hair and fingernails, replacing wear loss (scale growth direction indicated by red arrows in Fig. 2.32b,c) [246]. The number of scales remains constant during adolescence [247].

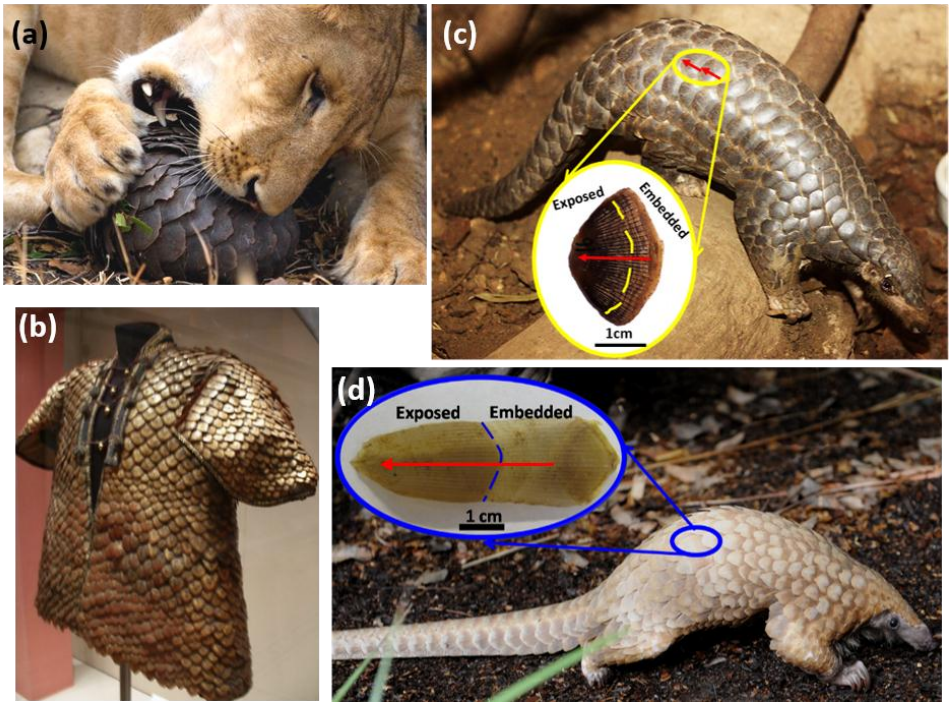

Figure 3.32 (a) The protective function of the pangolin scales from the lion (predator) (http://www.animal-space.net/2010/12/lion-vs-pangolin.html); (b) An armor coat made of pangolin scales (http://commons.wikimedia.org/wiki/File:Coat_of_Pangolin_scales.JPG?uselang=zh-cn); (c) Chinese pangolin (ground type) (http://commons.wikimedia.org/wiki/File:Zoo_Leipzig_-_Tou_Feng.jpg) and the scale; (d) African Tree pangolin. Arrows indicate the scale growth direction.

From limited reports based on the histological structure and distribution of bound phospholipids, bound sulfhydryl groups, and disulfide bonds [49], pangolin scales can be divided into dorsal, intermediate and ventral regions through the cross section. This was suggested to be homologous with primate nails, whereas other investigators report that the

pangolin scales consists of both α- and β-keratins [248], a feature of reptilian scales.

The scales need exceptional wear resistance for burrowing, thus there are a few studies on the abrasive properties [248], [249], and hydration effect [41]. In abrasion, a rotary disc drives wet abrasive sliding against scale specimens, and results from different abrasives and different sliding orientations were analyzed [248]. In dry tribological tests, the wear behavior of a steel block sliding against scale specimens under different loads and velocities was reported [249] (Fig. 2.33a), and The wear rate increases first as the loading increases, and then decreases. Higher velocity leads expectantly to higher wear rate (Fig. 2.33b). The water-induced recovery of mechanical properties via indentation and bending of pangolin scales was also examined [41].

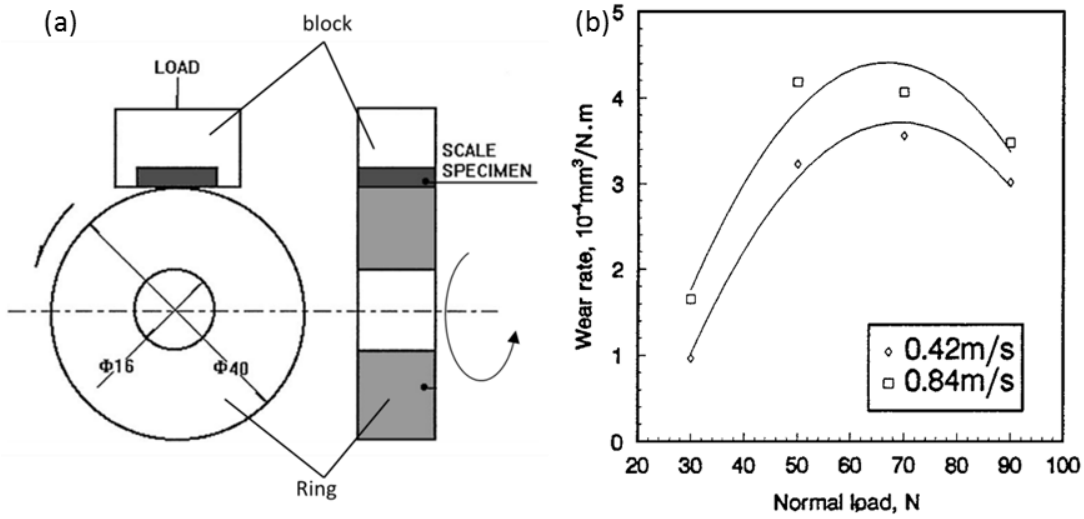

Figure 3.33 . (a) Schematic diagram of the block-on-ring wear test used to determine for wear rate (in volume per unit energy) of pangolin scales; (b) wear rate as a function of normal load for two sliding velocities sliding velocities: 0.42 and 0.84 m/s; as wear rate increases with velocity [249].

3.5 Bioinspired designs

Bioinspiration is classified, as presented by Meyers and Chen [20], into traditional and molecular-based. In traditional bioinspiration, we try to copy the characteristics of biological materials using combinations of synthetic materials that are completely different but provide equivalent or similar mechanical response. The classic example is Velcro, based on the burrs of seeds but using synthetic materials to achieve the hooking-unhooking capability. Molecular-based bioinspiration is a much more complex process because we mimic the molecular structure. The use of biological molecules to develop synthetic equivalents to the biological materials is a pursuit with significant potential pay-off.

3.5.1 Tradional bioinspiration

It is suggested that the structure of hedgehog spine and porcupine quills [134], [250] are optimally designed to resist buckling loads. Aluminum tubes filled with aluminum foam resisting compressive loading and buckling analogous to the quill and spine, with similar structural design and reinforcement mechanism, were manufactured [251]. It is also reported that a novel composite with similar structure as horns and hooves, with a “forest” grown on the surface of laminate, exhibits enhanced mechanical properties [252]. Fig. 2.34a shows the schematic of processing the 3D composite that involves the growing of carbon nanotubes on the fiber cloth, stacking the matrix-infiltrated nanotube-grown fiber cloth and pressing the plates. Fig 2.34b shows the structures of the SiC fabric cloth with

and without the perpendicularly grown carbon nanotubes. Compared with the base composite (G_{IC}=0.95 kJm^{-2}), the nano-tube infiltrated composite showed large improvement of interlaminar fracture toughness, G_{IC}= 4.26 kJm^{-2}, and this approaches the properties of the most fracture-resistant biological materials known, e.g. hoof wall with J_{crit}=5.63 kJm^{-2} (critical J-integral value) at 53% RH [181], [187].

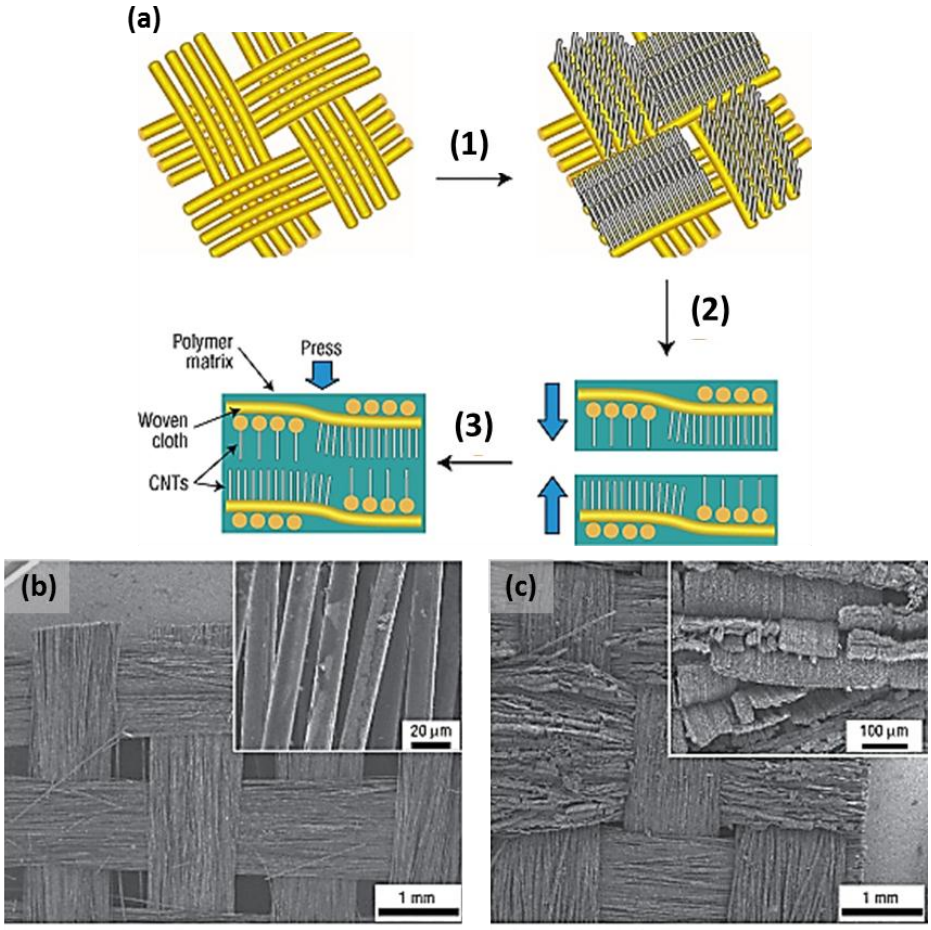

Figure 3.34 (a) Processing for the manufacture of 3D carbon nanotubes (CNT) composite: (1) aligned CNTs grown perpendicular to SiC fiber cloth; (2) stacking of matrix-infiltrated (blue color) CNT-grown fiber cloth; (3) 3D nanocomposite plate fabrication by hand lay-up. (b) Scanning electron micrograph of the plain-weave SiC fabric cloth. Insert: higher magnification of the individual fibers. (c) Scanning electron micrograph of the cloth with CNTs grown perpendicularly on the surface. Insert: higher magnification image [252].

The hierarchical architecture of feathers has been mimicked to manufacture novel carbon fiber reinforced polymers with nanofibrous fractal interlayers as weight-saving composites [253]. Fig. 2.35a shows the how the feather fractal architecture is imitated: the rachis (mm), barbs (μm) and barbules and hooklets (nm) correspond to the carbon fiber, electrospun fibers and carbon nanotubes (CNT), respectively. The electrospun fibers with carbon nanotubes inside are the main interlayer reinforcement that enhance the ultimate strength of composite, which is compared with conventional laminated composite in Fig. 2.35b. The synthesis includes: (1) prepare polymer solution for electrospun fibers: cellulose acetate in acetone solution with CNT added; (2) obtain the layers: the CNT polymer solution is used to electrospin fibers (shown in Fig. 2.35c) on a target which is the carbon fiber bed; (3) form the composite: consolidate the layers through lay-up within resin (vacuum and 180 ^{o}C). Fig. 2.35d shows the fractured morphology of the CNT reinforced electrospun fiber interlayer within the composite. The feather-inspired composite achieves higher mechanical properties than conventional carbon fiber reinforced polymers: the storage modulus increased 85%, the flexural strength (307 ± 32 MPa) and modulus (38 ± 2 GPa) increased 51% and 54%, respectively, and the Mode II fracture toughness (892 ± 90 Jm^{-2}) increased 165%. Taking into consideration the weight saving (specific weight 1.62 ± 0.02 gcm^{-3}, 6% reduction than conventional carbon fiber reinforced polymers) together, this CNT reinforced interlayered composite demonstrates the potential for applications in several industry, such as automobiles, aerospace, marine, and sports [253].

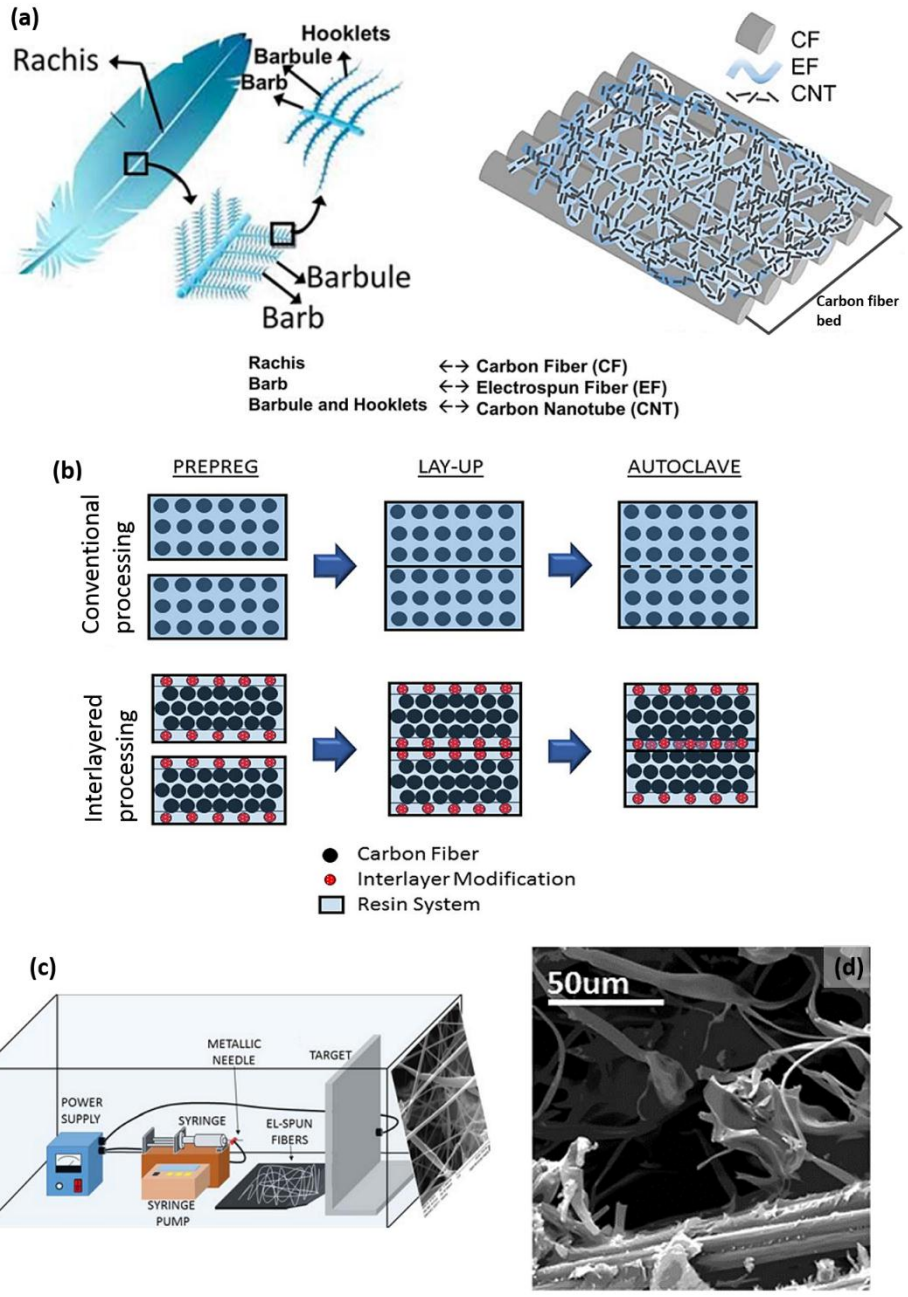

Figure 3.35 The feather-inspired composite with electrospun fiber interlayers: (a) the feather fractal architecture of rachis, barbs and barbules and the inspired the structure consisting of carbon fibers, electrospun fibers and carbon nanotubes; (b) conventional laminate composite and interlayered laminate; (c) electrospinning apparatus with the electrospun fibers on the right; (d) flexural fractured surface of the composite at the carbon nanotube reinforced electrospun fiber interlayer [253].

The North American porcupine quills show interesting features that can be applied

to the development of bio-inspired medical devices [254]. The quills have microscopic backward-facing barbs at the conical black tip (Fig. 2.36a-c), which enables an easy penetration but strong tissue adhesion through the deployment and bending of barbs during removal (Fig. 2.36d). Compared with barbless quill (experimentally removed barbs) and African porcupine quill (naturally barbless), the barbed quill shows significant lower penetration force and work of penetration, which is needed for some medical devices (e.g. needles, vascular tunnelers), but higher pull-out force and work of removal, which is the important property of tissue adhesives (Fig. 2.36e). Fig. 2.36f-g shows synthetic replica molded polyurethane (PU)-barbed quill that reproduces the surface topography of the North American porcupine quills and PU-barbless quill, and penetration tests reveal that the barbed quills show 35% less force (Fig. 2.36h). Prototypic hypodermic needles with barbs were fabricated, and the PU-barbed needle shows 80% less penetration force compared with the PU-barbless needle (Fig. 2.36i-j). The high tissue adhesion of the quills is also imitated through fabricating prototypic quill-mimatic patches that have replica molded PU-barbed and PU-barbless quills (Fig. 2.36k). The PU-barbed quill patch shows significantly higher adhesion force and interaction with the tissue than the PU-barbless quill patch (Fig. 2.36l-n), which is useful for the development of mechanically interlocking tissue adhesives [254].

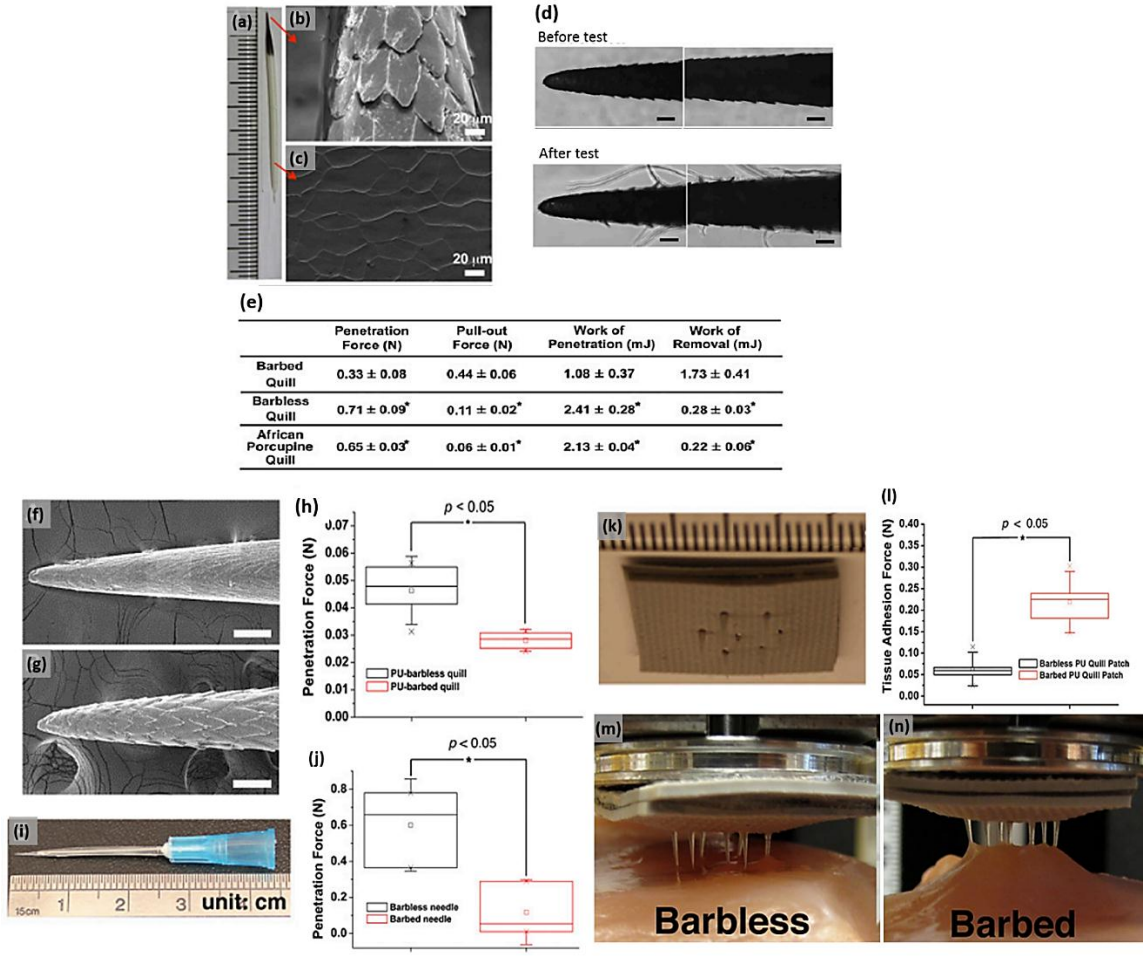

(e)

	Penetration Force (N)	Pull-out Force (N)	Work of Penetration (mJ)	Work of Removal (mJ)
Barbed Quill	0.33 ± 0.08	0.44 ± 0.06	1.08 ± 0.37	1.73 ± 0.41
Barbless Quill	0.71 ± 0.09*	0.11 ± 0.02*	2.41 ± 0.28*	0.28 ± 0.03*
African Porcupine Quill	0.65 ± 0.03*	0.06 ± 0.01*	2.13 ± 0.04*	0.22 ± 0.06*

Figure 3.36 The porcupine quills and the bio-inspired designs: (a) North American porcupine quill; scanning electron micrographs of (b) the quill tip showing the deployable barbs and (c) quill base showing the smooth scale-like surface; (d) optical micrographs of porcupine quills before penetration and after removal; note the deployment and bending of the barbs; (scale bars: 100 μm) (e) experimental results of barbed quill, barbless quill and African porcupine quill from penetration/removal tests (mean±SD); scanning electron micrographs of the synthetic quills using replica molding and polyurethane (f) PU-barbless quill and (g) PU-barbed quill (scale bars: 100 μm); (h) the forces required to penetrate barbed and barbless PU quills into muscle tissue to 4 mm depth; (i) the fabricated quill-inspired needle; (j) the forces required to penetrate barbed and barbless quill-inspired needles into a human skin model; (k) the fabricated quill-inspired patch consisting of seven PU quills; (l) adhesion forces from barbless and barbed PU quill patches; the interacting with muscle tissue of (m) barbless PU quill patch and (n) barbed PU quill patch during retraction [254].

Whale baleen has inspired a self-cleaning filter system, the Baleen Filter patented

by the University of South Australia [255], [256], for industrial wastewater filtration. This technology imitates how whales collect organisms through their baleen and how they keep the baleen clean and free from long-term deposits by combining a sweeping action of the tongue and the reversing of water flows. The Baleen Filter utilizes fine sieves, which are made from stainless steel or polymers and use a special woven wire screen-mesh in a planar form, which can separate organic and inorganic matter from waters to less than even 5 micron. The successful trials across industries, such as meat and by-products, food and dairy, mining and municipal, have demonstrated that the Baleen filter can be used in traditionally difficult applications, and reliably and cost efficiently separate matter, whether solid, semi-aqueous or immiscible, from wastewater streams with suspended solids and fat in high or variable concentrations [257].

There are a number of products having similar mechanism as or inspired by the pangolin scales which function as flexible dermal armor. The Dragon Skin® is a type of ballistic vest made by Pinnacle Armor, using the design of circular overlapping discs similar as the pangolin scales. The overlapping discs made of silicon carbide create a highly flexible vest and are intended to resist bullet penetration. Another product that imitates the pangolin scales is the Pangolin backpack by Cyclus Manufacture® [258]. The pangolin backpack has large, hard overlapping layers made of inner tubes of recycled tire, and each layer closure is retractable due to magnets. It is water resistant, and provides shock absorption through adjustable padded straps and full comfort by airflow back channels,

durable and protective with personal style.

3.5.2 Molecular-based bioinspiration

The egg capsules of the oviparous gastropods (*Pugilina cochlidum* and *Busycotypus canaliculatus*) are keratin-like biopolymers that display outstanding mechanical properties. This is to a large extent due to the α↔βreversible transformation that occurs on tension loading. There is no synthetic polymer equivalent and therefore Miserez and co-workers [259] have been working at recreating the structure by using advanced biology techniques and biomimetic self-assembly of molecules. Fibrin, myosin II, keratin, and the keratin-like proteins in the egg capsules have intermediate filaments which can undergo the α→β transformation. Thus, the studies on the egg capsules have direct relevance for keratins because the same methodology can be used.

The initial stages are to self-assemble the peptides into nano-fibrils with excellent control. This was done by Banwell et al. [260] who produced coiled coils synthetically. These short nanofibrils were used to construct hydrogel scaffolds in tissue engineering applications. However, the egg capsule proteins exhibit a Young's modulus of 50-100 MPa, which is orders of magnitude larger than hydrogels. They can undergo reversible strains of up to 170% and this leads to an extraordinary energy absorption capability. The coiled coil domains in the intermediate filaments (IFs) vary in length from 10 to 50 nm and in diameter from 7 to 11 nm. Recent efforts by Fu et al. [261] have yielded much larger

coiled coil domains of α protein which can, on extension, transform into beta sheet domains.

Acknowledgements

Chapter 3, in part, is reprint of the publication: Wang B, Yang Wen, McKittrick J, Meyers M. (2016) “Keratin: Structure, mechanical properties, occurrence in biological organisms, and efforts at bioinspiration”, Progress in Materials Science, 76;229-318. The dissertation author is the first author of these manuscripts.

.

4 Pangolin scales

The armor function and toughening mechanisms of the pangolin scales have not been studied in detail, since they are not as well-known as their curl-up defense [262]. As one keratinous material, the fibrous structure in hierarchical levels of pangolin scales is absent, and mechanical characterization of the scales, key to the understanding of protective functions, remains significantly insufficient. Therefore, the correlation of the mechanical behavior to the nano- and micro-structures of pangolin scales is of great importance.

In an aim to understand the distinct protective function of pangolin scales, the present work investigates the overlapping mechanism, microstructure and mechanical properties. The organization of pangolin scales is compared with other scales; the morphology and the structure of pangolin scales are characterized and correlated to the mechanical behavior. The findings and analyses presented are aimed at providing fundamental knowledge to the development of new bioinspired armor designs

4.1 Materials

Typical scales from ground pangolins found in southern Asia, Chinese pangolin (*Manis pentadactyla*), and from typical arboreal pangolins in central Africa, African tree pangolin (*Manis tricuspis*) were studied in this work. The Chinese pangolin scales are dark brown or yellow-brown, and have dimensions 10-30 mm wide, 20-40 mm long and 0.4-3

mm thick; the African tree pangolin scales are russet or brownish yellow, and in average 18 mm wide, 40 mm long [247] and around 1.5 mm thick (Fig. 4.1). According to the shape and location on the body, two types of scales are observed: trunk scales, representative of the majority, with elongated or broad rhombic shape (Fig. 4.1a and b for African tree and Chinese pangolin scales, respectively), and scales at the tail edges with a folding shape at the middle of the scale with an average angle of 70~90^{o} (Fig. 4.1c). The scales show longitudinal ridges on external surface (indicated by blue lines in Fig. 2a,b) parallel to scale growth direction (growth line, red arrow, Fig. 4.1a.b). The Chinese pangolin scales from a host with unknown age were bought from a pharmacy in China, and might have been treated by boiling water (boiling water does not significantly affect the mechanical properties). The African tree pangolin scales were obtained from the San Diego Natural History Museum (the deceased African pangolin skin was stored in a dry container and only the internal surface of skin was preserved in a salt environment). Both kinds of scales were stored in dry containers in the laboratory with 50% relative humidity at room temperature before examination.

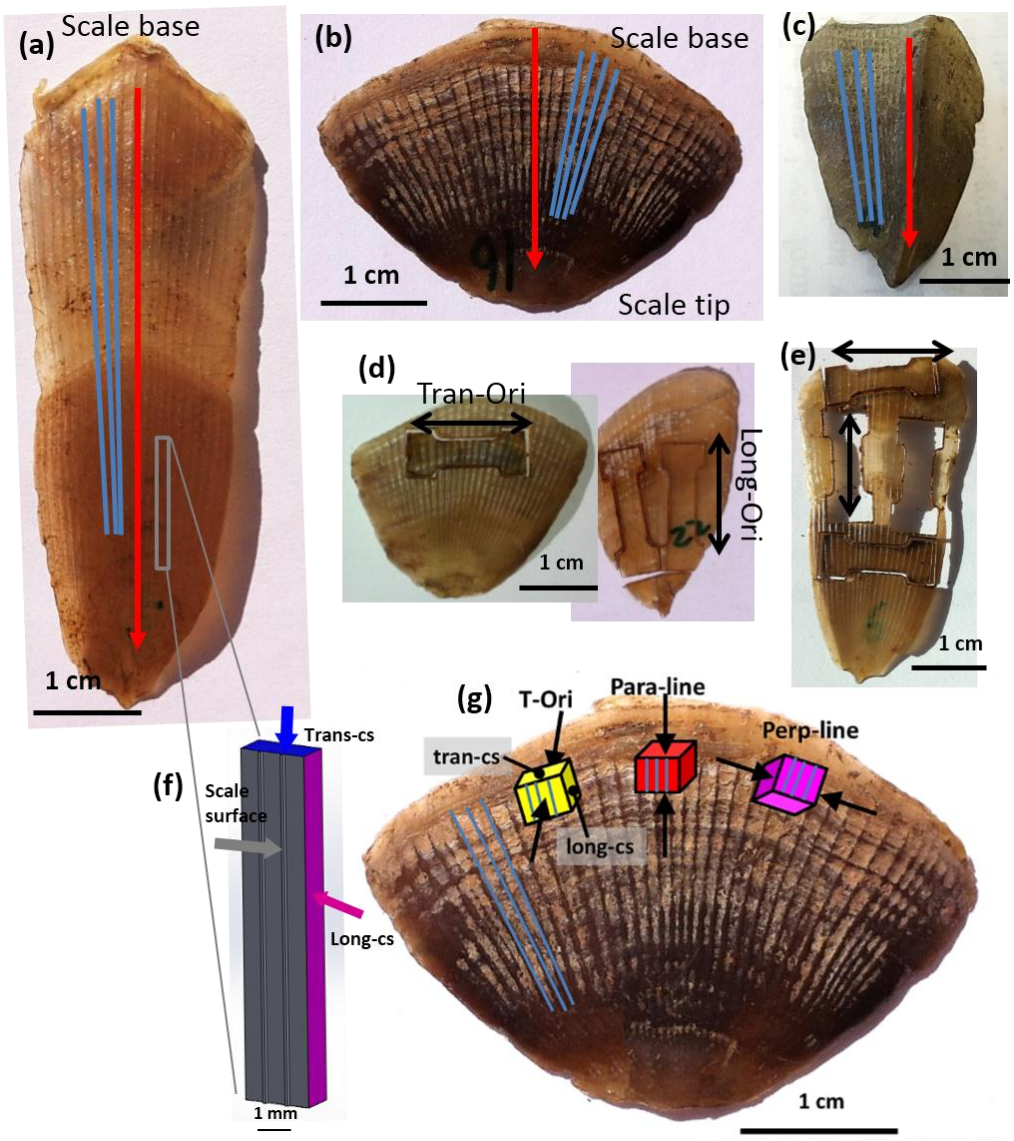

Figure 4.1 Pangolin scales and sample preparation. Typical rhombic scales from (a) African pangolin and (b) Chinese pangolin, the scale growth direction is shown (red line and arrows). Blue lines represent longitudinal ridges on external surface. The longitudinal and transverse directions are parallel and perpendicular to longitudinal ridges. (c) The second type of scales locate at the tail edges. Tensile specimens cut from (d) Chinese pangolin scales and (e) African pangolin scales in longitudinal orientation (Long-Ori) and transverse orientation (Tran-Ori). (f) Schematic showing the x-ray beams shooting the scale surface, transverse cross section (tran-cs) and longitudinal cross section (long-cs). (g) Compression in different orientations: loading through thickness orientation (T-Ori), loading along growth line direction (Para-line) and loading perpendicular to growth line direction (Perp-line).

4.2 Experimental procedures

4.2.1 Structural characterization

4.2.1.1 Optical microscopy

The Chinese and African tree pangolin scales were cut to obtain samples with external surface (ex surf), internal surface (in surf), transverse cross section (tran-cs, perpendicular to the longitudinal ridges) and longitudinal cross section (long-cs, parallel to the longitudinal ridges) for observation. The sampling of cross sections is illustrated in Fig. 4.1. All samples were mounted in epoxy (Buehler, Epoxy Resin and Epoxy Hardener), ground with graded sand papers (140#, 240#, 320#, 600#, 800, 1200#, 1500#) and polished using pastes (Aluminum oxides, 0.3μm and 0.05μm) on a LECO VP-160 machine.

4.2.1.2 Fluorescence microscopy

Scales were cut into small cubes and mounted in epoxy with tran-cs exposed and polished using the same procedure as optical microscopic observation. A fluorochrome technique involving Congo red, Titan yellow and Thioflavine T [49], [263] with certain modifications was used. Cubic mounted specimens were washed in ethanol and dehydrated prior to staining. 0.02% Congo red was made and matured for 24 hours, and specimens were immersed in a staining mixture of two parts of Congo red and one part of 0.1% Titan yellow for 1-2 hours. The specimens were rinsed in distilled water and immersed in 0.1% Thioflavin T for 3 min. After that, they were rapidly rinsed, dehydrated through a series of graded ethanol solutions (50%, 70%, 80%, 95%, 100%, 100%, 15 min for each), and

examined under ultraviolet light using an Axio Fluorescence Microscope. The keratinized cells of pangolin scales fluoresce mainly blue and the cell profiles could be readily observed.

4.2.1.3 Scanning electron microscopy

Scales were cut into small blocks with external and internal surfaces to examine. The tran-cs and long-cs samples were prepared via freeze fracture: scales were manually fractured after being submerged in liquid nitrogen. Then samples were fixed in 2.5% glutaradehyde for 2.5h, dehydrated completely in a progressive manner in graded ethanol solutions (30%, 50%, 75%, 80%, 95%, 100% twice, each for 30 minutes) and then placed in a critical point drying machine. All samples were coated with iridium prior to observation. Samples after tensile tests, microindentation and compression were directly coated with iridium for observation. For comparison, hair and feather rachis strips were deformed axially to fracture in tension, under conditions similar to the pangolin. The fractured segments were coated with iridium for observation. The hair was obtained from one of the authors, B. Wang, and the feathers were obtained from collected birds that died of natural causes (Federal Fish and Wildlife permit issued by US Fish and Wildlife Service). Phillips XL30 environmental scanning electron microscope equipped with energy dispersive X-ray detector and FEI XL30 Ultra High Resolution scanning electron microscope were used.

4.2.1.4 Transmission electron microscopy

A TGA-O_sO_4 (thioglycolic acid - osmium tetroxide) staining method [100] combined with post-staining of lead was used. Small blocks of pangolin scales (approximately 2 mm x 2 mm x 1 mm) were cut and pre-treated by immersing in 0.5 M Thioglycolic acid (pH 5.5) for 24 hours at room temperature to enhance the contrast. Then the specimens were washed with double-distilled water for 1 hour and immersed in 1-2% aqueous osmium tetroxide (O_sO_4) for 3 days at room temperature. Afterwards, the stained specimens were washed with distilled water, dehydrated to 100% ethanol through a series of graded alcohol solutions and then transited to 100% acetone through a graded mixture of ethanol and acetone. Then specimens were infiltrated using Spurr's low viscosity epoxy resin through a series of solutions with increasing amount of resin and decreasing amount of acetone (25% resin+75% acetone, 50% resin+50% acetone, 75% resin+25% acetone, 90% resin+10% acetone, 100% resin, 100% resin), each taking one day. Specimens were then placed in fresh resin and polymerized with appropriate orientation for 2 days at 65^oC. The embedded samples were trimmed and sectioned on a Leica Ultracut UCT ultramicrotome using a diamond knife. Silver sections were picked up and post-stained with lead for 60 seconds. An FEI Technai 12 (Spirit) (120 kV) electron microscope was used for examination.

4.2.1.5 X-ray diffraction (Wide-angle x-ray scattering)

Thin small pangolin strips (the longitudinal direction parallel to the growth line

direction, about 3 mm long, 2 mm wide and 0.35 mm thick) were exposed with x-rays generated by a Bruker X8 APEX II instrument mounted on a Bruker FR-591 Rotating Anode Generator with Cu Radiation and Helios MX optics (Fig. 4.1f). We used a monochromatic incident beam (Gu K-alpha, 0.15418 nm wavelength, beam size 100 μm) shooting perpendicular to the strips (at different angles) and the detector is behind the specimen about 60 mm away. Each specimen was exposed for 60 sec for five times, and the final pattern was a superposition of the five times intensity to show the characteristic spacings.

4.2.2 Mechanical testing

4.2.2.1 Microindentation

The scales were cut into small blocks and mounted in epoxy with external surface, internal surface, transverse and longitudinal cross sections (tran-cs and long-cs) exposed. All samples were ground with graded sand papers and polished using the same sample procedure as optical microscopic observation. The well-polished samples were tested using LECO M-400-H1 (LECO, Michigan) with an applied load of 100g holding for 15 seconds. Indentation measurements were performed on the external surface and internal surface along the growth line direction from scale base to tip, and on tran-cs and long-cs through scale thickness direction. Each data point reported is an average of three measurements.

4.2.2.2 Tensile testing

Dog-bone shape specimens were obtained using a laser cutting machine in

longitudinal (Long-Ori, along the growth line) and transverse orientations (Tran-Ori, perpendicular to the growth line), shown in Fig. 4.1d,e. The dog-bone shape specimens had dimensions of 21 mm in length, 1.8 mm in gauge width, and the gauge length of 8 mm. The thickness varied from 0.69 to 1.29 mm for Chinese pangolin scales, and from 0.41 to 0.52 mm for African tree pangolin scales. All of the samples were cut carefully to make sure that the gauge length region was sufficiently smooth, without curvatures or extrusions from the inner surface. The side edges of the samples were polished using a dremel tool to remove the laser-heat damage while the external and internal surfaces remained untouched. An Instron 3367 equipped with 30 kN load cell was used. The tests were carried out at strain rates ranging from 10^{-5}/s to 10^{-1}/s at room temperature and relative humidity of ~50 %. The average of consistent measurements of four specimens under each strain rate was reported. The fracture surfaces were coated with iridium for scanning electron microscopy.

4.2.2.3 Compression testing

The scales were cut and polished to achieve the compression specimens with a final dimensions of ~1.8×1.45×1.25 mm with some variation due to the natural thickness of the scales. Compressive behavior of the scales with loading in three orientations was investigated, as shown in Fig. 4.1g: through-thickness orientation (T-Ori) with compressive loading applied on both external and internal surfaces, parallel to the growth line direction (Para-line) with the loading applied on tran-cs, and perpendicular to growth line direction

(Perp-line) with loading applied on long-cs. All specimens were sampled from the embedded area of the scale, which is thicker than other parts of the scale. The tests were carried out on Instron 3367 under strain rate of 10^{-3}/s at room temperature and humidity. Average of three measurements of three specimens in each orientation was used.

4.3 Results and discussion

4.3.1 Scale overlapping mechanism

The architectural arrangement of overlapping scales shows interesting features, and the Chinese and African tree pangolin scales exhibit similar mechanism: each scale is in the center of neighboring scales arranged in a hexagonal pattern, and the internal surface partially covers three lower neighboring scales while the external surface is partially covered by three upper neighboring scales. On the internal surface, the upper rhombic region of the scale (black outline) connects to the skin, while the lateral two triangular parts (blue outlines) cover the neighboring bilateral scales, and the scale tip (green outline) covers the base of a lower scale; on the external surface, the embedded area (above the yellow dotted line) is covered under three upper neighboring scales, and the lower part is exposed (Fig. 4.2a,d). Fig. 4.2b,e shows the assembly of both pangolin scales: on the internal surface of scale (i), the side portions partially cover the laterally neighboring two scales (ii) and (iii), and the scale tip partially covers the base of the lower scale (iv); on the external surface of scale (iv), the embedded area above the yellow dotted line is covered

by three upper neighboring scales (ii), (i), and (iii). Fig. 4.2c,f shows the schematic of the overlapping pattern (dotted black, blue and green outlines represent internal surface, yellow dotted line represents external surface overlaid on the scales). This allows the scales to fully cover and protect the pangolin skin when the body moves or even curls into a ball.

The arrangement of African tree pangolin scales differs from that of Chinese pangolin scales in: (1) the shape and ratio of overlapping on the internal surface of scale; the triangles on internal surfaces in Fig. 4.2a and d are different, and the overlapping ratio on the internal surface (overlapped length over total length) for Chinese pangolin scale is about 30%, while for the African tree pangolin scale is about 70%; (2) the overlapping ratio on the external surface (embedded length over total length), for Chinese pangolin scale is about 19%, while that for African tree pangolin scales about 43%.

Since the African tree pangolins have scales more extensively overlapped (higher overlapping ratios on both internal and external surfaces), a point on the body is covered by three scale layers, similar to the fish scales of striped bass [264]. The difference is attributed to their different habitats and behavior. The Chinese pangolins walk on all fours very slowly, and dig burrows into the ground [265], whereas the African tree pangolins mainly live in trees, which involves more sophisticated body movements and higher degree of deformation. Their predators are also different. Therefore, the African tree pangolin covered by extensively overlapped scales minimizes the higher chances of skin exposure than the Chinese pangolin. Besides, the African tree pangolin scales have much higher

aspect ratio (length over thickness, 66~85) than the Chinese pangolin scales (10~30), which results in sharper edges, as shown in Fig. 2.31a, and a deterrent to even lions. This also helps to reduce the number of scales needed to cover body due to the larger area of each scale, thus saving weight.

Overlapping scales can slide and shift with respect to each other, forming a flexible protective surface [266]. This has led to the historically repeated use of scale armor by warriors. Understanding the overlapping mechanism provides useful insight to the design of modern armor. Incidentally, Lorica Squamata is a flexible Roman armor inspired by scaled reptiles [267]. Overlapping scales are commonly seen in fish, and their scalation patterns have been well documented [268]–[271]. The architectural arrangement includes morphometrics of individual scales (aspect ratio and shape), inter-scale connections and joints, the degree of imbrication, and scale orientation angle [272], [273].

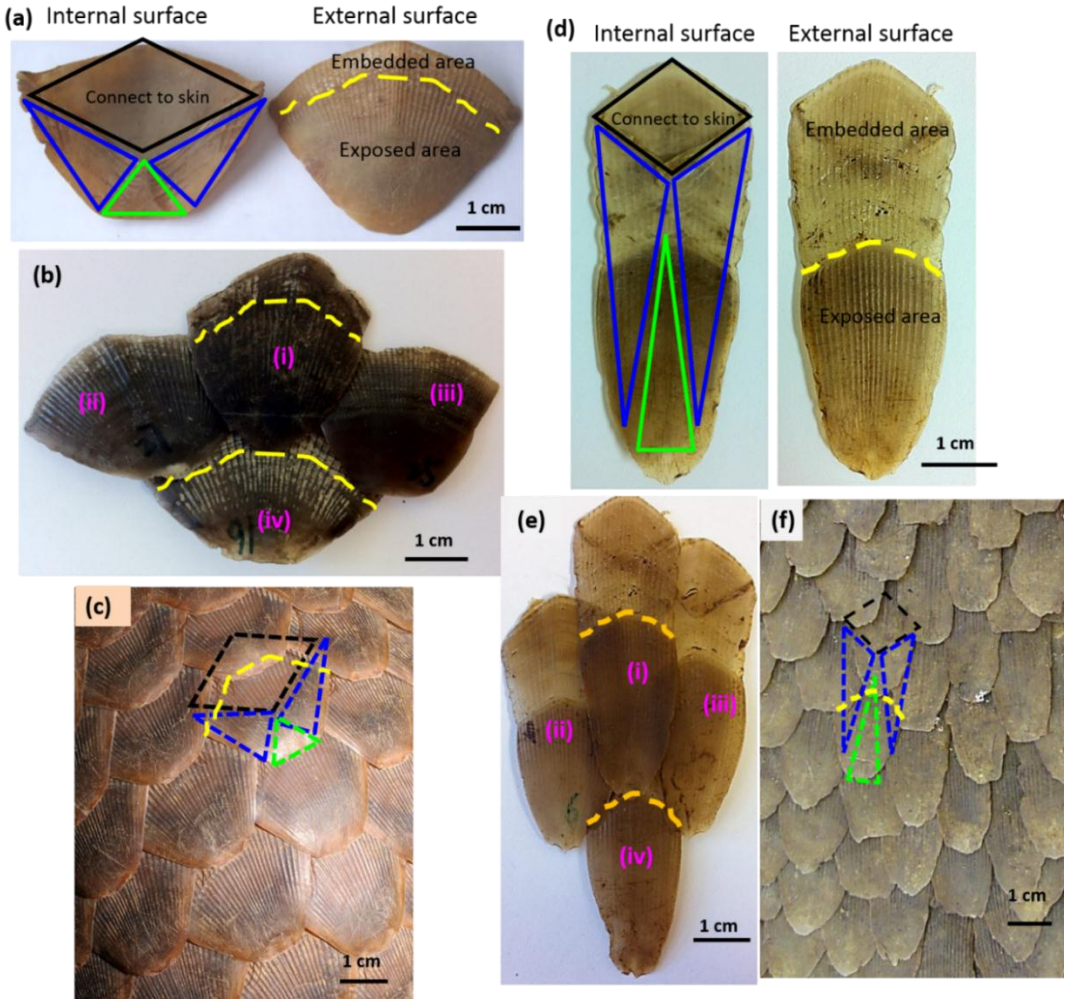

Figure 4.2 Overlapping mechanism of Chinese (a-c) and African tree (d-f) pangolin scales. (a) On the internal surface, the upper area connects to the skin, the lateral parts (blue triangles) and the scale tip (green triangle) overlap with three lower scales; on the external surface, the scale base above the yellow dotted line is embedded under upper three scales, while the region below the dotted line is exposed. (b) Assembling of the scales resembling the actual organization: internal surface of scale (i) covers its lateral neighboring scales (ii) and (iii) and a lower scale (iv), and the external surface of scale (iv) is covered by its upper neighboring scales (ii), (iii) and (i). (c) Scales on a Chinese pangolin, with schematic drawings of overlapping mechanism from (a). (d) The African tree pangolin scales with similar features as in (a), except different geometries. (e) Assembling of the African tree pangolin scales, similar as that in (b). (f) Scales on an African tree pangolin, overlaid with the overlapping mechanism from (d).

On the one hand, pangolin scales in this work show some similarities to the

overlapping structure of fish scales but exhibit different scale sizes and thicknesses. The values of aspect ratio for pangolin scales, 10~85, are in the range of fish scales, 25~100 [273], and the thickness progressively decreases towards the scale tip with thickest region around connecting to epidermis, a similar trend to fish scales [271]. Secondly, the degree of imbrication calculated as exposed length over total length of the scale measures the spatial overlap of fish scales, and varies from 0.24 to 1 for sixteen species of fish [268]. Using this definition, the degrees of imbrication of pangolin scales are about 0.81 (Chinese pangolin) and 0.57 (African tree pangolin), which also are within the range of fish scales. In addition, the scalation pattern of striped bass is reported as each scale overlapping with six other neighboring scales [271], with an imbrication degree of about 0.5, similar to the arrangement of African tree pangolin scales.

On the other hand, the overlapping of pangolin scales differs from fish scales. The pangolin scales are separated individual scales, with each one partially connected to skin; whereas, the fish scales, for instance, the striped bass, have a soft gel-like connective tissue, stratum spongiosum, between the scales [270], [271], which may be an adaptation to ease scale motion in the aquatic environment.

4.3.2 The structure of pangolin scale

4.3.2.1 Morphology and cuticle structure

Both Chinese and African tree pangolin scales show, as expected, similar

morphology and cuticle structure, except that the Chinese pangolin scale is shorter and wider than the African tree pangolin scale. Figs. 4.3a,b and e,f show that the external surfaces of both scales are convex and have longitudinal ridges with about 200 μm diameter (blue solid lines) extending from scale base to tip. Close observation of the external surfaces reveals elliptical shaped keratin scales (Fig. 4.3c,d,g,h) around 40~70 μm in diameter, ~1 μm in thickness, and overlapped in 3~5 layers. Higher magnification of the keratin scale shows the keratin mesh morphology (Fig. 4.3d).

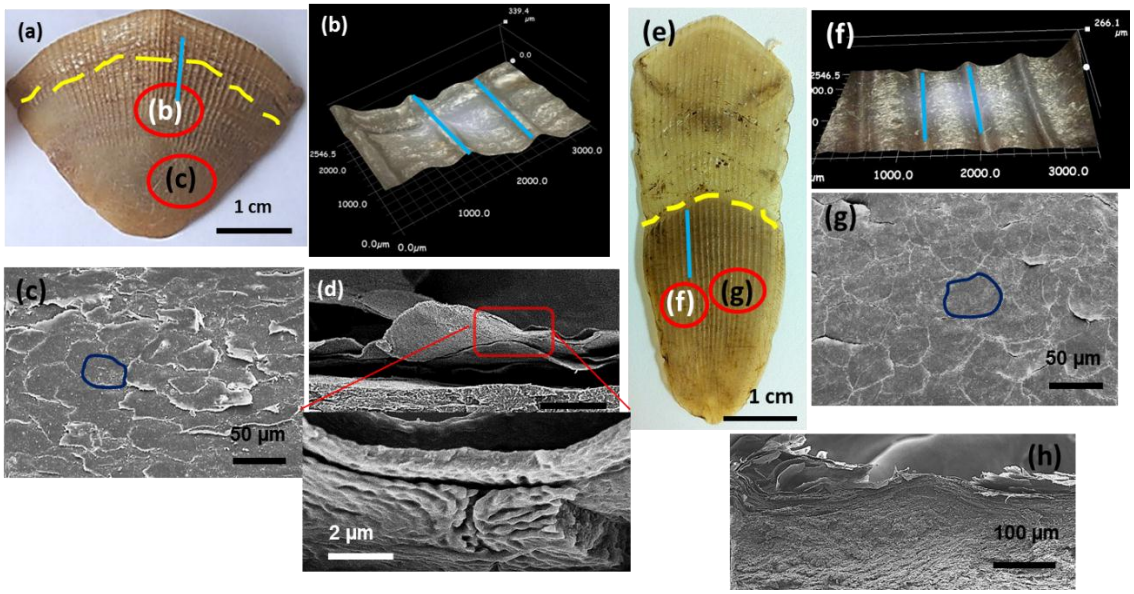

Figure 4.3 Scale surface structure: (a) Chinese pangolin scale. (b) 3D optical micrograph of the scale external surface showing the longitudinal ridges parallel with growth direction; (c) plane view of the external surface showing the keratinized cuticle cells; (d) transverse cross section of the scale at the superficial 3~5 layers of cuticle cells and an image of the keratin mesh morphology; (e) African pangolin scale. (f) 3D optical micrograph of the scale external surface showing the longitudinal ridges parallel with growth direction; (g) plane view of the external surface showing the keratinized cuticle cells; (h) transverse cross section of the scale at the superficial 3~5 layers of keratinized cells.

Similar keratin scales with comparable dimensions were reported briefly for

porcupine quills [274] and toucan beaks [213]. Pangolin scales are keratinized materials [49], and according to the keratinization process for most keratinized materials [90], they are flattened keratinocytes that have similar dimensions to the ones on the external surface of wool [86] and stratum corneum [155], [275]. For wool, the overlapping flattened cuticle cells, which differ from cortical cells in appearance, form the external cell layer, and the stratum corneum consisting of corneocytes are layers of these brick-shaped cells made of keratin mesh. Therefore, these keratin scales are the keratinized cells and different from those of the scale interior. The cuticle layer composed of flattened cuticle cells, forming a protective sheath around an inner layer of densely packed keratinized cells, is a typical structural feature of keratinous materials. It is also reported that the role of cuticular keratin cells in the bulk mechanical properties of keratin fibers is minimal, since the amorphous scales are weakly attached by the endocuticle and intercellular cement to the main fiber shaft [162].

4.3.2.2 Main interior structure

Both Chinese and African tree pangolin scales show three regions along the cross section, distinguished by different cell morphologies and orientations, and with different lamellar structures. From transverse cross section (tran-cs) of the scale (Fig. 4.4a), three regions were identified: the dorsal region (beneath the scale external surface) shows a fine structure with thin, wavy strip-like spacing (blue segments) which is parallel to the external

surface, with dimensions about 20~40 μm. The ventral region (close to the scale internal surface) shows a similar fine structure which is nearly straight and parallel to internal surface. The middle region, which constitutes the major part of the cross section, exhibits thicker cellular morphology tilted to the scale surface and with spacing that is larger than that of the dorsal and ventral layers. A planar view of the dorsal region of the scale in Fig. 4.4b (looking from the external surface) shows that the entire area exhibits homogeneous circular profiles of keratinized cells. Stained by Congo red, the keratinocytes (fluorescing blue) show clear cross sectional profiles (Fig. 4.4c,d,e), indicating that the spindle-shaped cells pile up to form the pangolin scale. In the dorsal region, the flattened cells are arranged in layers (around 10 cells thick) parallel to the external scale surface, with diameters about 20~50 μm and thickness 1~3 μm. The cells in the ventral region show similar morphology and arrangement as those in dorsal region, except that they are parallel to the internal surface. Keratinized cells in middle region are less flattened and usually oriented in an angle to the scale surface (tilted). They exhibit a larger size with diameter about 40~65 μm and thickness 6~10 μm. The three regions along the scale cross section agree with the reported three layers based on the histological structure and distribution of chemical constituents along cross section [49].

When fractured, pangolin scales show a lamellar structure formed by keratinized cells. Fig. 4.5a shows a transverse cross section (tran-cs) of a scale: the cell profiles flatten and form lamellae, and each lamella is one layer of cells. Scanning electron micrographs

of transversely fractured scales also confirms the lamellar structure (Fig. 4.5b,c), with about 2~5 μm thickness; by comparing the morphology and dimensions of the layered keratinized cells and lamellae, one lamella is formed by one sheet of flattened cells. Scanning electron microscopic observations of both transversely and longitudinally freeze fractured scales reveal that scales show crossed-lamellae (indicated by red arrows in Fig. 4.5d), and exhibit three regions with different morphologies. In the dorsal region, the lamellae are well defined , and are parallel to the external surface, with one lamella around 2 μm; in the middle region, the lamellae are larger and less ordered, sometimes showing poorly defined tilted crossed-lamellae with large varying sizes (2~8 μm) and sometimes regularly tilted crossed-lamellae (2~5 μm); in the inner region, the lamellar structure is similar to that of the dorsal region: the lamellae are parallel to the scale surface, with each lamella about 1.5~3 μm thick.

The lamellar structure is widely observed in keratinous tissues, e.g. hoof wall, horn sheath, and fingernail. The bighorn sheep horn shows longitudinally aligned lamellae (2~5 μm thick), which stack along the radial direction [276]. For hoof wall, it is reported that the tubular cortex cells are organized into concentrically arranged lamellae, where each lamella is composed of one layer of cells [181], which agrees well with our observation for pangolin scales. The lamellar thickness varies from 5 to 15 μm [181]. The fingernails have been considered to be similar to pangolin scales from histological and histochemical observations [49]; they show a poorly defined lamellar structure [206], [277], and also

exhibit three regions along the cross section: dorsal and ventral layers of crossed-fibers or fibers without preferred orientation, and an intermediate layer of transversely aligned fibers [206], [219], [278].

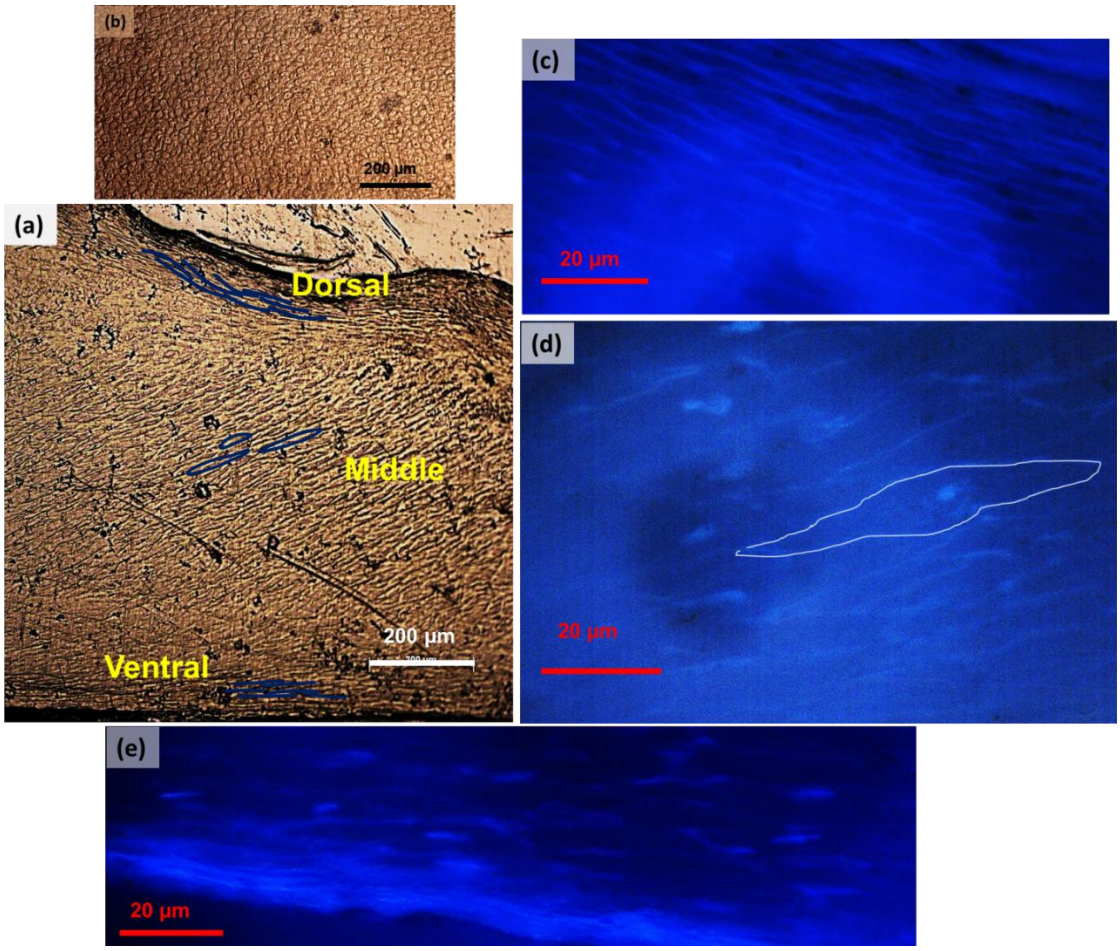

Figure 4.4 Structure of scale interior: (a) optical micrograph of transverse cross section showing the dorsal, middle and ventral regions of pangolin scale; blue lines represent profiles of keratinized cells. (b) Optical micrograph of plane view of dorsal region of the scale showing the circular cell profiles. Fluorescence micrographs of (c) dorsal region showing the flattened keratinized cells, (d) middle region of tilted and less flattened cells (light-blue curves), and (e) ventral region of flattened cells parallel to scale surface.

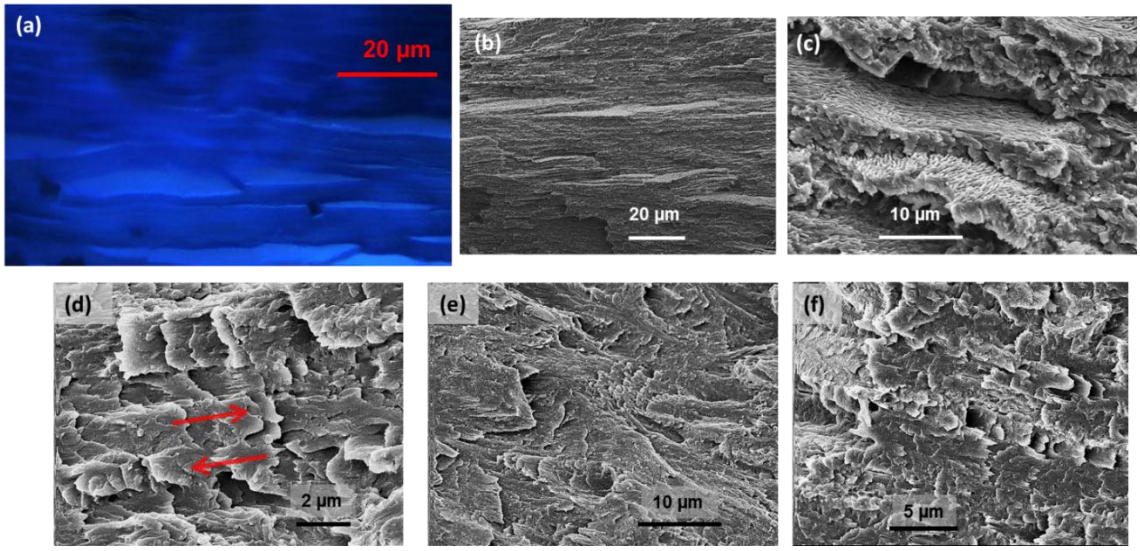

Figure 4.5 The lamellar structure formed by keratinized cells: (a) fluorescence micrograph of transverse cross section (tran-cs) of a scale, the cell profiles (upper) and the lamellae are clearly seen, indicating that keratinized cells form lamellae; (b) scanning electron micrographs of tran-cs of the scale showing (a) the lamellae and (c) that each lamella is one layer of cells. Scanning electron micrographs of the three regions showing the crossed-lamellae structure: (d) dorsal region, (e) middle region, and (f) inner region.

4.3.2.3 Crossed lamellae and crossed fibers

When freeze-fractured (cooled in liquid nitrogen and then impacted) or loaded at a relatively high strain rate (~10^{-1}/s), pangolin scales show a clear crossed-lamellar structure in dorsal, middle and ventral regions (Fig. 4.6a,b,c). These crossed lamellae occur on a spatial scale of ~5 μm. When stretched to fracture at low strain rate or in hydrated state, they show crossed fibers (Fig. 4.6d). These are significantly broader than the crossed lamellae, and occur on a scale of 50 μm. This is very different from other keratinous materials composed of uniaxial fibers whose fractures show fibers in one direction, e. g. human hair (Fig. 4.6e). A tearing mode fracture was applied to pangolin scales and other

keratinous materials with known fiber orientations (Fig. 4.7). The pangolin scales show a zigzag profile along the torn edge, indicating that the fibers are aligned in angles to the longitudinal direction; whereas the side views of torn fractured fingernails (torn transversely along the free edge) and feather rachis (torn along the longitudinal axis) both show smooth edges, implying the majority component being uniaxial fibers.

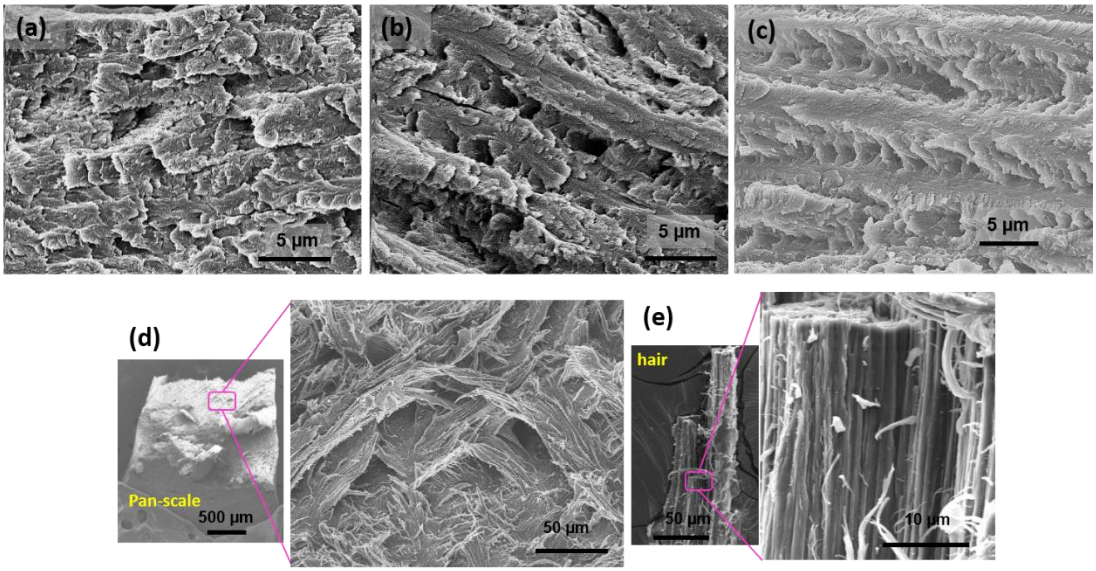

Figure 4.6 Crossed-lamellar and crossed fiber structure of pangolin scales: (a) dorsal region (freeze fractured), (b) middle region (freeze fractured), and (c) ventral region (10-1/s). Side views of tensile fractured specimens in three keratinized biological materials: (d) pangolin scale in hydrated state, showing crossed-fibers, (e) human hair composed of uniaxial fibers.

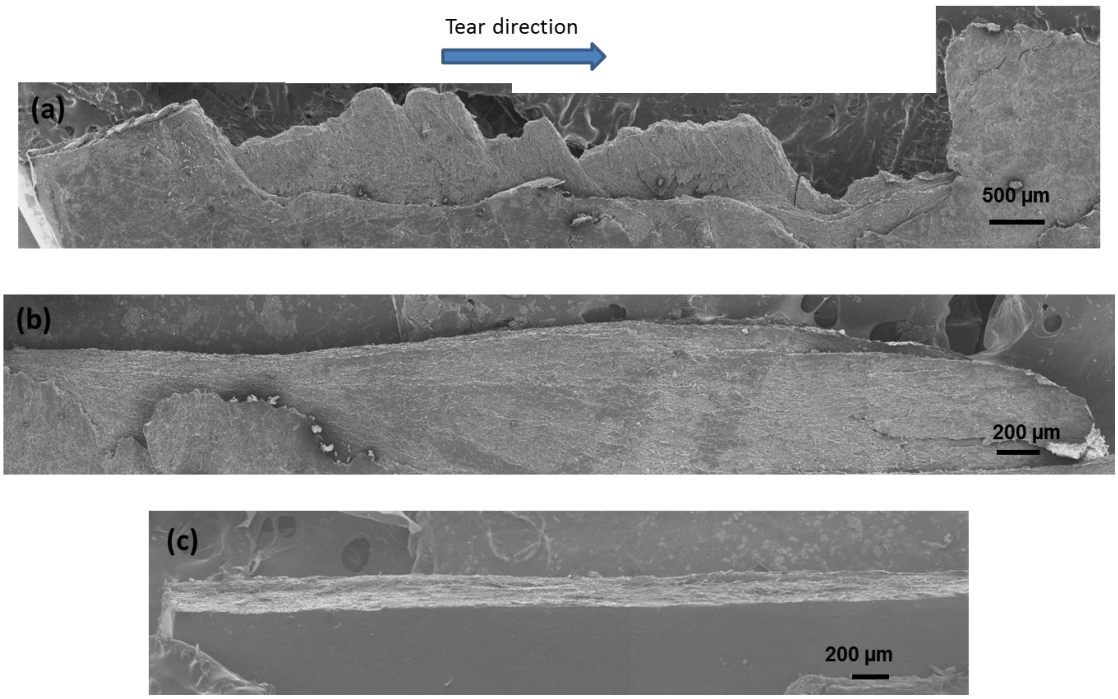

Figure 4.7 Side views of tear fractured (a) pangolin scale exhibiting zigzag profile, indicating that fibers are oriented in angles to scale longitudinal direction, whereas (b) fingernail and (c) feather rachis show smooth torn edge, indicating uniaxially aligned fibers.

From the above examination, it can be concluded that pangolin scales consist of crossed fibers aligned at angles to the scale growth direction. Though not usually seen in keratinous materials [206], it is an evolutionary design to achieve the protective function for pangolins. Wool and hair consist of axially oriented fibers, which is an optimized structure to resist the tensile forces from external stimuli. Nails show a dominant component of transverse fibers that direct cracks transversely rather than propagating into the delicate dermal tissue. Hoof wall and horn sheath are composed of concentrically and radially arranged lamellae with varying orientations of fibers, which provide exceptional crack diversion mechanisms to protect the inner tissue [181]. The lateral walls of feather rachis show crossed-lamellae and crossed fibers structure [206], [208], which contributes

to the torsional rigidity. For pangolin scales, external forces may come from biting, puncture and impact by predators and other environmental stimuli, and friction and scratch, all of which occur in unpredicted directions. A crossed-lamellar composite with fibers crossed with each other in a range of angles providing in-plane isotropy would be an optimized structure to sustain forces in diverse directions and, concomitantly, to increase the energy needed for crack propagation and redirecting cracks to the scale edges or tip.

4.3.2.4 Interlocking interface between cells and lamellae

One interesting structural feature of pangolin scales is the suture-like profile of the cell membrane complex, which creates an interlocking interface between keratinized cells and lamellae. Transmission electron micrographs of pangolin scales (plane view and transverse cross sectional specimens) show a suture-shaped structure about 25-50 nm thick: one densely stained layer enclosed by two less-dense layers (Fig. 4.8a), and the fine filaments with diameter about 3~5 mm (inside cells) were also observed (Fig. 8b). Considering that keratinized cells compose the pangolin scales and comparing them with the structure of wool and hair [142], this is the cell membrane complex in pangolin scales. However, unlike the cell membrane complex in wool and hair, the one in pangolin scales shows a suture-like profile, which is also captured via scanning electron micrographs (Fig. 4.8c,d): the suture wavelength is 250~450 nm, as observed by both transmission and scanning electron microscopy. The percentage of the interface (suture-like cell membrane

complex) is calculated to be about 7.84%. The interface thickness varied from 25 to 35 nm (clearly seen in Fig. 4.8b). The effect of such suture-like cell membrane complex is an interlocking interface between cells and thus the lamellae, as shown in Fig. 4.8d.

Suture structures at macro- and micro-scales have been found in a variety of biological materials [266], e.g. turtle shell [279], seashells [280] and deer skull [281], but the cell membrane complex at the nanoscale suture structure is first reported here. The suture structure mechanically contributes to the bonding strength at the interfaces while still controlling flexibility [266]. Mechanical studies on rigid suture joints of seashells with hierarchical structures reveal enhanced load bearing capability and flaw tolerance, and prevention of catastrophic failure [280]. The suture-like cell membrane complex in pangolin scales provides increased contact area and an interlocking interface, which leads to increased bonding strength and delamination resistance between lamellae.

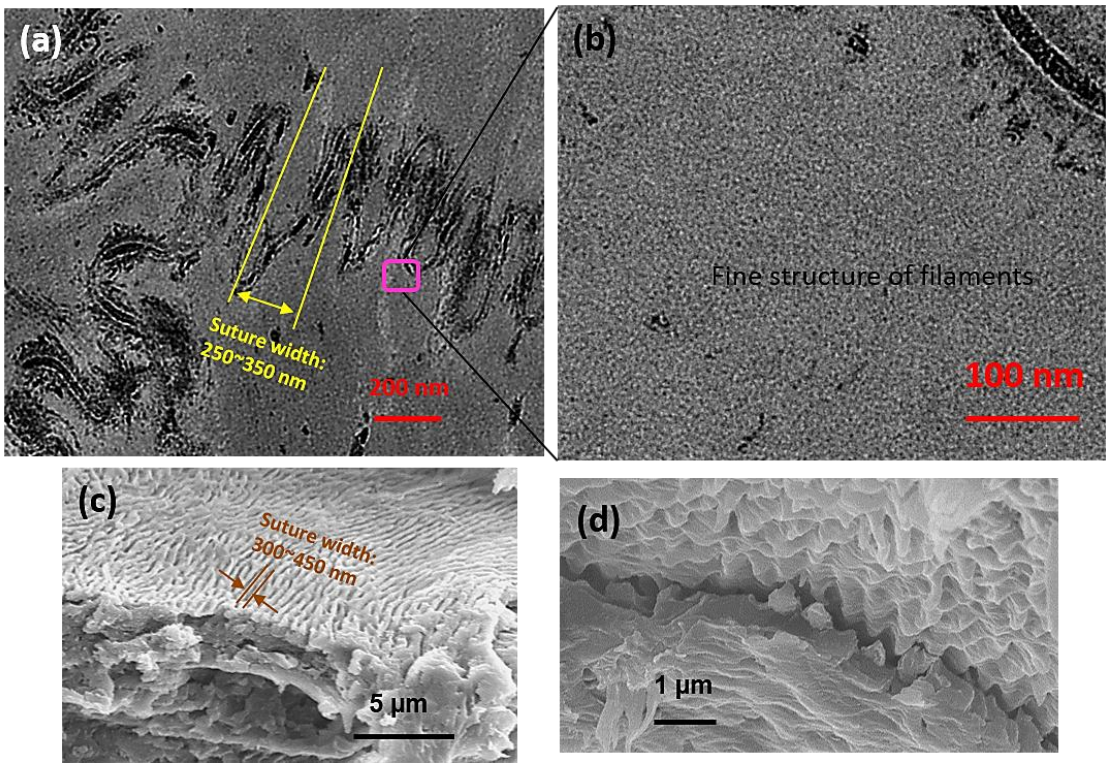

Figure 4.8 The suture-like cell membrane complex and the fine filaments of pangolin scales: (a) transmission electron micrograph of transverse cross section (tran-cs) of a scale. The cell membrane complex (about 25-50 nm thick) consists of one densely-stained central layer and two less dense layers, typical of keratinous materials, but interestingly shows suture-like profile (suture width ~350 nm); (b) transmission electron micrograph of the area in (a) showing the fine filaments about 3~5 nm in diameter inside cells. Scanning electron micrographs: (c) tran-cs of the scale, the lamellae also show fine suture-like protrusions, since they are formed from flattened keratinized cells; (c) and (d) the suture-like cell membrane complex provides interlocking interface between lamellae.

4.3.2.5 X-ray diffraction

α- and β-keratins have different crystalline structures, helix and pleated sheet. The characteristic spacings of the amino acid repetition groups in the keratin diffract x-rays and generate different patterns, which follows the Bragg's law [282]:

$$n\lambda = 2d \sin\theta \qquad (6)$$

where λ is the wavelength of incident x-ray, d the characteristic spacing of the lattice, and θ the angle between diffracted beam and the crystal plane. In a first-order reflection ($n=1$), with known λ, $\sin\theta$ can be calculated through the sample-recording film distance and the radii of the diffracted pattern, thus *d* values can be determined and marked on the diffracted pattern. The critical reflection differentiating α- and β-keratins is represented by the meridian reflection, 0.52 nm and 0.33 nm, respectively [283].

The pangolin scale strips, especially shooting the scale surface, generate two diffused rings for strips placed in all orientations (Fig. 4.9), meaning that the interplanar spacings are not exactly identical but different, and the disorder is relatively large. This agrees with SEM observation that the cuticle layer consists of loosely bonded cells with meshed-morphology, and is similar in nature to the cuticle cells of hair fibers [284].

In addition, the 0.51 nm meridional and the 0.97 nm equatorial reflections observed in the pattern of shooting scale surface (Fig. 4.9a,b,c). These two are also observed in patterns of shooting the long-cs which are tilted 9 and 13 degrees (according to Eqn. 4.1 to show the .051 nm diffraction) in Fig. 4.7h,i. This supports the presence of α-helices.

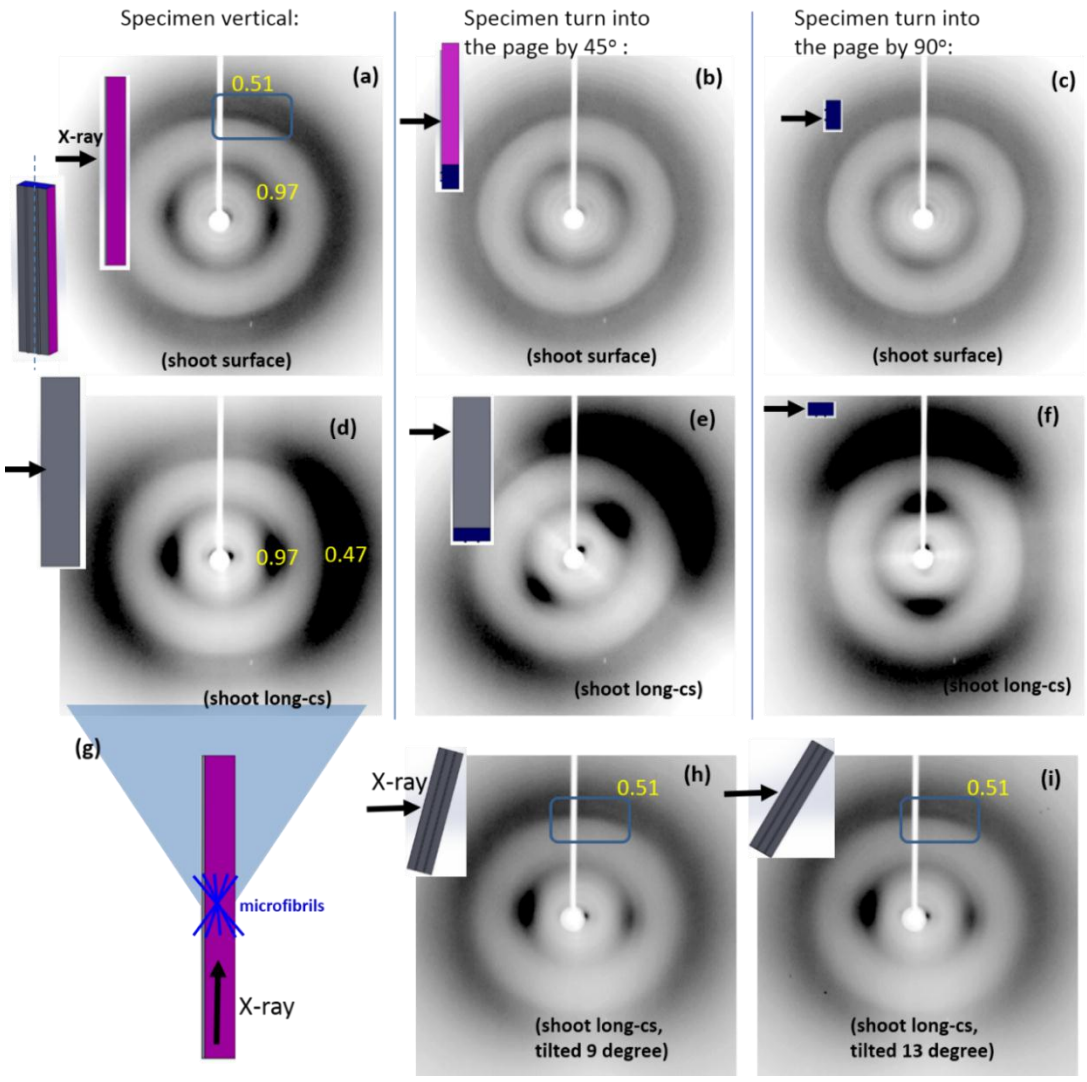

Figure 4.9 X-ray diffraction patterns of pangolin scale specimens. Top left is a schematic of the strip. (a,b,c) Diffraction patterns of x-ray shooting the scale surface with specimens vertical, turning into the page by 45 degree and turning into the page by 90 degree. (d,e,f) Diffraction patterns of x-ray shooting the long-cs with specimens vertical, turning into the page by 45 degree and turning into the page by 90 degree. (g) Illustration of the microfibrils aligned in a preferred range of directions and diffracting the x-rays to form a pattern in (d). (h,i) Diffraction patterns of x-ray shooting the long-cs with specimens tilted 9 and 13 degrees to show the characteristic 0.51 meridional reflection of α-keratin.

Besides, shooting the longitudinal section gives distinct patterns with two sets equatorial arcs, which change positions in accordance with the specimen direction (Fig. 4.9d,e,f). The equatorial 0.97 nm diffraction is present in both α- and β-keratins, while the

~0.47 nm diffraction may represent the distance between chains in a β-sheet, existence of β-keratin. This set of arcs are coalesced by a large number of spots diffracted by the specific sets of planes/periodic&ordered structure in all crystallites/microfibrils arranged in a preferred range of directions, schematically shown in Fig. 4.9g. This indicates that the axis of microfibrils is along the scale longitudinal direction, the microfibrils at are crossed in a range of angles, and such disorientation is suspect to occur within layers. This also is in agreement with the crossed-fiber structure.

Therefore, x-ray diffraction patterns of pangolin scales in various orientation indicate the constituting α-helices and possibly the β-sheet. Our Fourier transferred infrared spectrum of pangolin scales at Amide I band region also shows the presence of both α and β structures. The microfibrils are aligned in a preferred range of directions with the axis parallel to the growth line direction of the scale.

4.3.3 Mechanical behavior

4.3.3.1 Orientation effect on the mechanical behavior

Microindentation

Microindentation measurements in four orientations along scale growth line and scale thickness directions on both scales are shown in Fig. 4.10. The Chinese pangolin scales show a similar microhardness, fluctuating around 220 MPa, when indented on the external (ex surf) and internal (in surf) surfaces along scale growth line direction; this

suggests the same structure from scale base to tip. The African tree pangolin scales show slightly lower microhardness values, about 200 MPa, and a similar trend indenting on external and internal surfaces along the growth line direction. Indentation on the transverse (tran-cs) and longitudinal (long-cs) sections of Chinese pangolin scales generates the same microhardness value (Fig. 4.10b), implying an isotropic behavior of the scale, which agrees again with the structure of crossed-fibers between lamellae. The African tree pangolin scales show similar hardness on cross sections, albeit at a consistently slight lower value (~180 MPa).

The higher harness on the surfaces in comparison with on the sections may be understood from the relative orientations of the layered keratinized cells and loading direction: indenting on surfaces along scale growth line is applying a force in the denser orientation (scale thickness direction, highest compressive strength), while indenting along scale thickness is applying load in the cell plane direction (lower compressive strength). However, one should note that this difference is not significant. After indentation, the scales show clear smooth indents, and the lamellae are deformed without observed cracking (Fig. 9c), which corroborates the high ductility in compressive testing.

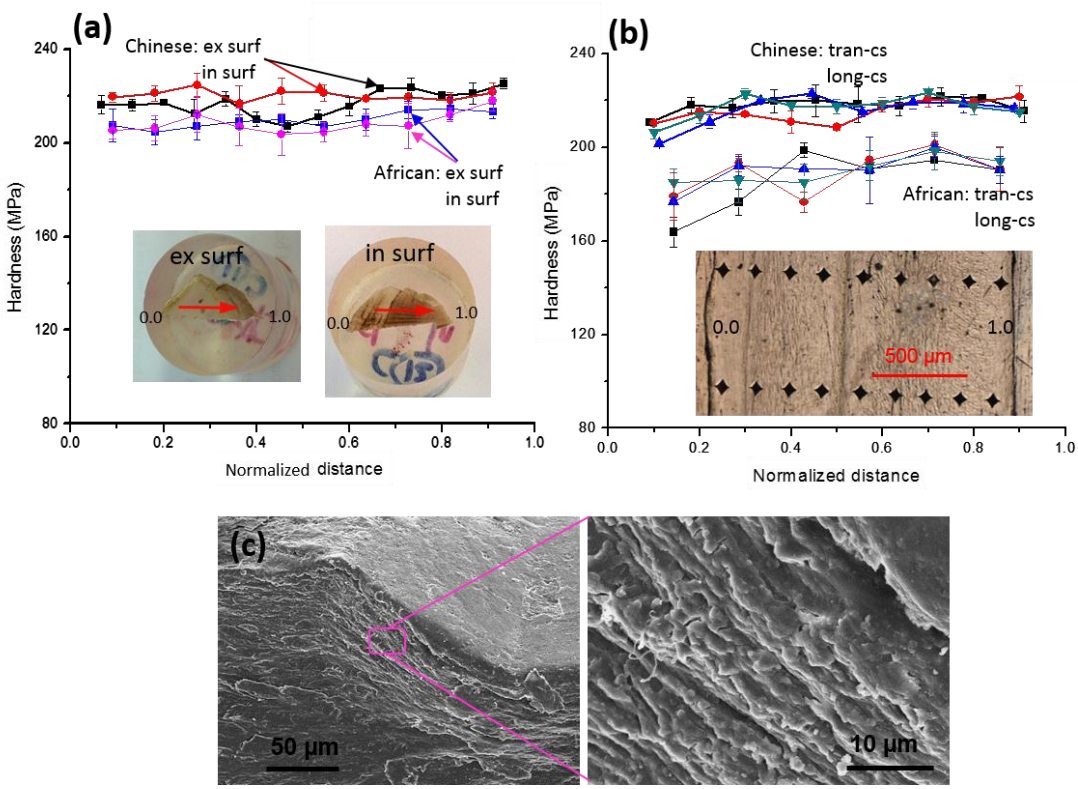

Figure 4.10 Mircohardness results of the scales: (a) hardness values of African tree and Chinese pangolins scale along on external surface (ex surf) and internal surface (in surf) along growth line direction (red arrows, from scale base to tip); (b) hardness values of African tree and Chinese pangolin scales indenting on transverse (tran-cs) and longitudinal (long-cs) along thickness direction. (c) Scanning electron micrographs of the indent (flat region in c) showing the compressed lamellae.

Tensile response

The tensile behavior of African tree and Chinese pangolin scales loaded in the longitudinal and transverse orientations (Long-Ori and Trans-Ori) is shown in Fig. 4.11a,b; the results are summarized in Table 4.1. Both exhibit similar stress-strain curves that show two stages: an elastic region that is fairly linear, and then a region with a gradually decreasing slope, the latter representing permanent deformation; the third stage is a negative slope, indicative of damage to the structure. This is somewhat different from the

three regions (elastic, yield, post yield) shown in stress-strain curves of most typical α-keratinous materials [206], such as wool [38] and hoof wall [285], but similar to β-keratinous materials, e.g. keratin rhamphotheca of bird beak [213], feather rachis cortex [286]. Such features suggest that the pangolin scales are not solely composed of α-keratin (verified by x-ray scattering patterns, unpublished results), but a combination of α- and β-keratins, since α-keratin usually generates stress-strain curves with an initial linear region and a plateau yield region followed by a stiffened post-yield region, implying the α to β transition. In addition, the pangolin scales show crossed lamellae, and the fibers are crossed between lamellae rather than uniaxially aligned; whereas the α-keratin fibers in, e.g. wool and hagfish slime threads [206], are perfectly aligned along the axis, and therefore, the α to β transition upon axial stretching is clearly visible by a plateau.

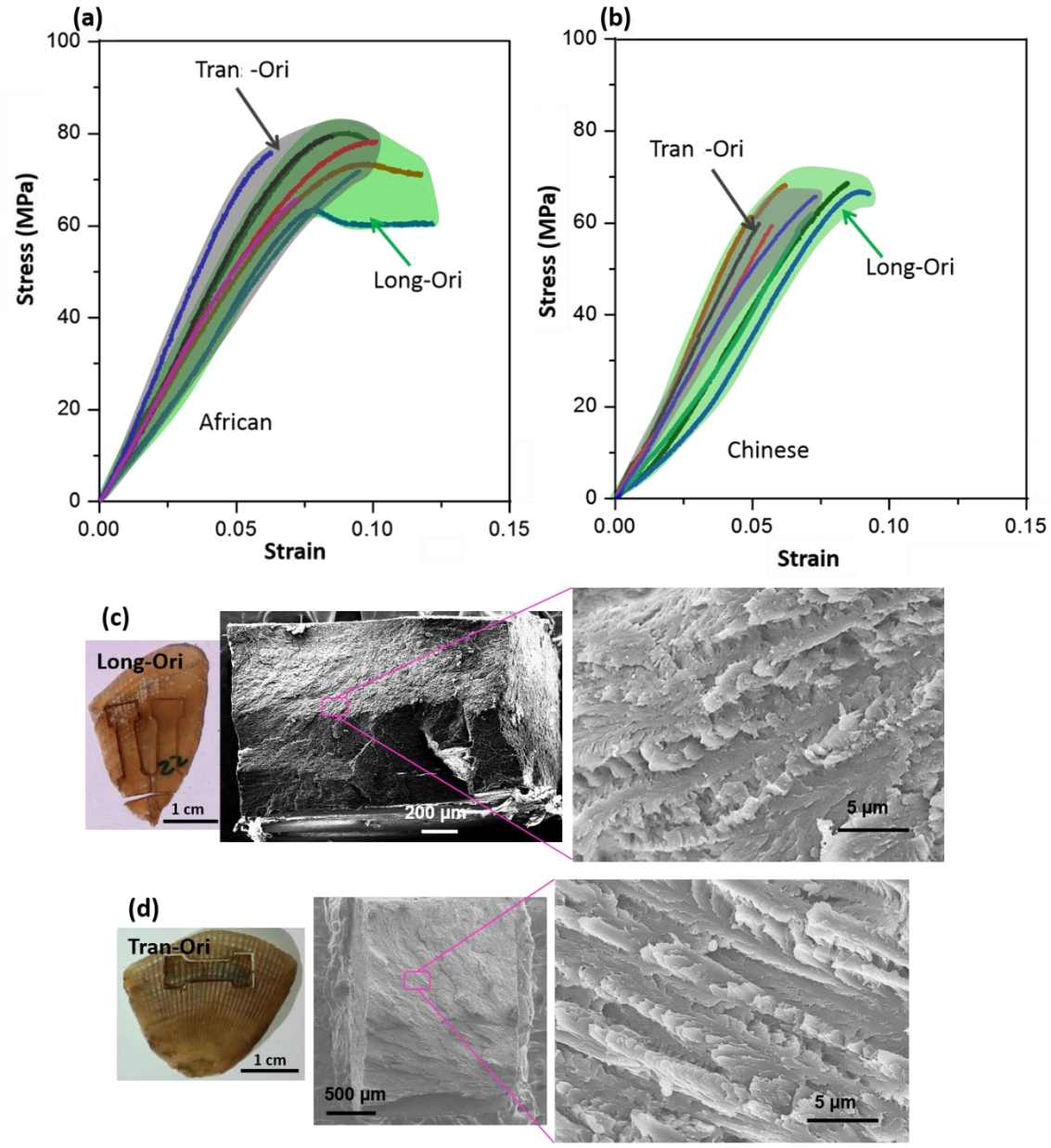

Figure 4.11 Tensile response of the (a) African pangolin and (b) Chinese pangolin scales loaded in longitudinal (Long-Or) and transverse (Tran-Ori). Fracture surfaces of Chinese pangolin scales from (c) Long-Ori and (d) Tran-Ori.

Table 4.1 Tensile results of African tree and Chinese pangolin scales in longitudinal and transverse orientations (± standard deviation).

		Strain rate (/s)	Young's modulus (GPa)	Tensile strength (MPa)	Breaking strain (%)	Toughness (MPa)
African tree pangolin scale	Long-Ori	10^{-5}	1.1±0.3	65.5±6.7	16.8±5.5	8.3±3.3
		10^{-4}	1.1±0.2	71.5±6.6	10.6±2.7	4.9±1.5
		10^{-3}	1.0±0.1	72.4±6.9	12.9±0.3	6.5±0.6
		10^{-2}	1.1±0.1	84.7±9.8	12.6±0.8	7.2±0.7
		10^{-1}	1.5±0.2	108. 7±6.0	12.0±3.6	8.4±3.3
	Tran-Ori	10^{-3}	1.2±0.2	74.2±5.1	8.4±1.4	3.6±0.9
Chinese pangolin scale	Long-Ori	10^{-5}	0.9±0.1	60.4±9.0	11.4±3.8	4.8±2.9
		10^{-4}	1.0±0.1	60.5±6.5	12.0±3.1	4.7±1.8
		10^{-3}	1.0±0.2	66.4±2.7	8.0±1.4	2.7±0.5
		10^{-2}	1.0 ±0.1	70.8±10.9	8.7±0.7	3.4±0.4
		10^{-1}	1.2 ±0.1	74.2±2.3	6.8±0.1	2.5±0.1
	Tran-Ori	10^{-3}	1.1±0.1	61.6±2.8	6.1±0.9	2.0±0.5

One interesting feature is that both scales show similar tensile behavior when stretched longitudinally and transversely: the ranges of stress-strain curves in the two orientations almost overlap each other (Young's modulus around 1 GPa, and tensile strength about 70 MPa), and the fracture surfaces in the two orientations show the same crossed-lamellae structure (Fig. 4.11c,d). These corroborate the structural observation that pangolin scales are composed of keratinized cells forming crossed lamellae that are the same in longitudinal and transverse orientations, thus exhibiting transverse isotropic tensile behavior. The toucan rhamphotheca (β-keratin) also shows no systematic difference in modulus and yield strength along the two orientations [213]. In contrast, most α-keratinous materials show superior mechanical properties in certain orientations for specific functions discussed previously, e.g. wool, hair, and hagfish slime fibers in the axial direction, and

nails along the lateral edge [206]. As mentioned earlier, this transverse-isotropic mechanical response is needed for the specific functionalities of the scale.

Compressive behavior

Compressive loads occur frequently during life of pangolin scales. Fig. 4.12 shows the compressive stress-strain curves of Chinese pangolin scales in three loading orientations; the results are summarized in Table 4.2. The compressive strength (stress at the onset of plateau region) shows highest value in the scale thickness direction (T-Ori), 127 MPa, followed by the loading parallel to the scale surface: Perp-line (113 MPa) and Para-line (92 MPa). This is advantageous for the scales since the most often experienced compressive force exerted predators (such as biting from lions) is perpendicular to the scale thickness plane. After a plateau region, the compressive stress rises continuously, squeezing specimens into a flattened disk without fracture, indicating good ductility and energy absorbance ability. The elastic modulus changes little among these three orientations, around 2.2 GPa, which agrees well with structural observation.

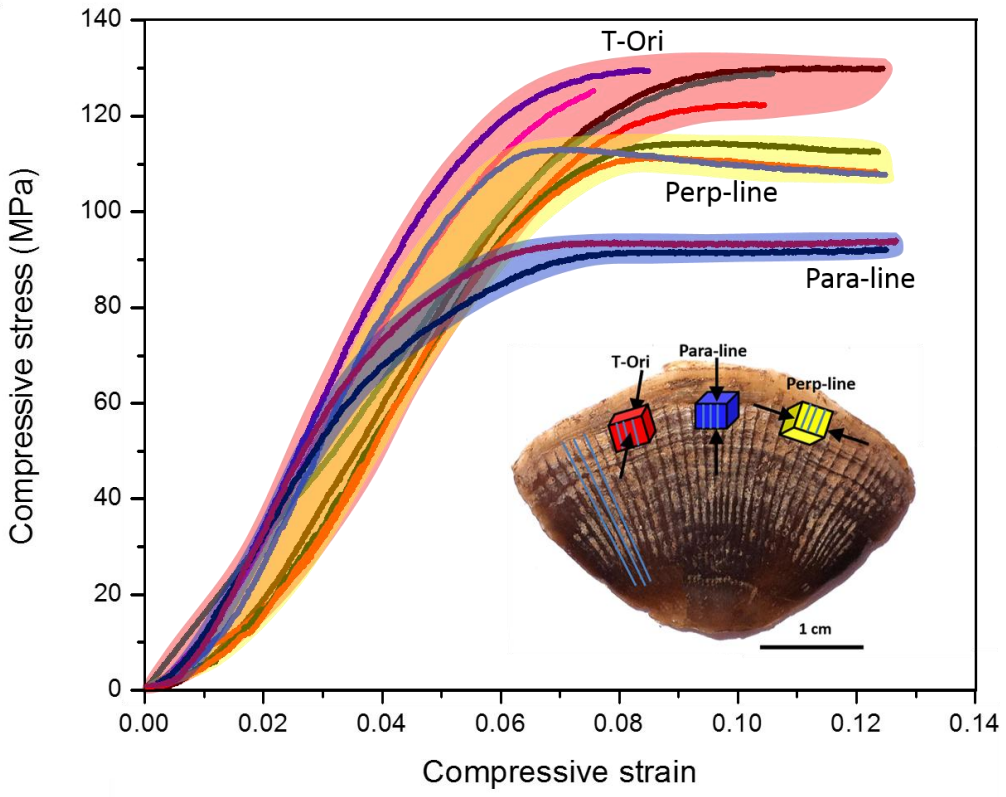

Figure 4.12 Compressive stress-strain curves of Chinese pangolin scales loaded in three orientations.

Table 4.2 Compression results of Chinese pangolin scales in three orientations (± standard deviation).

	Elastic modulus (GPa)	Compressive strength (MPa)
Thickness orientation (T-Ori)	2.2 ±0.3	127.3 ±2.9
Para-line	2.2 ±0.2	92.0 ±0.9
Per-line	2.3 ±0.3	112.8 ±1.1

The different compressive strengths but similar moduli among three orientations originate from the arrangement and dimensions of keratinized cells and the lamellar structure. The fibers are crossed between lamellae, thus loading in three orientations generate similar elastic moduli. In addition, the keratinized cells, which form lamellae, are

flattened and pile in layers through the scale thickness direction, resulting in a denser orientation than the cell plane direction (including Perp-line and Para-line orientations); therefore, loading in T-Ori leads to higher compressive strength than the other two loading directions. In the other orientations, axial splitting may occur along lamellar boundaries. The horn keratin from bighorn sheep (α-keratin) is reported to exhibit similar elastic modulus and yield strength when compressed longitudinally and transversely, but poorer properties in the radial direction, which was also attributed to the loading directions parallel or perpendicular to the lamellar orientations [276].

In brief summary, pangolin scales show transverse-isotropic properties, demonstrated from tensile, compressive and microindentation responses tested in different orientations, and slightly superior strength in the scale thickness direction than that in longitudinal and transverse orientations. This correlates with the structural design of the scales, which involves flattened keratinized cells forming lamellae and crossed fibers between lamellae. Such mechanical features are correlated with the protective functions for the pangolins, and are also requisite for body armor materials.

4.3.3.2 Effect of strain rate

Tensile stress-strain behavior

Fig. 4.13 shows the tensile behavior and strain-rate sensitivity of African tree and Chinese pangolin scales. The stress-strain curves, for all strain rates, show an elastic region followed by a region with decreasing slope and failure. For African tree pangolin scales,

as the strain rate increases from 10^{-5} to 10^{-1} /s, generally the Young's modulus and tensile strength increase from 1.1 to 1.5 GPa and from 65.5 to 108.7 MPa, respectively. The breaking strain decreases somewhat from 16.8% to 11.9%, while toughness (area under stress-strain curve) does not change in a consistent manner, varying from 8.29 MJ/m^3 at 10^{-5} /s, 4.92 MJ/m^3 at 10^{-4} /s to 8.39 MJ/m^3 at 10^{-1} /s. The Chinese pangolin scales exhibit similar tensile behavior, with slightly larger scattering at each strain rate, shown in Fig. 4.13b. The Young's modulus and tensile strength increase, though not significantly, with the increase of strain rate: from 0.9 GPa and 60.4 MPa at 10^{-5} /s to 1.2 GPa and 74.2 MPa at 10^{-1} /s, respectively. Both breaking strain and toughness decrease with increasing strain rate. At the strain rate of 10^{-4} /s, both pangolin scales show certain level of necking and obvious crazing (whitening of the necking region).

As expected for a viscoelastic material, pangolin scales become stiffer and stronger with increasing loading rate; the breaking strain and toughness do not change much for African tree pangolin scales, but decrease for Chinese pangolin scales. Such strain-rate dependence provides the pangolin scales an increased ability to combat impacts or strikes with higher stiffness and strength, and to absorb more energy to delay the onset of failure when loaded slowly, a key mechanism for coping with forces from the environment. This strain rate effect is crucial to body armor for humans. As the strain rate increases, large-scale movement of the molecules in a viscoelastic material is restricted, thus leading to increased modulus and strength, but a decreased maximum strain. When loaded slowly, the

chains of the polymer composite are able to deform to a larger degree and to slide past each other, allowing the scales to absorb more energy before failure.

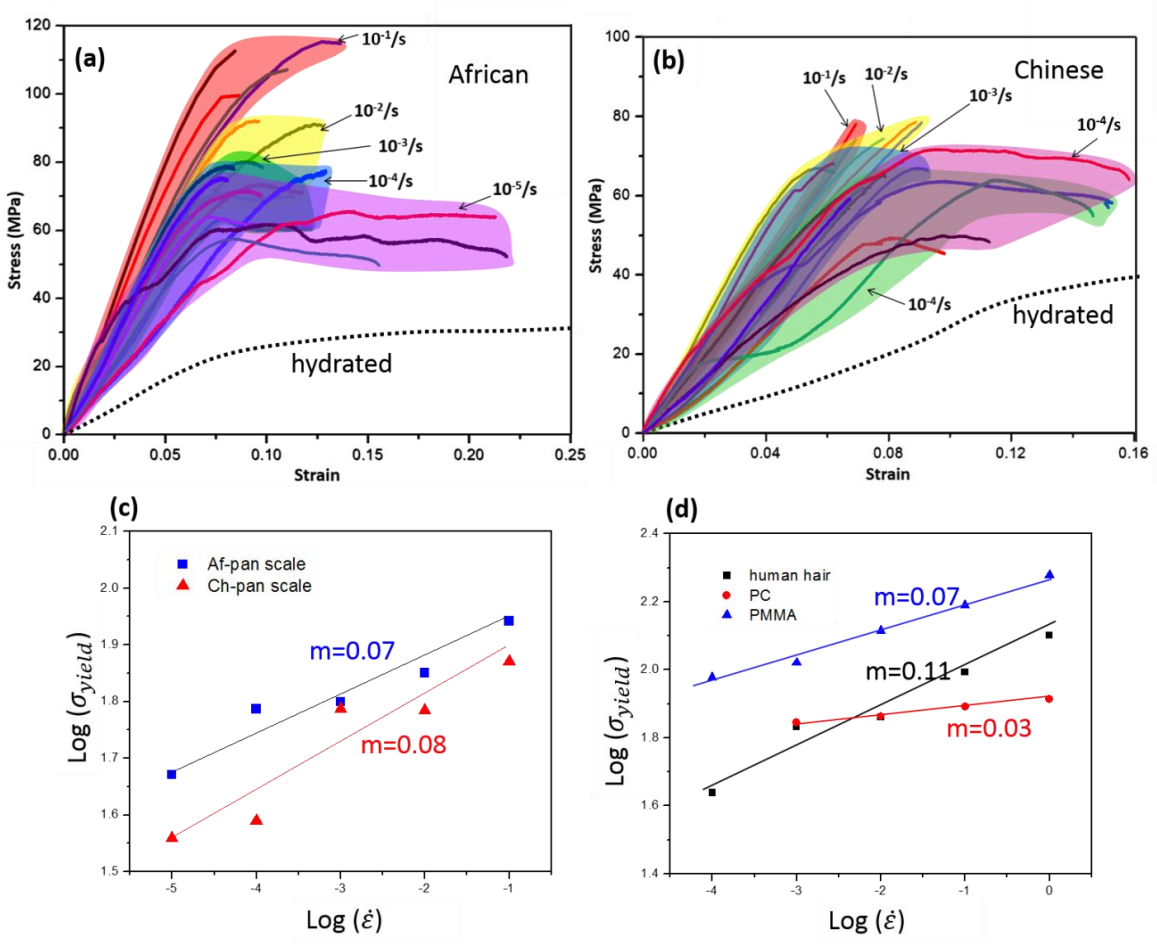

Figure 4.13 Strain rate and hydration sensitivity of pangolin keratin: (a) tensile stress-strain curves of African tree pangolin scales stretched longitudinally (Long-Ori) at different strain rates, and the hydrated 100% relative humidity, dotted curves), showing significant decrease in strength and stiffness; (b) tensile stress-strain curves of Chinese pangolin scales stretched longitudinally (Long-Ori) at different strain rates, and the tensile behavior of the hydrated specimen (100% relative humidity, dotted curves); (c) strain rate sensitivities of African tree and Chinese pangolin scales, calculated via Eq. (2) with yield stresses obtained from (a) and (b); (d) strain rate sensitivities of human hair (keratinous material) and typical polymers (polycarbonate, PC, and polymethyl methacrylate (PMMA).

The strain rate sensitivity of pangolin scales can be characterized by the strain rate sensitivity index, *m* [287]:

$$\sigma_y = K\dot{\varepsilon}^m \quad (7)$$

where σ_y and $\dot{\varepsilon}$ are the yield stress and strain rate, K is a constant. Therefore, *m* can be calculated through Eq. (8):

$$m = \frac{\partial \ln \sigma_y}{\partial \ln \dot{\varepsilon}} \quad (8)$$

The yield stresses for African tree and Chinese pangolin scales were calculated from the stress-strain curves and show increased values with increasing loading rate. Fig. 12c plots the $\ln \sigma_y - \ln \dot{\epsilon}$ curves for African tree and Chinese pangolin scales; the values of *m* are 0.070 and 0.081, respectively. The variation of yield stress from 10^{-5} /s to 10^{-1} /s for African tree pangolin scales is slightly smaller than that of Chinese pangolin scales, leading to a slightly smaller calculated strain rate sensitivity. Generally, African tree and Chinese pangolin scales show similar strain rate dependent behavior, and the strain rate sensitivity index values are comparable.

Figure 4.13d provides values of the strain rate sensitivity, *m*, for different materials as a comparison: common polymers, e.g. polycarbonate (*m*=0.03), polymethyl methacrylate (*m*=0.07) exhibit similar *m*. Yu et al. [180] report the strain-rate sensitivity for human hair equal to 0.11 (Fig. 4.13d).

A high strain-rate sensitivity also observed in other keratinous materials, such as wool [288] and equine hoof wall. Kasapi and Gosline [285] report an increasing Young's modulus (0.28 GPa at 10^{-3}/s to 0.85 GPa at 70/s) and yield strength with increasing strain rate for hydrated hoof wall keratin. The viscous component in wool has been considered

the matrix proteins [289], while the fibrous phase (microfibrils) contribute to the initial elasticity. The bird beak rhamphotheca (β-keratin) shows a pull-out fracture mode at low strain rate (5×10^{-5}/s) and brittle fracture (keratin scales were torn) at higher strain rate (5×10^{-2}/s). The transition of fracture mode was explained in terms of the competition between viscoplastic shear of the interscale glue and tensile fracture of the scales [150]. Since pangolin scales consist of α- and β-keratins, the amorphous matrix proteins and the fibrous phase are probably the viscous and elastic components, respectively, and the bonding between keratinized cells/lamellae plays a role in determining mechanical properties.

Another notable feature of keratinous materials is the hydration effect. The tensile stress-strain curves of hydrated (100% relative humidity) African tree and Chinese pangolin scales are overlaid in Figs. 4.13a,b (dotted curves), respectively. Both show significantly decreased Young's modulus and tensile strength but increased tensile strain (breaking strain not shown). The high hydration sensitivity is widely seen in other keratinous materials, e.g. human hair [286], stratum corneum [145], fingernails [206], feathers [286]. Based on extensive studies of α-keratin fibers, such humidity effect has been largely attributed to the interaction between water molecules and the amorphous matrix proteins, in which water may act cross link between chains, break down the secondary bonding and work as a plasticizer, thus reducing the stiffness and increasing the segmental mobility [206].

Fractography

Fig. 4.14 shows the tensile fracture surfaces of Chinese pangolin scales as strain rate increases from 10^{-5} to 10^{-3} , and to 10^{-1} /s. It is clear that they become smoother with increasing loading rate, and the fracture mode changes from fiber tear and fracture, lamella pull-out, to trans-lamellar fracture. At low strain rate (10^{-5} /s), lamellae are able to deform and delaminate into fibers (Fig. 4.14a), thus showing a rough fractured surface with torn fibers. A strain rate of 10^{-3} /s allows lamellae to move and shear, but not sufficiently to completely delaminate into fibers, thus exhibiting broken and pull-out lamellae with mesh-like surface (due to suture-like cell membrane complex). At relatively high strain rate (10^{-1}/s), lamellar movement is restricted, and lamellae are torn and fractured, displaying a smooth fracture surface with crossed-lamellae orientations. Such fracture mode change with increasing strain rate is also observed in hoof wall (α-keratin) [285] and bird beak rhamphotheca (β-keratin) [150], [213]. The hoof wall shows highest degree of tubule pull-out fracture at lowest strain rate, and a more brittle surface fractured at impact. The crack propagation involves both parallel with and across the tubules depending on positions along the hoof wall thickness. As mentioned earlier, the bird beak rhamphotheca shows viscoplastic shear between scales (keratinized cells) at low strain rate and tensile fracture of the scales (keratinized cells) at high strain rate.

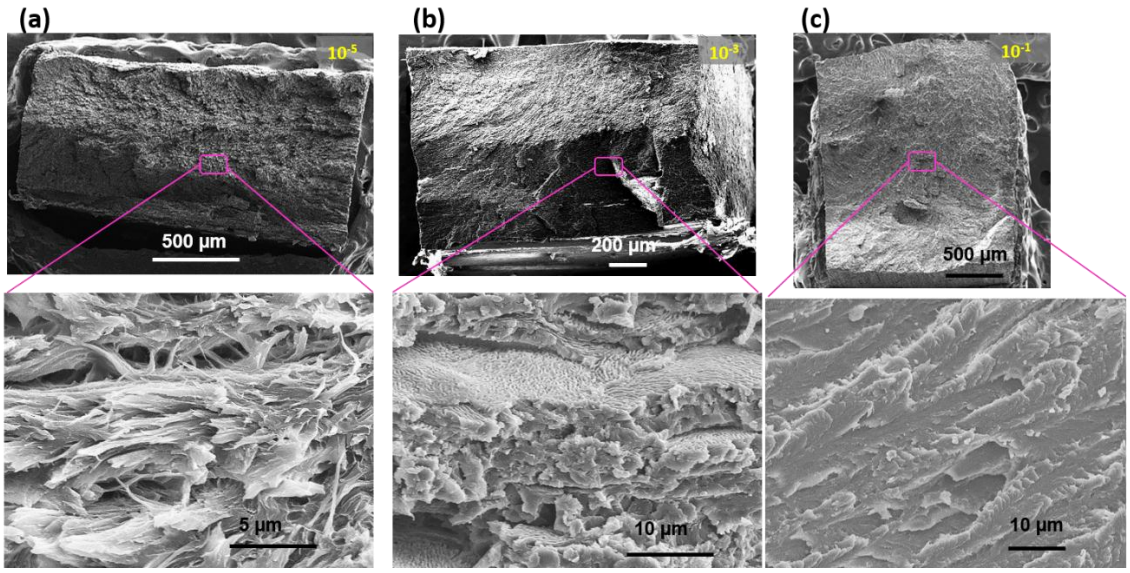

Figure 4.14 Tensile fractured surfaces of the pangolin scale at (a) 10-5/s, (b) 10-3/s and (c) 10-1/s. The fracture mode changes from fiber tear and fracture (lamellae delaminate into fibers) to lamella pull-out (lamella with surface suture) and trans-lamella fracture (smooth lamellar & cross-lamellar fracture) as strain rate increases.

Pangolin scales show fracture surfaces of cracks following intercellular boundaries (between lamellae) at intermediate strain rates, and fracture surfaces indicating cracks through cells and interfaces (across lamellae) at lower and higher strain rates. This is similar to hoof wall that has a complex hierarchical structure featuring differentially oriented lamellae in tubules and intertubular materials [285]. The structural features of pangolin scales contribute to an enhanced toughening to resist fracture. The crossed-lamellae with fibers aligned in different orientations between layers make cracks propagate across lamellae more difficult, while the suture-like interfaces between lamellae increase the lamellar bonding, which requires more energy for delamination, and creates a tortuous crack path, dissipating more energy.

4.4 Summary

The pangolin is the only known mammal with the adaptation, keratinous scales covering the main body as dermal armor. The scales are solid, being composed of piled keratinized cells organized in layers and showing crossed-lamellae structure, very different from other keratinous materials. The microfibrils are oriented in a preferred range of directions, crossing with each other. This offers a transverse isotropy property, which is favorable to the pangolin to resist external forces from various directions. The strain rate sensitivity allows the scales to be stiffer to combat with impact loads, while enable the scales to deform and absorb energy when loaded mildly/repeatedly. The scales overlap in a hexagonal pattern so that one point on the body is covered by three scale layers, providing very good coverage and allowing large body movement at the same time. These findings and analysis contributes new understanding to the current knowledge library of biological keratinous materials, and will provide insights into developing new armor materials.

Acknowledgements

Chapter 4, in part, is from the manuscript submitted to Acta Biomaterialia: Wang B, Yang W, Sherman V, and Meyers M. (2016) “Pangolin armor: overlapping, structure,

and mechanical properties of the keratinous scales". The dissertation author is the first author of this paper.

5 Feather shaft

Flight feathers of volant birds, encountering the aerodynamic forces during flight, primarily bend and twist [200]; they need to be lightweight, stiff, strong and yet flexible enough, properties that have been sought for by material scientists. The feather shaft represents a naturally refined structure optimized for flight functions, which, when interpreted to gain useful insights for engineered structures, involves shape design, structure and mechanical properties.

The geometry of feather shaft has been described, whereas the mechanical implications not known. While there has been general knowledge about the fibrous structure of cortex involving axial fibers, circumferential fibers and crossed-fibers, direct observations clarifying and locating the fibers at the different cortical regions along the shaft length are far from enough to a full clear understanding of the shaft structure. In addition, high-resolution mechanical tests are needed to verify the fibrous structure. More importantly, the rachis has been oversimplified as a hollow cylinder, with calamus overlooked, and the buckling and flexural behavior of such a sandwiched composite have been rarely studied.

In a quest to understand the structural design and an aim to address the above issues, this work provides a thorough and rigorous analytical study of the biomechanics of the feather shaft, correlating to the features involving the composite design and the hierarchical

structure. Our findings are to provide useful insights to the development of novel functional structures that could reproduce the remarkable properties of the feather shaft.

5.1 Materials

Flight feather shafts from a juvenile California gull (*Larus californicus*) and an American crow (*Corvus brachyrhynchos*) were collected, after the natural death of the birds, under the Federal Fish and Wildlife Permit, and the shafts were used for structural analysis and mechanical testing. The feathers were stored and studied at room temperature and humidity.

5.2 Experimental procedure

5.2.1 Structural observation

For optical microscopic observation, the feathers shafts were cut into six segments along the shaft axis (numbered as 1, 2, 3, 4, 5 and 6) from the proximal to the distal end (Fig. 5.1a). Then all segments were embedded in epoxy with transverse sections exposed, and polished using a series of graded sand papers up to 2400# and finally polishing paste (0.3 μm aluminum oxides). For scanning electron microscopy (SEM), transverse and longitudinal sections of feather shaft segments were obtained by cutting and folding and/or breaking at different positions along the shaft length, and coated with iridium for observation. The lateral walls of feather rachis cortex were submerged in liquid nitrogen, fractured in longitudinal direction and coated with iridium. Axio Fluorescence Microscope

and Phillips XL30 environmental scanning electron microscope at Nano3 facility at Calit2, UCSD were used.

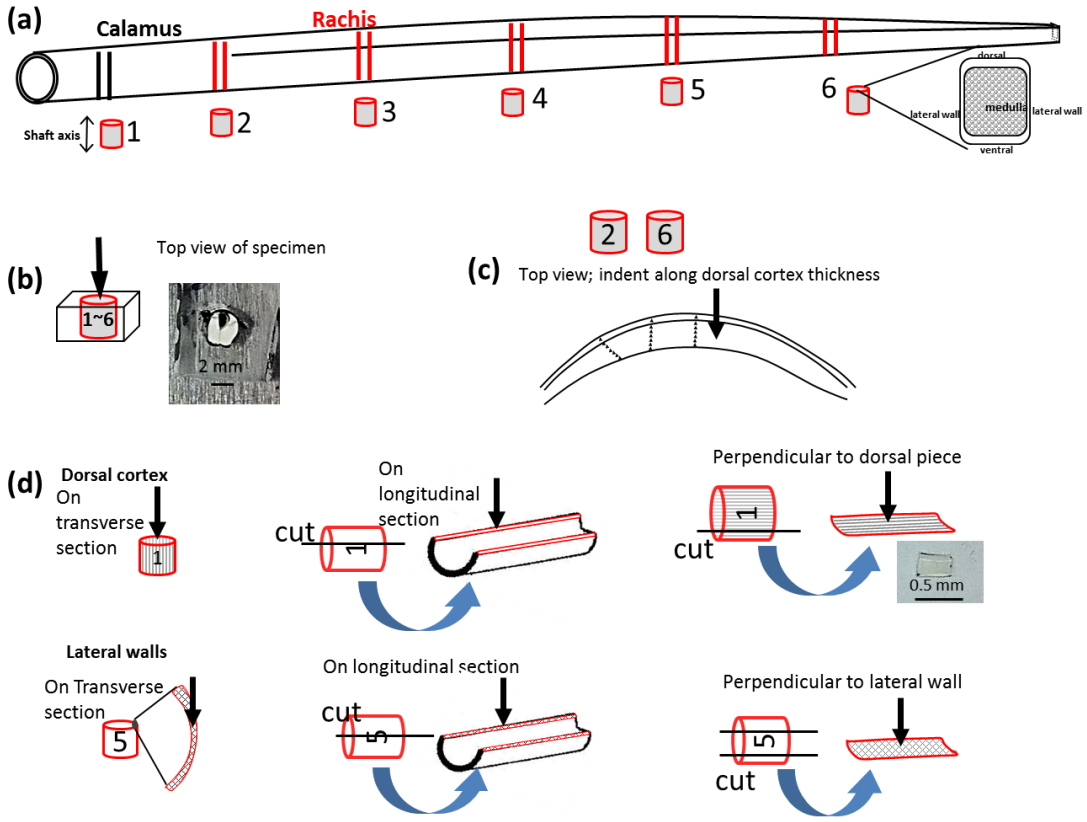

Figure 5.1 Sample preparation for structural observation and nanoindentation: (a) schematic of a seagull flight feather shaft consisting of calamus and rachis; the dorsal, lateral and ventral regions of shaft cortex are indicated. Shaft segments were cut along the shaft axis with numbers 1~6 representing positions along the shaft axis from the calamus to the distal end; (b) indentation on transverse sections along shaft length (positions 1~6) and an image of top view of one specimen; (c) indentation on dorsal region along cortex thickness at positions 2 and 6; (d) indentation along three loading orientations: dorsal cortex at position #1 on transverse section, on longitudinal section and perpendicular to dorsal piece (insert: photo of a polished dorsal piece); lateral wall at position #5 on transverse section, longitudinal section and perpendicular lateral wall piece.

For transmission electron microscopy (TEM), TGA-OsO_4 staining [232] combined with post-staining of lead was used. Pieces of ventral cortex (approximately 3 mm by 2 mm) from seagull feather rachis were pre-treated by immersing in 0.5 M thioglycolic acid

(pH 5.5) for 24 hours at room temperature to enhance contrast between the filaments and matrix. Then the pieces were washed with double-distilled water for 1 hour and immersed in 1-2% aquaeous osmium tetroxide (OsO_4) for 3 days at room temperature. The stained pieces were washed with distilled water, dehydrated to 100% ethanol through a series of graded alcohol solutions and then transited to 100% acetone through graded mixture of ethanol and acetone. Then specimens were infiltrated using Spurr's low viscosity expoxy resin through a series of solutions with increasing amount of resin and decreasing amount of acetone (25% resin+75% acetone, 50% resin+50% acetone, 75% resin+25% acetone, 90% resin+10% acetone, 100% resin, 100% resin), each taking one day. Specimens were then placed in fresh resin and polymerized with appropriate orientation for 2 days at 65^{o}C. The embedded specimens were trimmed and sectioned on a Leica Ultracut UCT ultramicrotome using diamond blade. Silver sections were picked up on filmed grids, post-stained with lead for 60 seconds, and further coated with graphite. An FEI Technai 12 (Spirit) (120 kV) electron microscope was used for examination.

5.2.2 Mechanical testing

5.2.2.1 Nanoindentation

The feathers shafts were cut into six segments of approximately ~4 mm in height from proximal (calamus) to the distal end (feather tip), and were numbered as 1, 2, 3, 4, 5, 6 representing their normalized distance from feather proximal point (see Fig. 5.1a). They

were mounted in epoxy and the transverse sections were polished in the same way as structural observation. Then the mechanical variation of dorsal, lateral and ventral regions along shaft length (positions1→6) was investigated via indenting on transverse sections of the six cortex sections (Fig. 5.1b). In addition, mechanical variation along dorsal cortex thickness on transverse sections at positions 2 and 6 (representing the calamus and the distal rachis) was examined via indenting on dorsal cortex (Fig. 1c). Thirdly, mechanical variation in different loading orientations was investigated by indenting on transverse section, longitudinal section and piece surface of dorsal cortex at position 1 and those of lateral wall at position 5 (Fig. 5.1c).

All specimens were placed in a fume hood for 2 days to obtain ambient condition prior to testing. The specimens were fixed on a steel block using Super Glue and care was taken to ensure that the glue layer was thin enough to have minimal impact on material testing procedures. A nanoindentation testing machine (Nano Hardness Tester, Nanovea, CA, USA) and a Berkovich diamond tip (Poisson's ratio of 0.07 and elastic modulus of 1140 GPa) were used. All specimens were indented with 20 mN of maximum force, loading and unloading rate of 40 mN/min, and 20 s of creep.

The hardness and reduced Young's moduli were calculated from the load-displacement curves according to ASTM E2546 & the Oliver Pharr method [290], [291], which is installed in the Nanovea tester. A value of 0.3 for Poisson's ratio of feather keratin was used according to the reported values of keratinous materials in the literature (0.25 for

sheep horn [292]; 0.3 for fingernails [293]; 0.37-0.48 for hair keratin [294]). An average of five consistent measurements for each position was reported.

5.2.2.2 Tensile test

The variation of dorsal, ventral and lateral cortex along the shaft length is examined. Feather shafts were divided into three segments along the shaft length (calamus, middle shaft and distal shaft). Then, dorsal, lateral and ventral cortex pieces along the shaft axis of each segment were excised (the medullary core was carefully removed to avoid scratches on cortex) to obtain thin rectangular strips (Fig. 5.2a). The termini of each rectangular strip were fixed with lock tite glue in two sand paper sheets, leaving a test gauge length of 10 ± 1.05 mm. Fig. 5.2a shows one tensile specimen ready for test. The width was 2.00 ± 0.21 mm, and the thickness varied from 0.29 mm to 0.10 mm. An Instron 3342 machine equipped with 500N load cell was used, and all specimens were loaded in the direction of feather shaft axis at room temperature at a strain rate of 10^{-3}/s.

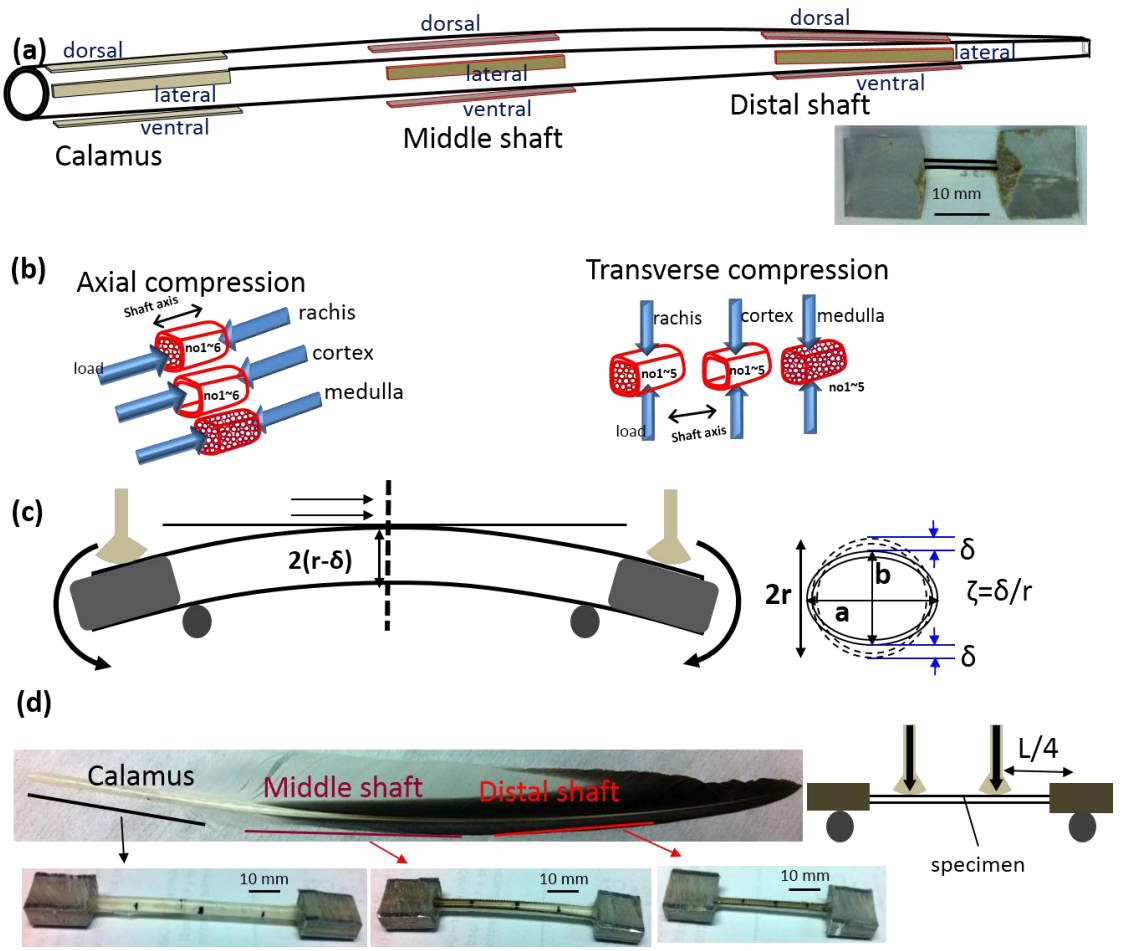

Figure 5.2 (a) Tensile tests on thin strips at dorsal, lateral and ventral regions at calamus, middle shaft and distal shaft, with a photo of specimen ready for test. (b) Axial and transverse compression specimens, both include rachis, cortex and medulla. (c) Pure bending of thin circular tubes, and the Brazier effect: the original circular cross section (dashed circles) deforms into an oval shape. The degree of ovalization, ζ, is characterized by the ratio of δ over r. (d) Four-point flexure along the shaft length including calamus, middle shaft and distal shaft; the two ends of each specimen were embedded in epoxy and square tubes.

5.2.2.3 Compressive behavior

Specimens for two types of tests were prepared. For axial compression, rachises (P#3-left and P#5-left) were cut consecutively into twelve sections (six sections for each rachis), the medulla of every other section was removed to obtain cortex specimens so that

each rachis specimen follows cortex specimen along the rachis length: ax-rachis-no.1, ax-cortex-no.1, ax-rachis-no.2, ax-cortex-no.2, etc. (Fig. 5.2b). All are in near rectangular prism shape, about 3 x 3 x 4.5 mm^3 in size. Another rachis (P#4-left) was cut into consecutive sections and the exterior cortex were removed to obtain five foamy medullary specimens in near rectangular prism shape: ax-medulla-no.1 to ax-medulla-no.5, about 2 x 2 x 2 mm^3 in size.

For transverse compression, symmetrical feathers and same sample preparation was used, except the loading is dorsal-ventrally transverse (Fig. 5.2b). Rachises of Primary#3-right and Primary#5-right feathers were cut into twelve consecutive sections with the medulla of every other section removed. Medullary specimens were obtained from Primary#4-right feather rachis. Rachis, cortex (tr-rachis-no.1, tr-cortex-no.1, tr-rachis-no.2, tr-cortex-no.2, etc.) and medulla (tr-medulla-no.1, to tr-medulla-no.5) specimens in transverse loading are shown in Fig. 5.2b. Cross sectional areas of all specimens were determined by using Image J calculations on optical micrographs of the specimens. All tests were in ambient environment at a strain rate of 10^{-3}/s.

5.2.2.4 Pure bending

Three types of polymeric tubes (thin circular hollow straws) with different diameters and thicknesses were used. The elastic moduli of the straw materials were determined by cutting dog-bone shape pieces along the axis of the straws, gluing the ends

in sand paper and stretching the specimens in an Instron machine (Instron 3343). All straw materials have similar elastic modulus (~1 GPa). The two ends of each tube were inserted by fitted tapered inserts, and the loads were applied downwards onto the two distal ends, creating a uniform bending moment within the central region, as shown in Fig. 5.2c. A camera captures images during bending to measure the height and width of the arc (bent tube); thus the bending radius is calculated to obtain the curvature (κ). A digital caliper measures the dimensions of the cross section at the middle of the tube as loading increases (horizontal and vertical distances corresponding to major and minor axes of the ovalized cross section), so that the measured degree of ovalization (defined as $\zeta=\delta/r$, Fig. 5.2c) can be obtained. At least three tubes for each type were tested and measured.

5.2.2.5 Three-point flexure

Three-dimensional (3D) printed polymer tubes (polylactic acid, PLA) with square and circular cross sections for flexural test were used to study the underlying mechanical principles of the shape factor. Both types of PLA tubes have the same thickness (2.54 mm) and cross sectional area, and the dimensions are: 21x21x203 mm^3 and 25x25x203 mm^3 for square and circular tubes, respectively. All PLA tubes, four specimens for each type, were tested in three-point bending till fracture, with the span length 5.8 times the specimen depth. An Instron 3367 equipped with 30 kN load cell was used, and all specimens were tested at room temperature at a nominal strain rate of 10^{-3}/s. Calculations were done by Origin 8.5.

5.2.2.6 Four-point flexure

Whole primary flight feather shafts (Primary#1-#3) were divided into three segments along the shaft length: calamus, middle shaft and distal shaft. The shaft segments were loaded in four-point bending with the distance of loading noses being one half of the support span, shown in Fig. 5.2d. This flexure was chosen since it creates a uniform moment between the loading noses, which provides accurate examination of the flexural behavior along the shaft length. Cantilever beam bending was avoided because of relatively inaccurate measurements of flexural deflection (due to the longitudinal curvature of the shaft and large displacement) and the limits of no failure modes involved. Three-point bending was not adopted because it produces significant local stress concentration at the load point, which is not the usual case for flight feathers, and underestimates the failure stress.

The two ends of each whole shaft segment were embedded in epoxy in short, thin and square aluminum tubes to prevent twisting of the segments during test. Loadings were applied on the shaft segments and care was taken to prevent compressing tubes and assure free rotation of the ends. Rubber pads on loading noses and supporting bars were used to prevent local concentrated damages. The dorsal surfaces of specimens were loaded until the load drops, which ultimately simulates the real stress condition of flight feathers [295]. Specimens ready for testing are shown in Fig. 5.2d. All shaft specimens have a ratio of

support length over specimen depth (at middle point) being 16:1, following the ASTM D6272, and the loading rate was 0.01 mm/s at room temperature for all specimens.

5.3 Results and discussion

5.3.1 Shape factor of flight feather shaft

5.3.1.1 Structure observation

The flight feather shafts from seagull and crow exhibit similar features, shown in Fig. 5.3. Transverse sections of both shafts at the calamus show elliptical compact cortices. At the region between calamus and the proximal rachis (umbilicus, positions 2 & 3), the cortex shows a near heptagonal shape with a groove at the middle of ventral surface (blue rectangles in Fig. 5.3b,c) where a transverse septum (pink dotted lines) starts to develop. The ventral groove aligns axially along the shaft and is present for the entire rachis. The foamy medulla (substantia medullaris) appears from inner surface of ventral cortex. Towards the distal rachis, the size of the cortex decreases and the cortex is gradually filled with medulla with dorsal-ventrally oriented transverse septa. The inner surfaces of cortices of seagull and crow feather shafts are relatively smooth, which differs from the well-developed dorsal ridges of pigeon feathers [200], [296].

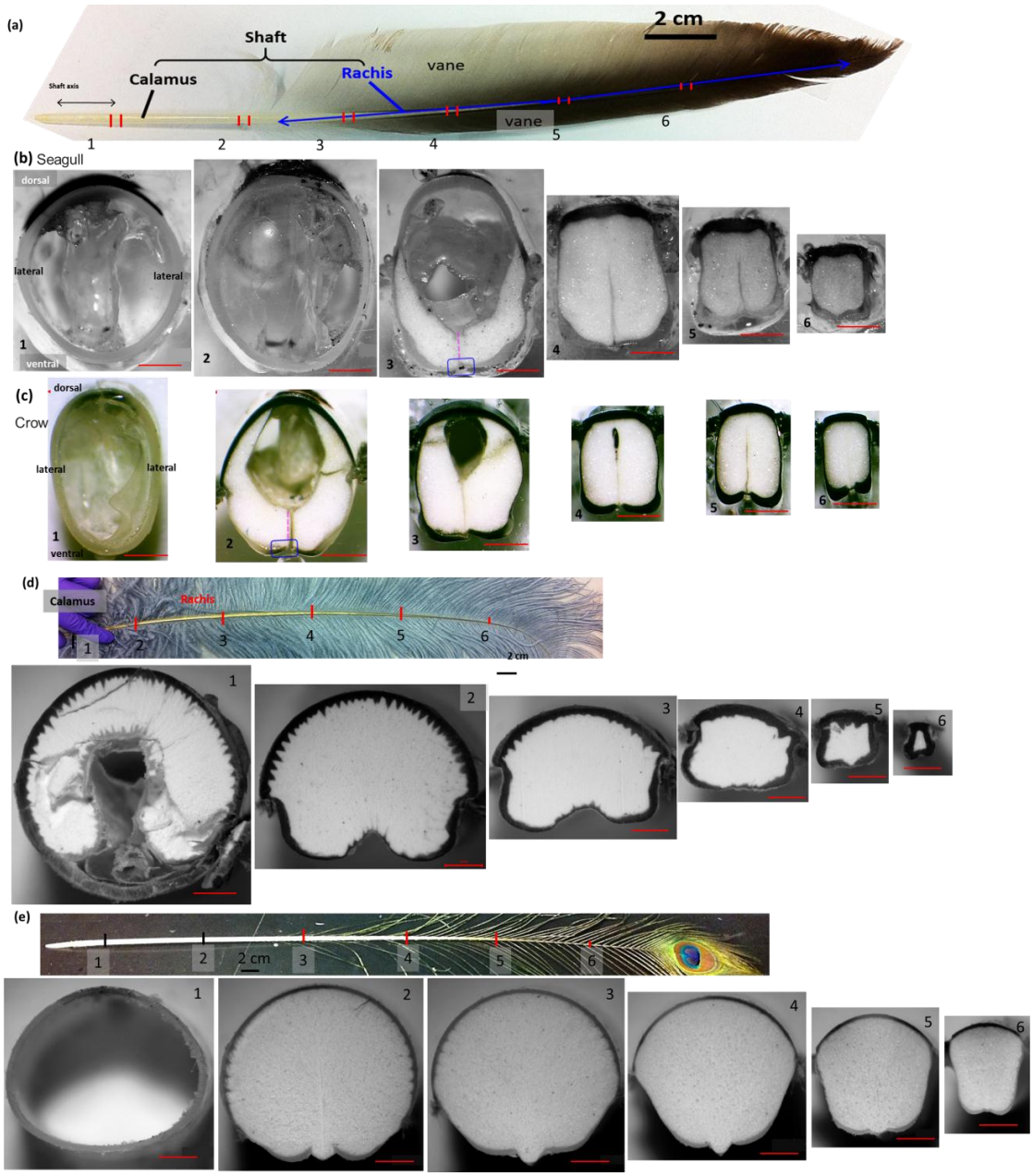

Figure 5.3 Cross sectional shape change along feather shafts: (a) seagull wing flight feather; numbered shaft represents the normalized distance from the calamus to the distal shaft; optical micrographs of transverse sections of (b) seagull and (c) crow feathers along the shaft length; (d) ostrich wing feather, numbered shaft and optical micrographs of the transverse sections showing the cortex shape; (d) peacock tail feather, numbered shaft and optical micrographs of the transverse sections showing the cortex shape.

For both feather shafts, the thickest and largest cortex was observed at the junction

of calamus and the beginning of rachis, favorable for the mechanical demand during flight: the thicker cortex has a higher ability to transmit the forces to the bones and tendons of the wing [200], [297], [298]. Besides, as an airfoil whose aerodynamic center and pressure center lie at approximately one quarter of the length, the cortex here enables the shaft to withstand the largest bending moment and stress. In addition, towards the distal rachis, the dorsal and ventral cortices are much thicker than the lateral walls (~10 times thicker). This resembles a naturally designed I-beam in that the majority material is distributed at the upper and lower regions to resist the maximum stresses. Interestingly, the rectangular/square cortex at the distal rachis shows a slightly shorter height on one lateral wall (facing front, the leading edge [206]). This allows the feather shaft to twist downwards or upwards to dissipate energy when subjected to high forces or bending moments, a strategy developed by birds to protect the shaft from permanent damage.

A salient feature, the shape change of cortex from circular at the proximal (calamus) to square/rectangular towards the distal rachis, is strikingly different from the circular cortex of flightless feathers, e.g. ostrich wing feathers and peacock tail (Fig. 5.3d,e), which reported to be circular through all shaft length [202], [203]. Flight feathers from other flying birds, e.g. pigeon[296], barn owl [200], and seriema [286], show this similar shape factor. Additionally, the thicknesses of dorsal, lateral and ventral regions of cortices of both flightless feather shafts are kept the same along the shaft length (~235 μm and ~111 μm for ostrich wing and peacock tail feathers), and the flightless feathers have relatively longer

rachis region, about 96% and 94% of total shaft length for peacock tail and ostrich wing feathers, respectively.

This shape change of cortex plays a pivotal role in adjusting the area moment of inertia and thus the flexural stiffness along the shaft length. The feather shaft needs to minimize the profile drag mainly through reducing the amount of material and dimensions of the cortex [45], [299]; meanwhile, it also needs to modulate the bending stiffness (product of *E* and *I*), along the length to sustain the complex forces at the base and to minimize the increasing deflection towards the distal rachis. The area moment of inertia, *I*, is correlated with the amount of material and the cross sectional shape of a beam; a uniformly high value of *I* from a large amount of material would be mechanically favorable but too heavy for the bird to fly [45], [207]. Thus changing the shape is an ingenious option to decrease the overall weight of the feather.

Beams with the same cross sectional area but different shapes give different area moment of inertia values, e.g. for circular and square beams with the same cross sectional area ($a^2 = \pi r^2$), the square one has larger area moment of inertia ($I_{rec} = \frac{a^4}{12} = \frac{\pi^2 r^4}{12}$ $> I_{cir} = \frac{\pi r^4}{4}$) and thus higher flexural stiffness. Importantly, a square cross section has advantages over a circular one in resisting cross sectional change during bending. The calamus needs to be circular to insert smoothly into and connect well with the tissue; while once coming out of skin, the rachis gradually becomes square. The flexural behavior of tubes, which feather shaft resambles, involves both the material's structure and the shape

[300]. It will be shown here, by testing square and round hollow tubes in bending, that the former can maintain the sectional shape, whereas the circular one ovalizes, thus affecting area moment of inertia and flexural stiffness.

5.3.1.2 Three-point bending

The bending responses of 3D printed PLA tubes with same cross sectional area were examined to answer the question: *why does the feather shaft choose a square shape towards the distal rachis*? For three-point bending, the flexural stiffness is calculated as [301]:

$$EI = \frac{dF}{d\delta}\frac{L^3}{48} \tag{9}$$

where E is the flexural modulus, F, δ and L are the flexural load, flexural deflection and supporting span. The flexural modulus is thus:

$$K = \frac{EI}{I} \tag{10}$$

where I is the area moments of inertia of the tubes ($I_{circular} = \frac{\pi[r^4-(r-t_c)^4]}{4}$, where r and t_c are the radius and thickness; $I_{square} = \frac{a^4-(a-2t_s)^4}{12}$, where a and t_s are the side length and thickness).

Flexural load-deflection curves of all tubes are plotted in Fig. 5.4a. Square tubes show consistently higher slope, and the flexural stiffness and modulus, determined by Eqns. (9-10) are approximately 24.2% larger than circular ones. This indicates the higher efficiency (higher ability per unit area) of square tubes (representing rachis) in resisting

bending and minimizing flexural deformation than the circular ones which represent calamus. In addition, circular tubes, with a large scattering, exhibit load-deflection responses that deviate significantly from initial linear region, indicating a decreasing value of *I* due to cross sectional shape change: the section changes from circular to oval. This effect is called "ovalization". Fig. 5.4b shows that the circular tube exhibits a certain degree of ovalization (dashed lines); whereas the cross section of square tube maintains almost the original shape. By calculation, the original *I* values of circular and square tubes before test are almost the same; however, the cross sectional shape changes differently during test, resulting in different changes in *I*, and thus different flexural properties.

When loaded in flexure, the square tube delays the onset of shape change because of having a flat and large contact area that relieves stress concentration; whereas the circular tubes start ovalization readily due to loading on much smaller contact region. In addition, the orthogonal edges of square tubes can restrict further transverse deformation and thus resist the cross sectional shape change, but for circular tubes, the flattening/ovalization proceeds gradually from the loading point invading towards the whole cross section, leaving less material in original shape to sustain load. The larger cross sectional shape change, the more loss in area moment of inertia, and the less ability to resist further flexural deflection. Therefore, the square tubes have higher ability to maintain cross sectional shape and resist the in-situ decrease of *I* to keep desired flexural stiffness than the circular tubes. This provides clues to understand why the bird feather shaft starts round but

ends square: the changing cross sectional shape to be square, which provides higher area moment of inertia per unit area to preserve reasonable flexural stiffness, could counterbalance partially the large reduction in area moment of inertia caused by the shaft tapering towards the distal free end to reduce profile drag and save required energy.

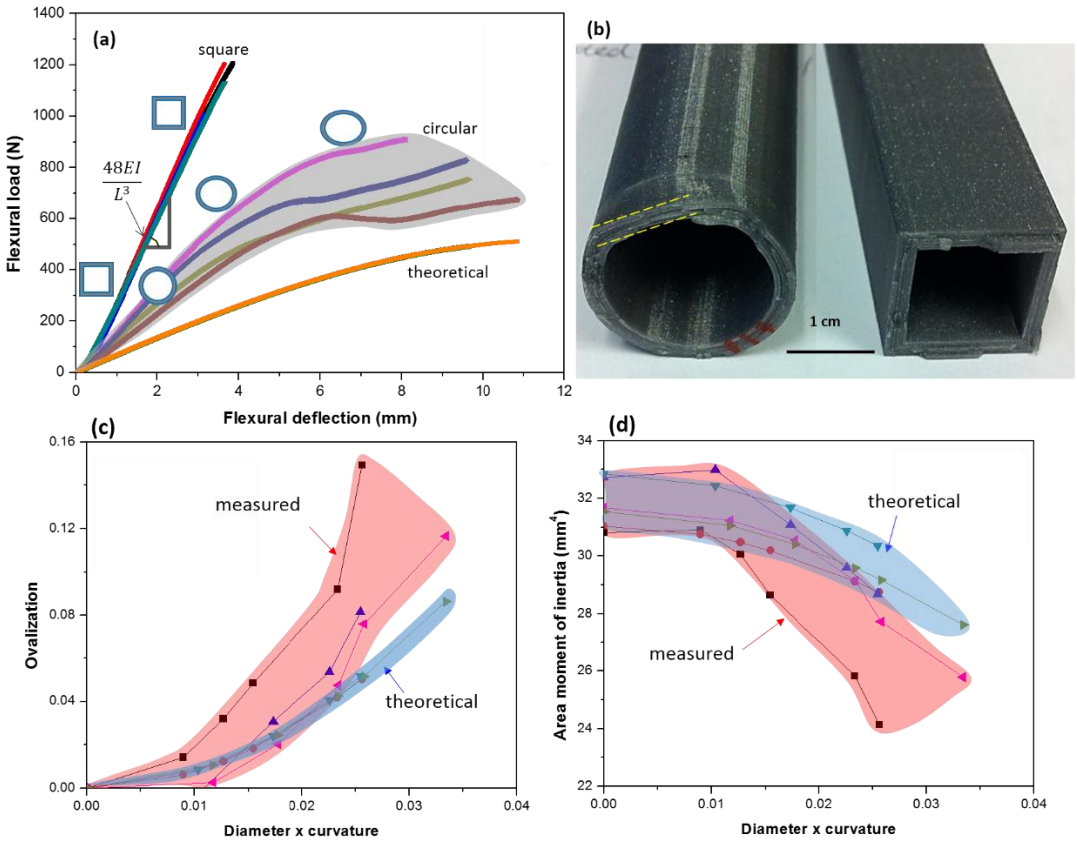

Figure 5.4 Flexural behavior of the 3D-printed PLA tubes with circular and square shapes: (a) flexural load-deflection curves, overlaid with theoretical calculated curves for circular tubes considering ovalization; (b) photo of the fractured surfaces. Pure bending of circular hollow PP tubes: plots of (c) measured degree of ovalization versus bending curvature (dimensionless), and (d) measured area moments of inertia versus bending curvature (dimensionless); overlaid plots shaded in blue are from theoretical calculations.

5.3.1.3 Pure bending

Upon bending, circular tubes ovalize, called Brazier effect [302] (degree of

ovalization, ζ, shown in Fig. 5.2c), thus changing *I* and affecting the bending stiffness. We present the change in area moment of inertia as a function of increasing bending moment and compare it with experimental results on PP (Polypropylene) tubes of various diameters (7.4~11.5 mm). At a given bending curvature, the measured degree of ovalization is:

$$\zeta_{me} = \frac{d-b}{d} \tag{11}$$

where *d* and *b* are the measured original diameter and the minor axis of the ovalized cross section (vertical height) of the tube. The measured area moment of inertia is:

$$I_{me} = \frac{\pi}{4}\left(\frac{a}{2}\right)\left(\frac{b}{2}\right)^3 - \frac{\pi}{4}\left(\frac{a}{2}-t\right)\left(\frac{b}{2}-t\right)^3 \approx \frac{\pi}{4}\frac{(b^3+3b^2a)}{8}t \tag{12}$$

where *a* is the measured major axis of the ovalized cross section (horizontal dimension) of the tube. Fig. 1e,f shows plots of ζ_{me} and I_{me} versus bending curvature of representative tubes. With increasing bending curvature, tubes show increasing degree of ovalization, but decreased area moment of inertia.

This ovalization can also be theoretically calculated; upon bending, ovalization minimizes total strain energy of the system. Thus a theoretical degree of ovalization is [303]:

$$\zeta_{th} = \kappa^2 r^4 \frac{(1-\nu^2)}{t^2} \tag{13}$$

where *K*, *r* and *t* are the bending curvature, original radius of the tube and thickness of the tube, and ν is Poisson's ratio of the material. The theoretical area moment of inertia is derived as a function of ovalization degree [303]:

$$I_{th} = \pi r^3 t\left(1 - \frac{3}{2}\zeta_{th} + \frac{5}{8}\zeta_{th}^2\right) \tag{14}$$

where ζ_t is the theoretical value of degree of ovalization calculated from Eqn. (13). The theoretically calculated degree of ovalization and area moment of inertia as a function of bending curvature are overlaid on experimentally measured values in Fig. 5.4c,d.

The calculated degree of ovalization of all types of tubes, with increasing bending curvature, increases monotonically, and agrees with the experimentally measured values. For area moment of inertia, both theoretical and experimentally measured values show clear decrease with increasing bending curvature. The theoretical area moment of inertia versus bending curvature shows consistently similar slope, and the range generally overlaps the experimental results. The two other types of tubes show similar behavior (Fig. S2), except larger scattering due to the minor difference in diameter magnified by the relationship that the area moment of inertia relates to r^3 of the tube (Eqn. 14). Therefore, the measured and theoretical degree of ovalization and area moment of inertia as functions of increasing bending curvature in circular tubes agree with each other, and demonstrate the intrinsic deficiency of a circular tube in maintaining area moment of inertia, thus deteriorating the flexural stiffness.

This theoretical ovalization is used to determine theoretical flexural load-deflection curves for the circular PLA tubes in three point bending. An expression for the bending curvature as a function of the deflection at the center point is derived as:

$$\kappa = \frac{16\delta}{L^2} \tag{15}$$

For each measured δ (deflection), using Eqns. (15), (13), (14), we obtain the

theoretical area moment of inertia $I_{th,\delta}$; and plug into the equation for a center-loaded beam, the flexural load is calculated as:

$$\mathrm{P} = \frac{48E}{L^3}\delta I_{th,\delta} \quad (16)$$

The plot is labeled ‘theoretical and presented in Fig. 5.4a; the curves are below the measured values but show the same trend as experiments.

5.3.2 Layered fibrous structure of cortex

5.3.2.1 The layered structure of cortex along shaft length

The shaft cortices of both seagull and crow feathers show a complex layered structure composed of differently oriented fibers along the shaft length, which correlates to the mechanical functions from the calamus to the distal rachis. At the calamus, the entire cortex (dorsal, lateral walls and ventral regions) of seagull feather consists of a thin outer layer and a thick inner layer. At the proximal rachis, the dorsal cortex is composed of a thinner outer layer and a thick inner layer, but towards the lateral walls the outer layer gradually disappears with only one layer present (Fig. 5.5b-lateral). The ventral region shows uniform one layer (Fig. 5.5b-ventral). At the distal rachis, no outer layer is observed for the entire cortex. The crow feather shows similar feature: cortex at the calamus shows a thin outer layer and a thick inner layer (Fig. 5.5d-dorsal, lateral, ventral), the dorsal cortex becomes thinner at the proximal rachis (Fig. 5.5e-dor), and disappears towards the distal rachis (Fig. 5.5f), while lateral walls and ventral cortex show one layer for the entire rachis.

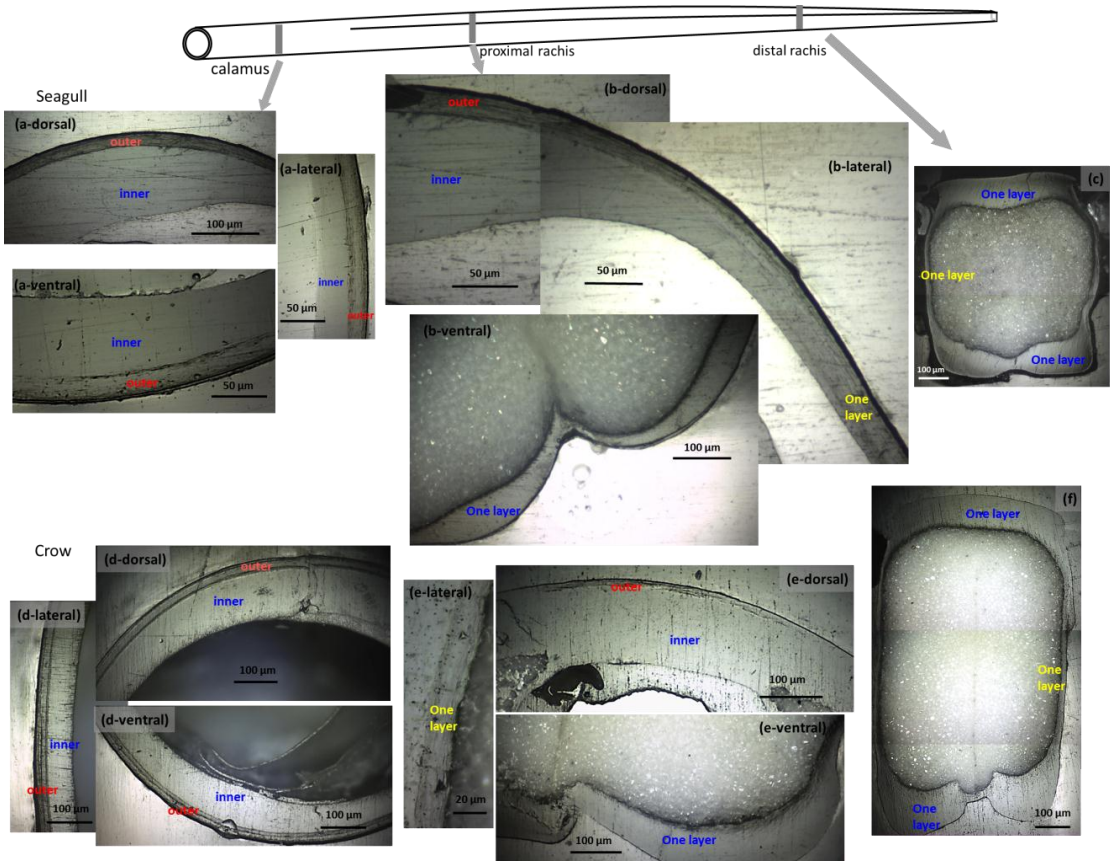

Figure 5.5 Optical micrographs of the transverse sections of feather shafts from the calamus to the distal shaft, showing the layered structure varying depending on local corticale regions and positions along the shaft length. Seagull feather: (a) calamus, (a-dorsal) dorsal region, (a-lateral) lateral wall, (a-ventral) ventral region; (b) proximal rachis, (c) distal rachis. Crow feather shaft shows similar layered structure: (d) calamus; (e) proximal rachis; (f) distal rachis. The outer layer and inner layer are indicated in red and blue, and the one layer in lateral wall in yellow.

5.3.2.2 The hierarchical fibrous structure

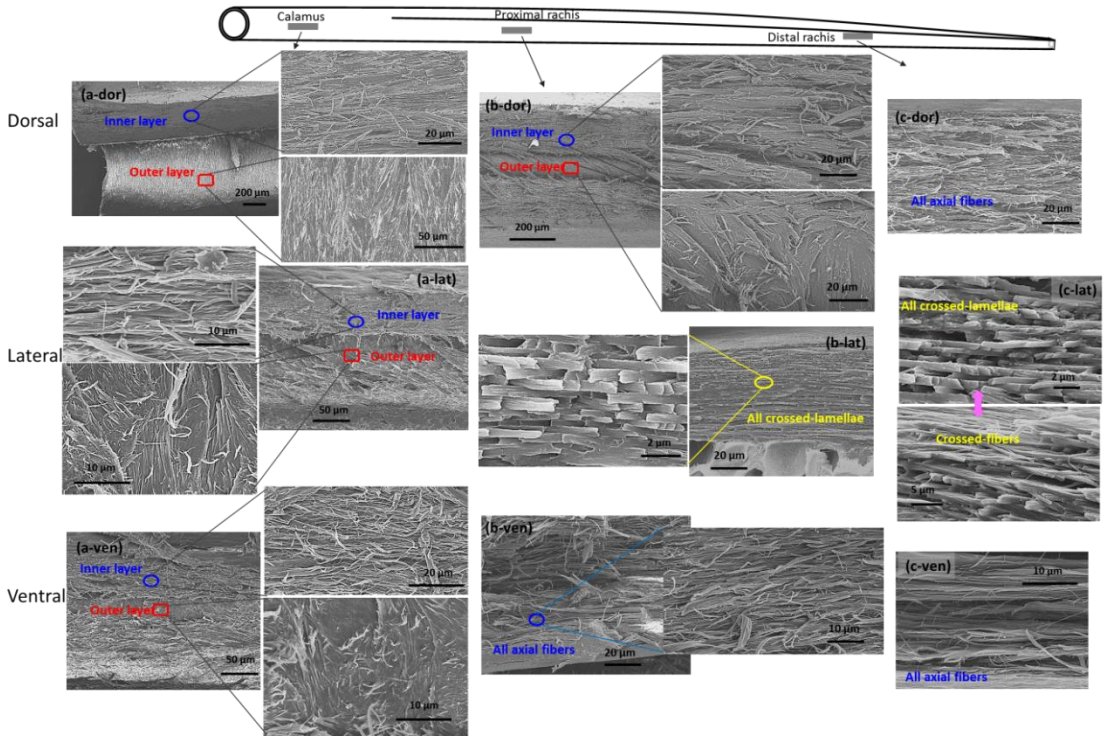

Figure 5.6 Scanning electron micrographs of the longitudinal sections at the dorsal, lateral and ventral regions of the cortex from seagull feather: at the calamus, the dorsal (a-dor), lateral (a-later), ventral (a-ven) regions all show a majority of axial fibers covered by circumferential fibers (the view is looking from the internal surface of the cortex); at the proximal rachis, the dorsal region (b-dor) shows the inner axial fibers and the outer circumferential fibers, whereas the lateral walls (b-lat) show crossed-lamellae and the ventral region (b-ven) exhibits only axial fibers; at the distal rachis, both the dorsal (c-dor) and ventral (c-ven) regions are composed of axial fibers, and the lateral walls (c-lat) of crossed-lamellae, indicating crossed-fiber structure.

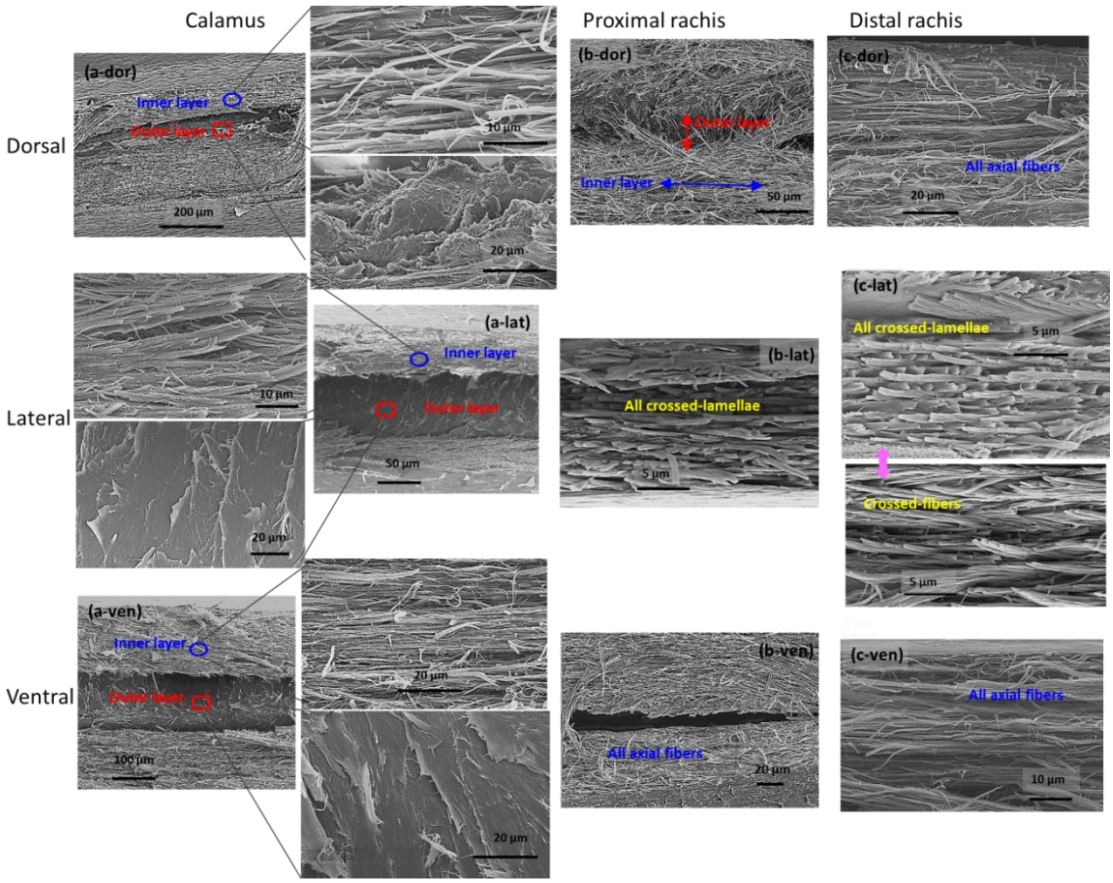

Figure 5.7 Scanning electron micrographs of the longitudinal sections at the dorsal, lateral and ventral regions of the cortex from crow feather, which shows the same fibrous structure as that of seagull: (a) at the calamus, (b) at the proximal rachis, (c) at the distal rachis.

Longitudinally folding and breaking the dorsal, lateral and ventral cortex pieces reveal that the layers are formed by differentially aligned fibers varying along shaft length (Fig. 5.6). At the calamus, the entire cortex exhibits a thick inner layer composed of longitudinally (axially) oriented fibers, and an outer layer of sheets of circumferentially aligned fibers (holding the broken inner layers and stopping the splitting of axial fibers), shown in Fig. 5.6a. At the proximal rachis, the dorsal cortex shows a thick inner layer of axial fibers and an outer layer of circumferential fibers, which may be at an obtuse angle

to the shaft axis; the ventral cortex is composed of solely axial fibers, whereas the lateral walls, made visible by freeze-fracture, consists of crossed-lamellae (Fig.5.6b). At the distal rachis where only one layer is present in the cortex, the dorsal and ventral regions are all composed of axial fibers while the lateral walls consist of crossed-lamellae, which is indicative of crossed-fibers (Fig. 5.6c). The crow feather shaft cortex shows the same fibrous structure, as seen in Fig. 5.7. Details about the thicknesses of the layers and orientations of the fibers of seagull and crow feathers are in Tables 5.1 and 5.2, respectively.

Table 5.1 Thicknesses of the layers in dorsal, lateral and ventral cortices along shaft length from seagull feather (μm).

		#1	#2	#3	#4	#5	#6
Dorsal cortex	Outer layer (circumferential fibers)	22.80	15.95	14.20	9.92	5.77	96.29 (axial fibers)
	Inner layer (axial fibers):	137.00	140.50	107.04	79.74	81.73	
Lateral cortex	Outer layer (circumferential fibers)	21.92	10.96	28.89 (crossed-fibers)	9.99 (crossed-fibers)	8.97 (crossed-fibers)	12.04 (crossed-fibers)
	Inner layer (axial fibers)	53.82	33.89				
Ventral cortex	Outer layer (circumferential fibers)	21.93	8.50	72.70 (axial fibers)	83.72 (axial fibers)	99.67 (axial fibers)	101.11 (axial fibers)
	Inner layer (axial fibers)	91.70	85.63				

Table 5.2 Thicknesses of the layers in dorsal, lateral and ventral cortices along shaft length (μm) from crow feather.

		#1	#2	#3	#4	#5	#6
Dorsal cortex	Outer layer (circumferential fibers)	21.66	7.22	9.68	192.86 (axial fibers)	195.65 (axial fibers)	91.48 (axial fibers)
	Inner layer (axial fibers):	158.88	101.11	127.58			
Lateral cortex	Outer layer (circumferential fibers)	19.26	12.04 (crossed-fibers)	9.68 (crossed--fibers)	19.28 (crossed-fibers)	14.17 (crossed-fibers)	14.44 (crossed-fibers)
	Inner layer (axial fibers)	81.85					
Ventral cortex	Outer layer (circumferential fibers)	21.66	67.40 (axial fibers)	91.48 (axial fibers)	192.86 (axial fibers)	195.65 (axial fibers)	129.99 (axial fibers)

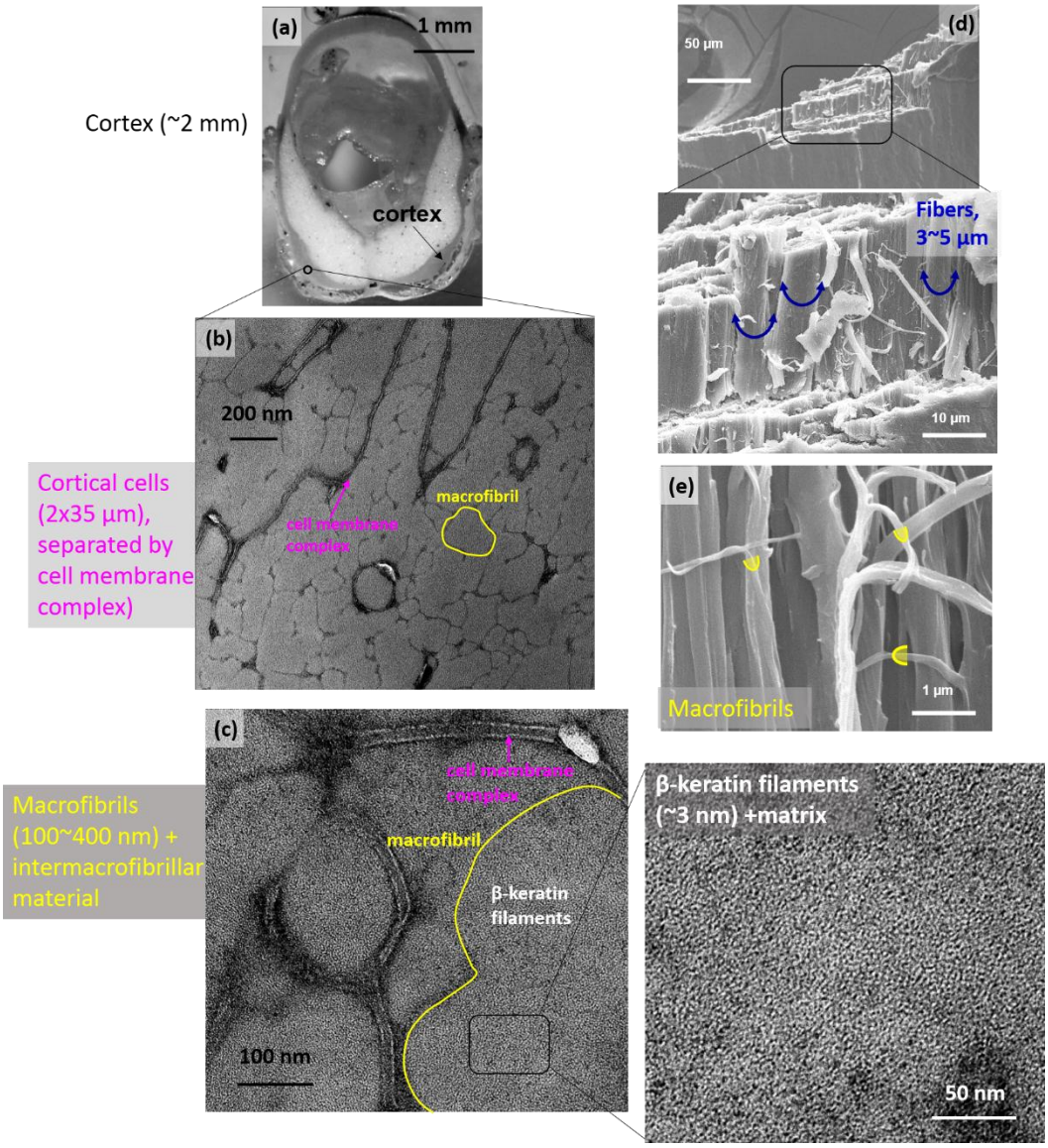

Figure 5.8 The hierarchical fibrous structure of seagull rachis: (a,b,c) transmission electron micrographs of transverse sections showing the cortex, cortical cells separated by cell membrane complex, macrofibrils outlined by intermacrofibrillar material, and β-keratin filaments embedded in matrix. Scanning electron micrographs of tensile fractured ventral strip of rachis, lateral view: (d) axially aligned fibers, bulk fibers about ~5 μm (blue doubled arrows). (e) An image shows the macrofibrils (50-300 nm in diameter, yellow semi-circules), which agree with those in transmission electron micrographs.

Transmission electron micrographs of the ventral region of rachis cortex reveal a hierarchical fibrous structure (Fig. 5.8): the rachis cortex is ~2 mm, which consists of

keratinized cortical cells (~20 μm wide and 30~50 μm long, from scanning electron micrographs). The cells are separated by cell membrane complex, which shows characteristic one densely-stained central layer (δ) by two less-dense layers (β), total about 22-26 nm thick, similar as that in other keratinzed materials, e.g. rat claw [48] and wool [142]. Inside the cells are fibrils measured about 100~400 nm clearly outlined by the densely stained material (black peripheries). Considering these fibrils are in the same structural hierarchy level of macrofibrils in α-keratin, e.g. human hair, they are macrofibrils and intermacrofibrillar material. Within the macrofibrils, β-keratin filaments, or microfibrils in the literature being the structural counterpart in α-keratin (intermediate filaments), with circular cross sections ~3 nm in diameter are delineated by the O_sO_4+lead stained matrix. The filamentous nature and the structural hierarchy of feather keratin are similar to those of the α-keratin, while differences exist: (1) the fairly distinct regions of well aligned microfibrils or specialized patterns of microfibrils packing in α-keratin are rare, meaning a high degree of randomness in filamentous organization in feather keratin [100]. This may be due to the historically unclear about the differently aligned fibrils in the cortex. (2) The necessity to use post-lead staining for matrix indicate that the cystine content of the matrix is not so greatly different from microfibrils as α-keratin, though results suggestive of an amorphous matrix [100].

Scanning electron micrographs of tensile fractured rachis cortex strips reveal fibers measuring ~5 μm wide and smaller fibers (50~300 nm in diameter) composing the former

ones (Fig. 5.8d,e), the latter being macrofibrils observed from transmission micrographs. Taking into consideration that each lamella in the lateral walls (Fig. 5.6b,f) represents one layer of keratinized cells, the cortical cells can be estimated about 1~3 μm thick. Therefore, the hierarchical fibrous structure of feather cortex involves: (1) crystalline β-keratin filaments (~3 nm in diameter) embedded in amorphous matrix proteins; (2) nanoscale filaments and matrix compose macrofibrils (~200 nm in diameter) surrounded by amorphous intermacrifibrilar material within keratinized cells; (3) these two further organize into fibers about 5 μm in diameter; (4) fibers bonded together form the cortex about 2 mm wide and ~180 μm thick.

5.3.2.3 Nanoindentation

The feather cortex can be considered as a fiber-reinforced composite, thus the superior mechanical properties being in the fiber direction [304], [305]. Since the fibrous keratins are cross-linked intracellularly [48] and there has not evidence that the filaments pass through the cell membrane complex [128], a possible length of a β-keratin filament and a macrofibril would be the cell length (30~50 μm); therefore, the β-keratin filaments, macrofibrils and fibers are long compared with their width [128], and the mechanical behavior will be close to that of a composite with continuous fibers [14], [128].

Nanoindentation was performed to investigate the fibrous structure. The differences in reduced modulus and hardness on the feather cortex are resulted from the direct changes

in fiber orientation among the different cortical regions and along the shaft length. In the simple case of a composite with uniaxially aligned fibers, the modulus with loading parallel to the fiber orientation is higher than that with loading perpendicular to them (Fig. 5.9a,b): loading parallel means that most forces are endured by fibers and the fiber buckling is impeded by the surrounding matrix (hierarchical levels of the fibrous structure help prevent fiber buckling), while loading perpendicular would split the fibers and a portion of the force goes into the softer amorphous matrix.

Nanoidentation measurements on the transverse section along dorsal cortex at the calamus (position 2) and the distal rachis (position 6) are shown in Figure 5.9c,d for seagull and Fig. 5.10a,b for crow. At the calamus, the decrease in modulus and hardness in going from the inner layer to the outer layer indicates the change of fiber orientations (indenting on longitudinal fibers then on circumferential fibers). For seagull and crow, the modulus is ~7.5 GPa and decreases to ~5.0 GPa in the outer layer. In the distal rachis, the outer layer of circumferential fibers no longer exists and only longitudinally arranged fibers form the dorsal and ventral cortex. Correspondingly, the hardness and modulus are uniform across the entire normalized distance.

The local mechanical properties of lateral walls also exhibits different variation from that of the dorsal and ventral cortex along the shaft length (Fig. 5.9e,f and Fig. 5.10c,d). The hardness and modulus of the lateral wall shows a decrease from the proximal region (calamus) to the distal end (distal rachis) of the feather shaft, because the axial fibers

are present in the calamus but crossed-fibers compose lateral walls in the rachis part. On the other hand, the dorsal and ventral regions of the feather cortex show a slight variation or constancy throughout the shaft length (from proximal to distal). The crossed-fibers composing the lateral walls of rachis part in contrast to the majority of axial fibers in the dorsal region of calamus is further confirmed, since indenting on dorsal pieces in different directions generate high anisotropic results while indenting on lateral walls give relative comparable values (Fig. 5.9g,h and Fig. 5.10e,f).

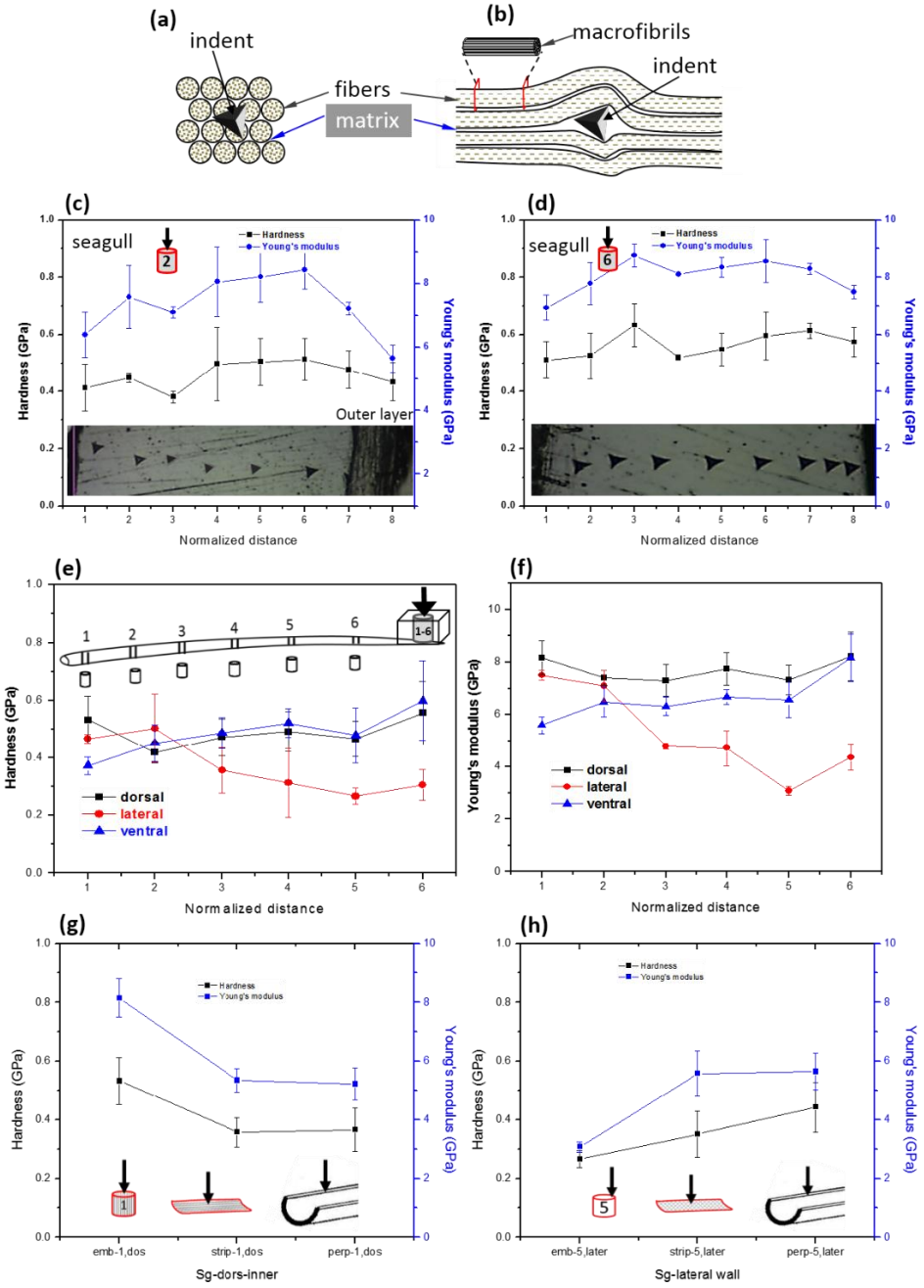

Figure 5.9 Indenting on composite of uniaxial fibers with indenting (a) parallel and (b) perpendicular to the fiber direction. The fibers are composed of macrofibrils in the feather cortex. Nanoindentation results from seagull feather shaft: along dorsal cortex thickness from inner to outside (c) at the calamus and (d) the distal rachis (position #6); (e,f) on dorsal, lateral and ventral regions along the shaft length; (g,h) on dorsal and lateral pieces in different loading directions. Each data point represents an average of five measurements and error bars represent standard deviations.

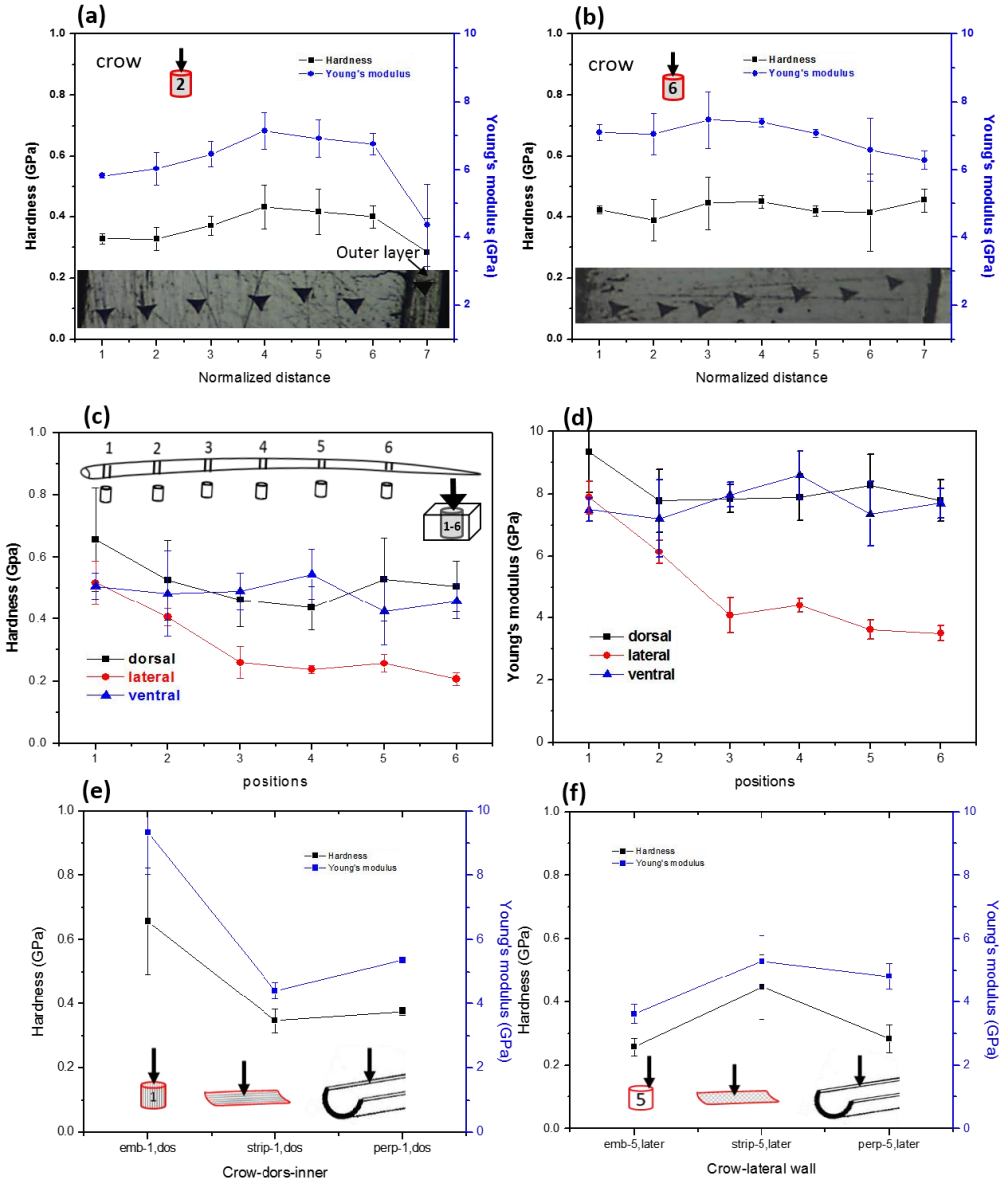

Figure 5.10 Nanoindentation results from crow feather shaft: along dorsal cortex thickness from inner to outside (a) at the calamus (position #2) and (b) the distal rachis (position #6); (c,d) on dorsal, lateral and ventral regions along the shaft length; (e,f) on dorsal and lateral pieces in different loading directions. Each data point represents an average of five measurements and error bars represent standard deviations.

5.3.2.4 Discussion on the fibrous cortex and the structural design

The increase in the axial fibers and decrease in the circumferential fibers are

important to the flexural properties of feather shaft. The dorsalventral flexural stiffness is the product of the area moment of inertia (I) and the longitudinal Young's modulus (E) [45]. The latter is determined by the local fibrous structure. As the shaft bends, the cortex at calamus with circumferential fibers enclosing a majority of axial fibers provides robust mechanical support and meanwhile prevents the axial fibers from splitting. Cameron et al. [207] reported a higher value of E towards the rachis tip due to a higher axial alignment of fibers. Here we specify that it is in the dorsal and ventral cortices that the amount of axially aligned fibers increases, which leads to a higher E of rachis towards the distal end, thus, compensating the decrease in I due to the reduced material to ensure necessary flexural stiffness.

Interestingly, the entire lateral cortex of both rachises consists of crossed-lamellae, which are formed by crossed fibers (firstly directly observed), which can provide necessary dorsalventral flexibility and prevent damages to the feather shaft. During bending, the dorsal and ventral cortex provide stiffness, while the lateral walls allow the shaft to flex with reasonable strain under dangerous loads, thus delaying the onset of buckling and failure [208]. Besides, the crossed-fibers structure may be a key in limitting damages from barbs. The barbs, carrying arrays of hooked barbules, anchor to the rachis at the lateral walls and generate larger displacements [306], [307] and multi-directional stresses. A crossed-fibers structure would be more robust to sustain the displacements and resist the stresses than the axial fibers, which are anisotropic and prone to split.

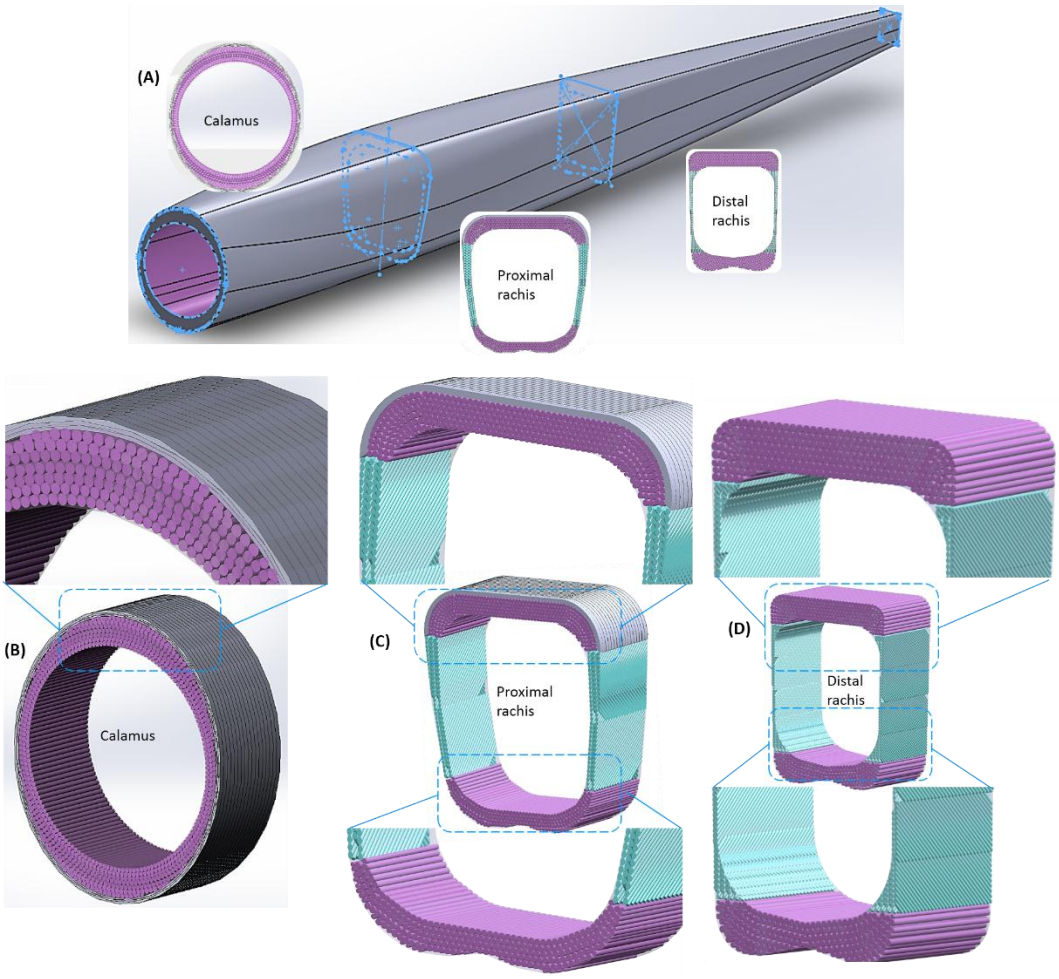

Figure 5.11 Structural model of the feather shaft cortex. (a) The cross section changes from circular at the calamus to near rectangular at rachis. The layered fibrous structure of cortex: (b) at the calamus, all the cortex consists of a thin outer layer of circumferential fibers and a thick inner layer of axial fibers; (c) at the proximal rachis, the dorsal cortex consists of a thinner outer layer of circumferential fibers covering axial fibers, the lateral walls of crossed-fibers and the ventral cortex of axial fibers; (d) at the distal rachis, the dorsal and ventral regions are composed of axial fibers and the lateral walls of crossed-fibers.

On the other hand, the crossed-fibers can enhance the torsional rigidity, thus controlling twisting during lift or strike. The crossed-fibers are aligned 45^{o} to the shaft axis, the same orientation to the largest stress in which the material will fracture/split under torsion [308]. At the same time, this rigidity is complemented by the axial fibers in the

dorsal and ventral cortices, which facilitate twisting. Twisting is known to lower the bending moment before causing local buckling of thin-walled cylinders [295], [309], and dissipate energy to avoid permanent damage. Therefore, the crossed-fibers in the lateral walls and the predominant axial fibers covered by a gradually decrease of circumferential fibers in the dorsal and ventral cortex work synergistically to provide optimized mechanical properties for the feather shaft.

The structural design of the feather shaft is illustrated in Fig. 5.11, and key features are summarized as the following:

- *Shape factor*: the cross section of cortex changes from circular at the proximal (calamus) to square towards the end (distal rachis), with significantly thickened dorsal and ventral cortices. This provides higher bending stiffness per unit area and increases the ability to resist sectional shape change during flexure to retain the initial stiffness. The cortical shape also allows the shaft to twist under dangerously high loading, thus avoiding failure.
- *Layered fibrous structure*: at the calamus, the entire cortex shows a bulk inner layer of axial fibers covered by a thin (15%) outer layer of circumferential fibers. For the dorsal and ventral cortex, the outer layer becomes thinner as the axially aligned fibers gradually compose the whole dorsal and ventral cortices towards the distal rachis, whereas the lateral walls for the entire rachis show crossed-fiber structure (Fig. 5.11b). This is the first report of directly observed crossed-fiber configuration.

- *Synergy*: the shape factor and the fibrous structure create a structure that is longitudinally strong, dorsalventrally stiff and torsionally rigid, yet capable of prescribed deflection and twisting at a minimum of weight: (a) at calamus and proximal rachis, the thick cortex is strong and able to prevent splitting of the axial fibers; (b) the shape factor and the increase in volume fraction of axial fibers lead to higher efficiency in dorsalventral bending stiffness towards the shaft end, therefore, compensating the decrease of area moment of inertia caused by material reduction; (c) the crossed-fibers in the lateral walls provides necessary bending flexibility; (d) the crossed-fibers provide torsional rigidity, while the axial fibers in dorsal and ventral cortex and the rachis cortical shape allow the shaft to twist under dangerous loads.

5.3.3 Porous and fibrous medulla

The feather rachis possesses a porous cellular core called medulla, a closed-cell foamy structure that has hierarchical levels of porosity at micro- and nano-scales. The medulla in rachis from proximal to distal shows near round cells with a diameter about 20-30 μm (Fig. 5a, micro-scale porosity). Higher magnification images reveal that the cell walls are composed of curved weaving fibrils (about 40-130 nm in diameter), while the spaces between fibrils resulting in the porosity at the next down nanoscale level, which further decreases density. It is interesting that the cell walls are connected and strengthened by fibrous struts at junctions and interfaces of cell walls (indicated by yellow rectangles in

Fig. 5c,d). At the interface between cellular medulla and cortex (Fig. 5e,f), the fibrils forming medullary cell walls merge well with the fibrils comprising the cortex.

The foam-like medulla of feather rachis shows up during embryogenesis [98], [104], indicating their important roles in functionalities. The enhanced coherence within medulla and strengthened bonding between medulla and cortex, by the first time reported here, contribute to the mechanical integrity and energy absorbance of the shaft. It is experimentally found that when cortex strips (applies to dorsal, ventral and lateral walls) are loaded in axial tension, specimens with a thin layer of medulla delay the fracture significantly and show flat fracture surface compared with specimens without medulla fractured soon into pieces, indicating that medulla prevents the splitting of cortex. In addition, bending of shaft involves not only tension but also compression of the cortex and medulla. It has been documented, from a number of other similar biological materials, e.g. porcupine quills, plant stems [133], [310]–[312], wood [311], [313], that a porous core acts as an energy absorber to increase the buckling resistance, while minimizing the weight, of such a solid shell over foamy core structure, in which the interface of shell and foamy core plays a vital role.

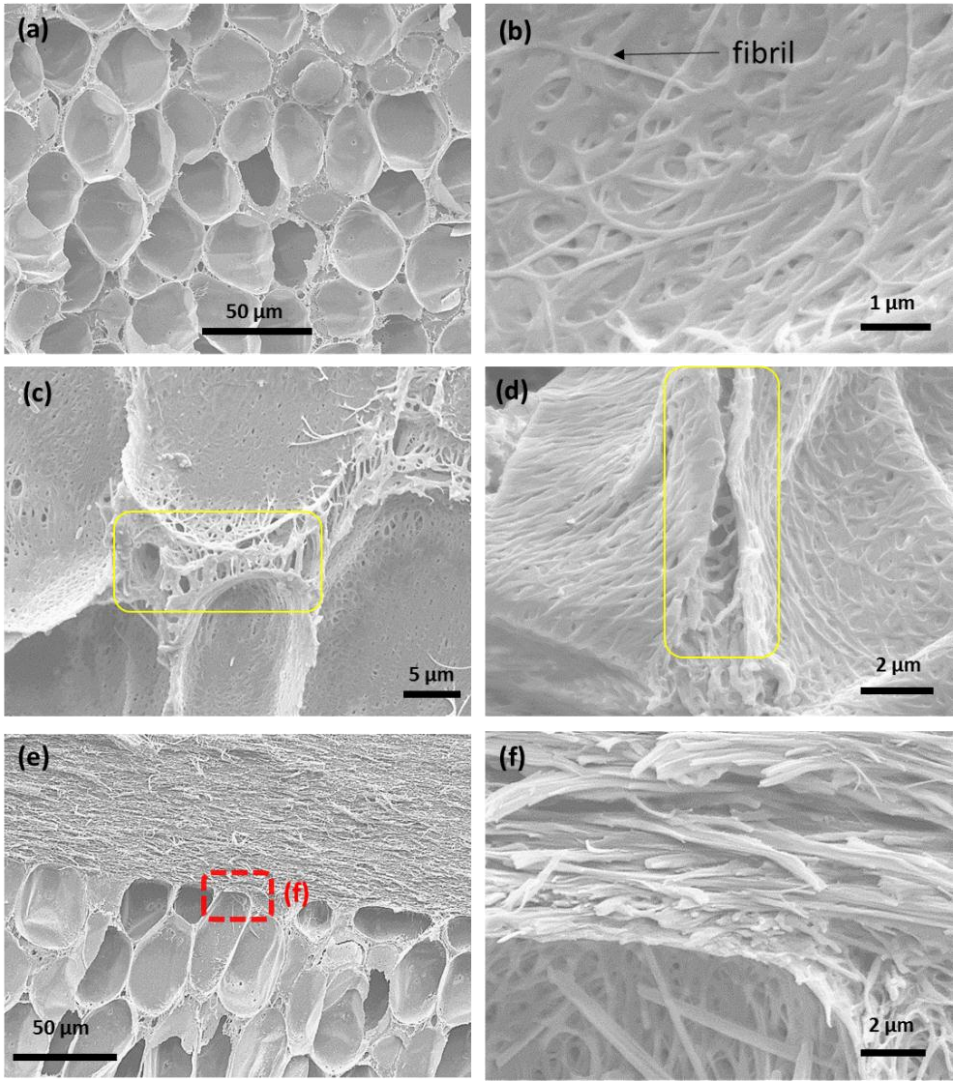

Figure 5.12 Scanning electron micrographs of the medulla: (a) closed-cell foam-like structure; the cells show near round shape with about 20-30 µm in diameter; (b) higher magnification image of the cell walls reveals the fibrous and porous structure at nanoscale, arrow pointing to fibrils; (c) and (d) the fibrous struts that connect and strengthen the cell wall interfaces (yellow rectangles); (e) longitudinal section of distal rachis at the interface of medulla and cortex; (f) higher magnification image of the area in red dotted rectangle in (e), the fibrils of cell walls merge well with those composing the cortex.

5.3.4 Tensile response

The feather cortex has anisotropic properties. Examination of the tensile responses of cortex strips of dorsal, lateral and ventral regions along the shaft length is presented in

Fig. 5.13, and the data are summarized in Table 5.3. All stress-strain curves show an initial elastic region, where the Young's modulus is determined, followed by a short non-linear deformation region and failure.

The dorsal cortex shows clearly increasing Young's modulus and tensile strength from the calamus to the distal shaft (37.5% and 49.5% increase, respectively), while breaking strain does not vary much. The ventral cortex exhibits a similar trend, but not as significant. This is within expectation, since both regions show an increasing fraction of axially aligned fibers. This is consistent with reports that towards the distal shaft the volume of circumferential fibers decreases [314], [315], and the Young's modulus increases [207]. However, the lateral walls shows evidently decreased Young's modulus and tensile strength (26% and 46% decrease, respectively), and the breaking strain also decreases. This is due to the fact that the lateral walls change structure from circumferential fibers enclosing a majority of axial fibers at the calamus to crossed fibers at the rachis. The fibers are not aligned with the tensile direction and therefore the strength is reduced. The lateral walls are significantly thinner than the dorsal and ventral cortex, and therefore produce more delicate specimens and larger scattering results.

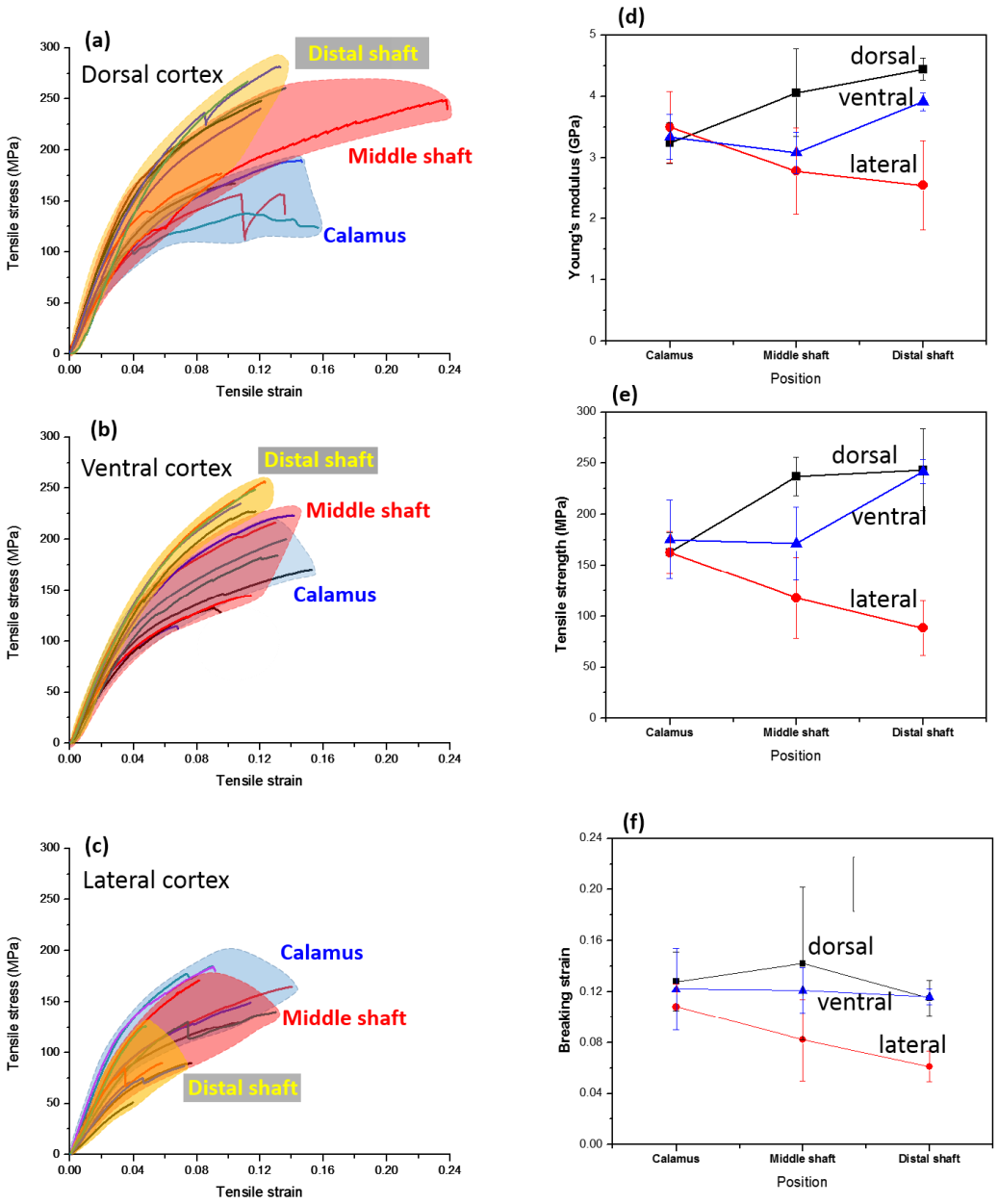

Figure 5.13 Tensile responses of seagull cortex strips along the shaft length: stress-strain curves of (a) dorsal cortex, (b) ventral cortex, (c) lateral cortex at the calamus, middle shaft and distal shaft; Variation of (d) Young's modulus, (e) tensile strength, (f) breaking strain of the dorsal, lateral and ventral cortex strips along the shaft length.

In addition, at the calamus, the dorsal, ventral and lateral walls generate almost the same modulus (~3.3 GPa), strength (166.9 MPa) and breaking strain (0.12), which agrees

with the homogeneous two layered fibrous structure described (Fig. 5.13d,e,f). At the middle shaft, the dorsal and ventral cortex are stronger and stiffer than the lateral walls since the latter is composed of crossed-fibers. The ventral cortex is slightly weaker and more compliant, which may be due to a ventral groove being a weak point and thus prone to split before fracture. The dorsal and ventral cortex at the distal shaft show similar modulus, strength and breaking strain as a result of the constituent axial fibers, while lateral walls are much weaker and more compliant.

Table 5.3 Tensile results of dorsal, ventral and lateral cortex strips along the shaft length. Errors represent standard deviations of five valid measurements.

		Young's modulus (Gpa)	Tensile strength (MPa)	Breaking strain
Calamus	Dorsal	3.2±0.3	162.9±19.1	0.13±0.02
	Ventral	3.3±0.4	175.3±38.8	0.12±0.03
	Lateral	3.5±0.6	162.6±21.1	0.11±0.02
Middle shaft	Dorsal	4.1±0.7	237.2±18.7	0.14±0.06
	Ventral	3.1±0.3	171.3±35.8	0.12±0.02
	Lateral	2.8±0.7	117.9±39.7	0.08±0.03
Distal shaft	Dorsal	4.4±0.2	243.5±40.2	0.12±0.01
	Ventral	3.9±0.2	241.9±11.5	0.12±0.01
	Lateral	2.6±0.7	88.4±26.5	0.06±0.01

Being very light, the feather shaft shows specific strength (density normalized) of 68 kNm/kg (using the measured density of solid keratin of 1.2 g/cm^3 and tensile strength of 200 MPa) that is on the same order of engineering alloys, e.g. 304 Stainless steel 65

kNm/kg, titanium alloys 100-300 kNm/kg, indicating the preeminence of being both strong and lightweight.

The deformation and fracture mechanisms also depend on the particular cortical regions and locations along the shaft length, originated from the differently aligned fibers. At the calamus, dorsal, lateral and ventral specimens all show (Fig. 5.14a) transverse straight fracture due to the rupture of majority axial fibers, few splitting and axial cracks because of circumferential fibers holding axial fibers, and delamination/peeling off of axial fibers. At the middle shaft, the dorsal and ventral regions also exhibit transverse straight fracture, whereas the lateral walls show transverse zigzag fracture view (Fig. 5.14d). Delamination and clear axial cracks appear, but not totally detached, in the dorsal region, which is attributed to the thinner outer layer of circumferential fibers. The cracks often deflect along the cortical cell boundaries. The ventral region, composed of solely axial fibers, split longitudinally into pieces with several fiber bundles bridging the extensive cracks. At the distal shaft, both dorsal and ventral regions show a transverse straight fracture view and a larger degree of axial splitting/cracking, with fibers peeling off or delamination. The lateral walls show zigzagged fracture view, and the axial crack is deflected due to crossed fibers (Fig. 5.14g).

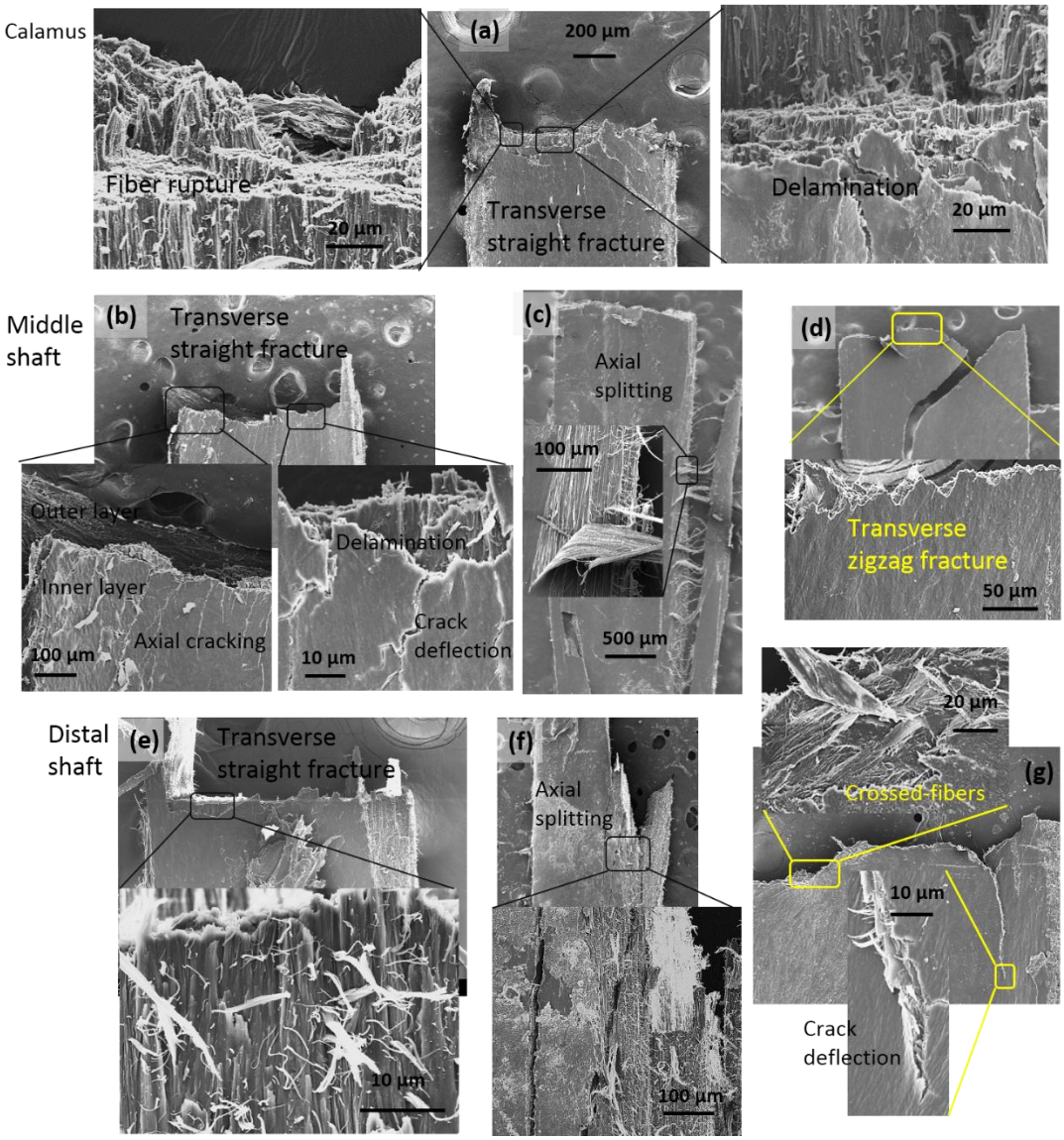

Figure 5.14 Side views of tensile fractured cortex specimens along the shaft length: at the calamus (a), the dorsal, lateral and ventral regions all show a transverse straight fracture due to rupture of the axial fibers, the circumferential fibers covering axial fibers, delamination and peeling off. The middle shaft (b) shows the same transverse straight fracture with axial cracking, crack deflection, and delamination, the ventral region (c) shows significant axial splitting, whereas (d) the lateral walls show transverse zigzag fracture due to crossed-fibers. At the distal shaft, the dorsal and ventral regions (e,f) exhibit transverse straight fracture, while the lateral walls (g) show cross fibers in layers and crack deflection.

The axial fibers rupture, creating a transverse straight fracture view, and tend to

split axially, the degree of which depends on the existence of circumferential fibers. Axial fibers also peel off or delaminate, and sometimes show bridging effects. The circumferential fibers, present at the calamus and middle shaft, hold axial fibers together, providing good bonding, while the crossed-fibers produce a transverse zigzag fracture view, lead to fiber bridging and deflect axial cracks. These differ from the flightless feather rachis where fiber rupture is the dominant failure [203].

5.3.5 Compressive behavior

5.3.5.1 Axial compression

A quantitative study of the compressive behavior considering for the first time a more accurate geometry and featuring the deformation mechanism and the function of medulla for feather rachis is presented. Fig. 5.15a shows the axial compressive force-displacement curves of cortex, medulla and rachis (cortex enclosing medulla) specimens with an enlarged plot for representative medulla sample. Filling the cortex with medulla leads to significant increase in the load bearing capacity in all specimens: forces at first peak or beginning plateau region of rachis almost double those of cortex. In addition, cortex samples split at the ends. This failure advances with increasing load, and leads to a sudden decrease in load (first load drop, indicated in Fig. 5.15a). No sudden load drop due to unexpected splitting was observed in rachis. The medulla shows a force-displacement curve that is typical for cellular materials: a linear elastic region with ~0.02 GPa stiffness,

a stress plateau correlating to the progressive compressing and collapse of foam cells, and a densification region, indicating the characteristic ability of energy absorbance. The values are comparable to those of medulla reported by Liu et al. [203] and Bonser [139]. Detailed results are summarized in Table 5.4.

Fig. 5.15c-e shows the morphologies of medulla after compressive load removed. No significant cracks were observed, and the foam cells are clearly compressed, showing stretched morphologies perpendicular to loading direction. The heavily bent and deformed cell edges (Fig. 5.15e) are not fully recovered, while the fibril bundles as struts at cell wall interfaces still remain good bonding. The cortex shows that axial cracking/splitting and subsequent buckling initiate from the ends, and the cracks propagate continuously (Fig. 5.15f). The rachis shows strikingly different deformation behavior: the cortex and medulla show good bonding without obvious separation observed, the buckling at the end is more uniform, and there are microcracks in the wrinkled region, a toughening mechanism to absorb energy before failure (Fig. 5.15h). In addition, severely compressed rachis show axial cracking/splitting, but toughening mechanisms also appear, e.g. crack deflection, ligament bridging and fiber bridging (Fig. 5.15i). These indicate a significant increase in the buckling resistance and the toughness in the rachis due to the presence of medulla inside the cortex.

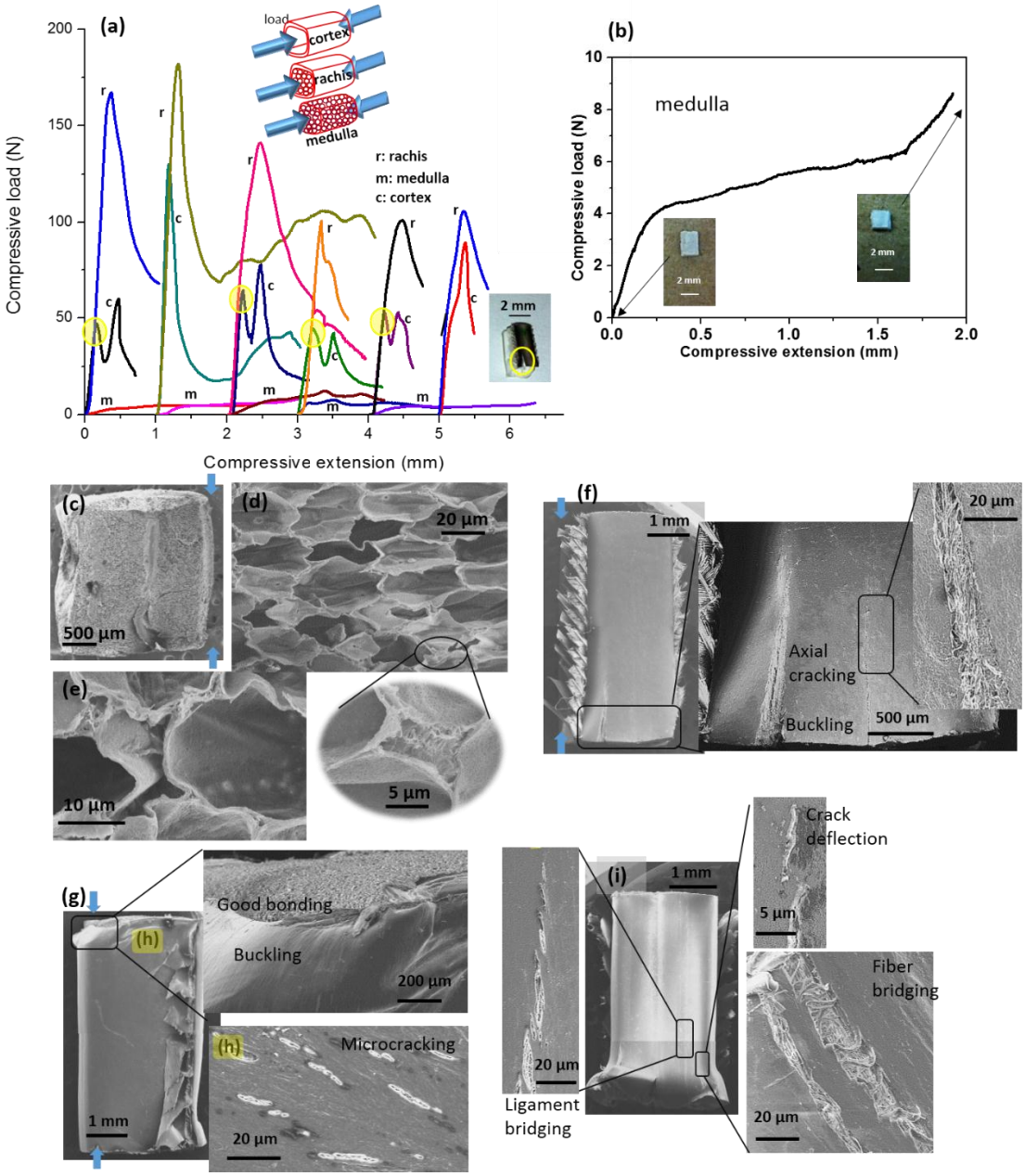

Figure 5.15 Axial compression. (a) Load-extension curves of the cortex, medulla and rachis specimens. The first load drop in cortex is due to axial splitting. (b) Load-extension curve of medulla. Scanning electron micrographs of (c) compressed medulla (blue arrows indicate loading direction), (d) medullary cells showing deformed shape, while the fibril bundles at the cell interface remain connected; (e) the deformed cell edges. (f) Compressed cortex with axial cracking and buckling. (g-h) Compressed rachis with uniform buckling and microcracking. (i-j) Severely compressed rachis with toughening mechanisms.

Table 5.4 Compressive results in axial and transverse loading orientations of cortex, medulla and rachis. Errors represent standard deviations of five valid measurements.

	Young's modulus (MPa)	Compressive strength (MPa)	Strain at strength
axial-cortex	1840 ±630	53.8 ±19.9	0.04 ±0.02
axial-medulla	18 ±12	1.3 ±0.3	0.18 ±0.07
axial-rachis	452 ±99	21.9 ±4.2	0.07 ±0.02
transverse-cortex	0.91 ±0.55	0.1 ±0.04	0.15 ±0.05
transverse -medulla	3.56 ±0.86	0.7 ±0.2	0.26 ±0.06
transverse -rachis	19.91 ±6.77	1.3 ±0.4	0.094 ±0.04

The cortex specimens resemble a hollow square tube, each four faces of which are rectangular plates, therefore the problem is formulated as buckling of plate elements of columns [318], [319]. The buckling stress, σ_{cort}, of axially compressed square tube is [318], [319]:

$$\sigma_{cort} = \frac{\pi^2 E}{3(1-\nu^2)}\frac{t^2}{a^2} \tag{17}$$

where *E*, *a*, *t* and ν are the elastic modulus, side width of the square tube, tube thickness, and Poisson's ratio. Inserting the corresponding values, 4 GPa, 2.17 mm, 0.142 mm and 0.3 from cortex-#3 specimen, we obtain buckling stress of 61.7 MPa, which is in strong agreement with experimental result, 58.1 MPa, compared to the only reported compression of feather cortex based on cylinder 136.5 MPa versus experimental value of 92.4 MPa [203].

The cellular medulla shows closed-cell foam structure, and the relative Young's modulus (modulus of medulla over that of solid) is obtained from Gibson and Ashby's equation [311]:

$$\frac{E_m}{E_s} = \varphi^2(\frac{\rho_m}{\rho_s})^2 + (1-\varphi)\frac{\rho_m}{\rho_s} + \frac{P_0(1-2\nu_m)}{E_s(1-\rho_m/\rho_s)} \quad (18)$$

where E_m and E_s are the Young's moduli of medulla and the solid cortex (m and s denote medulla and solid), ρ denotes density, φ and ν represent the volume fraction of solid contained in the medullary cell edges and the Poisson's ratio (0.33). P_0 is the gas pressure which is expected to be atmospheric pressure (~0.1 MPa). Calculating the relative density [311] by comparing the shape of cells from SEM images of medulla, one obtains $\frac{\rho_m}{\rho_s}$ equals 0.11. E_s is 4.0 Gpa from tensile tests on rachis cortex, φ is calculated by using the tetrakaidecahedra cells, being 0.703 [311]. Substituting these values, the estimated $\frac{E_m}{E_s}$ is 0.0386. This is larger than the ratio obtained from compressive measurements, 0.010 (0.018 GPa/1.84 GPa). It is possible that damage to the medulla was introduced during sample preparation. In addition, the cell walls are fibrous and porous, which should be weaker than the solid cell walls assumed in the equation. The relative modulus of seagull father rachis is larger than that of peacock's tail feather (0.00458) [203], but comparable to that of porcupine quills [250]. The seagull feather medulla show cell faces that may have thickness comparable to cell edges, and show fibrous struts at the most cell interfaces (Fig. 5.12c,d). These features stiffen the medulla to resist loading and deformation, thus generating a higher value of relative modulus.

The rachis, considered as a square tube filled with foam core under compressive loading, can be modeled as rectangular plates supported by an elastic foundation and subjected to in-plane axial compression [320], [321], shown in Fig. 5.16 with parameters.

Including effects of the foundation into the buckling of the plate and assuming a sinusoidal function for the deflection, the in-plane compressive force N_x is given as [321]:

$$N_x = D(\frac{\pi}{a})^2 \left[(\frac{ma}{l})^2 + 2 + (\frac{l}{ma})^2 \left\{1 + \frac{k}{D}(\frac{a}{\pi})^4\right\}\right] \quad (19)$$

where a and l are the side width and length of the square tube, $D = \frac{Et^3}{12(1-\nu^2)}$, k, m, are the flexural stiffness of plate, stiffness of foundation $k = \frac{2E_m}{a}$, number of half sine waves along the plate.

For a given square tube, the buckling force occurs at $\frac{\partial N_x}{\partial m} = 0$ with a certain integer value of $m = m^* = \frac{l}{a}\{1 + \frac{k}{D}(\frac{a}{\pi})^4\}^{\frac{1}{4}}$. Plugging this into Eqn. (19) we obtain the buckling load:

$$N_x = 2D(\frac{\pi}{a})^2 \left[\sqrt{1 + \frac{k}{D}(\frac{a}{\pi})^4} + 1\right] \quad (20)$$

This derived expression is in agreement with the equation presented by Moradi and Arwade [322] derived from Seide [323] Therefore, the buckling stress for a square tube with a foam core is:

$$\sigma_{cr}^{comp} = \frac{N_x}{a/2} = 4D\frac{\pi^2}{a^3}\left[\sqrt{1 + \frac{k}{D}(\frac{a}{\pi})^4} + 1\right] \quad (21)$$

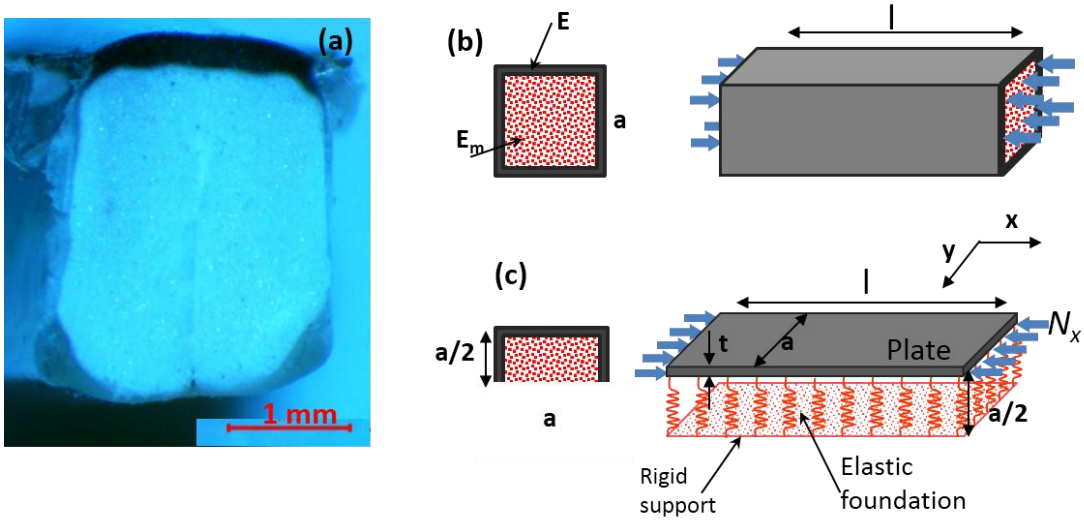

Figure 5.16 Axial compression model: (a) image of transverse section of one specimen; (b) schematics of the square tube with a foamy core under axial loading; (c) schematics of the plate supported by an elastic foundation under in-plane compressive loading.

Plugging in E=4.0 Gpa, ν=0.3, t=0.142 mm, a=2.17 mm, E_f=0.018 Gpa, one can calculate the buckling stress to be 12.71 MPa. Comparing with the experimental value, 27.3 MPa, the rachis shows significantly higher compressive buckling stress than that from Eqn. (21) (115% increase), indicating a synergistc effect in strengthening between the medulla and cortex. Firstly, Eqns. (19-21) are based on the Winkler foundation [324], which is composed of a series of isolated elastic springs without interactions between them (Fig. 5.16c). In the rachis, the medullary cells (the foundation) are closely connected by cell edges and faces and are strengthened by fibrous struts at cell interfaces. This creates an intrinsically strengthened foundation and thus an enhanced bracing of the medulla to the cortex, and thus stiffening in the rachis. In addition, the plate-on-elastic-foundation model (Fig. 5.16c) assumes a rigid attachment, which may detach easily with loading. In the rachis,

the interface of cortex and medulla shows fibrils well merged into each other (Fig. 5.12f), which leads to good bonding at the interface even after certain buckling deformation. The foamy medulla not only alleviates axial splitting but also introduces several crack shielding mechanisms, including microcracking, crack deflection, ligament and fiber bridging. All of these contribute to the enhanced strength and stiffness of the composite rachis.

5.3.5.2 Transverse compression

Fig. 5.17a shows the transverse compressive stress-strain curves of cortex, medulla and rachis, and values are in Table 5.4. All exhibit much lower modulus and strength than those loaded axially, the Young's moduli of cortex, medulla and rachis being 0.91, 3.56 and 19.91 MPa, respectively. This is understandable, since in the real natural system, the feather rachis bends and undergoes maximum axial compression on either the dorsal or ventral side frequently, whereas purely transverse compression is not that common. One salient feature is that the foamy medulla substantially increases the load bearing capacity of the cortex, the Young's modulus and strength increase by factors of 20 and 100, respectively, from cortex to rachis, indicating the significant strengthening effect of medulla transversely. It is also reported for the peacock tail feather rachis, the foamy medulla takes up to 96% of the total force, leaving 4% to the cortex [202].

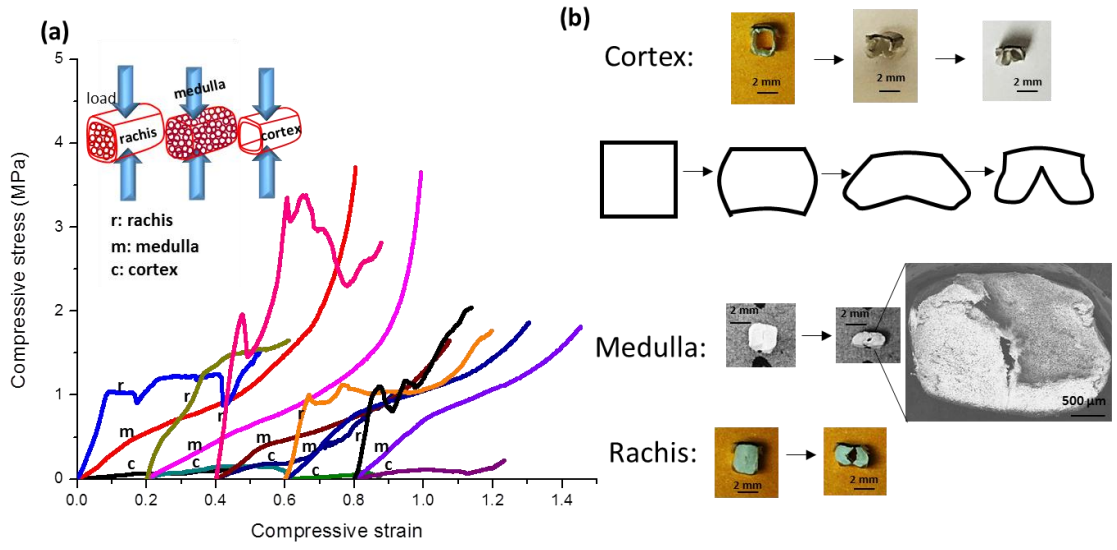

Figure 5.17 Transverse compression: (a) stress-strain curves of rachis, medulla and cortex specimens; (b) deformation mechanisms of cortex, medulla and rachis.

The cortex, under transverse compression, is mainly supported by thin lateral walls composed of crossed-fibers that are less stiff, and thus easily deform and buckle with increasing loading, as seen in Fig. 5.17b. The buckling load can be easily calculated from fundamental mechanics considering the compatibility of vertical and horizontal walls. While in axial compression, the load is supported by axial fibers in the thick dorsal and ventral cortex plus crossed fibers in lateral walls, thereby having much higher stiffness and strength. Nevertheless, no obvious cracking or breaking is observed; the lateral walls deform substantially and roll into the hollow core, which is different from the buckling and collapse of hollow square aluminum tubes [325].

The medulla shows similar stress-train behavior in transverse compression as axially, but exhibits significantly lower modulus (3.56 MPa) and strength (0.70 MPa). The

medullary cells are elliptical with similar dimensions in both transverse and longitudinal directions. Splitting along transverse septum dorsal-ventrally in the medulla occurs for most specimens (4/5), Fig. 5.17b, which is considered to account for the lower stiffness. The transverse septum (Fig. 5.3b) starts from ventral cortex towards, not reaching, the dorsal cortex; however, it is present throughout the height of axially compressed specimens, and buckles but not split (Fig. 5.15b). Therefore, the transverse septum exhibits a strengthening function axially, leading to stiffer and higher strength in axial compression. The composite rachis specimens, with much improved stiffness and strength, exhibit splitting along transverse septum (Fig. 5.17b), but remain connected at the dorsal and ventral cortex. It is concluded that the stiffening effect of medulla to the cortex is not deteriorate by the transverse splitting.

5.3.6 Flexural properties

5.3.6.1 Flexural behavior of the shaft as a composite beam

The feather shaft is a quintessential complex composite: a hollow cylinder at the calamus and a square shell enclosing a foam core at the rachis. The flexural stiffness of a specimen with constant cross section in four point bending is [301]:

$$\mathrm{K} = (EI)_{comp} = \frac{dF}{d\delta}\frac{a}{48}(3L^2 - 4a^2) \tag{22}$$

where F, δ are measured force and deflection, L is the support span, and a is the distance between one force application point and its nearest support point ($a=L/4$), with the subscript

representing composite. Considering the shaft as a composite beam (solid shell over porous core), the flexural stiffness can be derived as:

$$(EI)_{comp}=E_{comp}I_{comp}=E_{cort}I_{cort}+E_{medu}I_{medu} \quad (23)$$

E_{comp}, E_{cort}, E_{medu} and I_{comp}, I_{cort}, I_{medu} represent moduli of composite, cortex, medulla, and area moments of inertia of composite, cortex, medulla. For each shaft specimen, area moment of inertia of the section at the middle of the support length represents that of the specimen. By plugging in the compressive moduli of composite, cortex and medulla, and the area moments of inertia of cortex and medulla, we obtain I_{comp}:

$$I_{comp} = \frac{E_{cort}}{E_{comp}} I_{cort} + \frac{E_{medu}}{E_{comp}} I_{medu} \quad (24)$$

Theoretically, I_{cort} and I_{medu} should be both with respect to the neutral axis of the composite; however, due to the minor difference in centroid positions of rachis and medulla (~15 μm), I_{cort} and I_{medu} are calculated with respect to their own neutral axes (using SolidWorks by tracing the profiles of cortex and medulla imaged from the middle section of each specimen). The flexural modulus of the composite is:

$$E_{comp} = \frac{(EI)_{comp}}{I_{comp}} \quad (25)$$

And the flexural stress is:

$$\sigma = \frac{Mc}{I_{comp}} = \frac{Fac}{2I_{comp}} \quad (26)$$

c is half of the specimen depth. According the ASTM D6272, the flexural strain is:

$$\epsilon = 4.36\frac{2c\delta}{L^2} \quad (27)$$

The flexural stiffness, area moment of inertia and flexural modulus of shaft

specimen along the shaft length, calculated from experimental measurements using Eqns. (22-25), are shown Fig. 5.18. From the calamus to the distal shaft, the flexural stiffness decreases significantly (by 88%); the area moment of inertia increases by 9% at the middle shaft, but decreases clearly in the distal shaft (65%); the flexural modulus decreases in the middle shaft, but increases a little towards the distal shaft. This is drastically different from results if medulla is ignored and only the cortex is considered, in which flexural modulus and area moment of inertia decrease concurrently but flexural modulus increases from the calamus to the distal shaft. This indicates the influence of medulla on the flexural behavior of feather shaft. From the calamus to the middle shaft, the cortex tapers only slightly and is gradually filled with medulla. Therefore, the area moment of inertia increases little but flexural modulus decreases, from 5.81 to 1.44 GPa, since the flexural stiffness decreases. Towards the distal shaft, the cortex thickness decreases significantly (Fig. 5.18c), which overrules the filling of foamy medulla. Thus, the area moment of inertia decreases but the flexural modulus increases to 1.97 GPa. Values of area moments of inertia are consistently higher than those reported by Bachmann [200] and Purslow and Vincent [296], and flexural moduli vary differently from those tested in cantilever bending [200], due more to the incorporation of the medulla in this work.

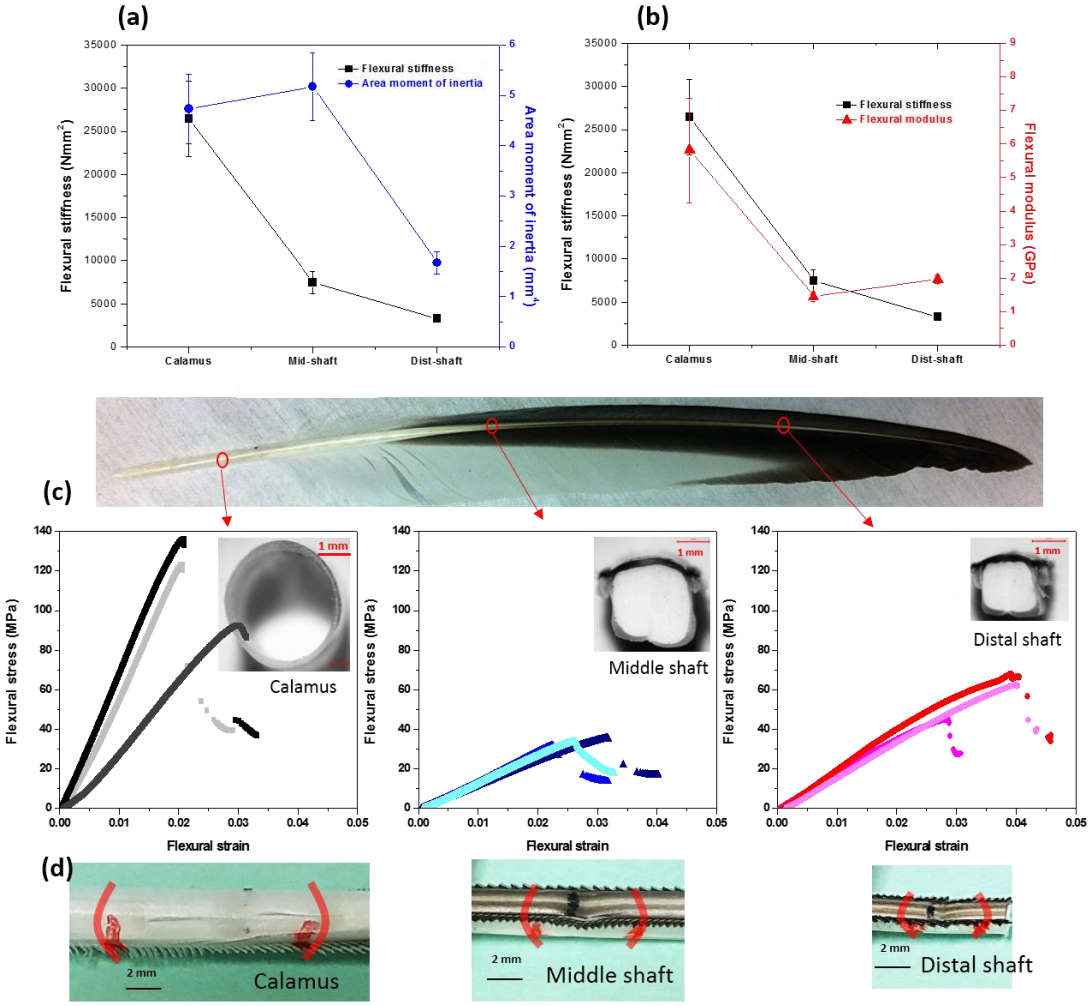

Figure 5.18 Flexural responses of seagull feather shaft: (a) flexural stiffness and area moment of inertia along the shaft length; (b) flexural stiffness and modulus along the shaft length; (c) flexural stress-strain curves of the calamus, middle shaft and the distal shaft, with the sectional views; (d) local buckling failure during flexure at the calamus, middle shaft and distal shaft.

Table 5.5 Four point bending results of the feather shaft (errors represent standard deviations).

	Flexural stiffness (Nmm^2)	Area moment of inertia (mm^4)	Flexural modulus (GPa)	Flexural strength (MPa)
Calamus	26466 ±4350	4.73 ±0.69	5.81 ±1.55	117.1 ±18.3
Mid-shaft	7465 ±1329	5.17 ±0.67	1.44 ±0.13	33.7 ±1.6
Dis-shaft	3259 ±288	1.67 ±0.22	1.97 ±0.12	58.3 ±9.8

Table 5.6 Flexural properties normalized by density along the feather shaft.

	Local density (kg/m^3)	Modulus/density ($N{\cdot}m/kg=m^2/s^2$)	Strength/density ($N{\cdot}m/kg=m^2/s^2$)
Calamus	ρ_s =1.2X10^3	4.9X10^6	98.4X10^3
Mid-shaft	0.320ρ_s =0.38X10^3	3.8X10^6	88.7X10^3
Dis-shaft	0.341ρ_s =0.40X10^3	4.9X10^6	145.7X10^3

Figure 5.18d shows the flexural stress strain curves of shaft segments along the length. The calamus specimens have a higher flexural stiffness and strength (117.1 MPa), than the distal shaft (58.3 MPa) and the middle shaft (33.7 MPa). These are the first reported failure strengths of feather shaft in flexure as a function of position.

It seems, from Table 5.5, that the flexural properties decrease from the calamus to the distal shaft. However, taking into consideration density, we reveal that the flexural efficiency (influenced by the sectional shape/material distribution and the amount of material), flexural modulus and strength normalized by local densities, vary differently along the shaft length. The local density can be calculated:

$$\rho = \rho_s f_s + \rho_m f_m \tag{28}$$

where f_s, f_m are averaged area fractions of the solid cortex and medulla at the calamus, middle shaft and distal shaft. At the calamus, the density equals that of the solid cortex (ρ_s); for the rachis region, $\frac{\rho_m}{\rho_s}$=0.11 from Section 5.3.5.1. Since $\rho_m = 1 - \rho_s$, $\rho = 0.89\rho_s f_s + 0.11\rho_s$. The area fractions of cortex along the shaft length, f_s, calculated by obtaining areas of cortex and medulla at each position using Solidworks via tracing profiles, are 1.0, 0.236, 0.260. Using these, the densities at the middle and distal shaft are 0.320ρ_s and

$0.341\rho_s$, respectively. By measuring the geometry of the calamus via microscope and the weight, ρ_s =1.2 g/cm^3; then the locally specific flexural moduli remain almost the same from the calamus to the distal shaft, being 4.9 X10^6 N·m/kg, while the specific flexural strength increases significantly, from 98.4X10^3 to 145.7 X10^3 N·m/kg (by 48%), listed in Table 5.6. This shows that in spite of the conspicuous decrease in all apparent flexural parameters (Table 5.5) from the calamus to the distal shaft, the flexural efficiency increases, a distinguishing feature that symbolizes the design nature of feather shaft: the substantial tapering of shaft to reduce profile drag is subtly compensated through mechanical efficiency, e.g. the shape factor changing from circular to square, the increasing amount of cortical axial fibers and the crossed-fibers, and the presence of the medulla stiffening the cortex and lightening the shaft.

5.3.6.2 Flexural failure mode

The feather shaft specimens fail in four point bending by local buckling on the compressive side (dorsal cortex), seen as the load drops on the flexural stress-strain curves (Fig. 5.18c). The calamus specimens collapse suddenly with significant axial cracking (Fig. 5.18d), showing about 40% load drop. The middle shaft, though with lower buckling strength, shows much alleviated load drop (~18%) and an indent on the dorsal surface. The distal shaft exhibits similar failure with a higher buckling strength and ~21% load drop. Therefore, filling the core of cortex with medulla is effective in reducing the risk of sudden

failure, and thus preventing the catastrophic collapse of the structure, which is more likely to be experienced by the distal shaft which does not have a supporting skin.

The feather shaft shows different mechanisms accompanying the flexural failure along the shaft length. The calamus exhibits several extensive axial cracks with slight fiber bridging and crack deflection (Fig. 5.19a,b), The middle shaft shows numerous transverse tracings on the dorsal buckled region caused by the compressive stresses experienced locally during flexure (Fig. 5.19c), typifying local buckling. A small number of fibers at the edge rupture, but are still held by the internal foamy medulla (Fig. 5.19d). In addition, the middle shaft, supported by the inner medulla, are evidence for crack deflection (Fig. 5.19e), uncracked ligament bridging and fiber bridging (Fig. 13f-g), and abundant microcracking (Fig. 5.19h) near the buckled region. The distal shaft shows similar deformation features near the buckled region, e.g. transverse tracings, microcracking, crack deflection and uncracked ligament bridging (Fig. 5.19i-j). These notable toughening mechanisms contribute to the load bearing capacity of the shaft and enhance the energy absorbance through allowing a considerate amount of deformation before failure; they originate from the inner foamy medulla which shares the forces and holds the fibers composing the solid cortex together, analogous to the toughening mechanisms observed in axial compression, thus preventing extensive axial cracking and splitting of the cortex in the calamus.

Another remarkable feature is the outstanding shape recovery of medulla even after

the shaft fails/buckles. Fig. 5.20 shows the sectional views of buckled rachis specimens. Under the buckled dorsal cortex region (the indent on the dorsal surface, Fig. 5.20a), the medullary cells throughout the inside space show the original normal shape and the intact strengthening fibrous struts between cell walls (Fig. 5.20c). For severely buckled rachis specimen which involves a small amount of ruptured fibers held by medullary cells, observation in higher magnification reveals that the seemingly separation of medulla along cortex is rather shallow (less than one cell diameter) and the medullary cells remain connected inside (Fig. 5.20e). This property arises from the hierarchical fibrous and porous structure being exceptionally deformable, recoverable and lightweight, which would be hardly obtained by other biological cellular structures with solid cell walls, e.g. porcupine quills. In addition, along the interface the cellular medulla and the solid cortex still bond very well, as the fibrils from both merge into each other well, seen in Fig. 5.20d (except only separation at ventral region in maximum tensile strain in one specimen), which ensures desired support from the medulla to the cortex. This retention of structural integrity lends support for the mechanism of shape recovery reported by Liu et al. [203].

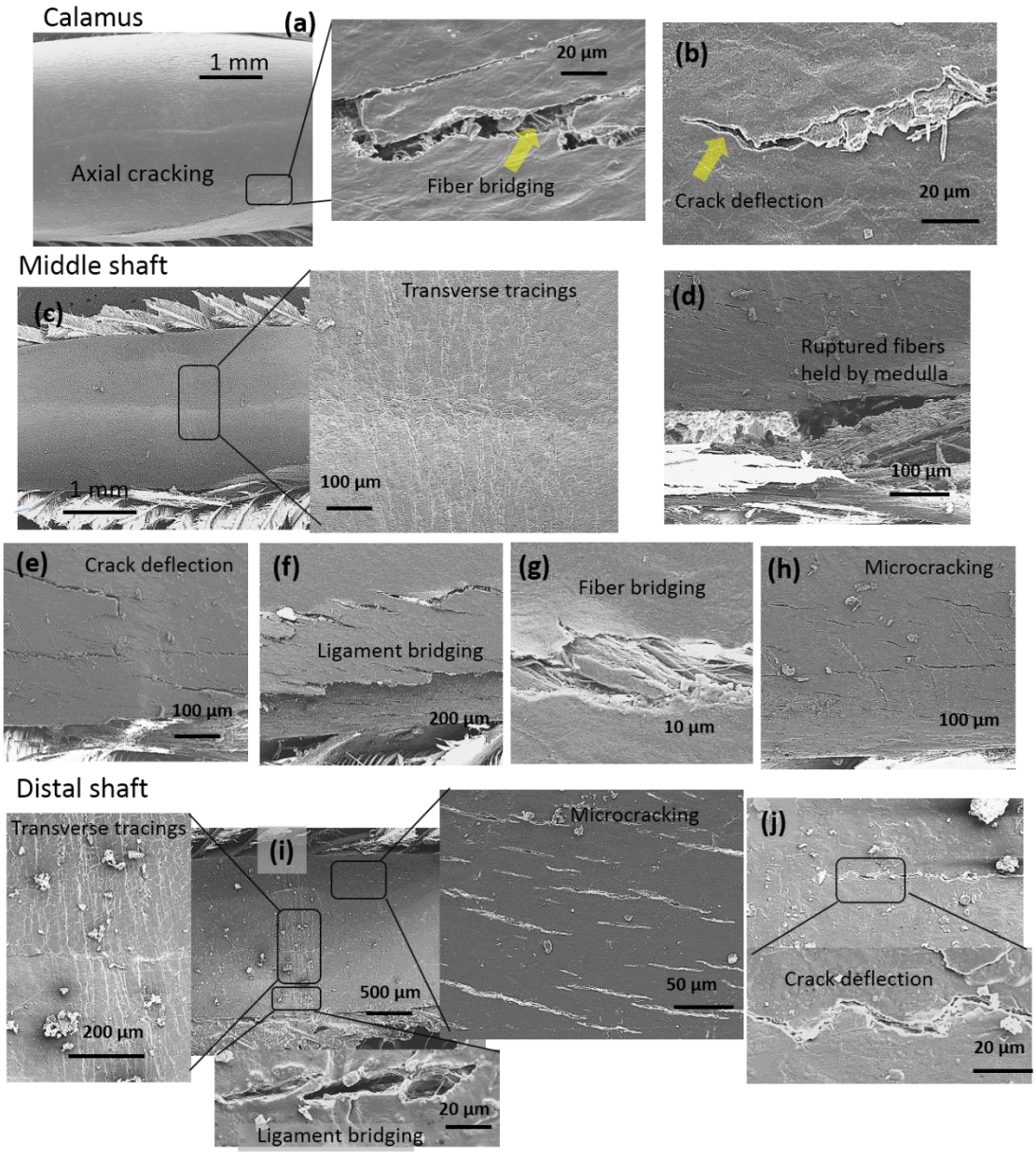

Figure 5.19 The dorsal views of the buckled feather shaft along the shaft length: (a,b) the calamus, showing significant axial cracking and minor crack deflection and fiber bridging; (c-h) the middle shaft, showing transverse tracings at the buckled region, and ruptured fibers held by the medulla, crack deflection, ligament and fiber bridging, and microcracking; (i-j) the distal shaft with similar features as those in the middle shaft.

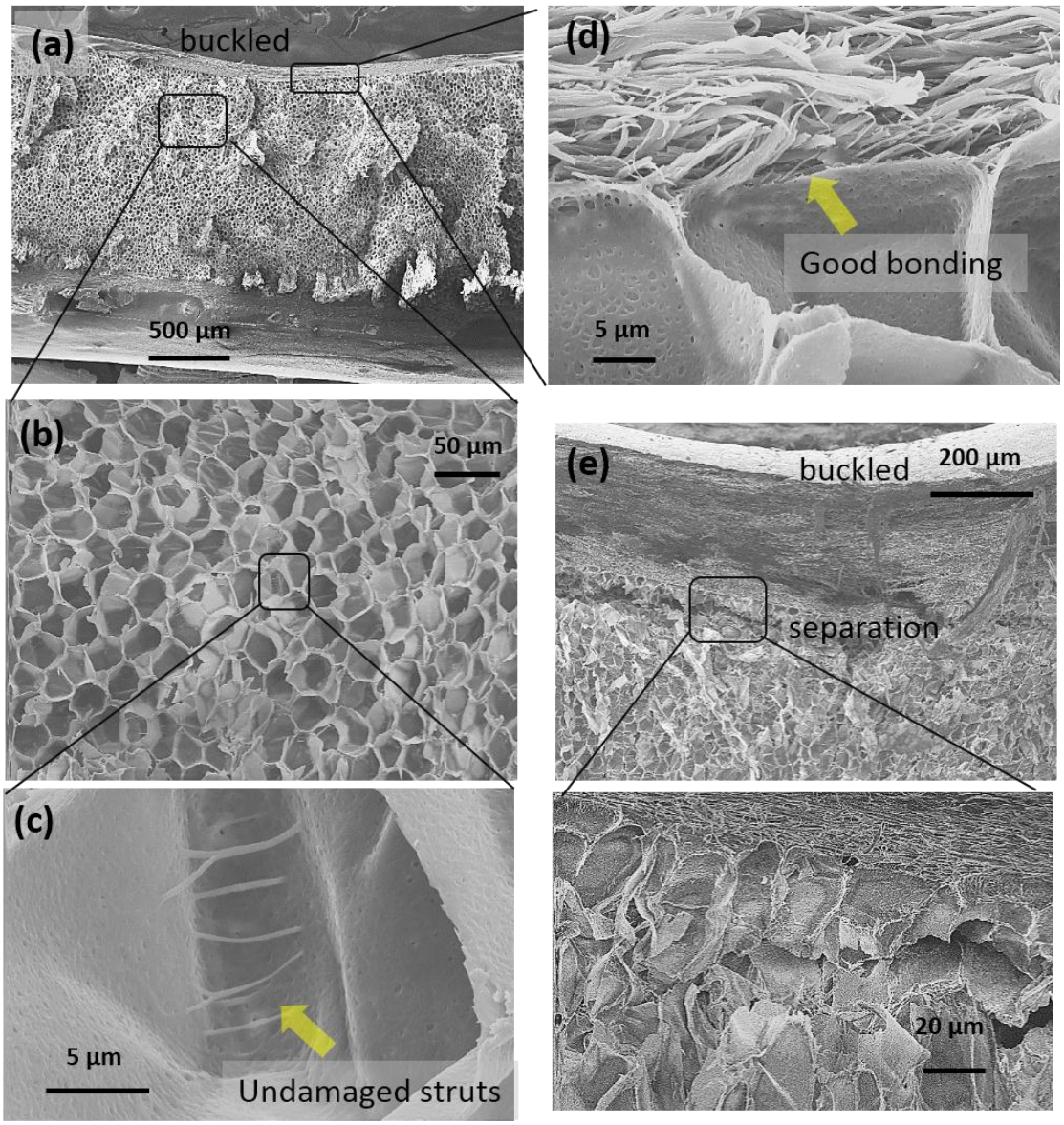

Figure 5.20 Sectional views of the buckled feather rachis: (a,b) the medullary cells show mostly original shape and show undamaged fibrous struts at inter-cell walls (c). (d) The bonding between medulla and cortex remains well. (e) The apparent separation within foamy medulla (below the cortex) is indeed very shallow, and the cells remain connected

5.4 Thoughts on bioinspired designs

The feather shaft shows impressive structural features and superior mechanical properties, which can provide useful knowledge in developing new materials and inspire

novel designs for our future. On the one hand, the sandwich structure, featuring a changing shape changing and complex fibrous solid cortex enclosing a hierarchically porous core, produces a structure that is lightweight, strong and stiff, yet reasonably flexible and reliable, properties that have always been the goal of many modern structural materials. In addition, the shape design and structure-property knowledge have value in developing functional materials for aerospace and land vehicle applications. Especially fascinating is the topic of autonomous cars, aerial vehicles, e.g. personal aircraft and/or skycars, drones, which are thought to drastically change our life and work in next generations [326]. Lightweight, strong and stiff, and renewable materials with ingenious shape designs, resembling the feather shaft, show a great potential for applications.

Additionally, the fibrous medulla inside the rachis having hierarchical porosities could provide useful guidance in developing deformable and recoverable scaffolds for biomedical applications. For instance, three dimensional porous scaffolds for culturing cells need to have interconnected network and mechanical properties matching the real tissue [327], which may be achieved through building up fibrous cell walls with nano- and micro-scale porosities using fibrils that have hierarchical structure.

5.5 Summary

The feather shaft represents a naturally optimized flight material, being strong and stiff yet with reasonable flexibility at a minimal weight penalty. The flexural property, being the primary concern, is ingeniously modulated with the tapering along the shaft

length through designs in both the structure and material, thus fulfilling all the local mechanical needs along the shaft length. It shows a shape factor, involving the cortex shape change from circular to square which increases bending stiffness per unit area and the ability to restrict sectional shape change, and a complex fibrous layered structure of cortex, consisting of differently aligned fibers which increase the longitudinal modulus and dorsal-ventral flexural flexibility; therefore, both lead to a structure that has increased flexural bending stiffness per unit area towards the distal end, compensating for the significant reduction in area moment of inertia due to the attenuation of cortex towards the distal shaft. The foam filling of cortex, medulla, in the rachis introduces toughening mechanisms, e.g. crack deflection, microcracking, and strengthens the rachis under axial compression. Bending behaviors of the whole shaft segments along the length, analyzed as composite beams, reveal that the density-normalized flexural stiffness is almost the same, and the flexural modulus increases by 48% towards the distal shaft. Although the foamy medulla fills the inside space and the shaft substantially tapers towards the distal end, which causes the decrease in area moment of inertia and flexural modulus, the specific flexural properties are modulated with respect to weight, indicating, again, the ingenuity of the feather shaft structure.

The shape factor, layered fibrous cortical structure and the composite design would provide invaluable insights in developing new lightweight but strong and stiff materials/structures highlighted for aircraft applications, e.g. unmanned aerial vehicles,

future commercial/personal skycars, and the shape design of airplanes. In addition, the hierarchical porous and fibrous medulla has potential in developing new porous structures for tissue engineering, such as biomedical scaffolds.

Acknowledgements

Chapter 5, in part, comes from the manuscripts: Wang B, Meyers M. (2016) “Light like a feather: a fibrous natural composite with a shape factor changing from round to square”; and Wang B, Meyers M. (2016) “Seagull feather shaft: the correlation between structure and mechanical responses”. The dissertation author is the first author of these manuscripts.

6 Conclusions

6.1 Concluding remarks

Keratins represent the most abundant structural filament-forming proteins in the epithelial cells, being chemically unreactive and mechanically robust, and constitute keratinous materials that are epidermal appendages among the toughest biological materials. They show diverse morphologies including fibers, solids, sandwiched structures, and serve a variety of important mechanical functions, e.g. stratum corneum as diffusion barrier, pangolin scales as body armor, hooves as energy-absorption and impact-resistance, horns as piercing opponents, feathers as withstanding repeated stress and aerodynamic forces, quills resisting buckling and penetration, and baleens enduring consistent flexure. As curiosity being the nature of humans, we are always fascinated about how these tissues, through their specialized structural organizations, fulfill the mechanical functions, of which knowledge could help people know more about the biological system we are living in. More importantly, from biomimetics perspective, a comprehensive understanding of the biochemistry, structure and mechanical properties of keratins and keratinous materials, provides a resourceful database and invaluable design principles for the development of new bioinspired structures. Of these, two keratinous materials, pangolin scales and the feather shaft, stand out with interesting mechanical functions originated from the hierarchical structures.

6.2 Pangolin scales

The distinct structural features and mechanical properties of pangolin scales, a unique protection strategy for a mammal, are uncovered focusing on understanding the design and protective functions. The following conclusions are drawn from characterization and testing:

- The overlap mechanism of both African tree (arboreal) and Chinese (ground) pangolin scales is that each scale sits in center of neighboring scales surrounding it in a hexagonal pattern; for each scale, the internal surface partially covers three lower scales, and the external surface is partially covered by upper three scales. The overlapping ratios on both the internal and external surfaces of Chinese and African tree pangolin scales are different due to the different shapes and dimensions.
- African tree and Chinese pangolin scales, composed of keratinized cells, show similar structure and mechanical properties. The scales have a cuticle structure composed of 3~5 layers of loosely attached keratinized cells with 40~70 μm in diameter and 0.5~1 μm in thickness. The interior structure consists of three regions: a dorsal region of flattened cells (diameter about ~30 μm and thickness 2~4 μm) forming crossed lamellae parallel to scale surface, a middle region of tilted and less flattened cells usually with larger dimensions (3~8 μm thick) constituting lamellae, and a ventral region that is similar to the dorsal region. At a still lower spatial scale, the nanostructure is comprised of filaments with 3-5 nm diameter. Each lamella is comprised of one layer of cells. Tensile deformation to failure

reveals crossed fibers between lamellae. X-ray diffraction patterns reveal the presence of α-helical structure and possible β-sheet, and the microfibrils are crossed in a range of directions. At the nanoscale, the scales show an interlocking interface between lamellae, which results from the suture-like cell membrane complex between keratinized cells.

- The tensile, compression and microindentation responses examined along different loading orientations reveal transverse isotropy in the plane of scale surface (E~1 GPa; ultimate strength ~ 70 MPa at 10^{-3} /s) and a slightly higher strength along the scale thickness direction, correlating with the structure of crossed fibers and lamellae and keratinized cells.

- The keratin in the pangolin scales is strain-rate dependent, characteristic of a viscoelastic material, which become stiffer and stronger at fast loading to combat impacts (at 10^{-1} /s, the Young's modulus and tensile strength reach 1.5 GPa and 108.7 MPa, respectively), and are able to absorb large amount of energy when loaded at low strain rate (at 10^{-5} /s). The strain rate sensitivity values are 0.07 and 0.08 for African tree and Chinese pangolin scales, typical of polymers and hair keratin. The fracture mode changes from fiber tear and rupture, lamella pull-out, to trans-lamellar fracture with increasing strain rate, akin to a ductile-to-brittle transition. Hydration plays an important role in mechanical behavior, leading to significantly decreased Young's modulus (~0.27 GPa) and tensile strength (~34 MPa).

The structural features and the corresponding mechanical properties of pangolin scales are distinct from other typical keratinous materials, because of the specific functionalities required in the protection. The knowledge gained in this investigation will help advance our understanding of the biological solutions in designing materials and promote more efficient bioinspired structures.

6.3 Feather shaft

The feather shaft represents a naturally refined functional material, whose structure has been oversimplified historically. The current work provides novel findings and quantitative analysis through a thorough study on the flight feather shafts, advancing our knowledge in feather biomechanics and promoting the development of innovative materials. Significant accomplishments are the following:

- The shaft design involves an ingenious combination of a solid cortex, which features a shape factor and differentially aligned fibers, and a porous medullary core that is also fibrous and has hierarchical porosities; both work synergistically leading to a lightweight, strong and stiff, yet reasonably flexible structure.
- The shaft cortex shows a complex hierarchical structure in multiple both length and space scales: the cortex, about 2 mm wide, is composed of keratinized cells about 30~50 μm long and 1 μm thick separated by a 25 nm thick cell membrane complex. Inside the cells are fibers about 5 μm, which are composed of macrofibrils measuring about 50~300 nm in diameter surrounded by intermacrofibrillar material observed through transverse

electron microscope. The macrofibrils are further comprised of β-keratin filaments (~3 nm) embedded in electron-dense matrix material. The fibers and fibrils vary in alignment depending on both the specific cortex regions and the position along the shaft length, including axial, circumferential and crossed orientations, verified through nanoindenation.

- The tensile responses of cortex strips of dorsal, lateral and ventral regions along the shaft length reveal an increasing Young's modulus in dorsal region towards the distal shaft, but consistently lower modulus in lateral walls throughout rachis, which corroborates the fibrous anisotropic structure. Transverse straight fracture due to rupture of axial fibers and axial splitting are the dominant mechanisms in the dorsal and ventral regions, accompanying crack deflection and fiber bridging, whereas the lateral walls show a zigzag fracture because of crossed-fibers.
- Axial compression reveals that the medulla prevents axial splitting and sudden load drop of cortex and introduces toughening mechanisms including good interfacial bonding, crack deflection and crack shielding. The cortex in axial compression is accurately modeled by a square tube model; a foam-filled square tube simulating the rachis reveals a synergy between the medulla and cortex in strengthening. Transverse compression indicates a substantial load bearing capacity enhancement due to the presence of medulla, by a factor of ~100.
- Four-point bending tests along the shaft length, analyzed accurately as a composite beam incorporating the medulla, generate decreasing flexural stiffness, area moment of

inertia, flexural modulus and strength towards the distal shaft. Nevertheless, the specific flexural stiffness almost remains the same value, and the specific flexural strength increases by 48%. Flexural failure occurs by local buckling on the compressive side, and filling the cortex with a foamy medulla prevents axial crack from propagating and introduces additional toughening mechanisms, e.g. crack deflection, uncracked ligament bridging, fiber bridging and microcracking.

7 Future work

We started investigating one marine keratin, the whale baleen, which shows interesting tubular structure but is mostly functioning as filtering apparatus enduring dynamic flexure, and the correlation between the structure and mechanical properties will be included as future work.

In addition, the pangolin scales show significant strengthening in preliminary dynamic compression test (Split-Hokinson Pressure Bar), and more impact tests will be conducted on pangolin scales. Also considering the crossed-fiber structure, the fracture behavior is another interesting aspect to study, and fracture toughness tests are in progress now.

For the feather shaft, the dissertation focuses mostly on flight feathers from volant birds; comparative study of flightless and flight feathers would be an interesting topic. Additionally, the layered fibrous structure of shaft cortex, being lightweight and stiff, can be reproduced using some novel manufacturing techniques, e.g. nano 3D printing, and the massive fabrication for potential application in aerial vehicles should be studied. While new porous scaffolds inspired by feather medulla are also worthy to try.

References

[1] M. A. Meyers, P.-Y. Chen, A. Y.-M. Lin, and Y. Seki, “Biological materials: Structure and mechanical properties,” *Prog. Mater. Sci.*, vol. 53, no. 1, pp. 1–206, 2008.

[2] W. Barthlott and C. Neinhuis, “Purity of the sacred lotus, or escape from contamination in biological surfaces,” *Planta*, vol. 202, no. 1, pp. 1–8, 1997.

[3] J. F. V Vincent, O. a Bogatyreva, N. R. Bogatyrev, A. Bowyer, and A.-K. Pahl, “Biomimetics: its practice and theory.,” *J. R. Soc. Interface*, vol. 3, no. 9, pp. 471–482, 2006.

[4] K. Autumn, M. Sitti, Y. a Liang, A. M. Peattie, W. R. Hansen, S. Sponberg, T. W. Kenny, R. Fearing, J. N. Israelachvili, and R. J. Full, “Evidence for van der Waals adhesion in gecko setae,” *Proc. Natl. Acad. Sci. U. S. A.*, vol. 99, no. 19, pp. 12252–12256, 2002.

[5] M. Sarikaya, “An introduction to biomimetics: a structural viewpoint.,” *Microsc. Res. Tech.*, vol. 27, no. 5, pp. 360–375, 1994.

[6] A. V. Srinivasan, G. K. Haritos, and F. L. Hedberg, “Biomimetics: Advancing Man-Made Materials Through Guidance From Nature,” *Appl. Mech. Rev.*, vol. 44, no. 11, p. 463, 1991.

[7] J. F. V Vincent, *Structural Biomaterials*, Revised ed. Princeton University Press, 1990.

[8] E. Baer, A. Hiltner, and R. J. Morgan, “Biological and Synthetic Hierarchical Composites,” *Phys. Today*, vol. 45, no. 10, p. 60, 1992.

[9] E. Arzt, “Biological and artificial attachment devices: Lessons for materials scientists from flies and geckos,” *Mater. Sci. Eng. C*, vol. 26, no. 8, pp. 1245–1250, 2006.

[10] P. Y. Chen, J. McKittrick, and M. A. Meyers, “Biological materials: functional adaptations and bioinspired designs,” *Prog. Mater. Sci.*, vol. 57, no. 8, pp. 1492–1704, 2012.

[11] D. Thompson, *On growth and form*. Cambridge: Cambridge University Press, 1917.

[12] L. J. Gibson and M. F. Ashby, *Cellular solids: structures and properties*. New York: Oxford: Pergamon Press, 1988.

[13] J. Currey, *Bones: Structure and mechanics.* New Jersey: Princeton University Press, 2002.

[14] S. A. Wainwright, W. D. Biggs, J. D. Currey, and J. M. Gosline, *Mechanical design in organisms*. New York: Halsted Press, John Wiley & Sons, INc., 1976.

[15] M. a Meyers, P.-Y. Chen, M. I. Lopez, Y. Seki, and A. Y. M. Lin, "Biological materials: a materials science approach.," *J. Mech. Behav. Biomed. Mater.*, vol. 4, no. 5, pp. 626–657, 2011.

[16] S. Weiner and L. Addadi, "Design strategies in mineralized biological materials," *J. Mater. Chem.*, vol. 7, no. 5, pp. 689–702, 1997.

[17] R. Wang and H. S. Gupta, "Deformation and fracture mechanisms of bone and nacre," *Annu. Rev. Mater. Res.*, vol. 41, pp. 41–73, 2011.

[18] P. Fratzl and R. Weinkamer, "Nature's hierarchical materials," *Prog. Mater. Sci.*, vol. 52, no. 8, pp. 1263–1334, 2007.

[19] M. Elices, *Structural Biological Materials design and structure-property relationships*. Elsevier Science Ltd., 2000.

[20] M. A. Meyers and P.-Y. Chen, *Biological materials science*. Cambridge, UK: Cambridge University Press, 2014.

[21] K. O. Stetter, "Extremophiles and their adaptation to hot environments," *FEBS Lett.*, vol. 452, no. 1–2, pp. 22–25, 1999.

[22] F. X. Sicot, M. Mesnage, M. Masselot, J. Y. Exposito, R. Garrone, J. Deutsch, and F. Gaill, "Molecular adaptation to an extreme environment: origin of the thermal stability of the pompeii worm collagen.," *J. Mol. Biol.*, vol. 302, no. 4, pp. 811–20, 2000.

[23] K. Chawla, *Composite Materials: Science and Engineering*, 3rd ed. Springer, 2012.

[24] L. J. Gibson, M. F. Ashby, and B. A. Harley, *Cellular Materials in Nature and Medicine*. Cambridge, UK: Cambridge University Press, 2010.

[25] U. G. K. Wegst and M. F. Ashby, "The mechanical efficiency of natural materials," *Philos. Mag.*, vol. 84, no. 21, pp. 2167–2186, 2004.

[26] M. F. Ashby, L. J. Gibson, U. Wegst, and R. Olive, "The Mechanical Properties of Natural Materials. I. Material Property Charts," *Proc. R. Soc. A Math. Phys. Eng. Sci.*, vol. 450, no. 1938, pp. 123–140, 1995.

[27] J. F. . Vincent, "Biomimetic materials," *J. Mater. Res.*, vol. 23, no. 12, pp. 3140–3147, 2008.

[28] J. W. C. Dunlop and P. Fratzl, "Biological Composites," *Annu. Rev. Mater. Res.*, vol. 40, no. 1, pp. 1–24, 2010.

[29] P. Harrison, P. Artymiuk, G. Ford, D. Lawson, J. Smith, A. Treffry, and J. White, "Ferritin: Function and structural design of an iron-storage protein," in *Biomineralization: Chemical and Biochemical Perspectives*, 1989, pp. 257–294.

[30] R. Blakemore, "Magnetotactic bacteria," *Annu. Rev. Microbiol.*, vol. 36, pp. 217–238, 1982.

[31] M. I. Lopez, P. Y. Chen, J. McKittrick, and M. A. Meyers, "Growth of nacre in abalone: Seasonal and feeding effects," *Mater. Sci. Eng. C*, vol. 31, no. 4, pp. 716–723, 2011.

[32] A. Y. M. Lin, P. Y. Chen, and M. A. Meyers, "The growth of nacre in the abalone shell," *Acta Biomater.*, vol. 4, no. 1, pp. 131–138, 2008.

[33] M. Sarikaya and I. Aksay, "Nacre: Properties, crystallography, morphology, and formation," in *Design and processing of materials by biomimetics*, M. Sarikaya and I. Aksay, Eds. Washington, DC: American Institute of Physics Press, 1993, pp. 35–86.

[34] E. Baer, "Advanced polymers," *Sci. Am.*, vol. 255, no. 4, pp. 178–190, 1986.

[35] E. Baer, J. Cassidy, and A. Hiltner, "Hierarchical structure of collagen and its relationship to the physical properties of tendon," in *Collagen: Biochemistry, biomechanics, biotechnology*, M. Nimni, Ed. New York: CRC Press, 1988, pp. 177–

199.

[36] J. M. Gosline, M. E. DeMont, and M. W. Denny, “The structure and properties of spider silk,” *Endeavour*, vol. 10, no. 1, pp. 37–43, 1986.

[37] F. Vollrath, “Strength and structure of spiders’ silks.,” *Rev. Mol. Biotechnol.*, vol. 74, no. 2, pp. 67–83, 2000.

[38] W. E. Morton and J. W. . Hearle, *Physical Properties of Textile Fibres*, 3rd ed. Manchester, UK: The Textile Institute, 1993.

[39] P. A. Coulombe and M. B. Omary, “‘Hard’and ‘soft’principles defining the structure, function and regulation of keratin intermediate filaments,” *Curr. Opin. Cell Biol.*, vol. 14, no. 1, pp. 110–122, 2002.

[40] J. McKittrick, P. Y. Chen, S. G. Bodde, W. Yang, E. E. Novitskaya, and M. a. Meyers, “The structure, functions, and mechanical properties of keratin,” *Jom*, vol. 64, no. 4, pp. 449–468, 2012.

[41] Z. Q. Liu, D. Jiao, Z. Y. Weng, and Z. F. Zhang, “Water-assisted self-healing and property recovery in a natural dermal armor of pangolin scales,” *J. Mech. Behav. Biomed. Mater.*, vol. 56, pp. 14–22, 2016.

[42] Z. Q. Liu, D. Jiao, Z. Y. Weng, and Z. F. Zhang, “Structure and mechanical behaviors of protective armored pangolin scales and effects of hydration and orientation,” *J. Mech. Behav. Biomed. Mater.*, vol. 56, pp. 165–174, 2016.

[43] da V. Leonardo, “Codex on the Flight of Birds,” *held Bibl. R. Turin, Italy*, 1505.

[44] K. Y. Wang, *The swallows make nests by clay: birds and their breeding*. Changchun, China: Changchun Press, 1998.

[45] R. H. C. Bonser and P. P. Purslow, “The Young’s modulus of feather keratin,” *J. Exp. Biol.*, vol. 1033, no. 4, pp. 1029–1033, 1995.

[46] H. Herrmann and U. Aebi, “Intermediate filaments: molecular structure, assembly mechanism, and integration into functionally distinct intracellular Scaffolds.,” *Annu. Rev. Biochem.*, vol. 73, pp. 749–789, 2004.

[47] J. Schweizer, P. E. Bowden, P. A. Coulombe, L. Langbein, E. B. Lane, T. M. Magin,

L. Maltais, M. B. Omary, D. A. D. Parry, M. A. Rogers, and M. W. Wright, “New consensus nomenclature for mammalian keratins,” *J. Cell Biol.*, vol. 174, no. 2, pp. 169–174, 2006.

[48] R. D. B. Fraser, T. P. MacRae, and G. E. Rogers, *Keratins: their composition, structure and biosynthesis*. Charles C Thomas, 1972.

[49] R. I. C. Spearman, “On the nature of the horny scales of the pangolin,” *J. Linn. Soc. Zool.*, vol. 46, no. 310, pp. 267–273, 1967.

[50] W. T. Astbury and A. Street, “X-Ray Studies of the Structure of Hair, Wool, and Related Fibres. I. General,” *Phil Trans R Soc L. A*, vol. 230, no. 681–693, pp. 75–101, 1932.

[51] W. T. Astbury and H. J. Woods, “X ray studies of the structure of hair, wool, and related fibres. II. The molecular structure and elastic properties of hair keratin,” *Phil Trans R Soc L. B*, vol. 114, no. 788, pp. 314–316, 1934.

[52] R. D. B. Fraser, T. P. MacRae, D. A. D. Parry, and E. Suzuki, “The structure of beta-keratin,” *Polymer (Guildf).*, vol. 10, pp. 810–826, 1969.

[53] R. D. B. Fraser and T. P. MacRae, “The structure of a-keratin,” *Structure*, vol. 14, no. September 1972, pp. 61–67, 1973.

[54] R. D. B. Fraser and D. A. D. Parry, “The structural basis of the filament-matrix texture in the avian/reptilian group of hard β-keratins,” *J. Struct. Biol.*, vol. 173, no. 2, pp. 391–405, 2011.

[55] D. A. D. Parry, “Personal communications.” 2014.

[56] H. Lodish, A. Berk, S. L. Zipursky, P. Matsudaira, D. Baltimore, and J. Darnell, *Molecular cell biology*, 4th ed. New York: W. H. Freeman and Company, 2000.

[57] R. S. Bear and H. J. Rugo, “The results of x-ray diffraction studies on keratin fibers.,” *Ann. N. Y. Acad. Sci.*, vol. 53, no. 3, pp. 627–648, 1951.

[58] B. Busson, F. Briki, and J. Doucet, “Side-chains configurations in coiled coils revealed by the 5.15-A meridional reflection on hard alpha-keratin X-ray diffraction patterns.,” *J. Struct. Biol.*, vol. 125, no. 1, pp. 1–10, 1999.

[59] A. Giroud and C. P. Leblond, “The keratinization of epidermis and its derivatives, especially the hair, as shown by x-ray diffraction and histochemical studies.,” *Ann. N. Y. Acad. Sci.*, vol. 53, no. 3, pp. 613–626, 1951.

[60] E. H. Mercer, *Keratin and keratinization: an essay in molecular biology.* Pergamon, 1961.

[61] R. Moll, W. W. Franke, and D. L. Schiller, “The Catalog of Human Cytokeratins : Patterns of Expression in Normal Epithelia , Tumors and Cultured Cells,” *Cell*, vol. 31, no. November, pp. 11–24, 1982.

[62] S. C. Tseng, M. J. Jarvinen, W. G. Nelson, J. W. Huang, J. Woodcock-Mitchell, and T. T. Sun, “Correlation of specific keratins with different types of epithelial differentiation: monoclonal antibody studies.,” *Cell*, vol. 30, no. 2, pp. 361–372, 1982.

[63] Y. J. Wu, L. M. Parker, N. E. Binder, M. A. Beckett, J. H. Sinard, C. T. Griffiths, and J. G. Rheinwald, “The mesothelial keratins: a new family of cytoskeletal proteins identified in cultured mesothelial cells and nonkeratinizing epithelia.,” *Cell*, vol. 31, no. 3 Pt 2, pp. 693–703, 1982.

[64] R. Moll, M. Divo, and L. Langbein, “The human keratins: Biology and pathology,” *Histochem. Cell Biol.*, vol. 129, no. 6, pp. 705–733, 2008.

[65] L. N. Jones, M. Simon, N. R. Watts, F. P. Booy, a. C. Steven, and D. a D. Parry, “Intermediate filament structure: Hard α-keratin,” *Biophys. Chem.*, vol. 68, no. 1–3, pp. 83–93, 1997.

[66] L. M. Dowling, W. G. Crewther, and D. A. Parry, “Secondary structure of component 8c-1 of alpha-keratin. An analysis of the amino acid sequence.,” *Biochem. J.*, vol. 236, no. 3, pp. 705–712, 1986.

[67] R. D. Fraser, T. P. MacRae, D. A. D. Parry, and E. Suzuki, “Intermediate filaments in α-keratins,” *Proc Natl Acad Sci U S A*, vol. 83, no. 5, pp. 1179–1183, 1986.

[68] R. D. B. Fraser and D. A. D. Parry, “Molecular packing in the feather keratin filament,” *J. Struct. Biol.*, vol. 162, no. 1, pp. 1–13, 2008.

[69] P. M. Steinert, R. H. Rice, D. R. Roop, B. L. Trus, and A. C. Steven, “Complete amino acid sequence of a mouse epidermal keratin subunit and implications for the

structure of intermediate filaments," *Nature*, vol. 302, no. 5911, pp. 794–800, 1983.

[70] J. Squire, P. J. Vibert, and A. Elliott, *Fibrous protein structure*. San Diego, US: Academic Press, 1987.

[71] P. M. Steinert and D. A. D. Parry, "Intermediate filaments: conformity and diversity of expression and structure.," *Annu. Rev. Cell Biol.*, vol. 1, pp. 41–65, 1985.

[72] W. G. Crewther and L. M. Dowling, "55-Effects of chemical modifications on the physical properties of wool: a model of the wool fiber," *J. Text. Inst. Trans.*, vol. 51, no. 12, pp. T775–T791, 1960.

[73] H. W. Harding and G. E. Rogers, "ε-(γ-glutamyl)lysine cross-linkage in citrulline-containing protein fractions from hair," *Biochemistry*, vol. 10, no. 4, pp. 624–630, 1971.

[74] B. Milligan, L. A. Holt, and J. B. Caldwell, "The enzymic hydrolysis of wool for amino acid analysis," *Appl Poly Symp*, vol. 18, pp. 113–125, 1971.

[75] I. J. O'Donnell and E. O. P. Thompson, "Studies on oxidized wool VI. Interactions between high and low-sulfur proteins and their significance in the purification of extracted wool proteins," *Aust J Biol Sci*, vol. 15, pp. 740–756, 1962.

[76] I. J. O'Donnell and E. O. P. Thompson, "Studies on reduced wool IV. The isolation of a major component," *Aust J Biol Sci*, vol. 17, pp. 973–978, 1964.

[77] P. Alexander and C. Earland, "Structure of wool fibers. Isolation of an α- and β-protein in wool," *Nature*, vol. 166, pp. 396–397, 1950.

[78] J. M. Swan, "Thiols, disulphides and thiosulphates: some new reactions and possibilities in peptide and protein chemistry," *Nature*, vol. 180, pp. 643–645, 1957.

[79] D. R. Goddard and L. Michaelis, "A study on keratin," *J. Biol. Chem.*, vol. 106, no. 2, pp. 605–614, 1934.

[80] B. S. Harrap and E. F. Woods, "Soluble derivatives of feather keratin. 1. Isolation, fractionation and amino acid composition," *Biochem. J.*, vol. 92, no. 1, pp. 8–18, 1964.

[81] A. Gennadios, *Protein-based films and coatings*. CRC Press, 2002.

[82] B. L. A. Holt, B. Milligan, and C. M. Roxburgh, “Aspartic acid, asparagine, glutamic acid, and glutamine contents of wool and two derived protein fractions,” *Aust J Biol Sci.*, vol. 24, no. 3, pp. 509–514, 1971.

[83] E. O. P. Thompson and I. J. O’Donnell, “Studies on reduced wool I. The extent of reduction of wool with increasing concentrations of thiol, and the extraction of proteins from reduced and alkylated wool,” *Aust J Biol Sci*, vol. 15, p. 757, 1962.

[84] B. S. Harrap and E. F. Woods, “Soluble derivatives of feather keratin. 2. Molecular weight and conformation,” *Biochem. J.*, vol. 92, no. 1, pp. 19–26, 1964.

[85] G. E. Rogers, “The structure and biochemistry of keratin,” in *The biological basis of medicine*, E. E. Bittar and N. Bittar, Eds. New York: Academic Press, 1969, pp. 21–57.

[86] R. C. Marshall, D. F. Orwin, and J. M. Gillespie, “Structure and biochemistry of mammalian hard keratin,” *Electron Microsc. Rev.*, vol. 4, no. 1, pp. 47–83, 1991.

[87] D. J. Kemp, P. Y. Dyer, and G. E. Rogers, “Keratin synthesis during development of the embryonic chick feather,” *J. Cell Biol.*, vol. 62, no. 1, pp. 114–131, 1974.

[88] K. Gregg and G. E. Rogers, “Feather keratin: composition, structure and biogenesis,” in *Biology of the integument*, J. Bereiter-Hahn, A. G. Matoltsy, and K. S. Richards, Eds. Berlin Heidelberg: Springer, 1986, pp. 666–694.

[89] L. Alibardi, L. Dalla Valle, V. Toffolo, and M. Toni, “Scale keratin in lizard epidermis reveals amino acid regions homologous with avian and mammalian epidermal proteins,” *Anat. Rec. - Part A Discov. Mol. Cell. Evol. Biol.*, vol. 288, no. 7, pp. 734–752, 2006.

[90] D. J. Tomlinson, C. H. Mülling, and T. M. Fakler, “Invited review: formation of keratins in the bovine claw: roles of hormones, minerals, and vitamins in functional claw integrity,” *J. Dairy Sci.*, vol. 87, no. 4, pp. 797–809, 2004.

[91] C. K. W. Mülling, “Three-dimensional appearance of bovine epidermal keratinocytes in different stages of differentiation revealed by cell maceration and scanning electron microscopic investigation,” *Folia Morphol. (Warsz).*, vol. 59, no. 4, pp. 239–246, 2000.

[92] C. Mülling and C. J. Lischer, “New aspects of etiology and pathogenesis of laminitis

in cattle," in *Recent Advances in Bovine Medicine, World Buriatrics Conf.*, 2002, pp. 2–13.

[93] A. G. Matoltsy, "Keratinization of the avian epidermis: an ultrastructural study of the newborn chick skin," *J. Ultrastruct. Res.*, vol. 29, no. 5–6, pp. 438–458, 1969.

[94] I. Brody, "The ultrastructure of the tonofibrils in the keratinization process of normal human epidermis," *J. Ultrastruct. Res.*, vol. 4, no. 3–4, pp. 264–297, 1960.

[95] S. Roth and W. H. Clark, "Ultrastructural evidence related to the mechanism of keratin synthesis," in *The Epidermis*, W. Montagna and W. C. Lobitz, Eds. New York: Academic Press Inc, 1964, p. 303.

[96] A. G. Matoltsy and T. Huszar, "Keratinization of the reptilian epidermis: an ultrastructural study of the turtle skin," *J. Ultrastruct. Res.*, vol. 38, no. 1, pp. 87–101, 1972.

[97] P. F. a Maderson, W. J. Hillenius, U. Hiller, and C. C. Dove, "Towards a comprehensive model of feather regeneration," *J. Morphol.*, vol. 270, no. 10, pp. 1166–1208, 2009.

[98] L. Alibardi and M. Toni, "Cytochemical and molecular characteristics of the process of cornification during feather morphogenesis," *Prog. Histochem. Cytochem.*, vol. 43, no. 1, pp. 1–69, 2008.

[99] L. Alibardi, "Ultrastructure of the feather follicle in relation to the formation of the rachis in pennaceous feathers," *Anat. Sci. Int.*, vol. 85, no. 2, pp. 79–91, 2010.

[100] B. K. Filshie and G. E. Rogers, "An electron microscope study of the fine structure of feather keratin," *J. Cell Biol.*, vol. 13, no. 1, pp. 1–12, 1962.

[101] H. P. Baden and P. F. Maderson, "Morphological and biophysical identification of fibrous proteins in the amniote epidermis.," *J. Exp. Zool.*, vol. 174, no. 2, pp. 225–232, 1970.

[102] L. Alibardi, "Immunolocalization of alpha-keratins and feather beta-proteins in feather cells and comparison with the general process of cornification in the skin of mammals," *Ann. Anat.*, vol. 195, no. 2, pp. 189–198, 2013.

[103] D. H. Matulionis, "Morphology of the developing down feathers of chick embryos.

A descriptive study at the ultrastructural level of differentiation and keratinization," *Z. Anat. Entw. Gesch*, vol. 132, no. 2, pp. 107–157, 1970.

[104] L. Alibardi, "Keratinization and lipogenesis in epidermal derivatives of the zebrafinch, Taeniopygia guttata castanotis (Aves, Passeriformes, ploecidae) during embryonic development," *J. Morphol.*, vol. 251, no. 3, pp. 294–308, 2002.

[105] E. Schmid, S. Tapscott, G. S. Bennett, J. Croop, S. a. Fellini, H. Holtzer, and W. W. Franke, "Differential location of different types of intermediate-sized filaments in various tissues of the chicken embryo," *Differentiation*, vol. 15, no. 1, pp. 27–40, 1979.

[106] W. Meyer and G. Baumgärtner, "Embryonal feather growth in the chicken.," *J. Anat.*, vol. 193 (Pt 4, pp. 611–616, 1998.

[107] J. M. Gillespie, "The proteins of hair and other hard α-keratins," in *Cellular and Molecular Biology of Intermediate Filaments*, R. D. Goldman and P. M. Steinert, Eds. Springer US, 1990, pp. 95–128.

[108] D. a D. Parry, "Hard α-keratin intermediate filaments: An alternative interpretation of the low-angle equatorial X-ray diffraction pattern, and the axial disposition of putative disulphide bonds in the intra-and inter-protofilamentous networks," *Int. J. Biol. Macromol.*, vol. 19, no. 1, pp. 45–50, 1996.

[109] D. L. Nelson and M. M. Cox, *Lehninger principles of biochemistry*, 5th ed. New York: W. H. Freeman and Company, 2008.

[110] F. H. C. Crick, "Is α-keratin a coiled coil?," *Nat. Publ. Gr.*, vol. 170, pp. 882–883, 1952.

[111] F. H. C. Crick, "The packing of α-helices: simple coiled-coils," *Acta Crystallogr.*, vol. 6, pp. 689–697, 1953.

[112] L. Pauling, R. B. Corey, and H. R. Branson, "The structure of proteins; two hydrogen-bonded helical configurations of the polypeptide chain.," *Proc. Natl. Acad. Sci. U. S. A.*, vol. 37, no. 4, pp. 205–211, 1951.

[113] J. McMurry and R. Fay, "Biochemistry," in *Chemistry*, 4th ed., Pearson Prentice Hall, 2003.

[114] D. Voet, J. G. Voet, and C. W. Pratt, *Biochemistry: life at the molecular level*, 3rd ed. New York: John Wiley&Sons, 2008.

[115] C.-C. Chou and M. J. Buehler, "Structure and mechanical properties of human trichocyte keratin intermediate filament protein.," *Biomacromolecules*, vol. 13, no. 11, pp. 3522–32, 2012.

[116] R. D. B. Fraser, T. P. MacRae, L. G. Sparrow, and D. a. D. Parry, "Disulphide bonding in α-keratin," *Int. J. Biol. Macromol.*, vol. 10, no. 2, pp. 106–112, 1988.

[117] C.-H. Lee, M.-S. Kim, B. M. Chung, D. J. Leahy, and P. a Coulombe, "Structural basis for heteromeric assembly and perinuclear organization of keratin filaments," *Nat. Struct. Mol. Biol.*, vol. 19, no. 7, pp. 707–715, 2012.

[118] S. V. Strelkov, H. Herrmann, N. Geisler, T. Wedig, R. Zimbelmann, U. Aebi, and P. Burkhard, "Conserved segments 1A and 2B of the intermediate filament dimer: Their atomic structures and role in filament assembly," *EMBO J.*, vol. 21, no. 6, pp. 1255–1266, 2002.

[119] A. A. Chernyatina, S. Nicolet, U. Aebi, H. Herrmann, and S. V. Strelkov, "Atomic structure of the vimentin central -helical domain and its implications for intermediate filament assembly," *Proc. Natl. Acad. Sci.*, vol. 109, no. 34, pp. 13620–13625, 2012.

[120] S. Z. Li, *Ben Cao Gang Mu*. Changchun, China: The Time Literature & Art Press, 2005.

[121] J. G. Rouse and M. E. Van Dyke, "A review of keratin-based biomaterials for biomedical applications," *Materials (Basel).*, vol. 3, no. 2, pp. 999–1014, 2010.

[122] J. Hofmeier, "Horn-lime plastic masses from keratin substances," Ger pat no 184915, 1905.

[123] H. N. Dale, "Keratin and other coatings for pills," *Pharmacol. J.*, vol. 129, pp. 494–495, 1932.

[124] C. Beyer, "The keratin or horny substance of the hair," Ger pat no 22643., 1907.

[125] R. D. . Fraser and T. P. MacRae, "Schematic diagram of the wool fibre," *Commonwealth Scientific and Industrial Research Organisation*. [Online].

Available:
http://www.csiropedia.csiro.au/display/CSIROpedia/Wool+fibre+structure.

[126] D. Rivett, C. Ward, L. Belkin, J. Ramshaw, and J. Wilshire, “Keratin and wool research,” in *The Lennox Legacy: the History of the CSIRO Laboratory at 343 Royal Parade Parkville*, Collingwood, VIC, Australia: CSIRO Publishing, 1996.

[127] J. M. Gillespie and M. J. Frenkel, “The diversity of keratins,” *Comp. Biochem. Physiol. Part B Comp. Biochem.*, vol. 47, no. 2, pp. 339–346, 1974.

[128] R. D. B. Fraser and T. P. MacRae, “Molecular structure and mechanical properties of keratins,” in *The Mechanical Properties of Biological Materials(Proceedings of the Symposia of the Society for Experimental Biology)*, J. F. V. Vincent and J. D. Currey, Eds. Cambridge, UK: Cambridge University Press, 1980, pp. 211–246.

[129] Y. Kawano and S. Okamoto, “Film and gels of keratin,” *Kagaku To Seibutsu*, vol. 13, no. 5, pp. 291–292, 1975.

[130] M. van de Locht, “Reconstitution of microfibrils from wool and filaments from epidermis proteins,” *Melliand Textilberichte*, vol. 10, pp. 780–786, 1987.

[131] H. Ito, T. Miyamoto, H. Inagaki, and Y. Noishiki, “Biocompatibility of denatured keratins from wool,” *Kobunshi Ronbunshu*, vol. 39, no. 4, pp. 249–256, 1982.

[132] G. Schwinger, K. Zanger, and H. Greven, “Structural and mechanical aspects of the skin of Bufo marinus (Anura, Amphibia).,” *Tissue Cell*, vol. 33, no. 5, pp. 541–547, 2001.

[133] J. F. V. Vincent and P. Owers, “Mechanical design of hedgehog spines and porcupine quills,” *J. Zool.*, vol. 210, no. 1, pp. 55–75, 1986.

[134] W. Yang and J. McKittrick, “Separating the influence of the cortex and foam on the mechanical properties of porcupine quills,” *Acta Biomater.*, vol. 9, no. 11, pp. 9065–9074, 2013.

[135] L. Farren, S. Shayler, and A. R. Ennos, “The fracture properties and mechanical design of human fingernails,” *J. Exp. Biol.*, vol. 207, no. 5, pp. 735–741, 2004.

[136] A. Kitchener, “Fracture toughness of horns and a reinterpretation of the horning behaviour of bovids,” *J. Zool.*, vol. 213, no. 4, pp. 621–639, 1987.

[137] A. Kitchener, “Effect of water on the linear viscoelasticity of horn sheath keratin,” *J. Mater. Sci. Lett.*, vol. 6, no. 3, pp. 321–322, 1987.

[138] A. Miserez, S. S. Wasko, C. F. Carpenter, and J. H. Waite, “Non-entropic and reversible long-range deformation of an encapsulating bioelastomer.,” *Nat. Mater.*, vol. 8, no. 11, pp. 910–916, 2009.

[139] R. H. C. Bonser, “The mechanical performance of meduallary foam from feathers,” *J. Mater. Sci. Lett.*, vol. 20, pp. 941–942, 2001.

[140] S. G. Bodde, M. A. Meyers, and J. McKittrick, “Correlation of the mechanical and structural properties of cortical rachis keratin of rectrices of the Toco Toucan (Ramphastos toco),” *J. Mech. Behav. Biomed. Mater.*, vol. 4, no. 5, pp. 723–732, 2011.

[141] J. McKittrick, P. Y. Chen, L. Tombolato, E. E. Novitskaya, M. W. Trim, G. a. Hirata, E. a. Olevsky, M. F. Horstemeyer, and M. a. Meyers, “Energy absorbent natural materials and bioinspired design strategies: A review,” *Mater. Sci. Eng. C*, vol. 30, no. 3, pp. 331–342, 2010.

[142] G. E. Rogers, “Electron microscope studies of hair and wool,” *Ann. N. Y. Acad. Sci.*, vol. 83, no. 3, pp. 378–399, 1959.

[143] G. E. Rogers, “Electron microscopy of wool.,” *J. Ultrastruct. Res.*, vol. 2, no. 3, pp. 309–330, 1959.

[144] L. J. Szewciw, D. G. de Kerckhove, G. W. Grime, and D. S. Fudge, “Calcification provides mechanical reinforcement to whale baleen alpha-keratin.,” *Proc. Biol. Sci.*, vol. 277, no. 1694, pp. 2597–2605, 2010.

[145] K. S. Wu, W. W. Van Osdol, and R. H. Dauskardt, “Mechanical properties of human stratum corneum: Effects of temperature, hydration, and chemical treatment,” *Biomaterials*, vol. 27, no. 5, pp. 785–795, 2006.

[146] S. F. Chou and R. A. Overfelt, “Tensile deformation and failure of North American porcupine quills,” *Mater. Sci. Eng. C*, vol. 31, no. 8, pp. 1729–1736, 2011.

[147] M. W. Trim, M. F. Horstemeyer, H. Rhee, H. El Kadiri, L. N. Williams, J. Liao, K. B. Walters, J. McKittrick, and S. J. Park, “The effects of water and microstructure on the mechanical properties of bighorn sheep (Ovis canadensis) horn keratin,” *Acta*

Biomater., vol. 7, no. 3, pp. 1228–1240, 2011.

[148] D. S. Fudge, K. H. Gardner, V. T. Forsyth, C. Riekel, and J. M. Gosline, "The mechanical properties of hydrated intermediate filaments: insights from hagfish slime threads.," *Biophys. J.*, vol. 85, no. 3, pp. 2015–2027, 2003.

[149] A. M. Taylor, R. H. C. Bonser, and J. W. Farrent, "The influence of hydration on the tensile and compressive properties of avian keratinous tissues," *J. Mater. Sci.*, vol. 39, no. 3, pp. 939–942, 2004.

[150] Y. Seki, M. S. Schneider, and M. a. Meyers, "Structure and mechanical behavior of a toucan beak," *Acta Mater.*, vol. 53, no. 20, pp. 5281–5296, 2005.

[151] M. C. G. Klein, J. K. Deuschle, and S. N. Gorb, "Material properties of the skin of the Kenyan sand boa Gongylophis colubrinus (Squamata, Boidae)," *J. Comp. Physiol. A Neuroethol. Sensory, Neural, Behav. Physiol.*, vol. 196, no. 9, pp. 659–668, 2010.

[152] B. Wang, W. Yang, and M. A. Meyers, "Unpublished results." 2014.

[153] P. A. Coulombe and P. Wong, "Cytoplasmic intermediate filaments revealed as dynamic and multipurpose scaffolds.," *Nat. Cell Biol.*, vol. 6, no. 8, pp. 699–706, 2004.

[154] "Scanning electron micrograph of stramtum corneum." [Online]. Available: http://feleciaroselabs.com/wp-content/uploads/2012/05/SC.jpg.

[155] G. Plewig and R. R. Marples, "Regional differences of cell sizes in the human stratum corneum. Part I," *J. Invest. Dermatol.*, vol. 54, no. 1, pp. 13–18, 1970.

[156] P. Ovaere, S. Lippens, P. Vandenabeele, and W. Declercq, "The emerging roles of serine protease cascades in the epidermis," *Trends Biochem. Sci.*, vol. 34, no. 9, pp. 453–463, 2009.

[157] Y. S. Papir, K. H. Hsu, and R. H. Wildnauer, "The mechanical properties of stratum corneum: I. The effect of water and ambient temperature on the tensile properties of newborn rat stratum corneum," *Biochim. Biophys. Acta (BBA)- ...*, vol. 399, pp. 170–180, 1975.

[158] Y. Yuan and R. Verma, "Measuring microelastic properties of stratum corneum,"

Colloids Surfaces B Biointerfaces, vol. 48, no. 1, pp. 6–12, 2006.

[159] K. S. Wu, M. M. Stefik, K. P. Ananthapadmanabhan, and R. H. Dauskardt, "Graded delamination behavior of human stratum corneum," *Biomaterials*, vol. 27, no. 34, pp. 5861–5870, 2006.

[160] K. Biniek, K. Levi, and R. H. Dauskardt, "Solar UV radiation reduces the barrier function of human skin," *Proc. Natl. Acad. Sci.*, vol. 109, no. 42, pp. 17111–17116, 2012.

[161] M. Feughelman and a. R. Haly, "The mechanical properties of wool keratin and its molecular configuration," *Kolloid-Zeitschrift*, vol. 168, no. 2, pp. 107–115, 1960.

[162] M. Feughelman, *Mechanical properties and structure of alpha-keratin fibers: wool, human hair and related fibers*. University of New South Wales Press, 1997.

[163] D. M. Lewis and J. A. Rippon, Eds., *The coloration of wool and other keratin fibres*. John Wiley, 2013.

[164] J. Fan and W. D. Yu, "Fractal Analysis of the Ortho-Cortex and Para-Cortex of Wool Fiber," *Adv. Mater. Res.*, vol. 197–198, pp. 86–89, 2011.

[165] M. Feughelman, "A Two-Phase Structure for Keratin Fibers," *Text. Res. J.*, vol. 29, no. 3, pp. 223–228, 1959.

[166] F.-J. Wortmann and H. Zahn, "The Stress/Strain Curve of -Keratin Fibers and the Structure of the Intermediate Filament," *Text. Res. J.*, vol. 64, no. 12, pp. 737–743, 1994.

[167] B. M. Chapman, "A Mechanical Model for Wool and other Keratin Fibers," *Text. Res. J.*, vol. 39, no. 12, pp. 1102–1109, 1969.

[168] M. Feughelman, "A Model for the Mechanical Properties of the -Keratin Cortex," *Text. Res. J.*, vol. 64, no. 4, pp. 236–239, 1994.

[169] W. G. Crewter, "The effects of disaggregating agents on the stress-strain relationship for wool fibers," *Text. Res. J.*, vol. 42, no. 2, pp. 77–85, 1972.

[170] B. M. Chapman, "A review of mechanical properties of keratin fibres," *J. Text. Inst.*, vol. 60, no. 5, pp. 181–207, 1969.

[171] J. W. S. Hearle, “The structural mechanics of fibers,” *J. Polym. Sci. Part C Polym. Symp.*, vol. 20, no. 1, pp. 215–251, 1967.

[172] J. W. S. Hearle, “A critical review of the structural mechanics of wool and hair fibres,” *Int. J. Biol. Macromol.*, vol. 27, no. 2, pp. 123–138, 2000.

[173] M. Feughelman, “Keratin,” in *Encyclopaedia of Polymer Science and Engineering, Vol. 8*, 2nd ed., New York: John Wiley and Son, Inc., 1987, pp. 566–600.

[174] E. G. Bendit, “A Quantitative X-Ray Diffraction Study of the Alpha-Beta Transformation in Wool Keratin,” *Text. Res. J.*, vol. 30, no. 8, pp. 547–555, 1960.

[175] L. R. G. Treloar, *The physics of rubber elasticity*. Oxford: Clarendon Press, 1975.

[176] M. J. Harrington, S. S. Wasko, a. Masic, F. D. Fischer, H. S. Gupta, and P. Fratzl, “Pseudoelastic behaviour of a natural material is achieved via reversible changes in protein backbone conformation,” *J. R. Soc. Interface*, vol. 9, no. 76, pp. 2911–2922, 2012.

[177] L. Kreplak, J. Doucet, P. Dumas, and F. Briki, “New aspects of the α-helix to β-sheet transition in stretched hard α-keratin fibers.,” *Biophys. J.*, vol. 87, no. 1, pp. 640–647, 2004.

[178] M. Feughelman and M. S. Robinson, “The Relationship Between Some Mechanical Properties of Single Wool Fibers and Relative Humidity1,” *Text. Res. J.*, vol. 37, no. 6, pp. 441–446, 1967.

[179] J. L. Woods, D. P. Harland, J. a. Vernon, G. L. Krsinic, and R. J. Walls, “Morphology and ultrastructure of antler velvet hair and body hair from red deer (Cervus elaphus),” *J. Morphol.*, vol. 272, no. 1, pp. 34–49, 2011.

[180] Y. Yu, B. Wang, and M. A. Meyers, “Unpublished results.” 2015.

[181] M. A. Kasapi and J. M. Gosline, “Design complexity and fracture control in the equine hoof wall,” *J. Exp. Biol.*, vol. 200, no. Pt 11, pp. 1639–1659, 1997.

[182] M. a Kasapi and J. M. Gosline, “Micromechanics of the equine hoof wall: optimizing crack control and material stiffness through modulation of the properties of keratin.,” *J. Exp. Biol.*, vol. 202, no. Pt 4, pp. 377–391, 1999.

[183] R. Nickel, “Über den Bau der Hufröhrchen und seine Bedeutung für den Mechanismus des Pferdehufes,” *Morph. Jb.*, vol. 82, pp. 119–160, 1938.

[184] M. L. Ryder, “Structure of rhinoceros horn,” *Nature*, vol. 193, pp. 1199–1201, 1962.

[185] J. E. Bertram and J. M. Gosline, “Fracture toughness design in horse hoof keratin.,” *J. Exp. Biol.*, vol. 125, pp. 29–47, 1986.

[186] J. Cook, J. E. Gordon, C. C. Evans, and D. M. Marsh, “A mechanism for the control of crack propagation in all-brittle systems,” *Proc. R. Soc. London A Math. Phys. Eng. Sci.*, vol. 282, no. 1391, pp. 508–520, 1964.

[187] J. E. Bertram and J. M. Gosline, “Functional design of horse hoof keratin: the modulation of mechanical properties through hydration effects.,” *J. Exp. Biol.*, vol. 130, pp. 121–136, 1987.

[188] T. M. Wright and W. C. Hayes, “Fracture mechanics parameters for compact bone-effects of density and specimen thickness.,” *J. Biomech.*, vol. 10, no. 7, pp. 419–430, 1977.

[189] D. H. Leach, “The structure and function of equine hoof wall,” University of Saskatchewan, 1980.

[190] D. Bardack, “First fossil lamprey: a record from the Pennsylvanian of Illinois,” *Science (80-.).*, vol. 162, no. 3859, pp. 1265–1267, 1968.

[191] “Hagfish.” [Online]. Available: http://www.ryanphotographic.com/myxinidae.htm.

[192] V. Zintzen, C. D. Roberts, M. J. Anderson, A. L. Stewart, C. D. Struthers, and E. S. Harvey, “Hagfish predatory behaviour and slime defence mechanism,” *Sci. Rep.*, vol. 1, pp. 1–6, 2011.

[193] “Hagfish slime and the threads.” [Online]. Available: http://bouncingideas.wordpress.com/2011/10/29/hagfish-slime-is-the-new-spiderweb-silk/.

[194] D. S. Fudge, N. Levy, S. Chiu, and J. M. Gosline, “Composition, morphology and mechanics of hagfish slime.,” *J. Exp. Biol.*, vol. 208, no. Pt 24, pp. 4613–4625, 2005.

[195] T. M. Winegard and D. S. Fudge, “Deployment of hagfish slime thread skeins

requires the transmission of mixing forces via mucin strands.," *J. Exp. Biol.*, vol. 213, no. Pt 8, pp. 1235–1240, 2010.

[196] E. A. Koch, R. H. Spitzer, R. B. Pithawalla, F. A. Castillos, and D. A. D. Parry, "Hagfish biopolymer: a type I/type II homologue of epidermal keratin intermediate filaments," *Int. J. Biol. Macromol.*, vol. 17, no. 5, pp. 283–292, 1995.

[197] D. S. Fudge and J. M. Gosline, "Molecular design of the alpha-keratin composite: insights from a matrix-free model, hagfish slime threads.," *Proc. Biol. Sci.*, vol. 271, no. 1536, pp. 291–299, 2004.

[198] H. P. Baden, L. A. Goldsmith, and L. Lee, "The importance of understanding the comparative properties of hair and other keratinized tissues in studying disorders of hair," in *The first human hair symposium*, A. C. Brown, Ed. New York: Medcom Press, 1974, pp. 388–398.

[199] F. B. Gill, *Ornithology*, 2nd ed. New York: W.H.Freeman and Company, 1994.

[200] T. Bachmann, J. Emmerlich, W. Baumgartner, J. M. Schneider, and H. Wagner, "Flexural stiffness of feather shafts: geometry rules over material properties," *J. Exp. Biol.*, vol. 215, no. 3, pp. 405–415, 2012.

[201] G. D. Macleod, "Mechanical properties of contour feathers," *J. Exp. Biol.*, vol. 87, pp. 65–71, 1980.

[202] I. M. Weiss, K. P. Schmitt, and H. O. K. Kirchner, "The peacock's train (Pavo cristatus and Pavo cristatus mut. alba) I. Structure, mechanics, and chemistry of the tail feather coverts," *J. Exp. Zool. Part A Ecol. Genet. Physiol.*, vol. 313 A, no. 10, pp. 690–703, 2010.

[203] Z. Q. Liu, D. Jiao, M. A. Meyers, and Z. F. Zhang, "Structure and mechanical properties of naturally occurring lightweight foam-filled cylinder – The peacock's tail coverts shaft and its components," *Acta Biomater.*, vol. 17, pp. 137–151, 2015.

[204] W. T. Astbury and T. C. Marwick, "X-Ray Interpretation of the Molecular Structure of Feather Keratin," *Nature*, vol. 130, no. 3278, pp. 309–310, 1932.

[205] K. M. Rudall, "X-ray studies of the distribution of protein chain types in the vertebrate epidermis," *Biochim. Biophys. Acta*, vol. 1, pp. 549–562, 1947.

[206] B. Wang, W. Yang, J. McKittrick, and M. A. Meyers, "Keratin: structure, mechanical properties, occurrence in biological organisms, and efforts at bioinspiration," *Prog. Mater. Sci.*, vol. 76, pp. 229–318, 2016.

[207] G. J. Cameron, T. J. Wess, and R. H. C. Bonser, "Young's modulus varies with differential orientation of keratin in feathers," *J. Struct. Biol.*, vol. 143, no. 2, pp. 118–123, 2003.

[208] T. Lingham-Soliar and N. Murugan, "A new helical crossed-fibre structure of β-Keratin in flight feathers and its biomechanical implications," *PLoS One*, vol. 8, no. 6, 2013.

[209] C. M. Laurent, C. Palmer, R. P. Boardman, G. Dyke, and R. B. Cook, "Nanomechanical properties of bird feather rachises : exploring naturally occurring fibre reinforced laminar composites," *J. R. Soc. Interface*, vol. 11, no. 101, p. 20140961, 2014.

[210] D. H. Clayton and P. Cotgreave, "Relationship of bill to grooming behavior in birds.," *Anim. Behav.*, vol. 47, no. 1, pp. 195–201, 1994.

[211] A. U. Luester, *Manual of pirrot behavior*. Wiley Blackwell Publishing, 2006.

[212] A. E. Rupley, *MANUAL DE CLÍNICA AVIÁRIA*. São Paulo: Português Brasileiro, 1999.

[213] Y. Seki, B. Kad, D. Benson, and M. a. Meyers, "The toucan beak: Structure and mechanical response," *Mater. Sci. Eng. C*, vol. 26, no. 8, pp. 1412–1420, 2006.

[214] Y. Seki, S. G. Bodde, and M. a. Meyers, "Toucan and hornbill beaks: a comparative study," *Acta Biomater.*, vol. 6, no. 2, pp. 331–343, 2010.

[215] A. Lin and M. A. Meyers, "Growth and structure in abalone shell," *Mater. Sci. Eng. A*, vol. 390, no. 1–2, pp. 27–41, 2005.

[216] R. E. Chapman, "Hair, wool, quill, nail, claw, hoof and horn," in *Biology of the Integument, Vertebrates, vol. 2*, J. Bereither-Hahn, G. A. Matoltsy, and K. Sylvia-Richards, Eds. Berlin/Heidelberg/New York: Springer-Verlag, 1986, pp. 293–312.

[217] W. E. Clark, "The problem of the claw in primates," *Proc. Zool. Soc. London*, vol. 106, no. 1, pp. 1–24, 1936.

[218] E. E. Thorndike, “A microscopic study of the marmoset claw and nail,” *Am. J. Phys. Anthropol.*, vol. 28, no. 3, pp. 247–261, 1968.

[219] H. P. Baden, “The physical properties of nail,” *J Invest Dermatol*, vol. 55, no. 2, pp. 115–122, 1970.

[220] R. M. Alexander, G. M. O. Maloiy, R. Njau, and a. S. Jayes, “Mechanics of running of the ostrich (Struthio camelus),” *J. Zool.*, vol. 187, no. 2, pp. 169–178, 2009.

[221] R. Bonser, “Hydration sensitivity of ostrich claw keratin,” *J. Mater. Sci. Lett.*, vol. 21, pp. 1563–1564, 2002.

[222] R. H. C. Bonser, “The Young’s modulus of ostrich claw keratin,” *J. Mater. Sci. Lett.*, vol. 19, pp. 1039–1040, 2000.

[223] D. H. Leach and G. C. Zoerb, “Mechanical properties of equine hoof wall tissue,” *Am. J. Vet. Res.*, vol. 44, no. 11, pp. 2190–2194, 1983.

[224] J. E. Douglas, C. Mittal, J. J. Thomason, and J. C. Jofriet, “The modulus of elasticity of equine hoof wall: implications for the mechanical function of the hoof,” *J. Exp. Biol.*, vol. 199, no. Pt 8, pp. 1829–1836, 1996.

[225] J. A. Wyld and A. H. Brush, “Keratin diversity in the reptilian epidermis,” *J. Exp. Zool.*, vol. 225, no. 3, pp. 387–396, 1983.

[226] J. A. Wyld and A. H. Brush, “The molecular heterogeneity and diversity of reptilian keratins,” *J. Mol. Evol.*, vol. 12, no. 4, pp. 331–347, 1979.

[227] P. F. A. Maderson, “Some Developmental Problems of the Reptilian Integument,” in *Biology of the Reptilia*, C. Gans, F. Billett, and P. F. A. Maderson, Eds. John Wiley & Sons, 1985, pp. 523–598.

[228] L. Landmann, “The skin of reptiles: epidermis and dermis,” in *Biology of the Integument, Vertebrates, vol. 2*, J. Bereither-Hahn, G. A. Matoltsy, and K. Sylvia-Richards, Eds. Berlin/Heidelberg/New York: Springer-Verlag, 1986, pp. 150–187.

[229] R. D. B. Fraser and D. A. D. Parry, “The molecular structure of reptilian keratin,” *Int. J. Biol. Macromol.*, vol. 19, no. 3, pp. 207–211, 1996.

[230] R. H. Sawyer, T. Glenn, J. O. French, B. Mays, R. B. Shames, G. L. Barnes, Jr., W. Rhodes, and Y. Ishikawa, "The Expression of Beta (β) Keratins in the Epidermal Appendages of Reptiles and Birds," *Am. Zool.*, vol. 40, no. 4, pp. 530–539, 2000.

[231] L. Alibardi and R. H. Sawyer, "Immunocytochemical analysis of beta (β) keratins in the epidermis of chelonians, lepidosaurians, and archosaurians," *J. Exp. Zool.*, vol. 293, no. 1, pp. 27–38, 2002.

[232] B. K. Filshie and G. E. Rogers, "The fine structure of α-keratin," *J. Mol. Biol.*, vol. 3, no. 6, pp. 784–786, 1961.

[233] N. J. Alexander, "Comparison of α and β keratin in reptiles," *Zeitschrift für Zellforsch.*, vol. 110, no. 2, pp. 153–165, 1970.

[234] L. Alibardi and M. Toni, "Cytochemical, biochemical and molecular aspects of the process of keratinization in the epidermis of reptilian scales," *Prog. Histochem. Cytochem.*, vol. 40, no. 2, pp. 73–134, 2006.

[235] N. J. Alexander and P. F. Parakkal, "Formation of α- and β-type keratin in lizard epidermis during the molting cycle," *Z Zellforsch*, vol. 101, no. 1, pp. 72–87, 1969.

[236] M. Toni and L. Alibardi, "Alpha- and beta-keratins of the snake epidermis," *Zoology*, vol. 110, no. 1, pp. 41–47, 2007.

[237] R. I. C. Spearman, "The epidermis of the gopher tortoise Testudo polyphemus (Daudin)," *Acta Zool.*, vol. 50, pp. 1–9, 1969.

[238] L. Alibardi, "Immunocytochemical observations on the cornification of soft and hard epidermis in the turtle Chrysemys picta.," *Zoology (Jena).*, vol. 105, no. 1, pp. 31–44, 2002.

[239] A. M. Bauer, A. P. Russell, and R. E. Shadwick, "Mechanical properties and morphological correlates of fragile skin in gekkonid lizards," *J. Exp. Biol.*, vol. 145, pp. 79–102, 1989.

[240] M.-C. G. Klein and S. N. Gorb, "Epidermis architecture and material properties of the skin of four snake species," *J. R. Soc. Interface*, vol. 9, no. 76, pp. 3140–3155, 2012.

[241] L. Landmann, "Keratin formation and barrier mechanisms in the epidermis of Natrix

natrix (Reptilia: Serpentes): An ultrastructural study," *J. Morphol.*, vol. 162, no. 1, pp. 93–126, 1979.

[242] R. Z. Wang and S. Weiner, "Strain-structure relations in human teeth using Moiré fringes.," *J. Biomech.*, vol. 31, no. 2, pp. 135–141, 1998.

[243] H. Fong, M. Sarikaya, S. N. White, and M. L. Snead, "Nano-mechanical properties profiles across dentin–enamel junction of human incisor teeth," *Mater. Sci. Eng. C*, vol. 7, no. 2, pp. 119–128, 2000.

[244] M. Briggs and P. Briggs, *The Encyclopedia of of World Wildlife*. Paragon Books, 2006.

[245] J. Kingdon, *East African mammals: an atlas of evolution in Africa. Vol. I*. Chicago: University of Chicago Press, 1974.

[246] M. E. Heath, "Manis pentadactyla," *The American Society of Mammalogist*, vol. 414. pp. 1–6, 1992.

[247] U. Rahm, "Notes on pangolins of the ivory coast," *J. Mammal*, vol. 37, no. 4, pp. 531–537, 1956.

[248] J. Tong, L. Q. Ren, and B. C. Chen, "Chemical constitution and abrasive wear behaviour of pangolin scales," *J. Mater. Sci. Lett.*, vol. 14, no. 20, pp. 1468–1470, 1995.

[249] J. Tong, Y. H. Ma, L. Q. Ren, and J. Q. Li, "Tribological characteristics of pangolin scales in dry sliding," *J. Mater. Sci. Lett.*, vol. 19, no. 7, pp. 569–572, 2000.

[250] G. N. Karam and L. J. Gibson, "Biomimicking of animal quills and plant stems: natural cylindrical shells with foam cores," *Mater. Sci. Eng. C*, vol. 2, no. 1–2, pp. 113–132, 1994.

[251] J. Banhart, "Aluminum foams : on the road to real applications," *MRS Bull.*, vol. 28, no. 4, pp. 290–295, 2003.

[252] V. P. Veedu, A. Cao, X. Li, K. Ma, C. Soldano, S. Kar, P. M. Ajayan, and M. N. Ghasemi-Nejhad, "Multifunctional composites using reinforced laminae with carbon-nanotube forests," *Nat. Mater.*, vol. 5, no. 6, pp. 457–462, 2006.

[253] V. M. Drakonakis, C. N. Velisaris, J. C. Seferis, and C. C. Doumanidis, “Feather-inspired carbon fiber reinforced polymers with nanofibrous fractal interlayer,” *Polym. Compos.*, 2014.

[254] W. K. Cho, J. A. Ankrum, D. Guo, S. A. Chester, S. Y. Yang, A. Kashyap, G. A. Campbell, R. J. Wood, R. K. Rijal, R. Karnik, R. Langer, and J. M. Karp, “Microstructured barbs on the North American porcupine quill enable easy tissue penetration and difficult removal,” *Proc. Natl. Acad. Sci. U. S. A.*, vol. 109, no. 52, pp. 21289–94, 2012.

[255] “Industrial wastewater filter technology inspired by nature,” *Filtr. Sep.*, vol. 40, no. 1, pp. 18–21, 2003.

[256] “Whalebone inspires filter technology,” *Filtr. Sep.*, vol. 44, no. 2, p. 10, 2007.

[257] Baleen Filters Pty Ltd, “Baleen filters.” [Online]. Available: http://www.baleenfilters.com/.

[258] Cyclus Manufacture, “Pangolin backpack.” [Online]. Available: http://www.pangolin.com.co/collections/main-collection.

[259] A. Miserez, C. Weaver, and O. Chaudhuri, “Biological materials and molecular biomimetics – filling up the empty soft materials space for tissue engineering applications,” *J. Mater. Chem. B Mater. Biol. Med.*, vol. 3, no. 1, pp. 13–24, 2015.

[260] E. F. Banwell, E. S. Abelardo, D. J. Adams, M. a Birchall, A. Corrigan, A. M. Donald, M. Kirkland, L. C. Serpell, M. F. Butler, and D. N. Woolfson, “Rational design and application of responsive alpha-helical peptide hydrogels,” *Nat. Mater.*, vol. 8, no. 7, pp. 596–600, 2009.

[261] T. Fu, P. A. Guerette, R. Y. Tan, H. Zhao, L. Schefer, R. Mezzenga, and A. Miserez, “Biomimetic self-assembly of recombinant marine snail egg capsule proteins into structural coiled-coil units,” *J. Mater. Chem. B*, 2015.

[262] W. Yang, I. H. Chen, B. Gludovatz, E. A. Zimmermann, R. O. Ritchie, and M. A. Meyers, “Natural flexible dermal armor,” *Adv. Mater.*, vol. 25, no. 1, pp. 31–48, 2013.

[263] A. Jarrett, R. I. Spearman, and J. A. Hardy, “The histochemistry of keratinization,” *Br J Dermatol*, vol. 71, pp. 277–295, 1959.

[264] D. Zhu, L. Szewciw, F. Vernerey, and F. Barthelat, “Puncture resistance of the scaled skin from striped bass: Collective mechanisms and inspiration for new flexible armor designs,” *J. Mech. Behav. Biomed. Mater.*, vol. 24, pp. 30–40, 2013.

[265] D. Challender, J. Baillie, G. Ades, P. Kaspal, B. Chan, A. Khatiwada, L. Xu, S. Chin, R. KC, H. Nash, and H. Hsieh, “‘Manis pentadactyla’. IUCN Red List of Threatened Species. Version 2014.2,” 2014.

[266] S. E. Naleway, M. M. Porter, J. Mckittrick, and M. A. Meyers, “Structural design elements in biological materials : application to bioinspiration,” *Adv. Mater.*, vol. 27, no. 37, pp. 5455–5476, 2015.

[267] H. Ehrlich, “Materials Design Principles of Fish Scales and Armor.,” in *Biological Materials of Marine Origin*, Springer Netherlands, 2014, pp. 237–262.

[268] V. D. Burdak, “Morphologie fonctionnelle du tegument ecailleux des poissons. Kiev: La Pensee Scientifique 1979 (in Russian). French translation.,” *Cybium*, vol. 10, pp. 1–147, 1986.

[269] F. J. Meunier and J. Castanet, “Organisation spatiale des fibres de collagene de la plaque basale des ecailles des Teleosteens,” *Zool. Scr.*, vol. 11, no. 2, pp. 141–153, 1982.

[270] D. G. Elliott, “Chapter 5-Integumentary system (Gross Functional Anatomy), Chapter 17—Integumentary System (Microscopic Functional Anatomy),” in *The Laboratory Fish*, Ostrander, G.K.: Academic Press, Oxford, England, 2000, pp. 95–108, 271–306.

[271] D. Zhu, L. Szewciw, F. Vernerey, and F. Barthelat, “Puncture resistance of the scaled skin from striped bass: Collective mechanisms and inspiration for new flexible armor designs,” *J. Mech. Behav. Biomed. Mater.*, vol. 24, pp. 30–40, 2013.

[272] W. Yang, B. Gludovatz, E. a. Zimmermann, H. a. Bale, R. O. Ritchie, and M. a. Meyers, “Structure and fracture resistance of alligator gar (Atractosteus spatula) armored fish scales,” *Acta Biomater.*, vol. 9, no. 4, pp. 5876–5889, 2013.

[273] A. Browning, C. Ortiz, and M. C. Boyce, “Mechanics of composite elasmoid fish scale assemblies and their bioinspired analogues,” *J. Mech. Behav. Biomed. Mater.*, vol. 19, pp. 75–86, 2013.

[274] W. Yang, C. Chao, and J. McKittrick, “Axial compression of a hollow cylinder filled with foam: A study of porcupine quills,” *Acta Biomater.*, vol. 9, no. 2, pp. 5297–5304, 2013.

[275] K. A. Holbrook and G. F. Odland, “Regional differences in the thickness (cell layers) of the human stratum corneum: an ultrastructural analysis,” *J Invest Dermatol*, vol. 62, no. 4, pp. 415–422, 1974.

[276] L. Tombolato, E. E. Novitskaya, P. Y. Chen, F. A. Sheppard, and J. McKittrick, “Microstructure, elastic properties and deformation mechanisms of horn keratin,” *Acta Biomater.*, vol. 6, no. 2, pp. 319–330, 2010.

[277] B. L. Lewis, “Microscopic studies of fetal and mature nail and surrounding soft tissue,” *AMA Arch Derm Syphilol*, vol. 70, pp. 733–747, 1954.

[278] L. Farran, a R. Ennos, and S. J. Eichhorn, “The effect of humidity on the fracture properties of human fingernails.,” *J. Exp. Biol.*, vol. 211, no. Pt 23, pp. 3677–3681, 2008.

[279] S. Krauss, E. Monsonego-Ornan, E. Zelzer, P. Fratzl, and R. Shahar, “Mechanical function of a complex three-dimensional suture joining the bony elements in the shell of the red-eared slider turtle,” *Adv. Mater.*, vol. 21, pp. 407–412, 2009.

[280] Y. Li, C. Ortiz, and M. C. Boyce, “Bioinspired, mechanical, deterministic fractal model for hierarchical suture joints,” *Phys. Rev. E - Stat. Nonlinear, Soft Matter Phys.*, vol. 85, no. 3, pp. 1–14, 2012.

[281] Y. Li, C. Ortiz, and M. C. Boyce, “A generalized mechanical model for suture interfaces of arbitrary geometry,” *J. Mech. Phys. Solids*, vol. 61, no. 4, pp. 1144–1167, 2013.

[282] B. D. Cullity, *Elements of X-ray diffraction*, 2nd ed. Menlo Park: Addison-Wesley Publishing Company, Inc., 1978.

[283] “Parry and Arrhenius, personal communications.” .

[284] F.-C. Yang, Y. Zhang, and M. C. Rheinstädter, “The structure of people’s hair,” *PeerJ*, vol. 2, p. e619, 2014.

[285] M. a Kasapi and J. M. Gosline, “Strain-rate-dependent mechanical properties of the

equine hoof wall.," *J. Exp. Biol.*, vol. 199, no. Pt 5, pp. 1133–1146, 1996.

[286] B. Wang and M. A. Meyers, "Unpublished results," 2016.

[287] E. W. Hart, "Theory of the tensile test," *Acta Metall.*, vol. 15, pp. 351–355, 1967.

[288] G. Danilatos and M. Feughelman, "Dynamic mechanical properties of α-keratin fibers during extension," *J. Macromol. Sci. Part B*, vol. 16, no. 4, pp. 581–602, 1979.

[289] B. M. Chapman, "36 — The ageing of wool Part II : the ageing of disorganized fibres," *J. Text. Inst.*, vol. 66, no. 10, pp. 343–346, 1975.

[290] W. C. Oliver and G. M. Pharr, "An improved technique for determining the hardness and elastic modulus using the load and displacement sensing indentation experiments," *J. Mater. Res.*, vol. 7, no. 06, pp. 1564–1583, 1992.

[291] W. C. Oliver and G. M. Pharr, "Measurement of hardness and elastic modulus by instrumented indentation: Advances in understanding and refinements to methodology," *J. Mater. Res.*, vol. 19, no. 01, pp. 3–20, 2004.

[292] F. L. Warburton, "Determination of the elastic properties of horn keratin," *J. Text. Inst. Proc.*, vol. 39, no. 7, pp. 297–308, 1948.

[293] L. Farran, A. R. Ennos, M. Starkie, and S. J. Eichhorn, "Tensile and shear properties of fingernails as a function of a changing humidity environment," *J. Biomech.*, vol. 42, no. 9, pp. 1230–1235, 2009.

[294] J. Lee and H. J. Kwon, "Measurement of stress-strain behaviour of human hair fibres using optical techniques," *Int. J. Cosmet. Sci.*, vol. 35, no. 3, pp. 238–243, 2013.

[295] W. R. Corning and A. A. Biewener, "In vivo strains in pigeon flight feather shafts: implications for structural design," *J. Exp. Biol.*, vol. 201 (Pt 22, pp. 3057–65, 1998.

[296] P. P. Purslow, J. F. V., and J. F. V Vincent, "Mechanical Properties of primary feathers from the pigeon," *J. Exp. Biol.*, vol. 72, pp. 251–260, 1978.

[297] N. Proctor and P. Lynch, *Manual of ornithology: Avian structure and function*. New haven and Lodon: Yale University Press, 1993.

[298] C. J. Pennycuick, *Modelling the flying bird*. London, UK: Elsevier, 2008.

[299] J. M. V. Rayner, “On aerodynamics and the energetics of vertebrate flapping flight,” *Comtemp. Math.*, vol. 141, pp. 351–400, 1993.

[300] M. Ashby, “Selection of Materials and shape,” in *Materials selection in mechanical design*, 4th ed., Elsevier Ltd, 2011, pp. 243–260.

[301] R. W. Fitzgerald, *Mechanics of materials*, 2nd ed. Addison-Wesley Publishing Company, Inc., 1982.

[302] L. G. Brazier, “On flexure of thin cylindrical shells and other thin sections,” *Proc. R. Soc. London A*, vol. 116, no. 773, pp. 104–114, 1927.

[303] C. R. Calladine, *Theory of shell structures*. Cambridge, UK: Cambridge University Press, 1983.

[304] M. W. Hyer, *Stress analysis of fiber-reinforced composite materials*. McGraw-Hill Companies, Inc., 1998.

[305] D. Hull and T. W. Clyne, *An introduction to composite materials*. Cambridge, UK: Press Syndicate of the University of Cambridge, 1996.

[306] A. Kovalev, A. E. Filippov, and S. N. Gorb, “Unzipping bird feathers.,” *J. R. Soc. Interface*, vol. 11, no. 92, p. 20130988, 2014.

[307] M. Butler and A. S. Johnson, “Are melanized feather barbs stronger?,” *J. Exp. Biol.*, vol. 207, no. Pt 2, pp. 285–293, 2004.

[308] T. Lingham-Soliar, “Feather structure, biomechanics and biomimetics: The incredible lightness of being,” *J. Ornithol.*, vol. 155, no. 2, pp. 323–336, 2014.

[309] W. C. Young, *Roark’s formulas for stress and strain*. New York: McGraw-Hill, 1989.

[310] G. N. Karam and L. J. Gibson, “Elastic buckling of cylindrical shells with elastic cores—I. Analysis,” *Int. J. Solids Struct.*, vol. 32, no. 8–9, pp. 1259–1283, 1995.

[311] L. Gibson and M. Ashby, *Cellular solids: Structure and properties*, 2nd ed. Cambridge: Cambridge University Press, 1997.

[312] M. A. Dawson and L. J. Gibson, “Biomimetics: extending nature’s design of thin-wall shells with cellular cores,” *Press WIT Trans. Ecol. Environ.*, vol. 87, pp. 145–

155, 2006.

[313] R. Weinkamer and P. Fratzl, “Mechanical adaptation of biological materials - The examples of bone and wood,” *Mater. Sci. Eng. C*, vol. 31, no. 6, pp. 1164–1173, 2011.

[314] C. Earland, P. R. Blakey, and J. G. Stell, “Studies on the structure of keratin. IV. The molecular structure of some morphological components of keratins.,” *Biochim. Biophys. Acta*, vol. 6, pp. 268–274, 1962.

[315] C. Earland, P. R. Blakey, and J. G. P. Stell, “Molecular orientation of some keratins,” *Nature*, vol. 196, pp. 1287–1291, 1962.

[316] R. O. Prum, “Development and evolutionary origin of feathers.,” *J. Exp. Zool.*, vol. 285, pp. 291–306, 1999.

[317] S. Pabisch, S. Puchegger, H. O. K. Kirchner, I. M. Weiss, and H. Peterlik, “Keratin homogeneity in the tail feathers of Pavo cristatus and Pavo cristatus mut. alba,” *J. Struct. Biol.*, vol. 172, no. 3, pp. 270–275, 2010.

[318] F. Bleich, *Buckling strength of metal structures*. New York: McGraw-Hill Book Companies, Inc., 1952.

[319] S. Filippov, E. Haseganu, and A. Smirnov, “Buckling analysis of axially compressed squared elastic tubes with weakly supported edges,” *Tech. Mech.*, vol. 20, no. 1, pp. 13–20, 2000.

[320] G. Gerard, *Introduction to structural stability theory*. McGraw-Hill Book Companies, Inc., 1962.

[321] S. Reid, T. Reddy, and M. D. Gray, “Static and dynamic axial crushing of form-filled sheet metal tubes,” *Int. J. Mech. Sci.*, vol. 28, no. 5, pp. 295–322, 1986.

[322] M. Moradi and S. R. Arwade, “Improving buckling response of the square steel tube by using steel foam,” *Struct. Eng. Mech.*, vol. 51, no. 6, pp. 1017–1036, 2014.

[323] P. P. Seide, “Compressive buckling of a long simply supported plate on an elastic foundation,” *J. Aerosp. Sci.*, vol. 25, no. 6, pp. 382–384, 1958.

[324] E. Winkler, *Die Lehre Von Elasticitaet Und Festigkeit*. Prague: H. Dominicus, 1867.

[325] N. Gupta and P. Ray, “Collapse of thin-walled empty and filled square tubes under lateral loading between rigid plates,” *Int. J. Crashworthiness*, vol. 3, no. 3, pp. 265–285, 1998.

[326] P. Moller, “Moller skycar.” [Online]. Available: http://moller.com/.

[327] B. Ratner, A. Hoffman, F. Schoen, and J. Lemons, Eds., *Biomaterials science: An introduction to materials in medicine*, 2nd ed. Elsevier Academic Press, 2004.